

Phase-field modeling of the influence of mechanical stresses on charging and discharging processes in lithium ion batteries

Zur Erlangung des akademischen Grades

DOKTORS DER INGENIEURWISSENSCHAFTEN

von der Fakultät für Maschinenbau des
Karlsruher Instituts für Technologie (KIT)

genehmigte

DISSERTATION

von

Dipl. Phys. Magalie Huttin
geboren am 20.01.1983
in Reims (Frankreich)

Tag der mündlichen Prüfung: 27.02.2014
Hauptreferent: Prof. Dr. M. Kamlah
Korreferent: Prof. Dr. H. J. Seifert

Preface

In the last past decades, the market in rechargeable electrochemical devices allowing the storage of energy has significantly grown. This increasing demand concerns various domains, from portable electronics to zero emission electric vehicles. Because they combine high energy density, high delivered voltage and low self-discharge, lithium ion batteries, one of the most promising and advanced secondary electrochemical systems, have been extensively used [1, 2]. The capability of lithium ion batteries to store energy is inherent to the presence of lithium ions in the electrode material. The lithium ions have the possibility to move between the two different electrodes, thereby releasing or consuming energy depending on if they move from the anode to the cathode or vice versa.

An important characteristic in view of applications which determines the quality of a secondary battery is its life time. Indeed, a rechargeable battery must be reliable over many cycles. Since lithium metal presents safety issues [3], most of the electrode materials are now made of so called intercalation materials [4, 5] that offer to the lithium ions a structured network where they are possibly inserted and released. Unfortunately, such kind of material exhibit capacity fade [6–8] under battery charging and discharging. Capacity fade may have different origins [9, 10]. One origin is due to the insertion and release of lithium ions into the crystalline host structure that give rise to host deformations [11, 12]. Thus, depending on both the applied flux magnitude and the mechanical and transport properties of the host crystalline structure, large stresses may arise and, as a consequence, possibly cause mechanical damages in the intercalation material [13, 14].

In this thesis, we focus on the lithium intercalation into a crystalline particle of some micrometers that is part of an assembly of interconnected small-sized particles forming the porous cathode of a lithium ion battery. In particular, we concentrate on particles made of lithium manganese oxide that exhibit, under particle charging and discharging, nonideal phenomena such as phase segregation [15, 16]. The purpose of this work is the analysis, by means of linear elasticity, of the effect of the phase segregation on the stresses. In this context, lithium insertion and extraction occur reversibly, thus, the present study is not adequate to account for the capacity fade happening under particle cycling where irreversible processes play an important role [17]. However, we could demonstrate [18] that considering the lithium ion diffusion coupled to mechanics when allowing for phase segregation within the cathodic particle leads to a drastic increase in the stress magnitude compared to systems where phase segregation is not accounted for.

Deutschsprachige Zusammenfassung

In den letzten Jahrzehnten ist die Nachfrage an wiederaufladbaren Batterien signifikant gestiegen. Dieser riesige Markt umfasst ein breites Spektrum an Produkten: von tragbaren kleinen elektronischen Geräten wie Mobiltelefone oder Notebooks bis zu größeren Geräten wie Elektroautos.

Wiederaufladbare Lithium-Ionen-Batterien, welche im Vergleich zu anderen Sekundärbatterien eine höhere Energiedichte sowie eine höhere Nennspannung aufweisen, sind sehr viel versprechend. In der Tat werden solche Batterien bereits im breiten Umfang in der Industrie verwendet. Trotz ihrer zahlreichen Vorteile altern Lithium-Ionen-Batteries jedoch relativ schnell. Aus diesem Grund werden heutzutage zahlreiche Studien durchgeführt, um die Zyklierbarkeit von Lithium-Ionen-Batterien — und somit ihre Lebensdauer — zu optimieren.

Das Speichern von Energie in Lithium-Ionen-Batterien wird durch die Einlagerung der Lithium-Ionen in den jeweiligen Elektroden, die Anode und die Kathode, ermöglicht. Während der Batterieentladung wandern die Lithium-Ionen durch den Elektrolyt von der Anode in die Kathode. Das Kathodenmaterial besteht üblicherweise aus einem sogenannten Interkalationsmaterial, welches sich in Form aneinandergrenzender Partikeln von einigen Mikrometern Größe im Elektrolyt eingetaucht befindet. In dieser Arbeit betrachten wir Lithium-Manganoxid (LMO) als Kathodenmaterial.

Bei Raumtemperatur weist dieses Material eine Spinell-Gitterstruktur auf, welche ein dreidimensionales Netzwerk an Zwischengitterplätzen für die Lithium-Ionen-Einlagerung zur Verfügung stellt. Im Laufe der Batterieentladung lagern sich die Lithium-Ionen auf diesen Zwischengitterplätzen ein. Im Kathodenpartikel können während dieses Prozesses je nach Gesamtmenge an Lithium-Ionen im Wirtsmaterial zwei verschiedene kubische Phasen mit unterschiedlichen Lithium-Konzentrationen entstehen.

In dieser Arbeit benutzen wir ein Phasenfeldmodell, um die Lithium-Interkalation und deren mechanischen Auswirkungen auf das Wirtsmaterial zu beschreiben. Im Allgemeinen beruht die Phasenfeldmodellierung auf einem Freie-Energie-Funktional, welches bezüglich seiner natürlichen Variablen minimiert wird. Im gegebenen Fall sind die natürlichen Variablen die lokale Lithium-Konzentration sowie die lokale mechanische Verschiebung. Das Auftreten von Phasensegregation wird zunächst im Rahmen der Molekularfeldtheorie d.h. in der “Mean-Field”-Approximation, und ohne mechanische Kopplung nachgewiesen. Unter der Annahme einer attraktiven Wechselwirkung zwischen benachbarten Lithium-Ionen im Kristall zeigt die “Mean-Field”-Freie-Energie unterhalb einer bestimmten Temperatur, der kritischen Temperatur, einen Konkavitätsbereich für bestimmte Werte der mittleren Lithium-Konzentration. Die Existenz dieses Bereiches ist ein Hinweis für das Auftreten von Phasensegregation. Bei festgelegter mittlerer Lithium-Konzentration im Kathodenpartikel ist es mit Hilfe der Maxwell-Konstruktion möglich, den jeweiligen Anteiler der verschiedenen Phasen im Partikel zu erhalten. Die freie Energiedichte des Freie-Energie-Funktional hat im Wesentlichen die gleiche Form wie die “Mean-Field”-Freie-Energie; die mittlere Lithium-Konzentration wird nun durch die lokale Lithium-Konzentration ersetzt. Da der Aufbau einer Phasengrenze zwischen Phasen unterschiedlicher Lithium-Konzentrationen Energie kostet, wurde ein zusätzlicher Term, der sogenannte Gradiententerm, in der freien Energiedichte hinzugefügt. Dieser Term bestraft den Aufbau von Lithium-Konzentrationsgradienten im Partikel. Ferner ist die mechanische Auswirkung der Lithium-Interkalation auf das Wirtsmaterial durch die sogenannte Verformungsenergie berücksichtigt worden.

Die Ergebnisse der Phasenfeldsimulationen zeigen, dass den Aufbau Phasen unterschiedlicher Lithium-Konzentrationen hohe mechanische Spannungen im Partikel verursacht. Somit kann das Auftreten von Phasensegregation als eine mögliche Ursache für das mechanische Versagen der Partikeln aufgefasst werden, was die schnelle Alterung der Batterie unter mehreren Ent- und Beladungszyklen erklären kann. Außerdem haben wir auch gezeigt, dass sowohl die angelegte Flusstärke an der Partikeloberfläche als auch die Partikelgeometrie eine bedeutsame Rolle für die Größe der auftretenden mechanischen Spannungen spielen.

List of Symbols

\bar{n}	Averaged number of lithium occupation or averaged lithium concentration
σ	Stress tensor [Pa]
σ_a	Stress tensor applied at the particle surface [Pa]
ε	Total strain tensor
ε^{el}	Elastic strain tensor
ε^{Li}	Intercalation-induced strain tensor
C	Stiffness tensor [Pa]
J	Local lithium flux within the cathodic particle [$\#/m^2 s$]
J^{ch}	Lithium flux induced by lithium concentration gradients only [$\#/m^2 s$]
J^{cp}	Stress-induced lithium flux only [$\#/m^2 s$]
J_a	Lithium flux applied at the particle surface [$\#/m^2 s$]
n	Outgoing unit vector normal to the particle surface
u	Mechanical displacement [m]
η	Overpotential [V]
Γ	Total number of nearest-neighboring interstitial sites available for the lithium ions in the host material [J]
γ	Particle aspect ratio (ellipsoidal particle) in the reference state
κ	Interfacial energy term [J/m^2]
λ_1	Lamé's first coefficient
λ_2	Lamé's second coefficient
μ	Total chemical potential within the cathodic particle [J]
μ^{ch}	Chemical potential driven by the lithium concentration gradients only [J]
μ^{cp}	Chemical potential driven by the hydrostatic stress gradients only [J]

ν	Poisson ratio
∂V_0	Boundary surface of the particle in the reference state $[\text{m}^2]$
ϕ_l	Electrochemical potential in the liquid phase of the dualfoil model $[V]$
ϕ_s	Electrochemical potential in the solid phase of the dualfoil model $[V]$
Ψ	Total free energy $[\text{J}]$
ψ	Total free energy density $[\text{J}/\text{m}^3]$
Ψ^{ch}	Chemical free energy $[\text{J}]$
ψ^{ch}	Chemical free energy density $[\text{J}/\text{m}^3]$
Ψ^{es}	Elastic strain free energy $[\text{J}]$
ψ^{es}	Elastic strain free energy density $[\text{J}/\text{m}^3]$
Ψ^{gd}	Interfacial free energy $[\text{J}]$
ψ^{gd}	Interfacial free energy density $[\text{J}/\text{m}^3]$
σ_h	Hydrostatic stress $[\text{Pa}]$
$\tilde{\Omega}$	Dimensionless partial volume
$\tilde{\Omega}_0$	Constant dimensionless partial volume
a_0	Volume occupied by one lithium ion in the reference state $[\text{m}^3]$
C	C -rate
D_0	Diffusion coefficient $[\text{m}^2/\text{s}]$
E	Young's modulus $[\text{Pa}]$
E_0	Constant Young's modulus $[\text{Pa}]$
F	(Statistical) free energy $[\text{J}]$
J	(Statistical) grand canonical potential $[\text{J}]$
J_{an}	Incoming lithium flux normal to the particle surface $[\#/ \text{m}^2 \text{ s}]$
k_B	Boltzman constant, $k_B \approx 1.38 \cdot 10^{-23} \text{ J/K}$
L	Onsager coefficient $[\text{s}/\text{kg m}^3]$

N	Total number of lithium ions in the cathodic particle
n	Number of lithium occupation or lithium concentration
n_0	Number of lithium occupation or lithium concentration in the reference state
n_l	Lithium concentration in the liquid phase of the dualfoil model
n_s	Lithium concentration in the solid phase of the dualfoil model
r_0	Particle radius (spherical particle) in the reference state [m]
S	(Statistical) entropy [J/K]
T	Temperatur [K]
t	time [s]
U	Interaction energy between two nearest-neighboring lithium ions in the host material [J]
U_0	Intercalation energy of one lithium ion in the host material [J]
V_0	Volume of the cathodic particle in the reference state [m ³]
x	State of charge
x_0	State of charge in the reference state
\mathcal{N}	Total number of lattice sites available for the lithium ion intercalation
\mathcal{N}_A	Avogadro constant, $\mathcal{N}_A \approx 6.02 \cdot 10^{23} \text{ mol}^{-1}$
\mathcal{Z}_c	Canonical partition function
\mathcal{Z}_{gc}	Grand canonical partition function

Contents

Preface	iii
Deutschsprachige Zusammenfassung	vi
List of Symbols	vii
1 Introduction and generalities	1
1.1 Generalities on lithium ion batteries	1
1.2 Basics on lithium ion batteries	3
1.3 $\text{Li}_x\text{Mn}_2\text{O}_4$ as cathodic material	5
2 Overview on battery modeling	7
2.1 Multiscale modeling	7
2.1.1 Dualfoil and single particle modeling	7
2.1.2 Basics of the single particle modeling	9
2.2 Single particle modeling in the dilute solution approach	9
2.2.1 Theory	9
2.2.2 Particles of spherical symmetry	13
2.2.3 Particles of ellipsoidal symmetry	19
2.3 Dualfoil modeling	26
2.3.1 Theory	26
2.3.2 Effect of a nonconstant flux at the cathodic particle surface	31
2.3.3 Many-particle states	32
3 Phase-field modeling	37
3.1 Microscopic underlying structure	38
3.1.1 Crystalline structure	38
3.1.2 Microscopic Hamiltonian	41
3.1.3 Thermodynamical potentials	46
3.2 Mean-field approximation and beyond	48
3.2.1 Mean-field approximation and homogeneous state	48
3.2.2 Phase segregation and Maxwell construction	50
3.2.3 Coarse-graining	54
3.2.4 Host deformations	57
3.2.5 Total free energy of the system	60
3.3 Near to equilibrium	63
3.3.1 Equilibrium conditions	63
3.3.2 Evolution equations	64
3.3.3 Mathematical formulation	69

4	Phase-segregated states of the spherically symmetric particle model	73
4.1	Equilibrium states	74
4.1.1	Origin of the phase separation and system relaxation	74
4.1.2	Effect of the interfacial energy	80
4.1.3	Effect of the elastic strain energy term	82
4.2	Dynamical behavior	88
4.2.1	Different contributions to the flux	88
4.2.2	Effect of the phase segregation on the stresses	95
4.2.3	Coupling with the dualfoil model	99
4.3	Concentration-dependent material parameters	104
4.3.1	Motivation	104
4.3.2	Theory	108
4.3.3	Influence of the concentration-dependent material parameters in the dilute solution approach	111
4.3.4	Influence of the concentration-dependent material parameters in phase-field modeling	114
5	Influence of the particle geometry on the phase-segregated states	123
5.1	System states of the spherical particle	123
5.1.1	Influence of the model dimensionality	123
5.1.2	Influence of the system history	129
5.1.3	Effect of the lithium induced deformations	130
5.2	Equilibrium states of a particle of ellipsoidal symmetry	134
5.2.1	Influence of the particle aspect ratio	134
5.2.2	Effect of the lithium induced deformations	137
5.3	Dynamical states of a particle of ellipsoidal symmetry	143
6	Conclusion	151
A	Flux boundary condition at the inner particle boundaries	153
A.1	One-dimensional particle model	153
A.1.1	Boundary conditions at the particle center	154
A.1.2	Lithium flux at the particle center	160
A.2	Two-dimensional particle model	163
A.2.1	Derivation of the boundary conditions from the system symmetries	163
A.2.2	Reduction of the total number of boundary conditions	166
A.2.3	Lithium flux at the particle inner boundaries	167
B	Mean-field approximation	173
C	Estimate of the interfacial energy term	177
	Bibliography	189
	Acknowledgment	191

1

Introduction and generalities

Introduction

This introductory chapter is devoted to the understanding of the problems inherent to energy storage and delivering in lithium ion batteries (LIB's) with focus on lithium manganese oxide (LMO) as cathodic material.

First, a short review over different existing LIB systems will be established. The second part of this chapter provides some basic knowledge needed to understand how batteries, in general, may provide electric energy. And, finally, we will draw attention on LMO which is one of the most promising candidates to be used at the cathode of LIB's. However, despite its numerous advantages compared to other potential cathodic materials, LMO gives rise to battery capacity fade possibly enhanced by phase segregation and structural modifications happening during battery charging and discharging.

1.1 Generalities on lithium ion batteries

“Lithium ion batteries” is a general term that covers all kinds of batteries where the exchange species between the two different electrodes is the lithium ion Li^+ .

Batteries are commonly classified into two categories, being the primary and secondary batteries. Primary batteries refer to batteries that are used at most once for being discharged. On the contrary, secondary batteries are possibly used several times because of their ability to be recharged. A battery is potentially rechargeable when the chemical reactions that take place at both electrodes are at least partially reversible. In that case there are neither side reactions leading to electrochemically inaccessible phases nor significant losses of mechanical stability [4]. Indeed, even for rechargeable batteries, the electrochemical reactions are not completely reversible due to unavoidable irreversible processes that further lead to capacity fade under battery cycling. But, differently from primary batteries, secondary batteries are easily and safely rechargeable over many charging and discharging cycles before they get deteriorated. Increasing the number of possible cycles is nowadays a big concern on the route to improve the battery life time.

Compared to other battery systems, LIB's present many advantages inherent to the properties of the lithium element which is both the most electropositive and lightest metal. Indeed, LIB's generally deliver an high electrode potential. But, the most relevant advantage of LIB's over other battery systems is their elevated energy density, as illustrated in Fig. 1.1, which allows for integrating them into small electronic devices.

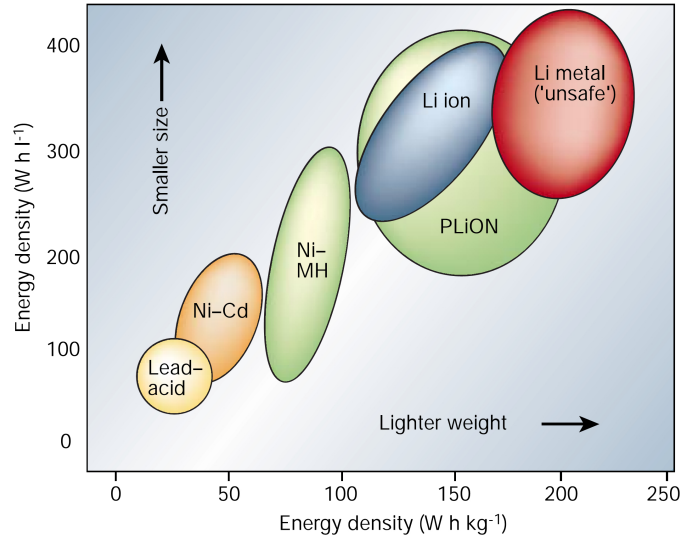


Figure 1.1: Comparison of different battery systems regarding the battery energy density obtained from Ref. [19].

Starting from now, we focus on rechargeable LIB's where, during discharging, lithium ions move from the anode to the cathode whereas, during charging, they move back from the cathode to the anode.

There exist plenty of potential candidates to be used as electrode materials [20]. Carbonaceous materials [21] like lithium graphite (Li_xC_6) are generally used as anodic material since they give the possibility to achieve a high delivered electrode potential. Despite an higher self-discharge rate compared to pure lithium metal, such materials significantly improve the battery reliability in term of safety. Indeed, due to the high reactivity of lithium metal, its utilization as anodic material has been limited because of safety issues [3, 22]. Among these problems, one can cite the formation of dendrites at the electrode surface that may penetrate the electrolyte and reach the cathode engendering a short circuit in the battery. Further, a short circuit in a battery induces overheating and gives rise to battery runaway [23].

In order to increase the surface in contact with the electrolyte and thus the ionic conductivity, cathodes of LIB's are usually made of an assembly of small-sized particles. Standard particle materials are insertion compound materials where the lithium ions are intercalated at specific locations into a crystalline host structure. Among these materials, we can mention Li_xFePO_4 , Li_xCoO_2 , Li_xNiO_2 and $\text{Li}_x\text{Mn}_2\text{O}_4$ (see Refs. [24–27] for an overview over these different materials). Especially, here, we focus on LMO which is one of the most promising cathodic materials. This material offers a three-dimensional spinel network for the lithium ion intercalation differently from Li_xFePO_4 on the one hand, and from Li_xCoO_2 and Li_xNiO_2 on the other hand, that only present one and two-dimensional networks for the lithium ion intercalation, respectively.

Despite its numerous advantages like its elevated energy density, high delivered voltage and low self-discharge, LIB's with LMO as cathodic particle material exhibit capacity fade [17] even after a very low number of cycles [14]. Capacity fade may have different origins like the existence of unwanted side reactions depending on the electrolyte composition [28, 29]. One important origin is the existence of phase segregation which may generate large stresses leading to particle crackings. A well-known model accounting for phase segregation is the sharp interface model [30, 31]. In this work, we attend to

quantify the stresses arising in a cathodic LMO particle using a phase-field model [32] where a smooth diffuse interface between the two different lithium concentration phases is possibly accounted for.

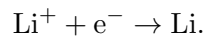
1.2 Basics on lithium ion batteries

In this part, we briefly review some basics to understand how a battery, and in particular a LIB, works. A battery is a device made, in the most simple case, of two different electrodes, the anode and the cathode, that are not directly in contact, but immersed in an electrolyte and connected to an external circuit by an electronic conductor as illustrated in Fig. 1.2. By definition, the electrode exhibiting the highest electrode potential or Fermi energy before battery discharging is called the anode, the other one being referred to as the cathode.

During the discharging, the battery delivers a current and hence furnishes to the external circuit electrical energy obtained through conversion of stored internal chemical energy present in the battery. The delivered current is a transport of electrons e^- from the anode to the cathode that is correlated with a transport of lithium ions Li^+ , also from the anode to the cathode. At the anode, lithium atoms are oxidized



and, at the cathode, the electrons and the lithium ions that have been transferred from the anode via the external circuit and the electrolyte, respectively, are recombined together by reduction

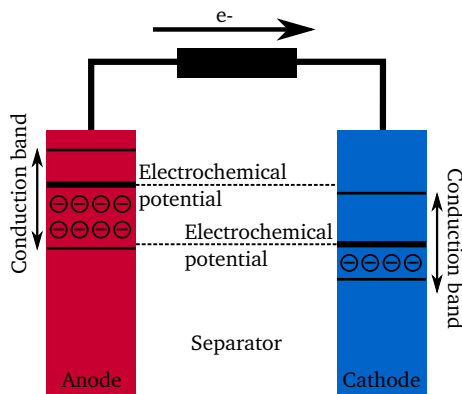


For both electrons and lithium ions to be spontaneously carried from the anode to the cathode, it is required that the electrodes, analogously to metals, allow for the transport of free electrons and that they exhibit a chemical potential difference. The electrode that shows the higher chemical potential is called the cathode, as opposite to the anode. That way, the negatively charged electrons minimize their energy when they move away from the anode into the cathode.

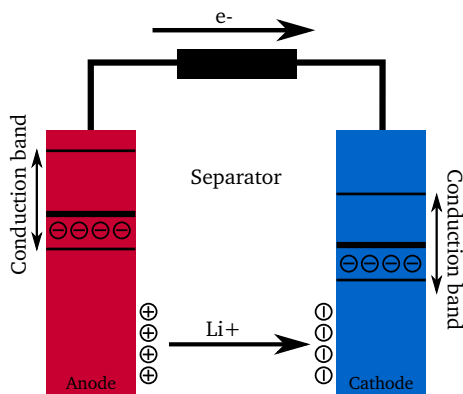
The positively charged lithium ions that are chemically bonded to the electrode and electrolyte materials first have to move from the anode into the electrolyte. There, they are transported from the anode surface to the cathode surface by both diffusion and migration before being finally inserted into the cathode. As schematically sketched in Fig. 1.2, the lithium ion transfer from one medium to the other is allowed only if their energy is minimized at each of these transfers.

Unfortunately, the transport of electrons and lithium ions from the anode into the cathode does not occur without energetic losses that may have different origins [33] like chemical side reactions, bulk and interfacial resistances of both electrodes and electrolyte, inelastic electrode deformations due to the lithium intercalation and release. Throughout this work, these nonreversible processes that all may induce battery capacity fade will be neglected and the transport of electrons and lithium ions from the anode to the cathode is assumed to be reversible¹.

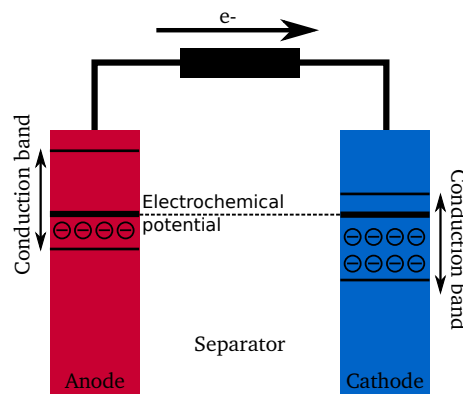
¹In this work, we only consider linear elasticity that does not account for mechanical fracture. However, we do not exclude hysteretic behavior induced by phase segregation.



(a) Battery state before discharging. The battery discharging possibly occurs only if the electrochemical potential at one of the two electrodes (the anode) is significantly higher than the electrochemical potential within the other electrode (the cathode) in order to allow for the spontaneous electronic transfer from the anode to the cathode.



(b) Battery state after the electrons have been released from the anode. The electrons rapidly move to the cathode surface whereas the lithium ions which need more time than the electrons to be transferred from the anode to the cathode via the electrolyte build surfacic charge at the anode surface. Further, this surfacic charges build an electric field that enhances the lithium ions diffusion towards the cathode by migration.



(c) Battery state at the end of the discharging after the lithium ions have been recombined after the electrons and inserted into the cathodic material. Compared to the initial state represented in Fig. 1.2(a), since free electrons have been transferred from the anode to the cathode, the anodic electrochemical potential diminishes whereas the cathodic electrochemical potential increases.

Figure 1.2: Sketch of the electronic state in both electrodes at different stages during battery discharging.

1.3 $\text{Li}_x\text{Mn}_2\text{O}_4$ as cathodic material

In the following and as said in Sec.1.1, we focus on LIB's made of LMO as cathodic material. LMO is a three-dimensional insertion compound allowing for the intercalation of a mobile guest species represented by the lithium ions into an host matrix made of $\text{Li}_{x_0}\text{Mn}_2\text{O}_4$, x_0 being a reference state of charge. During battery charging and discharging, lithium ions are either inserted into or released from the host matrix so that the state of charge x also equal to the lithium ion concentration changes.

LMO exhibits nonideal effects that may affect the lithium intercalation. Plenty of efforts based on experimental measurements [34–36] have been done to understand and compute the phase diagram of $\text{Li}_x\text{Mn}_2\text{O}_4$ as function of the state of charge x and of the temperature T . Depending on the temperature, this material possibly exhibits phase segregation [9] in the range of values $0 < x < 1$ where the crystalline host structure remains cubic spinel. At $x = 1$, it is commonly accepted and experimentally proven that, due to the Jahn-Teller distortion regarding the manganese ions [37], $\text{Li}_x\text{Mn}_2\text{O}_4$ undergoes a phase transition where the crystalline material becomes tetragonal. A theoretical study [38] also indicates the existence of lithium ordering at $x = 0.5$, often observed in intercalation systems [39], but on the existence of this ordering in LMO material, there is controversy in the experimental literature [40]. An example of the theoretically computed phase diagram for LMO as result of first-principle calculations is shown in Fig. 1.3. However, as already pointed out, this phase diagram exhibits several discrepancies

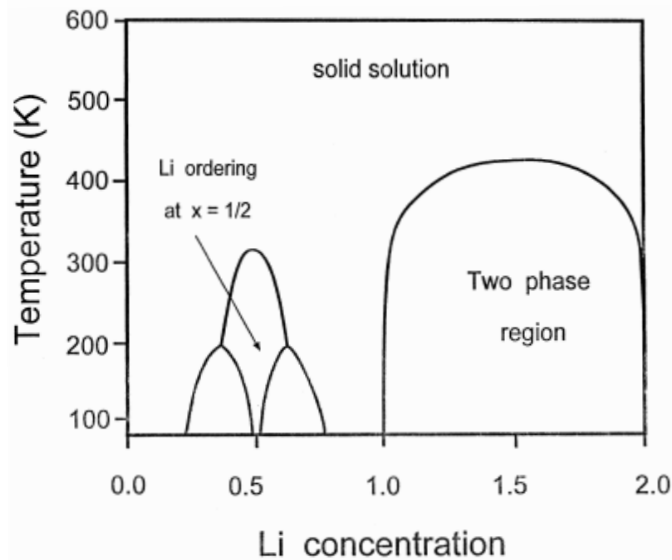


Figure 1.3: Example of a computed phase diagram for LMO material as function of both the temperature T and the state of charge x also equal to the lithium concentration n . The presently shown phase diagram has been calculated by A. V. der Ven et al. in Ref. [38].

with the experimentally observed phases.

In this work, neglecting the effect of lithium ordering, we focus on the phase segregation that happens at room temperature in the range of values $0 < x < 1$. Indeed, on the contrary to lithium ordering that probably has no significant influence on the stresses arising in the cathodic particle, phase segregation may induce large lithium concentration gradients at a mesoscopic scale and thus also large stress values.

Moreover, whereas lithium ordering seems to have no effect on the battery macroscopic quantities, the 4 V-plateau phase highlighted on the experimentally measured battery discharge curve is imputed to phase segregation [34, 40]. We further neglect the cubic to tetragonal transition at $x = 1$ since the cathodic state of charge is rarely driven up to one except for LIB delivering a large current density [9].

Conclusion

Over battery charging and discharging, since the lithium amount at the cathode is varied, LMO material is brought out of equilibrium. That way, the state of charge, usually driven between 0 and 1, possibly reaches values where phase segregation occurs.

In the next chapter (Chp. 2), based on the work done by Sastry [41] that neglects the phase segregation and uses in place a dilute solution approximation, a coupling term between the chemical potential and the hydrostatic stress is introduced to account for stresses induced by lithium intercalation into and release from the host material made of LMO. That way, it will be demonstrated that large stresses arise only if the system is driven far away from equilibrium.

In Chps. 4 - 5, the effect of phase segregation whose theory has been previously introduced in Chp. 3, is considered. In this context, for a system being in a phase-segregated state, even at equilibrium, stresses whose magnitude is significantly larger than those obtained by means of the usual dilute solution model are present.

2

Overview on battery modeling

Introduction

LIB's are complex systems described by numerous quantities that are all coupled via many interaction mechanisms, being predominantly electrochemical and mechanical. On the one hand, several macroscopic quantities are needed to represent the behavior of the entire LIB. On the other hand, since the electrodes are granular, lithium intercalation and release inside each of the particles that form the granular electrodes is described by means of microscopic quantities within a “single-particle model”.

In this chapter, we will briefly review the so-called “dualfoil model” [42] that accounts for the coupling between the microscopic and macroscopic quantities allowing for the understanding of the macroscopic behavior of porous LIB's. In this thesis we focus on the particle mechanics in the cathode under battery loading and unloading, thus we mainly analyze the lithium insertion and extraction into a single cathodic particle made of LMO. At this scale, the coupling between lithium diffusion and mechanics needed to explain the stresses arising at the particle level is modeled using a thermo-mechanical analogy developed by Prussin [43] in the context of linear elasticity.

The results obtained using a dilute solution model coupled to mechanics valid at the particle level are summarized. This analysis is based on the work by X. Zhang *et al.* [41] and no phase segregation is accounted for. The latter will be considered in the next three chapters (Chps. 3, 4 and 5) in the context of phase-field modeling.

Furthermore, in order to represent the battery behavior, this single-particle model with mechanics can be embedded into a macroscopic battery by means of the dualfoil model.

2.1 Multiscale modeling

2.1.1 Dualfoil and single particle modeling

As said in Sec. 1.1, cathodes made of LMO are granular meaning that they are made of an assembly of small-sized particles (around some micrometers), whose shape and exact size are not homogeneously distributed over the cathode as illustrated in Fig. 2.1. For modeling purposes, cathodic particles are here assumed to be of regular shapes being either perfectly spherical or ellipsoidal. A numerical study of particles of specific realistic shapes has been realized in Ref. [44, 45].

In order to improve the electronic conductivity, these particles are generally mixed together with carbon black [46]. LMO particles and carbon black usually are closely packed together and immersed

in the electrolytic solution meaning that these particles are interconnected and thus, as a consequence, all are coupled via interaction mechanisms.

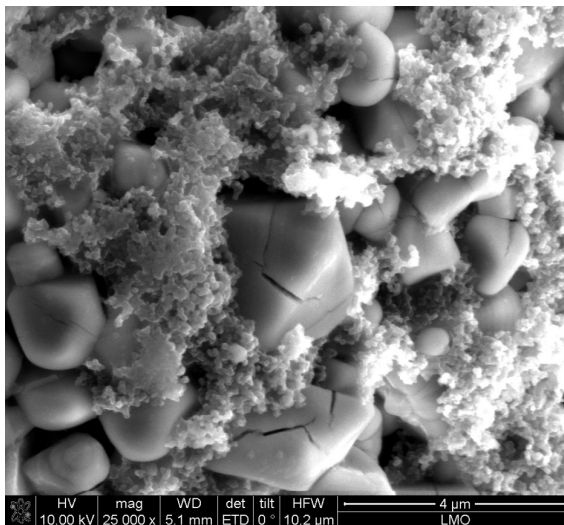


Figure 2.1: *Picture of cathodic particles made of LMO after lithium intercalation, courtesy of Di Chen, Reiner Mönig, Sven Glatthaar.*

The first kind of interaction is due to direct mechanical contact between nearest neighboring particles. Indeed, since lithium insertion and release into LMO particles induce volumetric changes, mechanical stresses at the contact surface between two interconnected particles are expected. By means of a homogenization method [47], the effect of the mechanics at the battery level has been taken into account in Ref. [48]. Nevertheless, for simplicity in the description of the lithium intercalation into LMO particles, the effect of the mechanics in the context of a macroscopic battery approach will be neglected in the following.

The second kind of interaction is the electrochemical coupling induced by the presence of the electrolyte that fills the interstices between the particles. This coupling can be described by means of the Butler-Volmer equation (see Eq. (2.73) of Sec. 2.3.1) that establishes a relationship between the lithium flux at the surface of a LMO particle located at a particular position in the cathode and the corresponding local overpotential. In this context, the lithium flux at the particle surfaces is a local quantity that also depends on time. An effectively one-dimensional battery model, also referred to as dualfoil model, that accounts for this interparticle electrochemical coupling has been proposed and implemented by Doyle and Newman [42] and will be briefly introduced in Sec. 2.3.1. Further, this model has been extended by R. E. García *et al.* [49] to study two-dimensional batteries.

In a first simplified approach presented in next section (Sec. 2.1.2), the local effect of the interparticle electrochemical interaction is neglected when describing the effect of the lithium ion diffusion on the stresses arising into a LMO particle. In this context, it is enough to consider a single LMO particle completely decoupled from the rest of the battery. In this kind of model, referred to as single-particle model, the lithium flux applied at the surface of the particle becomes an externally fixed boundary condition differently from the dualfoil model where the flux at the particle surfaces is a dynamical quantity determined by the Butler-Volmer equation.

2.1.2 Basics of the single particle modeling

In this part, a single three-dimensional cathodic particle is considered entirely decoupled from the rest of the battery. Within this approach the particle surface flux $J_{an} = -\mathbf{J}_a \cdot \mathbf{n}$ is fixed by means of boundary conditions. Here, \mathbf{n} is the surface normal which points out of the particle. Typically the flux magnitude is expressed in terms of a dimensionless number C referred to as the C -rate, as well as of geometrical particle properties in the initial state of charge x_0 ,

$$J_{an} = \pm \frac{C}{t_0} \frac{V_0}{a_0^3 S_0}. \quad (2.1)$$

Here, V_0 and S_0 denote the volume and surface area of the particle initially made of $\text{Li}_{x_0}\text{Mn}_2\text{O}_4$, the so-called host material. In the above equation, Eq. (2.1), the sign “+” stands for lithium insertion while “−” corresponds to lithium extraction. The theoretical C -rate considered here is related to the single cathodic particle and not, as usual, to the entire battery. It is defined such that for $C = 1$ the particle initially void of lithium, becomes completely filled with lithium after application of the flux Eq. (2.1) during one hour, i.e. $t_0 = 3600$ s. The quantity a_0^3 refers to the volume of host material that can accept at most *one* lithium ion, then the quantity V_0/a_0^3 is the maximal number of lithium ions that can be inserted inside of the particle. From these considerations, we deduce that the flux magnitude J_{an} has the unit of a number of lithium ions per unit of area and per time, i.e. it is expressed in $[\#/m^2 \text{ s}]$.

Similarly to the flux applied at the particle surface, the stresses arising at the particle surface are externally fixed by boundary conditions. As said in Sec. 2.1.1, the interparticle mechanical interaction is neglected meaning that there is no stress at the surface of the single cathodic particle.

A common approach to model the lithium intercalation into a single cathodic particle made of LMO is the dilute solution approximation where the interacting term describing the interaction between the lithium ions as well as some of the entropic terms are neglected. This approximation is valid only if the lithium amount present in the particle is very little compared to the maximal allowed lithium amount, $x \ll 1$, and cannot account for phase segregation that occurs during the lithium intercalation.

In this chapter, based on the work of Ref. [41], we present some results obtained using a dilute solution model coupled to mechanics whereas, in the next three chapters (Chps. 3, 4 and 5), we will introduce a phase-field model coupled to mechanics that accounts for nonideal effects induced by the phase segregation.

2.2 Single particle modeling in the dilute solution approach

2.2.1 Theory

We here introduce very briefly the theory of the dilute solution model coupled to mechanics. Its basic assumption is that the local number of lithium occupation is low, $n \ll 1$.

The local number of lithium occupation is a dimensionless quantity whose density n/a_0^3 integrated over the entire particle volume V_0 is equal to the total number of lithium ions N present in the particle,

$$\int_{V_0} dV \frac{n}{a_0^3} = N.$$

The local number of lithium occupation n is related to the lithium concentration c expressed in mol/m^3

by

$$\frac{n}{a_0^3} = c \mathcal{N}_A$$

where \mathcal{N}_A denotes the Avogadro constant. It is then also equal to

$$n = \frac{c}{c_{\max}}$$

where $c_{\max} = 1/a_0^3 \mathcal{N}_A$ is the maximum allowed lithium concentration (in mol/m³) related to a state of charge $x = 1$ in the host material $\text{Li}_x\text{Mn}_2\text{O}_4$. In that sense, the local number of lithium concentration n appears as a normalized lithium concentration and, in the following, it will be simply referred to as (local) ‘‘lithium concentration’’.

Historically, the dilute solution model predates its extension, the phase-field model. Since the theory of the latter will be introduced in Chp. 3 and reproduces the dilute solution model in the limit of low concentrations, we will omit the details here.

Similarly to the phase-field model, the driving equations for the dilute solution model are represented by a set of two differential equations that stand for the conservation of the number of lithium ions on the one hand and for the conservation of the the host material momentum, here equal to zero, i.e. mechanical equilibrium, on the other hand. A local formulation of these conservation laws is given by

$$\frac{\partial}{\partial t} \left(\frac{n}{a_0^3} \right) + \nabla \cdot \mathbf{J} = 0, \quad (2.2)$$

$$\nabla \cdot \boldsymbol{\sigma} = \mathbf{0} \quad (2.3)$$

where n , \mathbf{J} and $\boldsymbol{\sigma}$ denote the local lithium concentration, the local lithium flux and the local stress tensor, respectively. At this place, we remark that the expression of the lithium flux \mathbf{J} in $[\#/m^2 \text{ s}]$ is consistent with Eq. (2.2) if the time t has the unit of second.

For systems that are not driven far away from equilibrium, the local lithium flux \mathbf{J} , which is a nonequilibrium quantity, is proportional to the gradient of the chemical potential μ , which is an equilibrium quantity. According to the Onsager relation, it is expressed as [50]

$$\mathbf{J} = -L \nabla \mu. \quad (2.4)$$

Here, the phenomenological Onsager coefficient $L \geq 0$ quantifies the response of the system, namely the local lithium flux, to a perturbation which consists in a local variation of the chemical potential, driven, among other possible sources, by a the modification of the local lithium concentration in the system. In the dilute solution approximation, this coefficient is usually linear in the lithium concentration n and inversely proportional to the temperature T [50],

$$L = \frac{D_0 n}{a_0^3 k_B T} \quad (2.5)$$

where D_0 is the constant diffusion coefficient of the host material and k_B denotes the Boltzmann constant.

The chemical potential is expressed as a superposition of the chemical potential μ^{ch} induced by the solute, here represented by the lithium ions, in the crystalline host material and of the chemical potential μ^{cp} induced by the mechanical coupling with the host material,

$$\mu = \mu^{\text{ch}} + \mu^{\text{cp}}. \quad (2.6)$$

According to the Nernst law [51] valid in the context of a dilute solution where the species that form the solute do not interact each other, it holds

$$\mu^{\text{ch}} = \mu_0 + k_B T \ln n \quad (2.7)$$

where μ_0 is a temperature dependent reference chemical potential that does not need to be specified since the battery is considered as working at constant temperature. The chemical potential induced by the mechanical coupling is given by

$$\mu^{\text{cp}} = -\tilde{\Omega} a_0^3 \sigma_h \quad (2.8)$$

where $\tilde{\Omega}$ is the dimensionless partial volume of the lithium ions within the host material and $\sigma_h = 1/3 \sigma_{ii}$ the hydrostatic stress. The dimensionless partial volume is proportional to the partial molar volume, $\tilde{\Omega} = a_0^3 \mathcal{N}_A \tilde{\Omega}$ (in m^3/mol), and describes the relative volume change under variation of the lithium amount. It is usually treated as a constant of the model.

These two contributions to the chemical potential give rise to two flux terms

$$\mathbf{J}^{\text{ch}} = -L \nabla \mu^{\text{ch}}, \quad (2.9)$$

$$\mathbf{J}^{\text{cp}} = -L \nabla \mu^{\text{cp}} \quad (2.10)$$

via the Onsager relation Eq. (2.4). The conventional diffusion flux \mathbf{J}^{ch} drives the relaxation into the entropically favoured equilibrium state with homogeneous lithium concentration. The backaction of host deformations onto the lithium motion leads to the flux \mathbf{J}^{cp} which tends to drive the system towards an energetically favourable minimal-stress state corresponding to a minimization of the elastic strain energy of the system, see Chp. 3.

In linear elasticity the stress tensor $\boldsymbol{\sigma}$ linearly depends on the elastic strain tensor $\boldsymbol{\varepsilon}^{\text{el}}$ upon

$$\sigma_{ij} = C_{ijkl} \varepsilon_{kl}^{\text{el}} \quad (2.11)$$

where C_{ijkl} is the $ijkl$ -component of the fourth-rank stiffness tensor. In this work, the indices i, j, k and l range from 1 to 3 and are related to the three spatial coordinates. The summation convention is applied to repeated indices. The partial derivative with respect to the i -th coordinate is denoted by $,i$. When the state of charge $0 < x < 1$ the cubic host material is assumed to be isotropic and it holds

$$C_{ijkl} = \lambda_2 \delta_{ij} \delta_{kl} + \lambda_1 \left(\delta_{ik} \delta_{jl} + \delta_{il} \delta_{jk} \right)$$

where δ_{ij} denotes the Kronecker delta. The quantities $\lambda_1 > 0$ and λ_2 are Lamé's first and second parameters, respectively. Both of them depend on Young's modulus E and on the Poisson ratio ν of the host material

$$\lambda_1 = \frac{E}{2(1+\nu)}, \quad (2.12)$$

$$\lambda_2 = \frac{2\nu\lambda_1}{1-2\nu}. \quad (2.13)$$

For later purposes, we define the useful linear combination

$$\lambda = \frac{3\lambda_2 + 2\lambda_1}{3}. \quad (2.14)$$

Note that, for the first, the Young's modulus of the host material is assumed to be constant. Its constant value is referred to as E_0 .

In the considered system, it is assumed that the host material undergoes small deformations only. Then, the components of total strain tensor are related to the mechanical displacement \mathbf{u}

$$\varepsilon_{ij} = \frac{1}{2} (u_{i,j} + u_{j,i}). \quad (2.15)$$

The origin of the host material deformations is two-fold. One origin is the lithium intercalation which gives rise to isotropic volumetric strains. Analogously to strains induced by variation in the temperature [41], strains induced by variation in the lithium concentration are given by

$$\varepsilon_{ij}^{\text{Li}} = \frac{\tilde{\Omega}}{3} (n - n_0) \delta_{ij} \quad (2.16)$$

where n_0 is a reference homogeneous number of lithium occupation related to the reference state of the host material $\text{Li}_{x_0}\text{Mn}_2\text{O}_4$. The other origin of strain is mechanical stress. On the contrary to elastic strains, lithium induced strains are stress-free and are not a consequence of mechanical stresses. The elastic strains purely induced by mechanical stresses, needed in Eq. (2.11), are given by

$$\varepsilon_{ij}^{\text{el}} = \varepsilon_{ij} - \varepsilon_{ij}^{\text{Li}}.$$

In order to complete the driving equations Eq. (2.2) and Eq. (2.3) as well as the constitutive relationships Eq. (2.4) - Eq. (2.11), the boundary conditions holding at the particle surface ∂V_0 have to be specified. According to the considerations of Sec. 2.1.1, these boundary conditions read

$$-\mathbf{J} \cdot \mathbf{n} \Big|_{\partial V_0} = J_{an} \quad (2.17)$$

$$\boldsymbol{\sigma} \cdot \mathbf{n} \Big|_{\partial V_0} = \mathbf{0}. \quad (2.18)$$

During the lithium intercalation, it is assumed that the temperature remains constantly equal to $T = (273.15 + 25) \text{K}$. The material parameters obtained from both Ref. [41] and Ref. [52] are all summarized in Tab. 2.1.

Name	Symbol and unit	Value
Diffusion coefficient	D_0 [m ² /s]	$7.08 \cdot 10^{-15}$
Young's modulus	E_0 [GPa]	10
Poisson coefficient	ν	0.3
Lattice parameter at $x = 0.2$	a_i [Å]	4.0341
Lattice parameter at $x = 0.995$	a_f [Å]	4.1141

Table 2.1: Material parameters of $\text{Li}_x\text{Mn}_2\text{O}_4$.

Here, the concentration-dependent lattice parameter a , e.g. the low-concentration lattice parameter a_i as well as the high-concentration lattice parameter a_f of Tab. 2.1, is related to the face-centered cubic lattice built by the oxygen ions that form the host crystalline material as sketched in Fig. 3.1

of Sec. 3.1.1. Unless specified otherwise, the dimensionless partial volume, as a function of the lattice parameter,

$$\tilde{\Omega} = \frac{1}{a_0^3} \frac{\partial a^3}{\partial n}, \quad (2.19)$$

is assumed to be constant and is approximated by

$$\tilde{\Omega}_0 = \frac{1}{a_0^3} \left(\frac{a_f^3 - a_i^3}{n_f - n_i} \right). \quad (2.20)$$

In reality the surface flux is related to the lithium concentration at the particle surface by the Butler-Volmer relation (see Eq. (2.73)). It ensures that the flux vanishes when the surface concentration becomes either zero or one. However, within the single particle model, the surface flux is given by boundary conditions without consideration of the surface concentration. This may lead to unphysical lithium concentrations above one. To avoid this behavior, the single particle simulations are only run until the stop condition,

$$n \Big|_{\partial V_0} = 0 \text{ or } n \Big|_{\partial V_0} = 1, \quad (2.21)$$

is fulfilled.

2.2.2 Particles of spherical symmetry

Mathematical formulation

To describe the lithium intercalation into a cathodic particle of spherical symmetry with radius r_0 , we make use of the usual spherical coordinate system (r, θ, φ) with local orthonormal basis $(\mathbf{e}_r, \mathbf{e}_\theta, \mathbf{e}_\varphi)$. Furthermore, we assume that not only the particle geometry, but also the unknown functions, namely the lithium concentration n and the mechanical displacement \mathbf{u} , as well as the boundary conditions holding at the particle surface are invariant under rotation with respect to both the θ and φ coordinates. This implies that $\partial_\theta = \partial_\varphi = 0$ which allows for the replacement of the three-dimensional problem by an equivalent one-dimensional problem whose geometry is sketched in Fig. 2.2.

Because of this rotational invariance, the local lithium flux as well as its two different contributions introduced in Eq. (2.9) and Eq. (2.10) have a nonzero component along the radial direction only

$$\mathbf{J}^{\text{ch}} = -\frac{D_0 n}{a_0^3 k_B T} \frac{\partial \mu^{\text{ch}}}{\partial r} \mathbf{e}_r = -\frac{D_0}{a_0^3} \frac{\partial n}{\partial r} \mathbf{e}_r \quad (2.22)$$

$$\mathbf{J}^{\text{cp}} = -\frac{D_0 n}{a_0^3 k_B T} \frac{\partial \mu^{\text{cp}}}{\partial r} \mathbf{e}_r = \frac{D_0 \tilde{\Omega}_0 n}{k_B T} \frac{\partial \sigma_h}{\partial r} \mathbf{e}_r. \quad (2.23)$$

In the same way, the mechanical displacement $\mathbf{u} = u_r \mathbf{e}_r$. In the curvilinear spherical coordinate system the strain tensor,

$$\boldsymbol{\varepsilon} = \begin{pmatrix} \varepsilon_r & 0 & 0 \\ 0 & \varepsilon_t & 0 \\ 0 & 0 & \varepsilon_t \end{pmatrix},$$

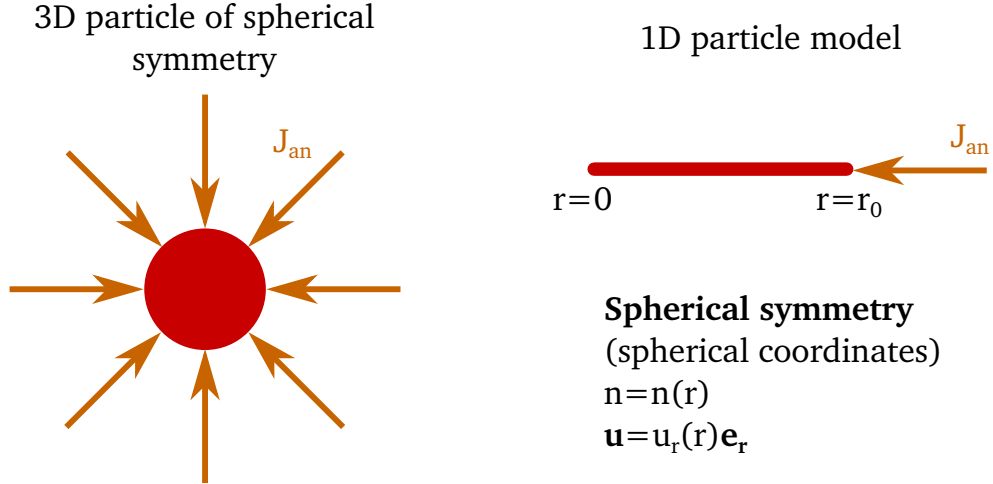


Figure 2.2: Particle of spherical shape. Due to the spherical symmetry, the three-dimensional problem reduces to a one-dimensional problem.

is diagonal. Its components could be calculated using Ref. [53],

$$\varepsilon_r = \frac{\partial u_r}{\partial r}, \quad (2.24)$$

$$\varepsilon_t = \frac{u_r}{r}. \quad (2.25)$$

Furthermore, according to the constitutive relation Eq. (2.11), the components of the stress tensor, formally expressed as

$$\boldsymbol{\sigma} = \begin{pmatrix} \sigma_r & 0 & 0 \\ 0 & \sigma_t & 0 \\ 0 & 0 & \sigma_t \end{pmatrix},$$

read

$$\sigma_r = 2\lambda_1\varepsilon_r + \lambda_2(\varepsilon_r + 2\varepsilon_t) - \lambda\tilde{\Omega}_0(n - n_0), \quad (2.26)$$

$$\sigma_t = 2\lambda_1\varepsilon_t + \lambda_2(\varepsilon_r + 2\varepsilon_t) - \lambda\tilde{\Omega}_0(n - n_0). \quad (2.27)$$

In spherical coordinates, the conservation of matter, Eq. (2.2), as well as the mechanical equilibrium, Eq. (2.3), are given by

$$\frac{\partial(r^2n)}{\partial t} + \frac{\partial}{\partial r} \left(a_0^3 r^2 (J_r^{\text{ch}} + J_r^{\text{cp}}) \right) = 0, \quad (2.28)$$

$$\frac{\partial\sigma_r}{\partial r} + \frac{2}{r}(\sigma_r - \sigma_t) = 0. \quad (2.29)$$

and are completed by the following set of boundary conditions

$$-J_r \Big|_{r=r_0} = J_{an}, \quad (2.30)$$

$$\sigma_r \Big|_{r=r_0} = 0, \quad (2.31)$$

$$\partial_r n \Big|_{r=0} = 0, \quad (2.32)$$

$$u_r \Big|_{r=0} = 0 \quad (2.33)$$

where Eq. (2.30) and Eq. (2.31) represent the boundary conditions that hold at the particle surface according to Eq. (2.17) - Eq. (2.18) whereas Eq. (2.32) and Eq. (2.33) stand for ‘‘artificial’’ boundary conditions valid at the particle center needed when reducing the three-dimensional problem to a one-dimensional rotational symmetric problem. Such artificial boundary conditions are needed to ensure the uniqueness of the solution to this mathematical problem, but they also are related to a more physical requirement: As demonstrated in App. A, they namely ensure that the lithium flux at the particle center vanishes. Indeed, in the considered source-free system, due to symmetry reasons, the lithium flux there has to be zero. Finally, initial values for the unknown functions have to be specified,

$$n \Big|_{t=0} = n_0, \quad (2.34)$$

$$u_r \Big|_{t=0} = u_{r0} \quad (2.35)$$

where both n_0 and u_{r0} are spatially constant.

Analytical solution

By neglecting the backaction of the host deformations on the lithium diffusion with setting $J_r^{\text{cp}} = 0$, the two driving equations Eq. (2.28) and Eq. (2.29) partially decouple. In particular, the local conservation of matter, Eq. (2.28), becomes now completely independent from the mechanical displacement,

$$\frac{\partial}{\partial t} (r^2 n) + \frac{\partial}{\partial r} \left(-D_0 r^2 \frac{\partial n}{\partial r} \right) = 0. \quad (2.36)$$

With the boundary conditions, Eq. (2.30) and Eq. (2.32) as well as the initial condition Eq. (2.34), V. R. Subramanian and R. E. White [54] solved this second-order time-dependent differential equation using a separation ansatz. They obtained

$$n(\tilde{r}, \tilde{t}) = \frac{1}{\tilde{r}} \sum_{m=1}^{\infty} \left(\frac{-2\delta}{\lambda_m^2 \sin(\lambda_m)} \right) \exp(-\lambda_m^2 \tilde{t}) \sin(\lambda_m \tilde{r}) + \frac{\delta}{2} \tilde{r}^2 + 3\delta \tilde{t} + \gamma - \frac{3}{10} \delta \quad (2.37)$$

where

$$\delta = -\frac{r_0 a_0^3}{D_0} J_{an}$$

and $\gamma = n_0$. Both dimensionless radial coordinate \tilde{r} and time \tilde{t} , defined as ,

$$\tilde{r} = \frac{r}{r_0},$$

$$\tilde{t} = \frac{D_0}{r_0^2} t$$

are introduced. The quantities λ_m refer to indexed solutions of the following equation:

$$\lambda_m = \tan \lambda_m > 0,$$

ordered such that $\lambda_m < \lambda_{m+1}$.

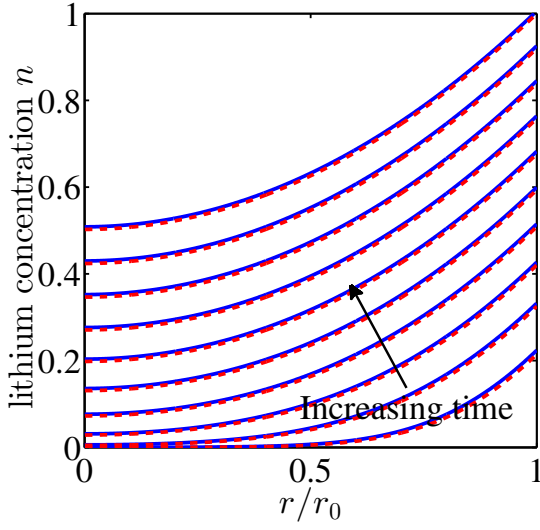
Furthermore, as also indicated in Ref. [41], the local mechanical equilibrium, Eq. (2.29) which is a time-independent second-order differential equation with respect to the radial mechanical displacement could be solved. After some transformations, the radial and tangential components of the stress tensor as well as the hydrostatic stress for given $n(\tilde{r}, \tilde{t})$ could be obtained,

$$\begin{aligned} \sigma_r(\tilde{r}, \tilde{t}) &= \frac{2\tilde{\Omega}_0 E_0}{3(1-\nu)} \left(\int_0^1 ds s^2 (n-\gamma) - \frac{1}{\tilde{r}^3} \int_0^{\tilde{r}} ds s^2 (n-\gamma) \right), \\ \sigma_t(\tilde{r}, \tilde{t}) &= \frac{\tilde{\Omega}_0 E_0}{3(1-\nu)} \left(\int_0^1 ds s^2 (n-\gamma) + \frac{1}{2\tilde{r}^3} \int_0^{\tilde{r}} ds s^2 (n-\gamma) - \frac{1}{2} (n-\gamma) \right), \\ \sigma_h(\tilde{r}, \tilde{t}) &= \frac{2\tilde{\Omega}_0 E_0}{9(1-\nu)} \left(-(n-\gamma) + 3 \int_0^1 ds s^2 (n-\gamma) \right). \end{aligned} \quad (2.38)$$

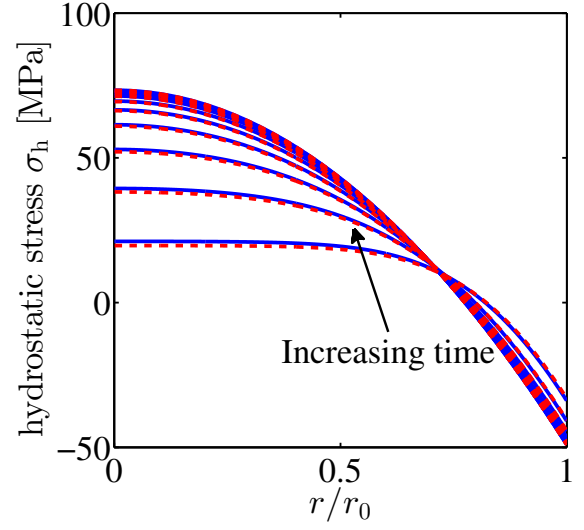
Fig. 2.3 demonstrates that there is a good agreement between the analytical results obtained using Eq. (2.37) and Eq. (2.38) truncated after 20 terms in the summation and the numerical results computed using the finite element software COMSOL.

As expected, during lithium insertion into the particle, the lithium concentration profile shows, at each time step, a maximum at the particle surface. In the same time, the hydrostatic stress profile exhibits a sign change, negative at the particle center and positive at the particle surface. This sign change is correlated with the local variation in the lithium concentration. Near the particle surface where the lithium ions are inserted this variation is positive and this region is compressed (negative hydrostatic stress). On the contrary, near the particle center, there is a lithium flux from the particle center to the particle surface in order to homogenize the lithium concentration over the entire particle and this region is under tensile stress state.

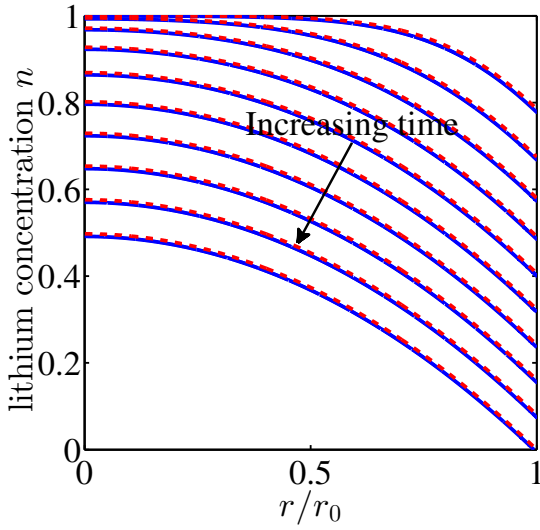
During the lithium extraction, at each time step, the lithium concentration profile possesses a minimum at the particle surface and, as a result, the hydrostatic stress values have the same order of magnitude as those obtained during lithium insertion but with opposite sign.



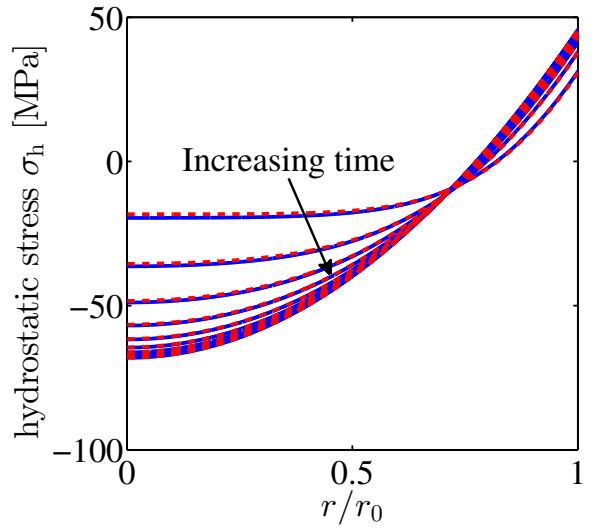
(a) Profiles of the lithium concentration during lithium insertion.



(b) Profiles of the hydrostatic stress during lithium insertion.



(c) Profiles of the lithium concentration during lithium extraction.



(d) Profiles of the hydrostatic stress during lithium extraction.

Figure 2.3: Lithium concentration and hydrostatic stress profiles obtained during both lithium insertion into and extraction out of a spherical cathodic particle of material. The red dashed curves have been obtained analytically whereas the blue solid curves correspond to numerically obtained solutions using the software COMSOL.

Effect of the stress-induced lithium diffusion

We now take into account the backaction of the host material deformations onto lithium diffusion. In this case no analytic solution is known and a numerical evaluation is performed using COMSOL. To analyze the effect of a nonzero stress-induced lithium flux J_r^{cp} , we define the “relative diffusion coefficient” \tilde{D}^{cp} by

$$J_r^{\text{cp}} = \tilde{D}^{\text{cp}} J_r^{\text{ch}}$$

with the conventional diffusion flux

$$J_r^{\text{ch}} = -\frac{D_0}{a_0^3} \frac{\partial n}{\partial r}. \quad (2.39)$$

As illustrated in Fig. 2.4, the calculated relative diffusion coefficient is positive, $\tilde{D}^{\text{cp}} > 0$, at each time step and over the entire particle. That means that the stress-induced lithium flux J_r^{cp} acts

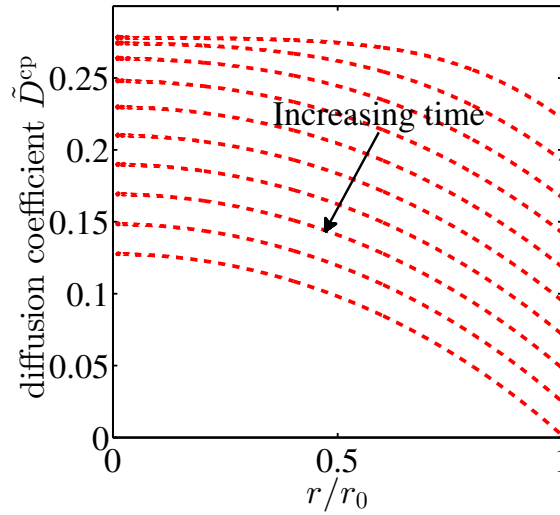


Figure 2.4: Profiles of the relative diffusion coefficient \tilde{D}^{cp} obtained at different times during lithium extraction from a spherical cathodic particle.

together with the flux J_r^{ch} , driven by gradients in the lithium concentration, to enhance the lithium diffusion from the high-concentration regions to the low-concentration regions. Hence, as represented in Fig. 2.5(a), the stress-induced lithium flux contributes to an enhanced lithium homogenization in the particle. Consequently, as seen in Fig. 2.5(b), the magnitude of the hydrostatic stress, at both the particle center and surface, is diminished as compared to the case where $J_r^{\text{cp}} = 0$.

This behavior is also reflected in Fig. 2.6 where the maximum of the hydrostatic stress magnitude reached during both lithium extraction and insertion, is shown as a function of the applied flux magnitude for the two different cases $J_r^{\text{cp}} = 0$ and $J_r^{\text{cp}} \neq 0$. As shown in Fig. 2.6(a), generated for equal material parameters and for two different particle radii, it appears that the maximum hydrostatic stress magnitude only depends on the product Cr_0^2 where C is related to the applied flux magnitude according to Eq. (2.1).

In regime ①, for low applied charge and discharge rate ($Cr_0^2/3600D_0 < 8.8$), we observe that the variation of the maximal value of the hydrostatic stress magnitude with respect to the applied

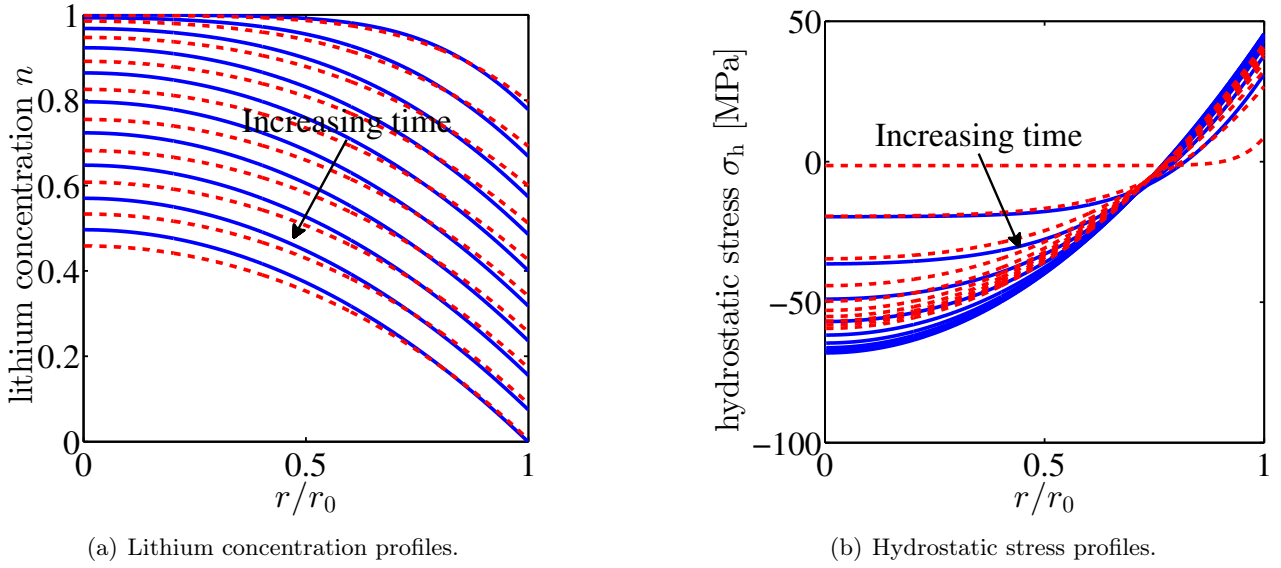


Figure 2.5: *Lithium concentration and hydrostatic stress profile at different times obtained during lithium extraction from a spherical cathodic particle of LMO. The blue solid curves correspond to the case $J_r^{\text{CP}} = 0$ as opposed to the red dashed curves where this quantity is nonzero.*

flux magnitude is almost linear. In this regime, during both lithium extraction and insertion, this maximum value is reached at the particle center. It is negative during lithium extraction and positive during lithium extraction.

Differently, in regime ②, for large applied charge and discharge rate ($Cr_0^2/3600D_0 > 8.8$), lithium diffusion towards the particle surface (lithium extraction) or towards the particle center (lithium insertion) is not sufficiently fast to prevent lithium depletion or accumulation at the particle surface, respectively. The stop condition Eq. (2.21) is quickly reached. At this time, high concentration gradients occur at the particle surface and the stress is maximum, negative during the lithium insertion and positive during the lithium extraction. Note that, the hydrostatic stresses obtained during lithium extraction are slightly smaller than those obtained during lithium insertion.

2.2.3 Particles of ellipsoidal symmetry

Mathematical formulation

In order to study the influence of the particle geometry, the particle shape, spherical until now, can be generalized to an ellipsoidal shape. An ellipsoid is completely characterized by its three semi-axes x_0 , y_0 , and z_0 . We, however, restrict our study to ellipsoidal particles which are symmetric under rotation around the z -axis, i.e. $x_0 = y_0 = \varrho_0$ as sketched in Fig. 2.7. We further define the aspect ratio γ as

$$\gamma = \frac{z_0}{\varrho_0}.$$

In the usual cylindrical coordinate system (ϱ, θ, z) with local orthonormal basis $(\mathbf{e}_\varrho, \mathbf{e}_\theta, \mathbf{e}_z)$, the aforementioned symmetry requirement means that the particle geometry remains invariant under shift

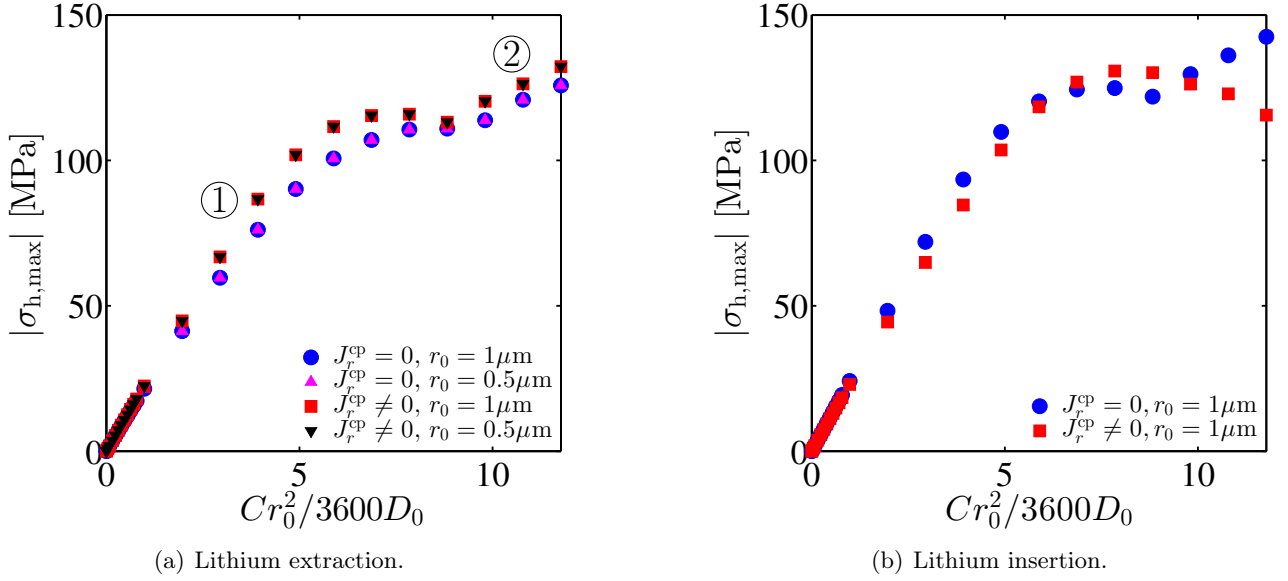


Figure 2.6: Maximum values of the hydrostatic stress magnitude reached during both lithium extraction and insertion as a function of the ratio $Cr_0^2/3600D_0$ or the two different cases $J_r^{\text{cp}} = 0$ and $J_r^{\text{cp}} \neq 0$. Additionally, during lithium extraction, the maximum of the hydrostatic stress obtained for two different particle radii is shown.

of the θ -coordinate. Similarly to the spherical particle introduced in the previous section, we assume, that not only the particle geometry but also the unknown functions and the boundary conditions exhibit this rotational invariance. It thus holds $\partial_\theta = 0$. Assuming in a similar way an additional symmetry under reflexion at the x - y -plane, $z \mapsto -z$ allows for the replacement of the three-dimensional problem by a two-dimensional problem as sketched in Fig. 2.7.

Under these considerations, the different contributions to the lithium flux expressed in cylindrical coordinates are given by

$$\mathbf{J}^{\text{ch}} = -\frac{D_0}{a_0^3} \left(\frac{\partial n}{\partial \varrho} \mathbf{e}_\varrho + \frac{\partial n}{\partial z} \mathbf{e}_z \right) \quad (2.40)$$

$$\mathbf{J}^{\text{cp}} = \frac{D_0 \tilde{\Omega}_0 n}{k_B T} \left(\frac{\partial \sigma_h}{\partial \varrho} \mathbf{e}_\varrho + \frac{\partial \sigma_h}{\partial z} \mathbf{e}_z \right). \quad (2.41)$$

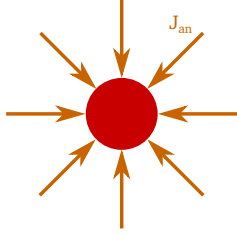
The components of the strain tensor,

$$\boldsymbol{\varepsilon} = \begin{pmatrix} \varepsilon_{\varrho\varrho} & 0 & \varepsilon_{\varrho z} \\ 0 & \varepsilon_{\theta\theta} & 0 \\ \varepsilon_{z\varrho} & 0 & \varepsilon_{zz} \end{pmatrix},$$

could be calculated using Ref. [53], and are related to the components of the mechanical displacement,

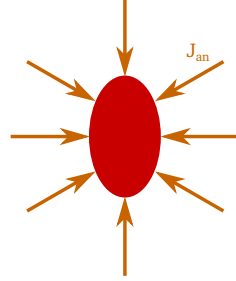
3D particle of spherical symmetry

$$\gamma = 1$$

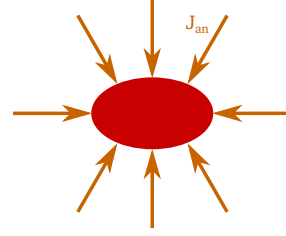


3D particle of ellipsoidal symmetry

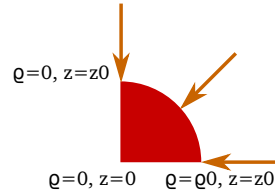
$$\gamma > 1$$



$$\gamma < 1$$



2D particle model



Ellipsoidal and mirror symmetries
(cylindrical coordinates)
 $n = n(\varrho, z)$
 $\mathbf{u} = u_\varrho(\varrho, z)\mathbf{e}_\varrho + u_z(\varrho, z)\mathbf{e}_z$

Figure 2.7: Particle of ellipsoidal shape with two equal semi-axis. Due to the ellipsoidal symmetry, the three-dimensional particle problem reduces to a two-dimensional problem.

$\mathbf{u} = u_\varrho \mathbf{e}_\varrho + u_z \mathbf{e}_z$, by

$$\varepsilon_{\varrho\varrho} = \frac{\partial u_\varrho}{\partial \varrho}, \quad (2.42)$$

$$\varepsilon_{\theta\theta} = \frac{u_\varrho}{\varrho}, \quad (2.43)$$

$$\varepsilon_{zz} = \frac{\partial u_z}{\partial z}, \quad (2.44)$$

$$\varepsilon_{\varrho z} = \varepsilon_{z\varrho} = \frac{1}{2} \left(\frac{\partial u_z}{\partial \varrho} + \frac{\partial u_\varrho}{\partial z} \right). \quad (2.45)$$

Using Eq. (2.11) the components of the stress tensor, formally defined by

$$\boldsymbol{\sigma} = \begin{pmatrix} \sigma_{\varrho\varrho} & 0 & \sigma_{\varrho z} \\ 0 & \sigma_{\theta\theta} & 0 \\ \sigma_{z\varrho} & 0 & \sigma_{zz} \end{pmatrix},$$

read

$$\sigma_{\rho\rho} = 2\lambda_1\varepsilon_{\rho\rho} + \lambda_2 \left(\varepsilon_{\rho\rho} + \varepsilon_{\theta\theta} + \varepsilon_{zz} \right) - \lambda\tilde{\Omega}_0 (n - n_0), \quad (2.46)$$

$$\sigma_{\theta\theta} = 2\lambda_1\varepsilon_{\theta\theta} + \lambda_2 \left(\varepsilon_{\rho\rho} + \varepsilon_{\theta\theta} + \varepsilon_{zz} \right) - \lambda\tilde{\Omega}_0 (n - n_0), \quad (2.47)$$

$$\sigma_{zz} = 2\lambda_1\varepsilon_{zz} + \lambda_2 \left(\varepsilon_{\rho\rho} + \varepsilon_{\theta\theta} + \varepsilon_{zz} \right) - \lambda\tilde{\Omega}_0 (n - n_0), \quad (2.48)$$

$$\sigma_{\rho z} = \sigma_{z\rho} = 2\lambda_1\varepsilon_{\rho z}. \quad (2.49)$$

In the curvilinear cylindrical coordinates, the conservation of matter Eq. (2.2) and the mechanical equilibrium Eq. (2.3), which is now a set of two differential equations, are given by

$$\frac{\partial(\rho n)}{\partial t} + \frac{\partial}{\partial \rho} \left(a_0^3 \rho \left(J_\rho^{\text{ch}} + J_\rho^{\text{cp}} \right) \right) + \frac{\partial}{\partial z} \left(a_0^3 \rho \left(J_z^{\text{ch}} + J_z^{\text{cp}} \right) \right) = 0, \quad (2.50)$$

$$\frac{\partial \sigma_{\rho\rho}}{\partial \rho} + \frac{\partial \sigma_{\rho z}}{\partial z} + \frac{1}{\rho} \left(\sigma_{\rho\rho} - \sigma_{\theta\theta} \right) = 0, \quad (2.51)$$

$$\frac{\partial \sigma_{\rho z}}{\partial \rho} + \frac{\partial \sigma_{zz}}{\partial z} + \frac{\sigma_{\rho z}}{\rho} = 0. \quad (2.52)$$

In cylindrical coordinates, the outgoing normal \mathbf{n} to the particle surface ∂V_0 is given by

$$\mathbf{n} = \frac{1}{\sqrt{\rho^2 + \left(\frac{z}{\gamma^2}\right)^2}} \left(\rho \mathbf{e}_\rho + \frac{z}{\gamma^2} \mathbf{e}_z \right).$$

Thus, according to Eqs. (2.17) - (2.18), it holds at the particle surface ∂V the following boundary conditions

$$-\left(\rho J_\rho + \frac{z}{\gamma^2} J_z \right) \Big|_{\partial V} = \sqrt{\rho^2 + \left(\frac{z}{\gamma^2}\right)^2} J_{an}, \quad (2.53)$$

$$\left(\rho \sigma_{\rho\rho} + \frac{z}{\gamma^2} \sigma_{\rho z} \right) \Big|_{\partial V} = 0, \quad (2.54)$$

$$\left(\rho \sigma_{z\rho} + \frac{z}{\gamma^2} \sigma_{zz} \right) \Big|_{\partial V} = 0. \quad (2.55)$$

In order to account for the particle symmetries when reducing the dimensionality of the problem, artificial boundary conditions along the particle symmetry axis and plane must be considered. They

read

$$\left. \frac{\partial n}{\partial \varrho} \right|_{\varrho=0,z} = 0, \quad (2.56)$$

$$u_{\varrho} \Big|_{\varrho=0,z} = 0 \quad (2.57)$$

$$\left. \frac{\partial u_z}{\partial \varrho} \right|_{\varrho=0,z} = 0, \quad (2.58)$$

$$\left. \frac{\partial n}{\partial z} \right|_{\varrho,z=0} = 0, \quad (2.59)$$

$$u_z \Big|_{\varrho,z=0} = 0, \quad (2.60)$$

$$\left. \frac{\partial u_{\varrho}}{\partial z} \right|_{\varrho,z=0} = 0. \quad (2.61)$$

As for the spherically symmetric problem of Sec. 2.2.2, these additional boundary conditions ensure that the present mathematical problem has an unique solution, but they also prevent from nonvanishing flux terms along the artificial boundaries of the current two-dimensional particle model, namely at $z = 0$ and at $\varrho = 0$, as it is demonstrated in App. A. To achieve the complete mathematical formulation of the lithium intercalation into a system of ellipsoidal symmetry, initial conditions for the unknown functions have to be specified,

$$n \Big|_{t=0} = n_0, \quad (2.62)$$

$$u_{\varrho} \Big|_{t=0} = u_{\varrho 0}, \quad (2.63)$$

$$u_z \Big|_{t=0} = u_{z0}. \quad (2.64)$$

Influence of the particle aspect ratio

We discuss here the influence of the aspect ratio on both the lithium concentration and the hydrostatic stress profiles. For low applied flux magnitudes, concentration profiles are relatively homogeneous and low stresses occur within the ellipsoidal particles. Fig. 2.8 shows lithium concentration and hydrostatic stress profiles within ellipsoidal particles of different aspect ratios during extraction at a relatively large applied flux magnitude, $C = 20$, where sizeable concentration gradients occur. The particle volume was kept constant at $V_0 = (4/3) \pi \mu\text{m}^3$ and the curves shown here are snap-shots at times when the mean concentration $\bar{n} \approx 0.5$. Main results are summarized in Tab. 2.2.

Let us make some explanatory remarks: For very flat particles ($\gamma \ll 1$) the concentration is almost independent of the z -coordinate, hence $n \approx n(\varrho)$. The situation is reversed for very elongated particles ($\gamma \gg 1$) where $n \approx n(z)$, while particles with perfectly spherical shape ($\gamma = 1$) show close to spherically symmetric concentration profiles, $n \approx n(r = \sqrt{\varrho^2 + z^2})$. The latter exhibit rather moderate spatial variations in the concentration, in contrast to strongly elongated or flat particles. Remarkably, despite the large concentration gradients in elongated particles, the arising stresses are comparatively small. This may seem counterintuitive at the first glance.

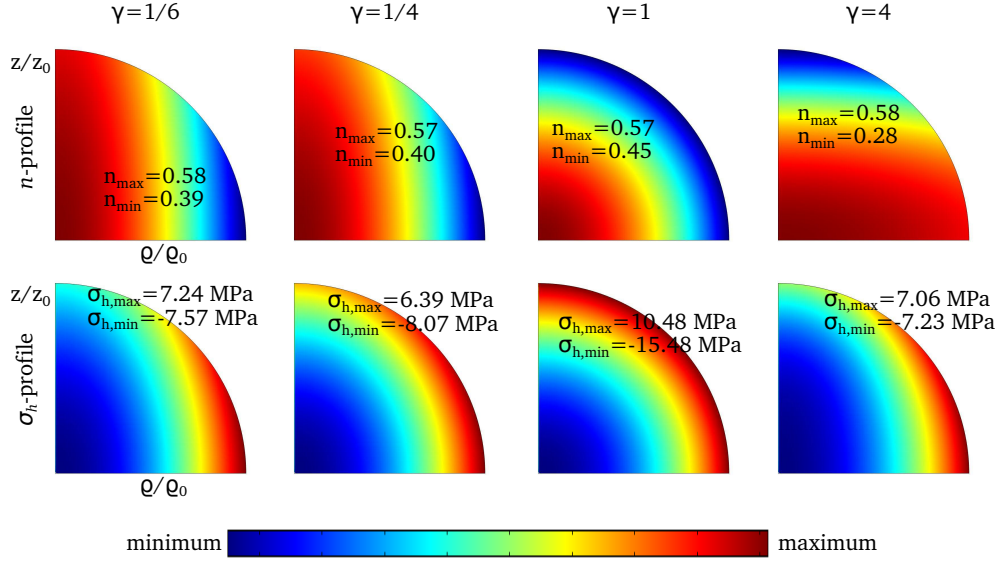


Figure 2.8: Lithium concentration and hydrostatic stress profiles for ellipsoidal cathodic particles of different aspect ratios but fixed particle volume equal to $V_0 = (4/3)\pi\mu\text{m}^3$ when $\bar{n} \approx 0.5$. These profiles have been obtained during lithium extraction at constant applied flux magnitude corresponding to $C = 20$.

Aspect ratio	Lithium concentration	Concentration gradient	Stresses
$\gamma \ll 1$	$n = n(\varrho)$	large	slightly larger
$\gamma = 1$	$n = n(r) = n(\sqrt{\varrho^2 + z^2})$	low	large
$\gamma \gg 1$	$n = n(z)$	large	slightly lower

Table 2.2: Behavior of the lithium concentration and stress profiles within ellipsoidal particles of different limit cases regarding the aspect ratio γ .

These observations can be interpreted as follows: The different concentration profiles are of geometric origin. Particles of elongated shape ($\gamma > 1$) have more surface per unit of particle volume in the vicinity of the particle “pole”, $(\varrho, z) = (0, z_0)$, as compared to the “equator” region of the particle, $(\varrho, z) = (\varrho_0, 0)$. Since the lithium extraction rate per area is the same at every point of the particle surface, the effective extraction rates in these two regions strongly differ. This leads to an enhanced lithium depletion in the pole regions as compared to the equator region. For $\gamma \gg 1$ and fixed volume the lateral extent ϱ_0 is very small and homogenization of the concentration by diffusion occurs very quickly in ϱ -direction. Hence, the concentration has only a weak ϱ -dependence.

Analogous arguments hold for the opposite limit of very flat particles ($\gamma \ll 1$), leading to a weak dependence of the concentration on the z -coordinate, and a drop of $n(\varrho)$ as one moves from the center $\varrho = 0$ towards the surface $\varrho = \varrho_0$ (during lithium extraction). The concentration profile in spherical particles is dominated by the large applied isotropic flux which leads to a spherically symmetric $n = n(r = \sqrt{\varrho^2 + z^2})$. This is not as obvious as one might think, since the mechanical coupling in general favors different concentration profiles. We will discuss this in greater detail in Chp. 5, where in the presence of phase segregation stresses are generally smaller for planar (i.e. uncurved) phase boundaries.

Based on the different concentration profiles we will argue now that elongated particles can maintain hydrostatic stress-free states in contrast to spherical and flat particles. Formally, the hydrostatic stress is equal to

$$\sigma_h = \frac{1}{3} \left(\sigma_{\varrho\varrho} + \sigma_{\theta\theta} + \sigma_{zz} \right) = \lambda \left(\varepsilon_{\varrho\varrho} + \varepsilon_{\theta\theta} + \varepsilon_{zz} - \tilde{\Omega}_0(n - n_0) \right),$$

according to Eqs. (2.46), (2.47) and (2.48). Hence, hydrostatic stresses vanish in the particle if

$$\varepsilon_{\varrho\varrho} + \varepsilon_{\theta\theta} + \varepsilon_{zz} = \tilde{\Omega}_0(n - n_0) \quad (2.65)$$

is satisfied. In particular, Eq. (2.65) is fulfilled when the diagonal components of the total strain tensor, ε_{ij} ($i = j$), are equal to the diagonal components of the lithium-induced strain tensor, $\varepsilon_{ij}^{\text{Li}}$ ($i = j$), respectively. In cylindrical coordinates, according to the set of Eqs. (2.42) - (2.44), this condition requires the displacement vector to satisfy

$$\frac{\partial u_\varrho}{\partial \varrho} = \frac{\tilde{\Omega}_0}{3}(n - n_0), \quad (2.66)$$

$$\frac{u_\varrho}{\varrho} = \frac{\tilde{\Omega}_0}{3}(n - n_0), \quad (2.67)$$

$$\frac{\partial u_z}{\partial z} = \frac{\tilde{\Omega}_0}{3}(n - n_0). \quad (2.68)$$

Usually these equations cannot be fulfilled simultaneously and the system is not able to completely avoid hydrostatic stresses by deformations. As an example, let us consider flat particles with nonconstant concentration $n(\varrho)$. To maintain a stress-free state, the displacement would have to be

$$u_\varrho = \varrho \frac{\tilde{\Omega}_0}{3}(n(\varrho) - n_0),$$

according to above Eq. (2.66). But this is clearly incompatible with the other condition, Eq (2.67),

$$\frac{\partial u_\varrho}{\partial \varrho} = \frac{\tilde{\Omega}_0}{3}(n(\varrho) - n_0),$$

because of nonconstant $n(\varrho)$. Hence hydrostatic stress necessarily arises in flat particles. The same is true for spherical ones.

In contrast, strongly elongated particles with nonconstant concentration $n(z)$ can easily avoid hydrostatic stress by the deformations

$$u_z(z) = \int_0^z dz' \frac{\tilde{\Omega}_0}{3}(n(z') - n_0), \quad (2.69)$$

$$u_\varrho(\varrho, z) = \varrho \frac{\tilde{\Omega}_0}{3}(n(z) - n_0), \quad (2.70)$$

for which $\sigma_{\varrho\varrho} = \sigma_{\theta\theta} = \sigma_{zz} = 0$, hence $\sigma_h = 0$. Thus, in this kind of particles, the generated hydrostatic stress is generally smaller.

Fig. 2.9 shows the maximal hydrostatic stresses reached during lithium extraction at different particle locations (at the particle center, pole and equator). The simulations were performed until the stop condition represented by Eq. (2.21) is fulfilled.

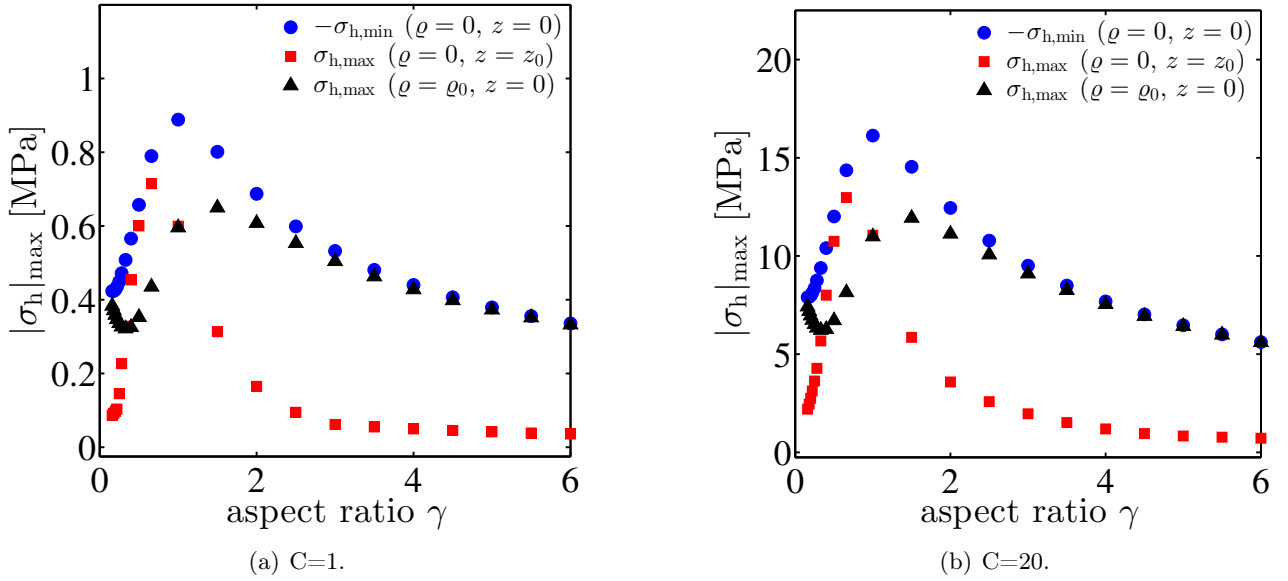


Figure 2.9: Maximum values of the hydrostatic stresses reached during lithium extraction from ellipsoidal particles of fixed constant particle volume $V_0 = (4/3) \pi \mu\text{m}^3$ as function of the aspect ratio γ . The curves shown here are related to particular spatial positions corresponding to the particle center, $(\varrho, z) = (0, 0)$, pole, $(\varrho, z) = (0, z_0)$, and equator, $(\varrho, z) = (\varrho_0, 0)$.

We observe that high applied flux magnitude gives rise to large stresses which can be attributed to higher concentration gradients. Numerical results imply that the stresses are proportional to the C -rate and otherwise show identical profiles as function of spatial coordinates, time and also aspect ratio.

The aspect ratio dependence is consistent with the previous remarks about geometry. For example, we already argued that for very elongated particles, $\gamma \gg 1$ ($\gamma \rightarrow \infty$), stresses tend to zero. For very flat particles, $\gamma \ll 1$, concentration gradients become significant near the equator at $(\varrho, z) = (\varrho_0, 0)$. Thus, in the limit $\gamma \rightarrow 0$ stresses may become infinite. They exhibit a local minimum for small but finite γ . Close to the symmetry axis ($\varrho = 0$) lithium concentration gradients become very small and stresses drop to zero as $\gamma \rightarrow 0$. For $0.3 < \gamma < 1$, the maximum hydrostatic stress holding at the particle surface is attained at the particle pole whereas, for $\gamma < 0.3$, this maximum is reached at the equator. The obtained results are qualitatively comparable to those obtained by E. Bohn (see Sec. 3.4.1 and particularly Fig. 25 of Ref. [55]).

2.3 Dualfoil modeling

2.3.1 Theory

Until now we concentrated on the single particle states during loading and unloading at constant applied flux without concern about the entire battery. As briefly introduced in Sec. 2.1.1, the granular LMO cathode is composed of many interconnected particles that electrochemically couple. In this section, we account for the granular electrode structure as well as for the electrochemical coupling between the electrode particles by means of an effective theory developed by Doyle and Newman [42].

As already mentioned in Sec. 1.2, the battery consists of two electrodes, the anode and the cathode, immersed in and connected by an electrolyte. During discharging, lithium ions are carried from the anode to the cathode via the electrolyte whereas, in the same time, electrons are transported, also from the anode to the cathode, via an external circuit. This spontaneous charge transfer occurs only if the electrochemical potential of the anode $-eE_{oc,an}$ initially exceeds the electrochemical potential at the cathode $-eE_{oc,cath}$ where $e \approx 1.6 \cdot 10^{-19}$ C is the elementary positive charge. We used the experimentally accessible open-circuit voltages E_{oc} of the electrodes, which we relate to their electrochemical potentials via the electronic charge $-e < 0$. The open-circuit voltages, $E_{oc,an}$ and $E_{oc,cath}$, of both the Li_yC_6 -anode and the $\text{Li}_x\text{Mn}_2\text{O}_4$ -cathode have been obtained from Refs. [40, 56] and are plotted in Fig. 2.10 as a function of the states of charge, y and x , respectively. They show that $-eE_{oc,an} > -eE_{oc,cath}$ is indeed satisfied. Typically the anodic and cathodic states of charge before battery discharging are chosen equal to $y = 0.56$ and $x = 0.17$, respectively.

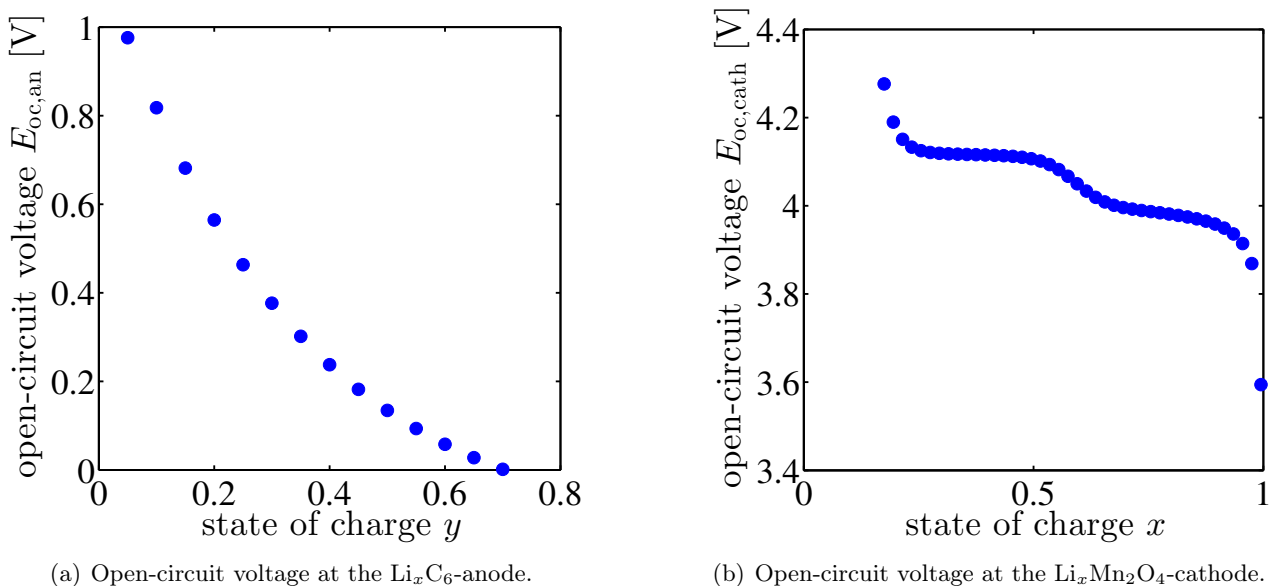


Figure 2.10: *Open-circuit voltage at both electrodes (measured with respect to the lithium metal electrode) as function of the state of charge x obtained from Ref. [40, 56].*

In order to increase the exchange surface and thus enhance the electronic and ionic transport, the electrodes consist of an assembly of small-sized particles of active material (Li_xC_6 at the anode, LMO at the cathode mixed together with carbon black). In both electrodes, these particles are immersed in the electrolyte. We here consider a mixture of Li_zPF_6 as salt and as solvent a binary composition of ethylene carbonate (EC) and dimethyl carbonate (DMC) with a ratio of EC:DMC=1:2 [56, 57]. This mixture represents an electrolyte commonly used in plastic LIB's [5]. Consequently, at each electrode there are two different phases present. On the one hand, there is a solid phase made of active material and carbon black and, on the other hand, there is a liquid phase, namely the electrolyte. At a macroscopic scale, the spatial distribution of these two different phases cannot be resolved. Hence, following the work done in Refs. [58, 59] that are based on an homogenization ansatz first introduced by Bruggeman [60], we assume that the porous electrodes are represented by a superposition of both a solid and a liquid phase (see Fig. 2.11), each of them being seen as a continuous medium.

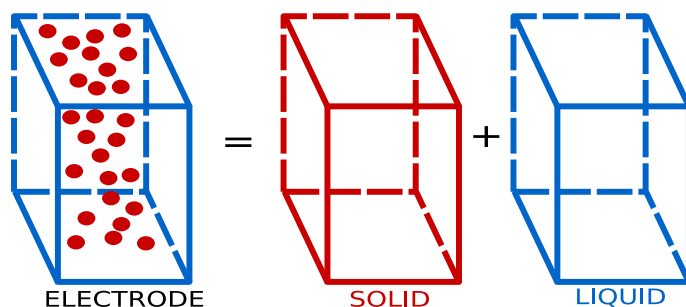
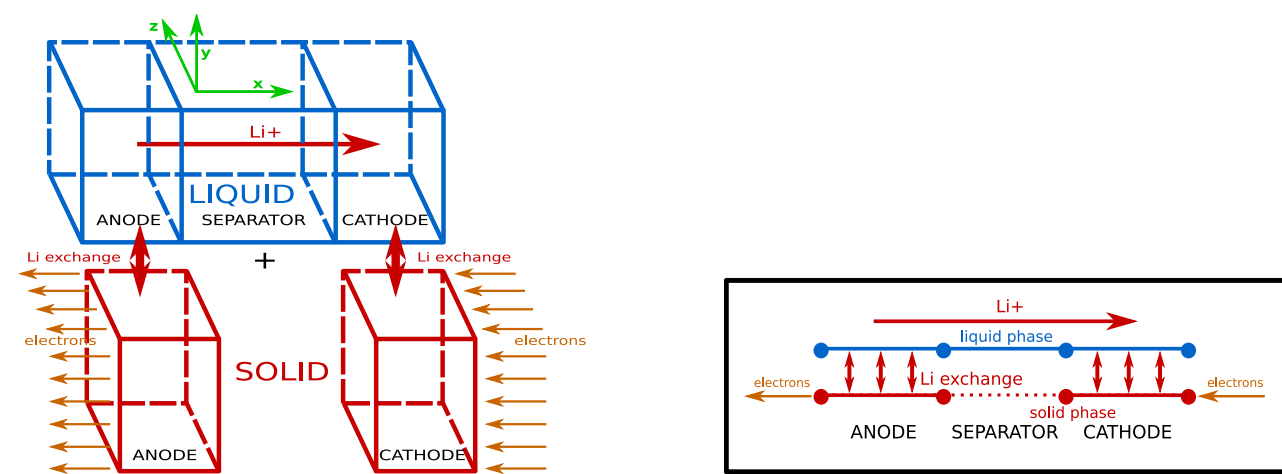


Figure 2.11: Granular electrodes composed of small sized particles made of active material (red spheres) immersed in the electrolytic solution sketched in blue. In a macroscopic battery model, the electrode particles represent a homogeneous continuous medium schematically sketched in red.

At the battery scale, the relevant electronic and ionic transport path is perpendicular to the electrode surfaces. Moreover, in order to limit the losses induced by the lithium ion transport through the electrolyte, the dimension of the battery along this direction is generally much smaller than along the other two directions that can be hence considered as infinitely extended. Thus, invoking symmetry reasons, the three-dimensional battery is modeled by a one-dimensional battery system as sketched in Fig. 2.12.



(a) Sketch of the three-dimensional battery. The liquid and solid phase are represented in blue and in red respectively.

(b) One-dimensional battery model. Since the relevant transport processes occur along the x -direction of the three-dimensional battery sketched in Fig. 2.12(a), the three-dimensional battery is replaced by a one-dimensional system.

Figure 2.12: Macroscopic three-dimensional porous battery represented by a one-dimensional battery system made of a superposition of both a liquid and a solid phase with lithium ion exchange between these two phases.

In both the solid and the liquid phases, charge conservation holds,

$$\begin{aligned}\nabla \cdot \mathbf{i}_s &= S_a e J_{an}, \\ \nabla \cdot \mathbf{i}_l &= -S_a e J_{an},\end{aligned}$$

where \mathbf{i}_s and \mathbf{i}_l are the current densities in the solid and liquid phase, respectively. The quantity S_a is the specific interfacial area defined as the electrode particle surface per unit of electrode volume. The term J_{an} represents the flux of lithium ions exchanged at the interface between the solid and the liquid phase. From a microscopic point of view, this quantity corresponds to the lithium flux

$$J_{an} = -\mathbf{J}_a \cdot \mathbf{n}$$

that holds at the surface of the electrode particles whose surface is conventionally oriented by their outgoing normal \mathbf{n} . Macroscopically, J_{an} is the flux that leaves the liquid phase to enter the solid phase. It consequently acts as a source term for each of these phases, considered separately.

The current densities are related to the electrochemical potentials, denoted by ϕ_s in the solid and ϕ_l in the liquid, as well as to the lithium concentration n_l in the liquid phase by

$$\mathbf{i}_s = -\kappa_s^{\text{eff}} \nabla \phi_s \tag{2.71}$$

$$\mathbf{i}_l = -\kappa_l^{\text{eff}} \left(\nabla \phi_l - \frac{k_B T}{e} (1 - t_+^0) \frac{\nabla n_l}{n_l} \right) \tag{2.72}$$

Eq. (2.71) is the standard Ohm's law for the electronic transport in a solid whereas Eq. (2.72) describes the transport of charges in an infinitely dilute binary liquid solution [61], driven by migration in the electric field $-\nabla \phi_l$ and by diffusion. The transference number t_+^0 [62] is the fraction of current carried by the lithium ions in the electrolytic solution. Indeed, in the electrolyte, all charged species and not only the lithium ions participate in the current transport.

In the liquid phase, the local conservation of lithium matter reads

$$\frac{\partial (\epsilon_l n_l)}{\partial t} + \nabla \cdot (-D_l^{\text{eff}} \nabla n_l) = - (1 - t_+^0) S_a J_{an}.$$

To take into account the porous electrode structure, effective electronic and ionic conductivities, κ_s^{eff} and κ_l^{eff} respectively, as well as an effective lithium ion diffusibility D_l^{eff} in the electrolytic solution, are introduced. According to Ref. [56], these effective parameters, compared to the bulk material values, are diminished by a factor that is a function of the electrode porosity ϵ_l .

In a macroscopic model of the battery, both the cathodic and anodic particles made of active material are replaced by a continuum covering the complete volume of the electrodes. In this context, each point of this continuum represents one electrode particle which can be modeled by means of the single particle model introduced in Sec. 2.2. Note that, at the battery level, lithium ion diffusion and stresses in the solid phase inside the particles cannot be accounted for. For this purpose, it is assumed that each point of the macroscopic electrodes stands for a three-dimensional particle of spherical symmetry, the latter being described by the spherically symmetric particle model introduced in Sec. 2.2.2. At this place, the driving equations, Eq. (2.28) and Eq. (2.29), related to the lithium ion transport in a spherical particle and its effect on the mechanics, are used.

The coupling between the macroscopic battery and the microscopic particles occurs via the lithium flux J_{an} . According to the Butler-Volmer relation [59] with anodic and cathodic apparent transfer

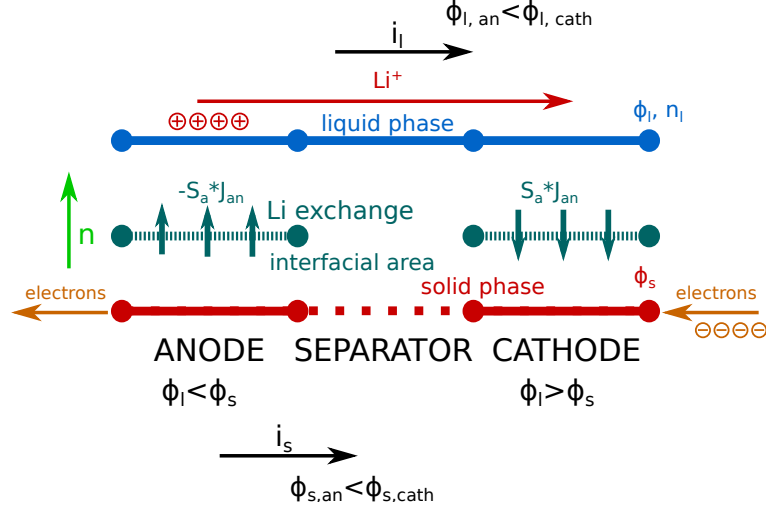


Figure 2.13: One-dimensional battery model represented by the superposition of both a liquid and a solid phase with lithium ion exchange between these two phases. Lithium ions are transported through the liquid phase whereas electrons are transported via the solid phase. The mechanisms shown here are related to the battery discharge. In case of battery charging, the inequalities as well as the arrow orientations representing the flux directions are reversed.

coefficients both equal to 1/2, the magnitude of this flux is given by

$$J_{an} = -\mathbf{J}_a \cdot \mathbf{n} = -J_0 \left(\exp\left(\frac{e\eta}{2k_B T}\right) - \exp\left(-\frac{e\eta}{2k_B T}\right) \right) \quad (2.73)$$

where the local surface overpotential is

$$\eta = \phi_s - \phi_l - E_{oc}. \quad (2.74)$$

The local equilibrium exchange lithium flux magnitude

$$J_0 = k_r \sqrt{n_l n_s (n_{s,max} - n_s)} > 0 \quad (2.75)$$

corresponds to the phenomenological lithium flux magnitude that holds at the electrode surface along its normal in both directions since, at equilibrium, the net lithium flux at the electrode surface is zero hence the battery does not deliver any current. Here, k_r is a rate constant describing both the anodic and cathodic semi-redox reactions. In contrast to the single-particle model, the local lithium flux J_{an} is not an externally fixed quantity but a dynamical variable whose time dependence is governed by the Butler-Volmer relation Eq. (2.73). During battery discharging, the quantity J_{an} is negative at the anode and positive at the cathode and thus $\eta > 0$ at the anode whereas $\eta < 0$ at the cathode. During battery charging, these quantities all change their sign.

Additionally, to achieve the complete mathematical formulation of the battery charging and discharging, boundary conditions at the interface between the electrodes and the current collectors “cc” which

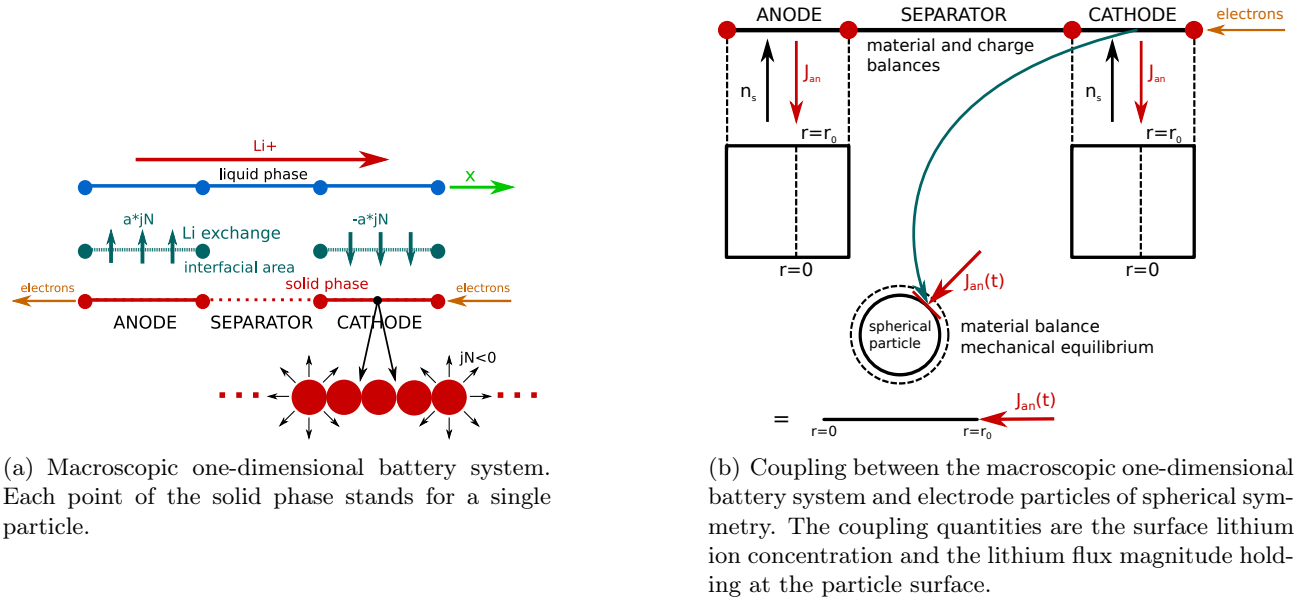


Figure 2.14: *Coupling between the one-dimensional battery system and the single particle model.*

represent the contacts to the external circuit, have to be specified. With

$$\phi_s \Big|_{\text{an,cc}} = 0, \quad (2.76)$$

$$|\mathbf{i}_s| \Big|_{\text{cath,cc}} = \pm i_0 C, \quad (2.77)$$

the galvanostatic charging and discharging of the battery at given C -rate is possibly described. In this context i_0 is the current density which charges or discharges the battery within one hour. In contrast to the single-particle model, the C -rate here refers now to the experimental C -rate of the entire battery. In our model, the current density i_0 is taken equal to 17.5 A m^{-2} for $C = 1$. Note that in practical applications the state of charge x of LMO cathode only varies in a range, usually $0.15 \lesssim x \lesssim 0.65$. Both i_0 and the C -rate have to be understood in this sense.

All needed material and design parameters related to the considered battery cell have been obtained from Ref. [56]. The additional material parameters necessary to describe the mechanical behavior of the cathodic particles are the same as those reported in Tab. 2.1.

2.3.2 Effect of a nonconstant flux at the cathodic particle surface

Fig. 2.15 shows the time-dependent lithium flux magnitude that enters three particles located at different spatial locations in the cathode, as well as their constant values averaged over time. This figure demonstrates that the average flux magnitude is large in the vicinity of the separator region and diminishes when approaching the current collector.

In the present dualfoil model, three different relevant time scales act together: the first one is related to the time needed by the lithium ions to diffuse into the anodic particles, the second one concerns the lithium ions transport in the electrolyte, and finally, the third one is related to the time needed by the lithium ions to diffuse into the cathodic particles. Moreover, the lithium flux at the surface

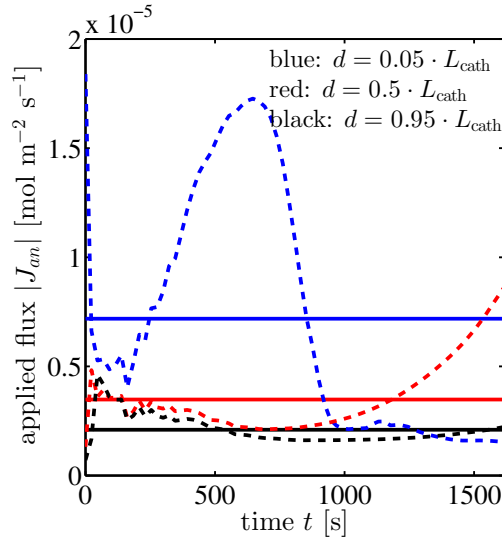


Figure 2.15: Particle surface flux over time during battery discharging ($C = 2$) at three different spatial locations: near the separator (blue curves), in the middle of the cathode (red curves) and close to the current collector (black curves). The parameter d refers to the distance of the considered cathodic particle to the separator region expressed in terms of the cathode thickness $L_{\text{cath}} = 183 \mu\text{m}$. The dashed and solid lines are respectively the time-dependent flux magnitude holding at the particle surface and its value averaged over time.

of the cathodic particles, determined by the Butler-Volmer relation Eq. (2.73) depends on numerous macroscopic and microscopic parameters whose different contributions cannot be easily separated. Thus a proper interpretation of the curves shown in Fig. 2.15 is very difficult.

Fig. 2.16 shows the lithium concentration and hydrostatic stress profiles within a spherical cathodic particle located in the middle of the cathode ($d = 0.5 \cdot L_{\text{cath}}$). We consider two cases: on the one hand, the time-dependent lithium flux magnitude (dashed red lines of Fig. 2.16(a)) is prescribed at the particle surface, and, on the other hand, the average constant flux magnitude (solid blue lines of Fig. 2.16(a)) is applied there.

A comparison between these two cases demonstrates that the lithium ions are slightly more homogeneously distributed over the single cathodic particle when the average flux magnitude is applied at the particle surface. Due to the Butler-Volmer relation, the time-dependent flux magnitude exhibits, at the end of the battery discharging, large variations leading to higher lithium concentration gradients near to the particle surface. As a consequence, as illustrated in Fig. 2.16(b), the hydrostatic stress magnitude reached in the particle embedded in the cathode becomes larger than those attained when the constant average flux magnitude is applied there.

2.3.3 Many-particle states

In the previous section we analyzed the effect of a nonconstant flux on a single particle state. Here, we concentrate on the many-particle state at the cathode. In order to study the equilibrium behavior of the battery we let the battery deliver a stepwise constant current with hold times during which the battery does not furnish any current. That way, we could analyze how the many-particle state relaxes

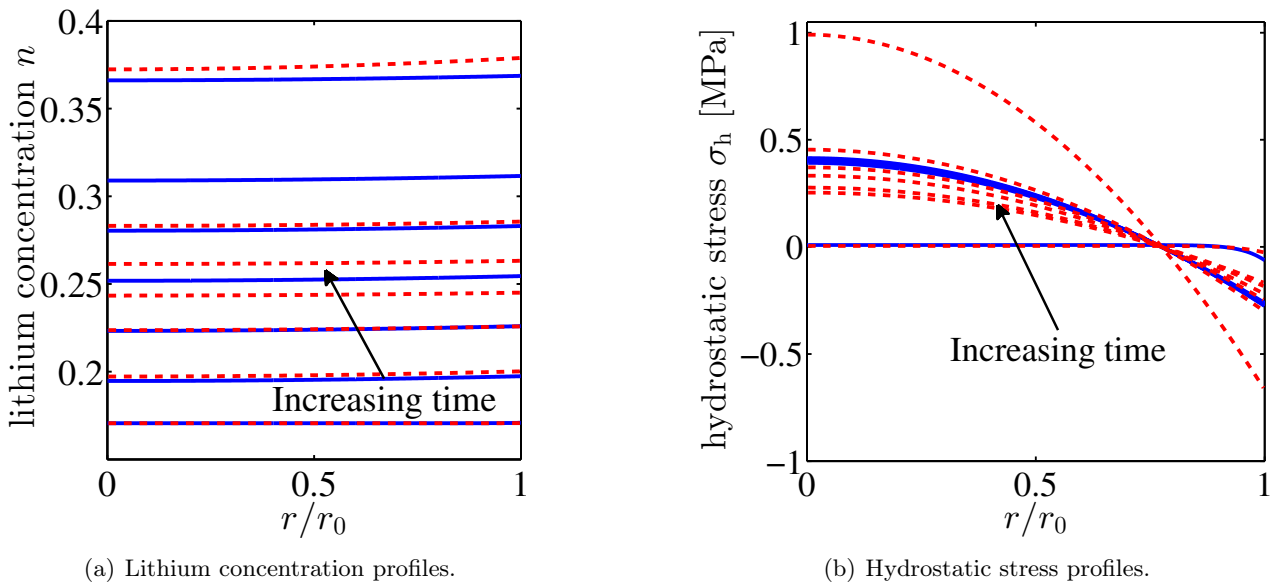


Figure 2.16: *Lithium concentration and hydrostatic stress profiles within a cathodic particle located in the middle of the cathode ($d = 0.5 \cdot L_{\text{cath}}$) during battery discharging at $C = 2$. The dashed red lines correspond to the case where a time-dependent flux, obtained through the Butler-Volmer relation Eq. (2.73) by means of the dualfoil model, holds at the single particle surface. On the contrary, the solid blue lines are obtained by application of a constant lithium flux at the particle surface corresponding to the average value of the time-dependent lithium flux.*

towards equilibrium, assumed to be reached at the end the hold times as shown in Fig. 2.17(a). In a similar fashion, once battery discharging finished, we simulate battery charging. As expected, during battery discharging the battery voltage decreases and during battery charging it increases, recovering completely from the voltage drop induced by the previous discharge.

In Fig. 2.17(b) the battery voltage attained at the end of the hold times is drawn as function of the cathodic state of charge x — also equal to the lithium concentration n averaged over the entire cathode — demonstrating that the processes of battery discharging and charging are completely reversible. Indeed, in the considered dualfoil model, no irreversible processes are taken into account, thus no capacity fade during battery cycling can be observed.

As shown in Fig. 2.17(c), in the many-particle state reached at the end of the relaxation, lithium ions are homogeneously distributed within the cathodic particles. However, since in the present dualfoil model there is no possibility for direct lithium ion transfer between the cathodic particles, the equilibrium single-particle state strongly depends on the particle location in the cathode.

Conclusion

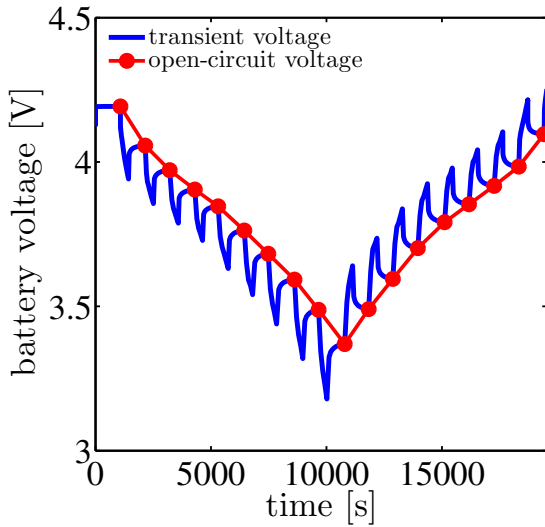
In this chapter, we have analyzed, by means of the dilute approach, the stresses arising in cathodic particles made of LMO material.

The electrochemical coupling between all cathodic particles that form the porous cathode of a LIB

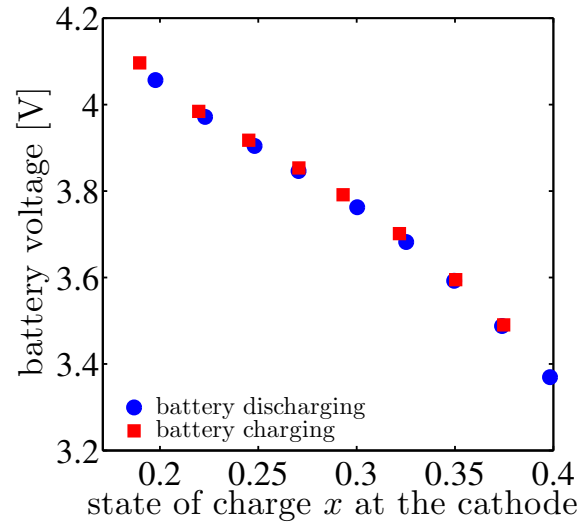
could be taken into account using the dualfoil model and was useful to demonstrate that each single particle being at a specific spatial location in the cathode relaxes towards an homogeneous state, different from the other neighboring particles.

Furthermore, we have demonstrated that large applied flux magnitudes which significantly drive the system far away from equilibrium, give rise to large concentration gradients leading, as a consequence, to large stresses inside of single cathodic particles of both spherical and ellipsoidal symmetry.

Due to the intrinsic correlation between large lithium concentration gradient and large stress magnitude, we expect that cathodic particles being in a phase segregated state where a smooth but usually sharp interface between regions of different lithium concentration holds, also exhibit large stresses independently of the applied flux magnitude. Thus, the next chapter 3 is devoted to the theory of a phase-field model to account for phase segregation that is also coupled to mechanics. The results obtained using this model are summarized separately in the two following chapters, Chps. 4- 5.

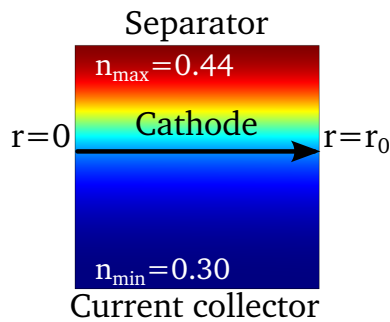


(a) Battery voltage over time during one cycle of battery discharging and charging with hold times. The red points correspond to equilibrium battery states whereas the blue solid line represents instantaneous voltage values.

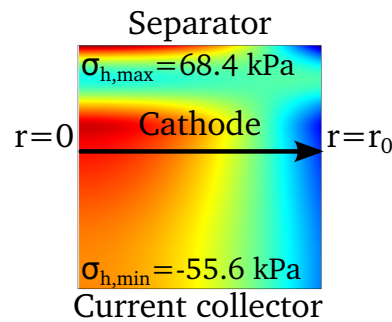



(b) Battery voltage versus the cathodic state of charge x at equilibrium during both battery charging and discharging. The battery states represented here are related to the equilibrium states shown in Fig. 2.17(a) (red points).

Lithium concentration



Hydrostatic stress



minimum  maximum

(c) Lithium concentration and hydrostatic stress profiles reached at the end of the relaxation time when the cathodic state of charge $x \approx 0.35$. This many-particle state corresponds has been obtained during the battery discharging process and has to be related with the circle blue point at $x \approx 0.35$ of Fig. 2.17(b). In this relaxed many-particle state, all cathodic particles exhibit a quasi stress-free state.

Figure 2.17: Battery states over one cycle of discharging and charging with hold times at $C = 1$.

3

Chapter 3

Phase-field modeling

Introduction

In the previous chapter (Chp. 2), we demonstrated by means of the commonly used dilute solution approach that large gradients in the lithium concentration induce large stresses in cathodic particles of both spherical and ellipsoidal symmetries.

While it is extensively reported in the literature that, at room temperature, LMO particles undergo phase segregation over variation of their average lithium concentration due to battery charging and discharging, the theoretical framework of dilute solution modeling does not allow to account for the occurrence of phase-segregated states.

Among the numerous indications that such phase-segregated states may arise, one can cite the measurement of the battery discharge curve which exhibits a plateau at 4 V [26]. Also *X*-rays measurements [36] corroborate the occurrence of phase segregation. At this place, the existence two cubic phases with different lattice parameters was revealed.

In this work we want to describe the lithium insertion and extraction into and from particles where phase-segregated lithium concentration states have the possibility to form in the particle. Further, by means of a coupling term already introduced in the dilute solution approach, we also want to account for the deformations of the host material that are induced by the lithium intercalation.

A class of mathematical methods to describe the lithium intercalation allowing the formation of a diffuse interface is referred onto the generic term of phase-field models [63]. In phase-field modeling, physical systems are treated at the mesoscopic scale where they are considered as heterogeneous regarding to a set of one or more variables that describe their state. Such phase-field models originate from the Ginzburg-Landau theory developed in the context of superconductivity [64] and can be used to describe a wide range of systems. Indeed, the theoretical framework of phase-field modeling was successfully used to investigate the physical state of various systems where phase transformations arise [65]. One of the most common example is the liquid/vapor transition originally described by the Van der Waals equation [66, 67]. Using the phase-field formalism, ferroelectric phase transitions [68, 69] as well many other structural changes of crystalline materials could also be described.

In the context of phase-field modeling, the system free energy is expressed as a functional [70] that depends on an order parameter, a local field, and on externally fixed parameters. In the present case, the local lithium concentration represents the order parameter. The externally fixed parameters are the temperature and the total amount of lithium ions in the system. By driving the external parameters, the value of the order parameter that minimizes the free energy functional may change. Usually — but

not in the present case — the order parameter is chosen such that it vanishes in the homogeneous phase and becomes different from zero in the heterogeneous phase. In such systems, the internal energy and the entropy of the system act in two opposite directions. While the internal energy contributes to the system “ordering”, the entropy enhances the “disorder” of the system. The “ordering” at low temperature is inherent to the microscopic system properties. It requires at least an attractive interaction between the different material compounds which favors the formation of clusters in the system.

By means of phase-field models that account for system heterogeneities at the mesoscopic scale the material behavior can be better understood. Indeed, differently from thermodynamics which simply deals with average macroscopic values, the existence of domains where the order parameter exhibits different values both nonzero is, here, accounted for. Further, the existence of such heterogeneities may have an influence on measurable macroscopic quantities.

The time evolution of the microstructure after having disturbed from equilibrium is possibly described by a phenomenological kinetic phase-field equation [71] whose formal expression is given either by the Ginzburg-Landau equation if the relevant field is a non-conserved quantity or by the Cahn-Hilliard equation if the field is conserved as in the present case.

In this chapter, we first start with a microscopic Hamiltonian expressed in terms of discrete localized variables representing the local number of lithium occupation as well as the local mechanical displacement. To account for phase segregation, we assume that an effective short range attractive interaction holds between two neighboring lithium ions [72]. Using a mean-field approximation [73], we then demonstrate that phase segregation may arise and further replace the mean-field free energy by a free energy functional by means of a coarse-graining procedure. Finally, we make use of the Cahn-Hilliard equation related to the local conservation of lithium matter to account for lithium intercalation into a crystalline cathodic particle made of LMO when the system is disturbed from equilibrium by application of an external lithium flux at the particle surface.

3.1 Microscopic underlying structure

3.1.1 Crystalline structure

At room temperature ($T = 293\text{ K}$), the cathodic particle made of $\text{Li}_x\text{Mn}_2\text{O}_4$ is crystalline meaning the ions that form this solid are periodically distributed over the space. Depending on the state of charge x at the cathode, the lithium ion amount within the present crystal may vary.

When the state of charge $0 < x < 1$, the oxygen ions O^{2-} constitute a face-centered cubic crystalline structure drawn in Fig. 3.1 whose lattice parameter a , however, depends on the state of charge and thus on the lithium concentration [74].

The manganese ions $\text{Mn}^{(4-x/2)+}$, whose oxidation number $(4 - x/2)$ [75, 76] depends on the lithium amount in the crystalline material [77], are located at interstitial octahedral lattice sites as schematically sketched in Fig. 3.2(a). In each face-centered cubic unit cell made of the oxygen lattice, which we refer to as elementary cell, there is a total of four octahedral interstitial sites. Among this four interstitial octahedral sites, only two are in average occupied by the manganese ions. However the manganese ions are not uniformly distributed over the crystalline cathodic material and we have to distinguish between two different kinds of elementary cells drawn in Fig. 3.3. In the first type of elementary cell (Type I) there are three manganese ions whereas in the second type (Type II) there is only one manganese ion. Due to the presence of these two different kinds of elementary cells, the crystalline structure made of oxygen and manganese ions has a lower symmetry than the crystalline structure made of oxygen ions

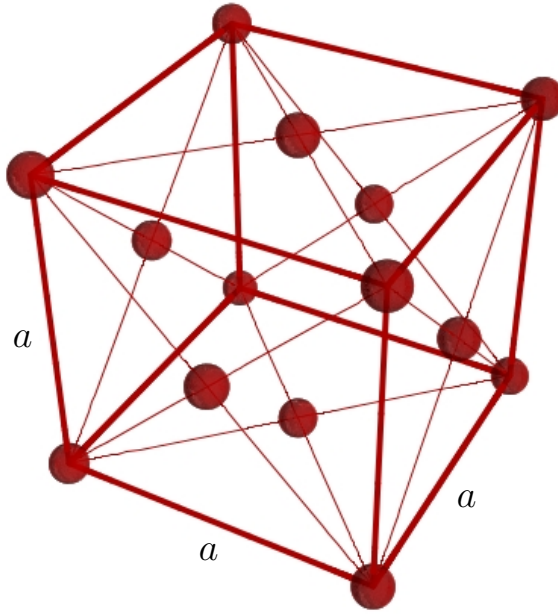


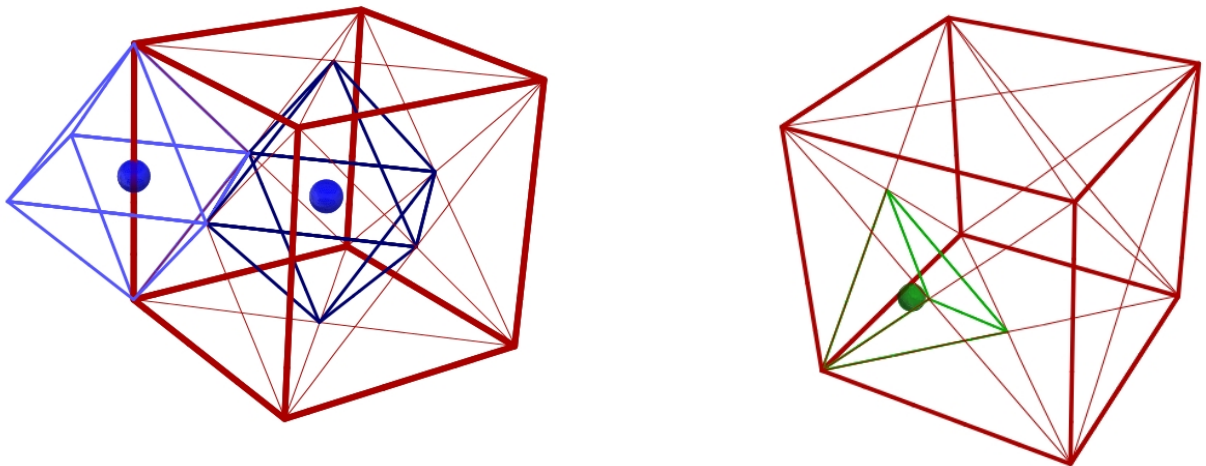
Figure 3.1: Elementary face-centered cubic cell built by the oxygen ions O^{2-} represented by the red spheres.

alone. An elementary cell of the full constituent is composed of two such different elementary cells as shown in Fig. 3.4(a).

The lithium ions Li^+ that are inserted into the crystalline material are located at interstitial tetrahedral lattice sites whose spatial location in the crystalline host structure is schematically sketched in Fig. 3.2(b). Similarly to the manganese ions, they are not uniformly distributed over the crystalline cubic structure. In cells of Type I with three manganese ions there is no interstitial lattice site available to intercalate lithium ions. In cells of Type II with only one manganese ion, there are two available interstitial lattice sites for the lithium ions, as shown in Fig. 3.3.

Thus the intercalation of the lithium ions does not break the symmetry of the crystalline structure whose periodicity remains the same as the crystal made of oxygen and manganese ions only. For $x = 1$ the crystalline structure of $LiMn_2O_4$ material is spinel [78] whose elementary cell is drawn in Fig. 3.4. In the spinel crystalline structure, the lithium ions are distributed over two face-centered cubic sublattices whose lattice parameters are both equal to $2a$. These two lattices are shifted from a length equal to $(\sqrt{3}/2)a$ oriented along the space diagonal of these sublattices as shown in Fig. 3.5.

The lithium ions Li^+ that are inserted into the host material have a fixed oxidation number equal to +1. Due to the state of charge variation, the manganese ions present in the cathodic crystalline material have a varying oxidation number [79]. For $0 < x < 1$, the oxidation number of the manganese ions is comprising between +3 and +4. In average this oxidation number equals $+(4 - x/2)$ to ensure the $Li_xMn_2O_4$ material being electrically neutral. For $x = 1$, the average oxidation number of the manganese ions is exactly equal to +3.5 which corresponds to a critical value of the crystalline material since, below this value the crystal undergoes a phase transition in term of the crystalline structure. Indeed, due to the Jahn-Teller effect [37], the cubic crystalline structure undergoes a tetragonal phase whose lattice parameters have been reported in Ref. [78].



(a) Octahedral interstitial lattice sites represented by the blue spheres.

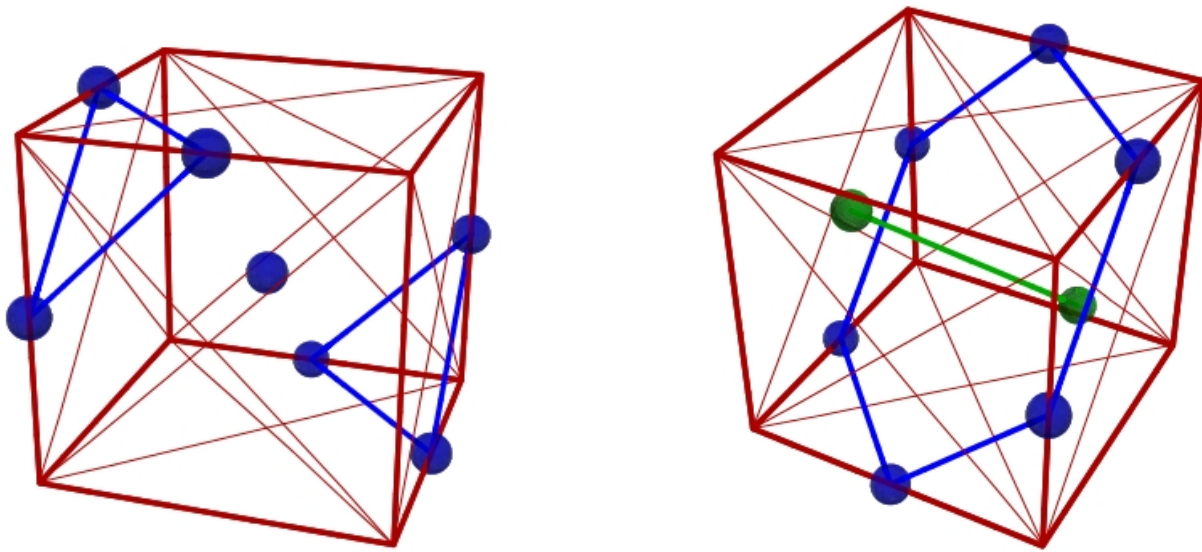
(b) Tetrahedral interstitial lattice sites represented by the green sphere.

Figure 3.2: Octahedral and tetrahedral interstitial sites in $Li_x Mn_2 O_4$. The solid red lines represent the face-centered cubic structure built by the ions O^{2-} .

In standard battery applications, during lithium insertion and extraction, the state of charge is usually maintained below one, so that the crystalline structure can be assumed to be cubic over charging and discharging¹. Nevertheless, for such intermediate states of charge, it is not clear [82–84] how the lithium ions distribute over the tetragonal sites. If no interaction would occur between the lithium ions and the different constituents of the host material, the lithium ions would be homogeneously distributed over the crystalline structure. But the fact that the lithium ions are distributed solely over some of the tetragonal sites indicates that they interact with the host material constituents. Such interactions may affect the material properties of the host material. Indeed, as already said at the beginning of this section, the variation of the lithium amount induces a slight modification of the lattice parameter a , but also, as reported in Ref. [85], changes in the band structure. Moreover, the interactions of the lithium ions with the host material may induce long-range effects like lithium ions ordering [82] or phase segregation [16, 32]. In the present work we will solely focus on phase segregation. The occurrence of phase segregation has been extensively reported in the literature: Measurements of battery discharge curves [86], measurements of the lattice parameter using both X -rays [16, 36, 87, 88] and neutron diffractions [89, 90] as well as theoretical calculations [38] all corroborate the existence of two distinguishable cubic phases exhibiting different “states of charge” whose values depend on the temperature.

In our work, phase segregation will be described using a coarse-graining approach (see Sec. 3.2.3), thus the knowledge of the exact distribution of the lithium ions over the interstitial lattice sites is not necessary. In this context and in order to simplify further notations and calculations, we consider that the lithium ions, instead of being distributed over the two cubic face-centered sublattices are distributed

¹The assumption that the crystalline structure remains cubic over charging and discharging becomes invalid if the battery is fastly charged or discharged. Indeed, due to fast charging and discharging, the lithium concentration n , whose average over the particle equals the state of charge x , may locally reach values larger than one even if $x < 1$. At this place, the crystalline structure instead of being cubic overall exhibits regions where it is locally tetragonal [80, 81].



(a) First kind of elementary cell (Type I).

(b) Second kind of elementary cell (Type II).

Figure 3.3: Sketch of the two kinds of elementary cell based on the face-centered cubic cell formed by the ions O^{2-} . The manganese and lithium ions are represented by the blue and green spheres, respectively.

over a single cubic lattice whose lattice parameter equals a . A representation of this “effective” sublattice is shown in Fig. 3.5). Note that this “effective” sublattice ensures the conservation of the lithium ion stoichiometry with respect to the other material constituents.

3.1.2 Microscopic Hamiltonian

As already outlined in the previous section, LMO is a material that may exhibit phase segregation depending on both the temperature and the lithium amount present in the crystalline structure. Phase segregation means that instead of being homogeneous over the entire system, the lithium concentration exhibits, even at equilibrium, regions with different lithium concentration values separated by a smooth interface as schematically sketched in Fig. 3.6. Phase segregation is a consequence of attractive interactions between the different material constituents [91]. Thus it was important to introduce the microscopic underlying structure (see Sec. 3.1.1). At this place we will describe phase segregation by means of a microscopic model accounting for an effective attractive lithium/lithium interaction.

Moreover, we also pointed out in the previous section that the symmetry of the crystalline structure exhibited by LMO is correlated with the lithium amount present in the material. Thus the coupling between the host material referred to as $Li_{x_0}Mn_2O_4$ — where x_0 denotes the lithium amount of the host material in the reference or initial state — and the lithium ions that are inserted into or released from the host material must be accounted for. At given temperature and lithium amount, the system internal energy is usually described by a Hamiltonian that depends on a set of microscopic variables.

A classical Hamiltonian without kinetic terms is a function of the spatial coordinates of each ion that forms the considered LMO crystal. Building such a Hamiltonian relies on the knowledge of the

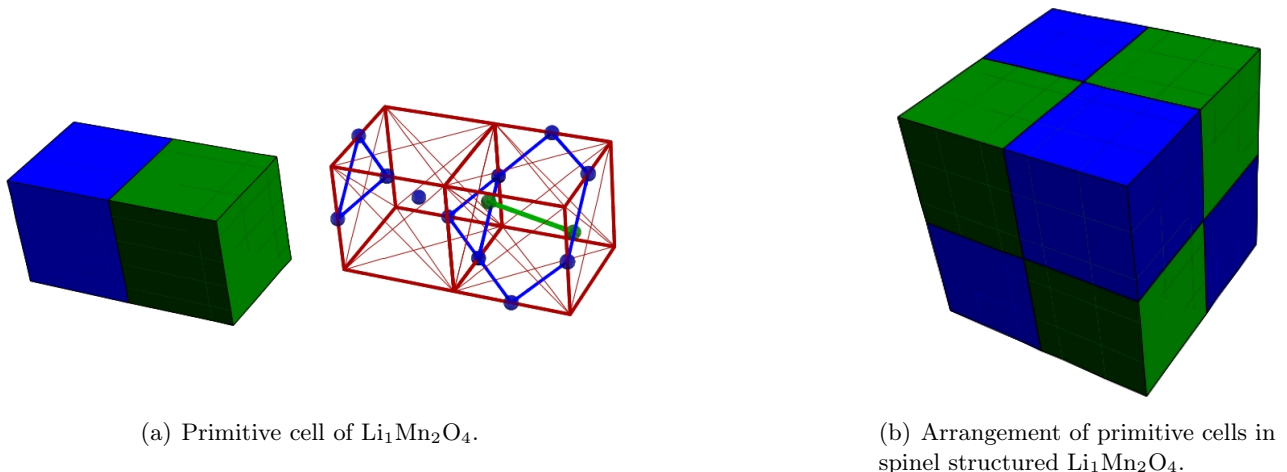


Figure 3.4: *Elementary cell of a spinel structured crystalline material. The cell of Type I and II are schematically sketched in blue and in green, respectively.*

interactions that act between the different material constituents at various length scales being both short- and long-range. The equilibrium positions of the different material constituents are those that minimize the Hamiltonian. Their computation is very costly and requires ab-initio calculations. Such calculations have been performed in Ref. [92, 93] in case of LMO ($0 < x < 2$). But, unfortunately, they are reliable only for a very small number of ions and cannot account for collective behavior induced by correlations that occur at a length scale much larger than the distance between two-neighboring species. Nevertheless ab-initio calculations remain a powerful method to predict the crystalline structure as well as the locations of the interstitial lattice sites available for the lithium ion intercalation. Indeed, the spinel structure exhibited by LMO (see Sec. 3.1.1), when the state of charge is $0 < x < 1$, as well as the lattice parameter as a function of the lithium amount could be obtained [74] in agreement with the experimental measurements reported in Ref. [94].

Due to the fact that ab-initio methods require significant computing resources and become even unfeasible when the spatial extent of the considered system reaches some micrometers (corresponding to about 10^{12} ions in total), this method is not practicable when the state of charge is going to be continuously varied because it requires the computation of the entire crystalline structure at each change in the lithium amount into the host material.

Alternatively, based on the work done by Vakarin et al. [95], it is possible to assume that variations in the lithium concentration in the host material only give rise to small host distortions. This assumption however excludes drastic changes of the crystalline host structure and thus cannot account for the cubic-to-tetragonal transition that has been experimentally observed at $x = 1$. Nevertheless, this assumption allows for some simplifications that avoid the computation of the whole crystalline structure at each change of the lithium amount in the host material.

Thus, under the assumption of small lithium-induced deformations, the Hamiltonian of the system \mathcal{H} is separated into two parts corresponding on the one hand to the Hamiltonian of the host material denoted by $\mathcal{H}_{\text{host}}$ and on the other hand to the Hamiltonian of the intercalated lithium ions referred to as \mathcal{H}_{Li} ,

$$\mathcal{H} = \mathcal{H}_{\text{host}} + \mathcal{H}_{\text{Li}}. \quad (3.1)$$

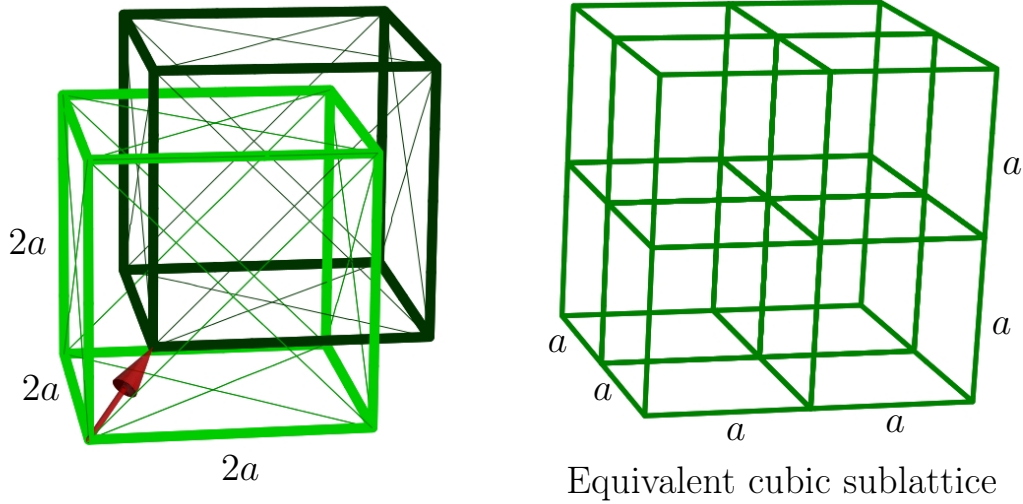


Figure 3.5: Schematic representation of the two-cubic face centered sublattices — sketched in dark and light green, respectively (on the left) — available for the lithium ions Li^+ in $\text{Li}_x\text{Mn}_2\text{O}_4$ ($0 < x < 1$) as well as of the equivalent “effective” cubic sublattice — sketched in medium green (on the right). The red arrow represents the shift of these two sublattices. This shift is equal to $(\sqrt{3}/2)a$ and is oriented along the space diagonal of these sublattices.

In a classical microscopic description, the Hamiltonian of the system is a function of the spatial coordinate of each ion that forms the crystalline $\text{Li}_x\text{Mn}_2\text{O}_4$ material as well as of the number lithium occupation of the interstitial lattice sites also referred to as site concentration. The spatial locations of both the oxygen and the manganese ions are formally denoted by $\{\mathbf{r}_{\alpha_1}, \mathbf{r}_{\alpha_2}\} \in \mathbb{R}^{4 \times 3\mathcal{N}} \times \mathbb{R}^{2 \times 3\mathcal{N}}$ where $\alpha_1 \in \{1, \dots, 4\mathcal{N}\}$ and $\alpha_2 \in \{1, \dots, 2\mathcal{N}\}$ are indices which denote the oxygen and the manganese ions, respectively. The number \mathcal{N} corresponds to the total number of interstitial tetrahedral lattice sites available for the lithium ions. The state of each of these sites is characterized by its spatial coordinate denoted by $\mathbf{r}_\alpha \in \mathbb{R}^3$ and by its lithium occupation number $n_\alpha \in \{0, 1\}$ where $\alpha \in \{1, \dots, \mathcal{N}\}$ is an index of all available interstitial lattice sites.

The host Hamiltonian $\mathcal{H}_{\text{host}}$ is a function of the variables $\{\mathbf{r}_{\alpha_1}, \mathbf{r}_{\alpha_2}, \mathbf{r}_\alpha, n_\alpha\}$ where the equilibrium positions of both the oxygen and manganese ions as well as the coordinates of the interstitial lattice sites available for the lithium ion intercalation may depend on the lithium ion distribution $\{n_\alpha\}$. For fixed total number of lithium ions in the crystalline LMO cathodic particle, the equilibrium host structure is represented by a set of equilibrium positions $\{\mathbf{r}_{\alpha_1}^0, \mathbf{r}_{\alpha_2}^0\}$ for both the oxygen and manganese ions and by the equilibrium lithium ion states $\{\mathbf{r}_\alpha^0, n_\alpha^0\}$. Further, provided that the lithium ion distribution $\{n_\alpha^0\}$ over the crystalline structure is homogeneous, this configuration can be chosen as reference which is related to the reference state of charge x_0 of the host material.

During lithium insertion into and extraction from the cathodic particle, the total number of lithium ions present in the system is varied. Changes in the lithium amount induce changes in the equilibrium positions of the oxygen and manganese ions as well as in the lithium ion configuration. If the total number of lithium ions in the system is varied not so much from the one corresponding to the reference lithium ion configuration, the host Hamiltonian may be written as a superposition of two Hamiltonians,

$$\mathcal{H}_{\text{host}} = \mathcal{H}_{\text{host}}^0 + \Delta\mathcal{H}_{\text{host}}$$

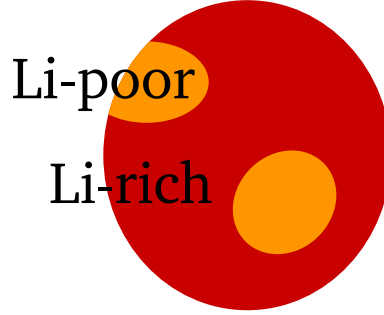


Figure 3.6: Schematic representation of a phase-segregated states in a cathodic particle made of LMO. The phase shown in red represents the high-concentration phase whereas the phase shown in yellow is related to the low-concentration phase. The interface between these two phases is smooth.

where $\mathcal{H}_{\text{host}}^0$ refers to the constant value of the host Hamiltonian when the microscopic system state is equal to $\{\mathbf{r}_{\alpha_1}^0, \mathbf{r}_{\alpha_2}^0, \mathbf{r}_{\alpha}^0, n_{\alpha}^0\}$. The Hamiltonian $\Delta\mathcal{H}_{\text{host}}$ stands for a perturbative Hamiltonian expressed as a function of the current lithium ion distribution $\{n_{\alpha}\}$ relatively to the reference lithium ion configuration $\{n_{\alpha}^0\}$. Moreover, since variations in the lithium amount are assumed to give rise to small host deformations, the perturbative Hamiltonian depends only on the mechanical displacements of the host lattice represented by the displacements of the interstitial lattice,

$$\mathbf{u}_{\alpha} = \mathbf{r}_{\alpha} - \mathbf{r}_{\alpha}^0, \quad \alpha \in \{1, \dots, \mathcal{N}\},$$

since here a topotactic lithium intercalation² is considered. That means that the displacement of nearest neighboring ions of different species in the host lattice are the same and equal to the displacement of the nearest neighboring interstitial lattice site. In that representation, the host Hamiltonian is expressed with regard to a reference lithium ion configuration. The crystalline host structure remains unmodified and only small host deformations leading to small changes in the lattice parameter, driven by changes in the lithium amount, are assumed. This allows for the decoupling of the host Hamiltonian into two contributions where the first one, $\mathcal{H}_{\text{host}}^0$, is simply a constant that is neglected when minimizing the host Hamiltonian with respect to the lithium ion configuration and the mechanical displacements of the host lattice. Finally it holds

$$\mathcal{H}_{\text{host}}\{n_{\alpha}, \mathbf{u}_{\alpha}\} = \underbrace{\mathcal{H}_{\text{host}}^0\{\mathbf{r}_{\alpha_1}^0, \mathbf{r}_{\alpha_2}^0, \mathbf{r}_{\alpha}^0, n_{\alpha}^0\}}_{\text{constant}} + \Delta\mathcal{H}_{\text{host}}\{n_{\alpha}, \mathbf{u}_{\alpha}\}.$$

The relevant perturbative term $\Delta\mathcal{H}_{\text{host}}\{n_{\alpha}, \mathbf{u}_{\alpha}\}$ is usually identified with the energetic contribution induced by short-range elastic interactions between the host material constituents that are driven by lithium concentration changes only. In Ref. [97, 98] this term is obtained from microscopic considerations based on short-range forces. In Ref. [99], this term is treated microscopically using a mean-field approximation, while, in this work, it will be directly treated by means of a linear elasticity theory commonly used in continuum mechanics (see Sec. 3.2.4). In this framework, it is implicitly assumed

²A topotactic intercalation denotes an intercalation where the structural changes of the host lattice under intercalation shows one or more crystallographically equivalent, orientational relationships to the crystal lattice of the parent phase [96].

that the host deformations are small and do not give rise to drastic structural changes of the host structure.

We now turn to the understanding of the Hamiltonian \mathcal{H}_{Li} as written in Eq. (3.1). This term represents the internal energy of the lithium ions which are inserted into or extracted from the host material and that are here considered as guest species. Thus the lithium ions are here not treated as part of the crystalline material but as impurities that feel the potential induced by the ions that form the host crystalline structure. Due to the periodicity of the host crystalline structure, this potential is periodic with regard to the spatial coordinates with minima that define the positions of the interstitial lattice sites.

Inserting a single lithium ion into the host material brings an additional energetic contribution U_0 to the internal system energy due to the formation of chemical bondings between the inserted lithium ion and the neighboring ions belonging to the host material. Because of the periodicity of the crystalline host structure, the value of U_0 does not depend on the specific interstitial lattice site chosen for the lithium ion intercalation. However, in the neighborhood of the intercalated lithium ion, these chemical bondings may give rise to a slight modification of the potential generated by the host material ions. Effectively, this potential change can be seen as an interaction U between nearest neighboring lithium ions.

The term U_0 stands for the interaction between the host material ions and the inserted lithium ions while the term U stands for the effective interaction between two nearest neighboring lithium ions. Both are potential energy terms and thus possibly depend on the distance between the two interacting species and consequently on the mechanical displacement \mathbf{u}_α . Under these assumptions the Hamiltonian representing the internal energy of the lithium ions reads

$$\mathcal{H}_{\text{Li}}\{n_\alpha, \mathbf{u}_\alpha\} = \sum_{\alpha} U_0(\mathbf{u}_\alpha) n_\alpha + \sum_{\langle \alpha, \alpha' \rangle} U(\mathbf{u}_\alpha, \mathbf{u}_{\alpha'}) n_\alpha n_{\alpha'}$$

where $\langle \alpha, \alpha' \rangle$ refers to a pair of nearest neighboring lattice sites available for the lithium ion intercalation. In Ref. [99], because the lithium-induced mechanical displacements are assumed to be small, both displacement-dependent potentials, $U_0(\mathbf{u}_\alpha)$ and $U(\mathbf{u}_\alpha, \mathbf{u}_{\alpha'})$, are approximated by means of a Taylor expansion performed up to 2nd order in the mechanical displacement. Such a Hamiltonian may be referred to as “distorsive lattice gas model” in contrast to the “rigid lattice gas model” [66, 67] where the displacement dependence of the potentials is neglected. For the purpose of this work, we make use of the rigid lattice gas model assumption and further assume that the potentials are constant.

Finally, the Hamiltonian Eq. (3.1) representing the lithium intercalation into the host crystalline LMO material is rewritten as

$$\mathcal{H}\{n_\alpha, \mathbf{u}_\alpha\} = \text{cst} + \Delta\mathcal{H}_{\text{host}}\{n_\alpha, \mathbf{u}_\alpha\} + U_0 \sum_{\alpha} n_\alpha + U \sum_{\langle \alpha, \alpha' \rangle} n_\alpha n_{\alpha'}. \quad (3.2)$$

In a first step, the term $\Delta\mathcal{H}_{\text{host}}\{n_\alpha, \mathbf{u}_\alpha\}$ standing for the elastic interactions between the host material constituents will be neglected. The remaining term corresponding to the rigid lattice gas model will be treated in the mean-field approximation (see Sec. 3.2.1) which turns out to be insufficient for the purpose of describing phase segregation. Thus the mean-field approximation will be extended by a coarse-graining approach (see Sec. 3.2.3) where the system free energy is replaced by a free energy functional. Further and finally, the elastic term is approximated by a coarse-grained functional (see Sec. 3.2.4) standing for the energetic contribution of the lithium-induced elastic deformations of the host material in the context of linear elasticity.

3.1.3 Thermodynamical potentials

For a large number of participating constituents in Hamiltonian Eq. (3.2), determining the unknown microscopic quantities being the lithium ion configuration $\{n_\alpha\}$ and the set of mechanical displacements $\{\mathbf{u}_\alpha\}$ that minimize the Hamiltonian is not possible. Indeed the total number of freedom degrees equal to $4N$ is too big. On the other hand, when the system is in contact with its environment, its microscopic state undergoes rapid fluctuations and is in general not accessible to experiments. Knowledge of the precise microscopic state is therefore almost instantly outdated and hence useless. In statistical physics, such a system is described by a “statistical ensemble” [100, 101], a set of microscopic states $\{n_\alpha, \mathbf{u}_\alpha\}$ which are reached with a certain probability $p(\{n_\alpha, \mathbf{u}_\alpha\})$ in the course of the fast fluctuations. Such ensembles are characterized by macroscopic variables that represent averages either over the entire system volume (thermodynamical quantities) or over a mesoscopic representative volume (coarse-grained quantities).

When changing from a microscopic description to a macroscopic description (by a statistical ensemble), information about the system state is lost. This loss is quantified by the system entropy defined as

$$S = -k_B \sum_{\{n_\alpha, \mathbf{u}_\alpha\}} p(\{n_\alpha, \mathbf{u}_\alpha\}) \ln p(\{n_\alpha, \mathbf{u}_\alpha\}).$$

In a macroscopic description of the system, the system entropy that corresponds to information loss is generally nonzero because the microscopic configurations are replaced by a set of averaged macroscopic quantities for which there usually exists numerous accessible microscopic configurations. At equilibrium, the entropy satisfies the maximum principle [102]. This means that, under given constraints, the probability distribution maximizes the entropy.

An example of such equilibrium statistical ensembles is the “microcanonical ensemble” [100] where the internal energy E and the total number of lithium ions N are fixed. The probability distribution is

$$p(\{n_\alpha, \mathbf{u}_\alpha\}) = \begin{cases} \frac{1}{W(E, N)} & \text{if } \mathcal{H}(\{n_\alpha, \mathbf{u}_\alpha\}) = E \text{ and } N(\{n_\alpha, \mathbf{u}_\alpha\}) = N \\ 0 & \text{otherwise} \end{cases}$$

where the quantity $W(E, N)$ is the total number of microscopic states with internal energy $\mathcal{H}(\{n_\alpha, \mathbf{u}_\alpha\})$ equal to E and number of lithium ions $N(\{n_\alpha\}) = \sum_\alpha n_\alpha$ equal to N .

While the microcanonical ensemble describes completely isolated systems, systems which are in contact with the environment and can exchange energy at fixed total lithium ions number N are described by the “canonical ensemble” [100]. In this situation, only the average internal energy \bar{E} is tuned by the Lagrange parameter $1/T$, the inverse of the temperature T . The probability distribution reads

$$p(\{n_\alpha, \mathbf{u}_\alpha\}) = \frac{1}{\mathcal{Z}_c(T, N)} \exp\left(-\frac{\mathcal{H}(\{n_\alpha, \mathbf{u}_\alpha\})}{k_B T}\right).$$

The normalization of this probability distribution, $\sum_{\{n_\alpha, \mathbf{u}_\alpha\}} p(\{n_\alpha, \mathbf{u}_\alpha\}) = 1$, is ensured by the canonical partition function,

$$\mathcal{Z}_c(T, N) = \sum_{\{n_\alpha, \mathbf{u}_\alpha\}} \delta_{N, \sum_\alpha n_\alpha} \exp\left(-\frac{\mathcal{H}\{n_\alpha, \mathbf{u}_\alpha\}}{k_B T}\right). \quad (3.3)$$

The canonical partition function, $\mathcal{Z}_c(T, N)$, is related to the free energy $F(T, N)$ by

$$F(T, N) = -k_B T \ln \mathcal{Z}_c(T, N).$$

The present equilibrium form minimizes the more general expression

$$\underbrace{F(T, N)}_{\text{not necessarily taken at equilibrium}} = \bar{E} - TS, \quad (3.4)$$

with average energy $\bar{E} = \sum_{\{n_\alpha, \mathbf{u}_\alpha\}} p(\{n_\alpha, \mathbf{u}_\alpha\}) \mathcal{H}(\{n_\alpha, \mathbf{u}_\alpha\})$. If we further allow the system to exchange not only energy but also lithium ions with the environment, the average lithium number \bar{N} is tuned by the additional Lagrange parameter, μ , the chemical potential. At equilibrium, such a system is described by the ‘‘grand canonical ensemble’’ and the probability distribution reads

$$p(\{n_\alpha, \mathbf{u}_\alpha\}) = \frac{1}{\mathcal{Z}_{\text{gc}}(T, \mu)} \exp\left(-\frac{\mathcal{H}(\{n_\alpha, \mathbf{u}_\alpha\}) - \mu N(\{n_\alpha\})}{k_B T}\right) \quad (3.5)$$

with the grand canonical partition function,

$$\mathcal{Z}_{\text{gc}}(T, \mu) = \sum_{\{n_\alpha, \mathbf{u}_\alpha\}} \exp\left(-\frac{\mathcal{H}(\{n_\alpha, \mathbf{u}_\alpha\}) - \mu N(\{n_\alpha\})}{k_B T}\right). \quad (3.6)$$

It is related to the grand canonical potential by

$$J(T, \mu) = -k_B T \ln \mathcal{Z}_{\text{gc}}(T, \mu) \quad (3.7)$$

which at equilibrium minimizes the more general expression

$$\underbrace{J(T, \mu)}_{\text{not necessarily taken at equilibrium}} = \bar{E} - TS - \mu \bar{N}. \quad (3.8)$$

In both the canonical and grand canonical ensembles, all available microscopic states even those with low probabilities are taken into account. Even at equilibrium, the system state is not a fixed quantity but oscillates between all available microscopic states. The system fluctuations averaged over time correspond to a macroscopic ensemble with average internal energy \bar{E} and average total number of lithium ions \bar{N} . In the thermodynamical limit, e.g. $\mathcal{N} \gg 1$, fluctuations of extensive variables such as E and N are negligible and all aforementioned ensembles are equivalent. Therefore we will no longer distinguish E and \bar{E} , N and \bar{N} .

In case of interaction between the material constituents, the evaluation of the grand canonical function is a complicated problem. Its calculation generally cannot be done without approximations. The most common one is the mean-field approximation where the summation over all available microscopic states is replaced by evaluation at the most probable microscopic configuration that is assumed to be homogeneous with respect to the lithium ion distribution. This approximation further allows for a simplification of the calculation of grand canonical potential Eq. (3.7). We will see in the next section, Sec. 3.2, how the mean-field approximation is put into action and we will demonstrate its failure for systems of attractively interacting constituents and how we can remediate.

3.2 Mean-field approximation and beyond

3.2.1 Mean-field approximation and homogeneous state

In this part, the free energy of a system of lithium ions intercalated into a crystalline structure made of LMO in the absence of host deformations is evaluated in the mean-field approximation. Since the lithium-induced host deformations are here neglected, the long-range elastic interactions represented by the perturbative Hamiltonian $\Delta\mathcal{H}_{\text{host}}\{n_\alpha, \mathbf{u}_\alpha\}$ are zero and the system Hamiltonian, Eq. (3.2), reduces to

$$\mathcal{H}\{n_\alpha\} = \overbrace{U_0 \sum_{\alpha} n_\alpha}^{\text{one-body term}} + U \underbrace{\sum_{\langle \alpha, \alpha' \rangle} n_\alpha n_{\alpha'}}_{\text{two-body term}} \quad (3.9)$$

which depends on the lithium ion distribution $\{n_\alpha\}$ only. This Hamiltonian stands for the internal energy of a system of lithium ions that may be intercalated at fixed spatial locations being the interstitial sites related to the “effective” cubic lattice sketched in Fig. 3.5 of Sec. 3.1.1. These fixed spatial locations are indexed by the parameter $\alpha \in \{1, \dots, \mathcal{N}\}$.

The Hamiltonian of Eq. (3.9) is a superposition of two terms. The former one is a one-body term that represents the internal energy of having a given lithium amount in the crystalline host material. This term does not depend on the lithium ion configuration over the system and thus is $\binom{\mathcal{N}}{N}$ -fold degenerate. The latter term is a two-body term that partially allows for the lifting of the system degeneracies since the internal energy now becomes dependent on the lithium ion configuration and not only on the lithium ion amount.

This two-body term represents a major complication when calculating the thermodynamical potentials. In the mean-field approximation, it is replaced by an effective one-body term under the assumption that the thermal fluctuation δn_α of an interstitial lattice state n_α is small in comparison with the lithium site concentration \bar{n} averaged over the entire crystalline structure. For $\delta n_\alpha \ll \bar{n}$ we put

$$n_\alpha = \bar{n} + \delta n_\alpha \quad (3.10)$$

that is inserted into Eq. (3.9). As we show in App. B in more details, by neglecting terms of order $\mathcal{O}(\delta n_\alpha \delta n_{\alpha'})$, we obtain the effective one-body Hamiltonian

$$\mathcal{H}_{\text{eff}}\{n_\alpha\} = \overbrace{(U_0 + U\Gamma\bar{n})}_{\text{effective field}} \sum_{\alpha} n_\alpha - \frac{\mathcal{N}U\Gamma}{2} \bar{n}^2. \quad (3.11)$$

The field felt by a lithium ion located at the interstitial lattice site α is an effective field obtained from the superposition of the one-body term of Hamiltonian Eq. (3.9) and an averaged field $U\Gamma\bar{n}$ engendered by all lithium ions that interact with the lithium ion at the interstitial lattice site α . Here, the quantity Γ refers to the total number of nearest neighboring interstitial lattice sites and, since the interstitial lattice is assumed as cubic, $\Gamma = 6$. In the mean-field approximation, the coupling between two nearest neighboring lithium ions occurs via an unknown but constant field, thus there is no more correlation between these ions. Consequently, the lithium site concentration may be assumed as homogeneous over the entire system.

In the considered system, the thermodynamical potential of interest to describe the lithium intercalation within the crystalline cathodic particle is the system free energy which depends on the temperature T , on the total number of lithium ions N present in the host material as well as on the particle volume V or more generally, in case of a solid material, on the strain tensor $\boldsymbol{\varepsilon}$. Because the lithium-induced deformations of the host material are neglected in Hamiltonian Eq. (3.9) the system free energy that can be calculated by means of this Hamiltonian depends on the temperature and the total number of lithium ions only and is referred to as $F(T, N)$.

The calculation of the system free energy by means of the Hamiltonian Eq. (3.9) requires the calculation of the canonical partition function $\mathcal{Z}_c(T, N)$, see Eq. (3.3). Its computation is complicated by the constraint that fixes the total number of lithium ions $N = \sum_{\alpha} n_{\alpha}$. To avoid this problem, instead of directly calculating the system free energy, we choose to calculate the system grand canonical potential $J(T, \mu)$ which is related to the free energy (see Eqs. (3.4) - (3.8)) by a Legendre transformation. It holds

$$F(T, N) = J(T, \mu) + \mu N \quad (3.12)$$

where the chemical potential μ is the conjugate variable of the total number of lithium ions,

$$N = - \left. \frac{\partial J(T, \mu)}{\partial \mu} \right|_T. \quad (3.13)$$

The grand canonical partition function, Eq. (3.6), is easier to calculate than the canonical one because the constraint term $\delta_{N, \sum_{\alpha} n_{\alpha}}$ in Eq. (3.3) is replaced by the ‘‘one-body term’’ $-\mu \sum_{\alpha} n_{\alpha}$ in Eq. (3.6). To easily compute the grand canonical partition function, instead of considering the Hamiltonian Eq. (3.9), we use the effective mean-field Hamiltonian Eq. (3.11) where the average site lithium concentration \bar{n} is identified with

$$\bar{n} = \frac{N}{\mathcal{N}} \quad (3.14)$$

since, in the mean-field approximation the lithium concentration is assumed to be homogeneous over the entire crystalline cathodic particle. In the grand-canonical ensemble \bar{n} is not a free variable but it is fixed by the self-consistency condition Eq. (3.13) which relates the chemical potential μ as function of the total number of lithium ions N .

As shown in App. B, this relation enables us to perform the Legendre transformation, Eq. (3.12), to obtain the system free energy,

$$F(T, \bar{n}) = \mathcal{N} \left(U_0 \bar{n} + \frac{U\Gamma}{2} \bar{n}^2 + k_B T (\bar{n} \ln(\bar{n}) + (1 - \bar{n}) \ln(1 - \bar{n})) \right), \quad (3.15)$$

and its associated conjugate quantities, namely the chemical potential $\mu(T, \bar{n})$ and the entropy $S(T, \bar{n})$, read

$$\mu(T, \bar{n}) = \left. \frac{\partial F}{\partial N} \right|_T = U_0 + U\Gamma \bar{n} + k_B T \ln \left(\frac{\bar{n}}{1 - \bar{n}} \right), \quad (3.16)$$

$$S(T, \bar{n}) = - \left. \frac{\partial F}{\partial T} \right|_N = -k_B \mathcal{N} (\bar{n} \ln(\bar{n}) + (1 - \bar{n}) \ln(1 - \bar{n})). \quad (3.17)$$

Note that the entropy Eq. (3.17) being independent of the interaction term U is the same as the entropy of a system of noninteracting lithium ions in the thermodynamic limit³.

3.2.2 Phase segregation and Maxwell construction

To simplify the study of the equilibrium states of the system, we introduce two quantities, α_1 and α_2 , so that

$$U_0 = \alpha_1 k_B T_{\text{ref}}, \quad (3.18)$$

$$U\Gamma = \alpha_2 k_B T_{\text{ref}}, \quad (3.19)$$

where T_{ref} is a reference temperature, here chosen equal to room temperature, $T_{\text{ref}} = 25^\circ\text{C}$. Using Eq. (3.18) and Eq. (3.19), the system free energy, Eq. (3.15), is rewritten as

$$F(T, \bar{n}) = \mathcal{N} k_B T \left(\alpha_1 \frac{T_{\text{ref}}}{T} \bar{n} + \frac{\alpha_2}{2} \frac{T_{\text{ref}}}{T} \bar{n}^2 + \bar{n} \ln(\bar{n}) + (1 - \bar{n}) \ln(1 - \bar{n}) \right). \quad (3.20)$$

The site free energy per unit of $k_B T$, defined as

$$f_{\text{site}}(T, \bar{n}) = \frac{F(T, \bar{n})}{\mathcal{N} k_B T} = \left(\alpha_1 \frac{T_{\text{ref}}}{T} \bar{n} + \frac{\alpha_2}{2} \frac{T_{\text{ref}}}{T} \bar{n}^2 + \bar{n} \ln(\bar{n}) + (1 - \bar{n}) \ln(1 - \bar{n}) \right),$$

is proportional to the system free energy, Eq. (3.20), and is shown in Fig. 3.7 as function of the average site lithium concentration for different temperatures. Above a certain temperature denoted by T_c and referred to as critical temperature,

$$T_c = -\frac{\alpha_2 T_{\text{ref}}}{4}, \quad (3.21)$$

the site free energy is a convex function of the average lithium concentration \bar{n} . In contrast, for lower temperatures, $T < T_c$, it exhibits a zone of concavity where the homogeneous lithium concentration states are not stable states of the system.

The zone of concavity corresponds to the set of values (T, \bar{n}) that satisfy the following condition:

$$\frac{\partial^2 f_{\text{site}}(T, \bar{n})}{\partial \bar{n}^2} < 0.$$

This inequality is never fulfilled if $\alpha_2 \geq 0$. Thus, for a system of noninteracting lithium ions, i.e. $\alpha_2 = 0$, or for a system of lithium ions that repel each other, i.e. $\alpha_2 > 0$, the site free energy remains a convex function of $\bar{n} \in [0, 1]$ for all $T > 0$. For an attractively interacting lithium ion system, i.e. $\alpha_2 < 0$, depending on the temperature, the site free energy may exhibit a zone of concavity. If $T > T_c$ the site free energy is convex for all $\bar{n} \in [0, 1]$. Otherwise, if $T < T_c$, the site free energy exhibits a zone of concavity corresponding to the interval $[\bar{n}_-, \bar{n}_+]$ with

$$\bar{n}_\pm = \frac{1}{2} \left(1 \pm \sqrt{1 - \frac{T}{T_c}} \right).$$

³In the thermodynamical limit, the total number of lithium ions is assumed to be large whereas the lithium ion density (equal to the total number of lithium ions per unit of volume) is taken constant.

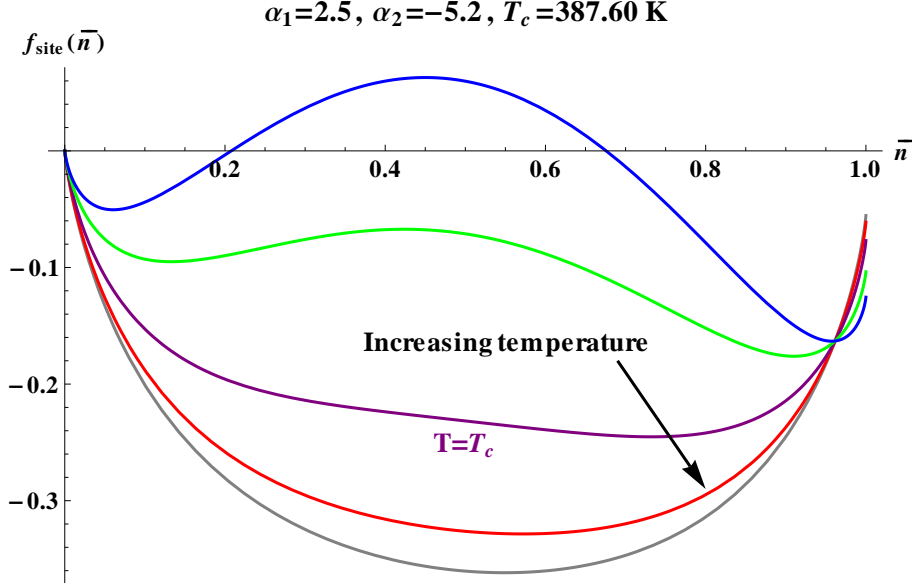


Figure 3.7: Site free energy $f_{\text{site}}(T, \bar{n})$ as function of the average lithium concentration \bar{n} for different temperatures. The curve drawn in purple corresponds to the case $T = T_c$. The blue and green curves exhibiting a zone of concavity both are related to temperatures lower than the critical temperature. Both the grey and red curves are convex over the interval $[0, 1]$ and hence correspond to temperatures larger than the critical temperature.

The existence of this zone of concavity indicates that homogeneous lithium concentration states do not always ensure the system free energy to be minimal, thus invalidating the mean-field approximation where the lithium concentration is assumed to be homogeneous over the entire system. In the concavity zone, the system becomes unstable towards phase segregation. In equilibrium, its bulk disintegrates into “macroscopic” regions with different lithium concentration. By means of the Maxwell construction, it is possible to construct such nonhomogeneous lithium concentration states related to a system free energy which is lower than that of the corresponding homogeneous states. For a mean-field free energy that exhibits a double-well structure, the Maxwell construction predicts that the system splits into regions with concentrations being either \bar{n}_{0-} or \bar{n}_{0+} . Their corresponding volume fractions, q and $(1 - q)$, respectively, are fixed by the average lithium concentration, according to

$$\bar{n} = q \bar{n}_{0-} + (1 - q) \bar{n}_{0+}.$$

Thus it is clear that phase segregation occurs when the lithium concentration is in the range $\bar{n}_{0-} < \bar{n} < \bar{n}_{0+}$. The free energy per site, $f_{\text{site}}^{\text{MC}}(T, \bar{n})$ obtained by the Maxwell construction, is equal to

$$f_{\text{site}}^{\text{MC}}(T, \bar{n}) = q f_{\text{site}}(T, \bar{n}_{0-}) + (1 - q) f_{\text{site}}(T, \bar{n}_{0+})$$

and now represents the system free energy. The system free energy is minimized by requiring that the concentrations, \bar{n}_{0-} and \bar{n}_{0+} , satisfy the following set of equations:

$$\begin{aligned} \frac{\partial f_{\text{site}}(T, \bar{n})}{\partial \bar{n}}(T, \bar{n}_{0-}) &= \frac{\partial f_{\text{site}}(T, \bar{n})}{\partial \bar{n}}(T, \bar{n}_{0+}), \\ f_{\text{site}}(T, \bar{n}_{0-}) - \bar{n}_{0-} \frac{\partial f_{\text{site}}(T, \bar{n})}{\partial \bar{n}}(T, \bar{n}_{0-}) &= f_{\text{site}}(T, \bar{n}_{0+}) - \bar{n}_{0+} \frac{\partial f_{\text{site}}(T, \bar{n})}{\partial \bar{n}}(T, \bar{n}_{0+}). \end{aligned}$$

This means that, at given temperature, the tangents to the site free energy evaluated at \bar{n}_{0-} and \bar{n}_{0+} , respectively, are equal, as shown in Fig. 3.8, which implies that the chemical potentials of both the low- and high-concentration phases are equal. For this reason, the Maxwell construction is also referred to

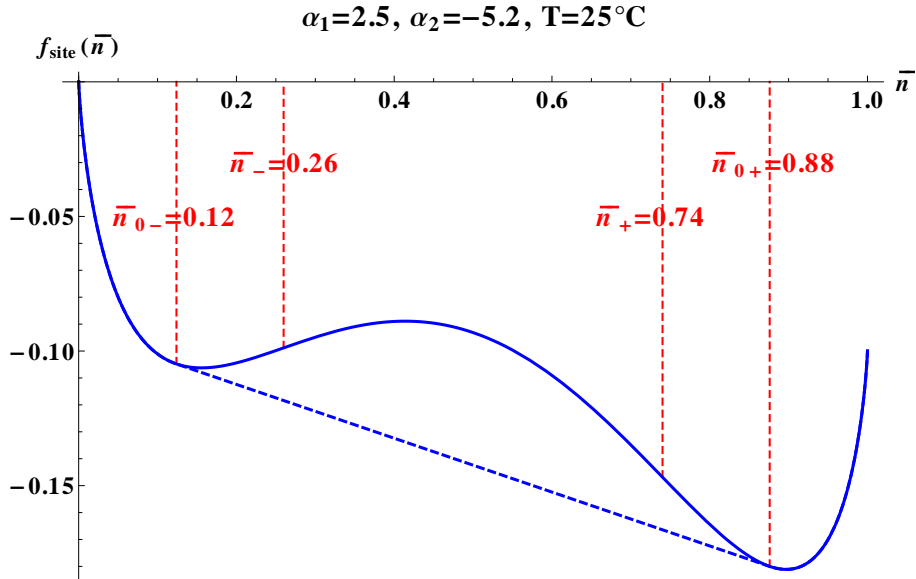


Figure 3.8: The solid blue line shows the path of the mean-field free energy at fixed temperature, $T = 25^\circ\text{C}$ which exhibits a double-well structure. The Maxwell construction or common tangent construction is represented by the dashed blue line.

as “common tangent construction”.

According to this construction, phase segregation arises not exactly when the concavity zone of the site free energy is reached, but for lithium concentration values that are outside of the interval defining this zone. Indeed, it holds

$$n_{0-} < n_- \text{ and } n_{0+} > n_+.$$

In the range of values belonging to the intervals $[n_{0-}, n_-]$ and $[n_+, n_{0+}]$, defining the “nucleation zone” of the system free energy, phase segregation arises only if the amplitude of the thermal fluctuations is so that the lithium concentration locally reaches values being in the concavity zone of the system free energy. Such a behavior is characteristic to first order phase transitions where the “new phase” has the possibility to grow inside of a matrix made of “old phase” [103]. This behavior is rather different from the one exhibited in the concavity zone of the system free energy also referred to as “spinodal zone” [87, 104]. In this zone, even infinitesimal thermal fluctuations give rise to phase segregation. Homogeneous states in the nucleation zone correspond to metastable states that are allowed provided that the thermal fluctuations do not locally drive the system in the spinodal zone. On the contrary, in the spinodal zone, the homogeneous states are unstable against the smallest fluctuations.

The Maxwell construction allows to predict without further complicated calculations the range of values where the lithium concentration state is either homogeneous or phase-segregated. In case of phase segregation (nucleation or spinodal decomposition), it yields the lithium concentration values $\bar{n}_{0\pm}$ reached in the two different phases as well as their proportion in the system, as illustrated in the phase diagram of Fig. 3.9. The different regimes and phase transitions reached at equilibrium and

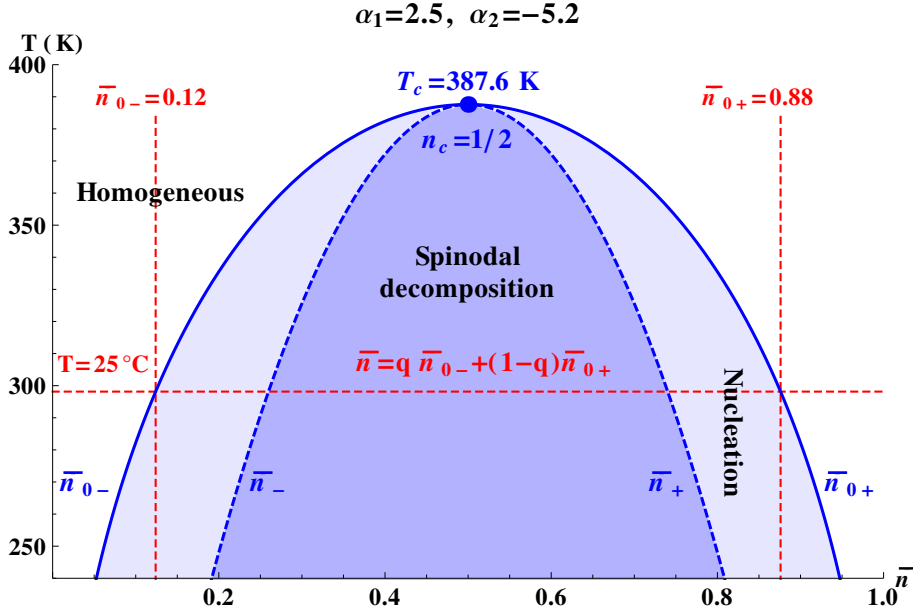


Figure 3.9: Phase diagram of a system of attractively interacting lithium ions. The blue solid and dashed lines represent $\bar{n}_{0\pm}(T)$ and $\bar{n}_{\pm}(T)$ as functions of the temperature T , respectively. The region above the curve $\bar{n}_{0\pm}(T)$ corresponds to homogeneous concentration. Between the curves $\bar{n}_{0\pm}(T)$ and $\bar{n}_{\pm}(T)$ nucleation occurs and below $\bar{n}_{\pm}(T)$ spinodal decomposition happens. During phase segregation and for a given average site concentration \bar{n} , the fraction of system volume being in the low-concentration phase \bar{n}_{0-} is q , while the rest of the system is in the high-concentration phase \bar{n}_{0+} .

schematically sketched in the phase diagram of Fig. 3.9 all are summarized in Tab. 3.1 as function of the externally fixed parameters being the temperature T and the average lithium concentration \bar{n} . During battery discharging and charging, lithium ions are inserted into and extracted from LMO particles which are located in the cathode. During lithium intercalation or release, we assume that the temperature T is maintained constant, equal to T_{ref} , which is significantly below the critical temperature T_c . On the contrary, the average lithium concentration \bar{n} is varied between 0 and 1. Thus, during battery charging and discharging, single LMO particles may undergo a first order phase transition when the average concentration \bar{n} becomes either greater than $n_{0-}(T_{\text{ref}})$ or less than $n_{0+}(T_{\text{ref}})$ as shown in the column “ $T < T_c$ ” of Tab. 3.1. At $T = T_{\text{ref}} < T_c$, depending on the average lithium concentration in the considered cathodic particle, both nucleation and spinodal decomposition are possible processes leading to phase segregation.

Despite its simplicity, the Maxwell construction is a powerful method to predict the state of a system where phase segregation may arise as function of externally fixed parameters being here T and \bar{n} . However, the Maxwell construction that is derived from the mean-field approximation where the correlations between the thermal fluctuations are neglected, does not provide a theoretical framework allowing for the understanding of the growth of a phase-segregated state from a homogeneous state. Neither is it able to describe realistically the lithium concentration profile at the boundary between the two different phases which is implicitly assumed to be discontinuous.

Based on the Maxwell construction, it is possible to model the lithium intercalation into a cathodic

$\bar{n} \backslash T$	$T > T_c$	$T = T_c$	$T < T_c$
$]0, \bar{n}_{0-}(T)[$ or $] \bar{n}_{0+}(T), 1[$	homogeneous	homogeneous	homogeneous
$\bar{n}_{0-}(T)$ or $\bar{n}_{0+}(T)$	homogeneous	homogeneous	1st order PT
$] \bar{n}_{0-}(T), \bar{n}_-(T)[$ or $] \bar{n}_+(T), \bar{n}_{0+}(T)[$	homogeneous	homogeneous	nucleation
$] \bar{n}_-(T), n_c(T)[$ or $] n_c(T), \bar{n}_+(T)[$	homogeneous	homogeneous	spinodal decomposition
$n_c(T) = 1/2$	homogeneous	2nd order PT	spinodal decomposition

Table 3.1: Summary of the different system states at equilibrium as function of the external parameters, the temperature T and the average lithium concentration \bar{n} . The term “PT” abbreviates “phase transition”.

particle made of LMO but it requires, at each time step, the tracking of the sharp phase boundary. To avoid this cumbersome tracking, we now turn to a formalism that accounts for a smooth interface between regions being in two different lithium concentration phases.

3.2.3 Coarse-graining and phase-field

Below the critical temperature T_c , the mean-field theory, based on the approximation that the thermal fluctuations of the microscopic state n_α are small compared to the mean value \bar{n} of all microscopic states averaged over the entire system, becomes invalid. Thus, in a microscopic point of view, for $T < T_c$, the two-body Hamiltonian, Eq. (3.9), cannot simply be replaced by the effective one-body Hamiltonian of Eq. (3.11) using the mean-field approximation, Eq. (3.10). Consequently, the evaluation of the system free energy becomes a much more complicated problem.

To overcome this difficulty the grand canonical partition function defined in Eq. (3.6) has to be reconsidered. In this equation, the microscopic quantities n_α can be decoupled by introduction of a field $n(\mathbf{r})$ using the Hubbard-Stratonovich transformation [105]. In that sense, the grand canonical partition function formally reads

$$Z_{\text{gc}}(T, \mu) = \int \mathcal{D}[n(\mathbf{r})] W[n(\mathbf{r})] \exp\left(-\frac{\mathcal{G}[n(\mathbf{r}), T, \mu]}{k_B T}\right). \quad (3.22)$$

Here, the summation $\sum_{\{n_\alpha\}}$ over all available discrete microscopic states of Eq. (3.6) has been replaced by a continuous integral $\int \mathcal{D}[n(\mathbf{r})]$, an integral, performed over the allowed configurations of the continuous field $n(\mathbf{r}) \in [0, 1]$. The mesoscopic field $n(\mathbf{r})$ can be thought of as the local average

$$n(\mathbf{r}) = \frac{1}{\Delta\mathcal{N}} \sum_{\alpha \in \Delta V(\mathbf{r})} n_\alpha$$

of the site occupation over a mesoscopic volume element $\Delta V(\mathbf{r})$ around the point \mathbf{r} containing $\Delta\mathcal{N}$ sites. This is in contrast to \bar{n} used in the mean-field approximation where averaging is performed

over the entire particle volume. The quantity $\mathcal{G} [n, T]$ is the “mesoscopic formulation” of the discrete quantity $\mathcal{H}\{n_\alpha\} - \mu \sum_{n_\alpha} n_\alpha$ as it appears in Eq. (3.6). It is equal to

$$\mathcal{G} [n(\mathbf{r}), \mu, T] = \int_{V_0} \frac{dV}{a_0^3} \left(U_0 n(\mathbf{r}) + \frac{U\Gamma}{2} n^2(\mathbf{r}) + \frac{\kappa}{2} |\nabla n(\mathbf{r})|^2 \right) - \mu \int_{V_0} \frac{dV}{a_0^3} n(\mathbf{r}) \quad (3.23)$$

which is a functional depending on the local field $n(\mathbf{r})$. To obtain Eq. (3.23) from Eq. (3.9), we have used:

$$\sum_{\alpha} n_{\alpha} = \int_{V_0} \frac{dV}{a_0^3} n(\mathbf{r}) \quad (3.24)$$

$$\sum_{\langle \alpha, \alpha' \rangle} n_{\alpha} n_{\alpha'} = \int_{V_0} \frac{dV}{a_0^3} \left(\frac{\Gamma}{2} n^2(\mathbf{r}) - a_0^2 |\nabla n(\mathbf{r})|^2 \right). \quad (3.25)$$

In the considered system, the parameter a_0 , as usual, is the lattice parameter of the interstitial lattice where the lithium ions can sit. The identity Eq. (3.25) has been obtained under the assumption that this interstitial lattice is cubic according to Sec. 3.1.1, hence $\Gamma = 6$. That way, an estimate of the parameter κ , introduced in Eq. (3.23), is given by

$$\kappa = -2Ua_0^2 < 0 \text{ for } U < 0,$$

according to the result obtained in App. C. The quantity $W [n(\mathbf{r})]$ in Eq. (3.22) corresponds to the total number of microscopic configurations that all induced the same locally averaged field $n(\mathbf{r})$ and hence contains all details related to the microscopic underlying structure. This quantity is estimated by

$$W [n(\mathbf{r})] = \exp \left(\frac{\mathcal{S}_0 [n(\mathbf{r})]}{k_B} \right)$$

where $\mathcal{S}_0 [n(\mathbf{r})]$ is the entropy of a *noninteracting* system of lithium ions. In the limit where $n(\mathbf{r}) \ll 1$, the Stirling approximation can be used and the system entropy is equal to

$$\mathcal{S}_0 [n(\mathbf{r})] = -k_B \int_{V_0} \frac{dV}{a_0^3} \left(n(\mathbf{r}) \ln n(\mathbf{r}) + (1 - n(\mathbf{r})) \ln (1 - n(\mathbf{r})) \right), \quad (3.26)$$

following the result of Eq. (3.17). Let us remark that this quantity is not identical to the entropy of a system of *interacting* lithium ions which is rather much difficult to estimate [106, 107]. Indeed the calculation of system entropy obtained at constant system internal energy is a complicated problem in the presence of nonvanishing interactions between the lithium ions.

We further introduce

$$\begin{aligned} \mathcal{J} [n(\mathbf{r}), T, \mu] &\equiv \mathcal{G} [n(\mathbf{r}), T, \mu] - T\mathcal{S}_0 [n(\mathbf{r})] \\ &= \int_{V_0} \frac{dV}{a_0^3} \left(U_0 n(\mathbf{r}) + \frac{U\Gamma}{2} n^2(\mathbf{r}) + \frac{\kappa}{2} |\nabla n(\mathbf{r})|^2 - \mu n(\mathbf{r}) \right. \\ &\quad \left. + k_B T \left(n(\mathbf{r}) \ln n(\mathbf{r}) + (1 - n(\mathbf{r})) \ln (1 - n(\mathbf{r})) \right) \right), \end{aligned} \quad (3.27)$$

according to Eq. (3.23) and Eq. (3.26). The grand canonical partition function defined in Eq. (3.22) then reads

$$Z_{\text{gc}}(T, \mu) = \int \mathcal{D}[\mathbf{n}(\mathbf{r})] \exp\left(-\frac{\mathcal{J}[\mathbf{n}(\mathbf{r}), T, \mu]}{k_B T}\right). \quad (3.28)$$

To evaluate the grand canonical partition function, the above integral has to be performed over all slowly varying field configurations $\mathbf{n}(\mathbf{r})$. Its calculation is mathematically involved and, instead, this integration is performed by means of the saddle-point approximation [108] where only the dominant term $n^*(\mathbf{r})$ of the integrand is accounted for. The latter satisfies the following equation:

$$\left. \frac{\delta \mathcal{J}[\mathbf{n}(\mathbf{r}), T, \mu]}{\delta \mathbf{n}(\mathbf{r})} \right|_{\mathbf{n}(\mathbf{r})=n^*(\mathbf{r})} \stackrel{!}{=} 0, \quad (3.29)$$

where δ is a notation for any functional derivative. Eq. (3.29) yields a relation between the chemical potential μ and the local (saddle-point) lithium concentration $n^*(\mathbf{r})$, denoted simply by $\mathbf{n}(\mathbf{r})$ in the following,

$$\mu = U_0 + U\Gamma \mathbf{n}(\mathbf{r}) + \kappa \nabla \cdot (\nabla \mathbf{n}(\mathbf{r})) + k_B T \ln\left(\frac{\mathbf{n}(\mathbf{r})}{1 - \mathbf{n}(\mathbf{r})}\right). \quad (3.30)$$

In a coarse-graining approach, the system free energy is defined as

$$\begin{aligned} \Psi[\mathbf{n}(\mathbf{r}), T] &\equiv \mathcal{J}[\mathbf{n}(\mathbf{r}), T, \mu] + \mu \int_{V_0} \frac{dV}{a_0^3} \mathbf{n}(\mathbf{r}) \\ &= \int \frac{dV}{a_0^3} \left(U_0 \mathbf{n}(\mathbf{r}) + \frac{U\Gamma}{2} n^2(\mathbf{r}) + \frac{\kappa}{2} |\nabla \mathbf{n}(\mathbf{r})|^2 \right. \end{aligned} \quad (3.31)$$

$$\left. + k_B T \left(\mathbf{n}(\mathbf{r}) \ln \mathbf{n}(\mathbf{r}) + (1 - \mathbf{n}(\mathbf{r})) \ln(1 - \mathbf{n}(\mathbf{r})) \right) \right). \quad (3.32)$$

Thus the chemical potential μ , Eq. (3.30), obtained in the saddle-point approximation appears as the functional derivative of the system free energy with respect to the local lithium concentration $\mathbf{n}(\mathbf{r})$,

$$\mu = \frac{\delta \Psi[\mathbf{n}(\mathbf{r}), T]}{\delta (\mathbf{n}(\mathbf{r})/a_0^3)}. \quad (3.33)$$

As we will see in a more concrete manner in Sec. 3.2.5, phase-field modeling is based on a given expression of the free energy functional of the system, here given by Eq. (3.32). In the present case, this expression is motivated by a microscopic Hamiltonian, Eq. (3.9), firstly treated in the mean-field approximation in Sec. 3.2.1. Using this approximation, it could be demonstrated that phase segregation arises as consequence of an effective short-range attractive interaction between intercalated lithium ions being located at fixed spatial locations corresponding to interstitial sites of a rigid sublattice in the host material. To account for phase segregation at the system length scale where the microscopic details cannot be considered⁴, we introduce in this section a free energy functional Ψ depending on the

⁴The system length scale is macroscopic and thus too big for a consideration of all microscopic details.

local coarse-grained concentration as spatially dependent field. In this formalism, the grand canonical partition function, Eq. (3.28), was introduced to explain how the commonly used expression of the free energy functional, Eq. (3.32), is obtained but is no longer used for further calculations. As suggested by its name, in the coarse-graining approach, microscopic details are ignored and all merged in the entropic term of the free energy functional, Eq. (3.26) which can be seen as the sole remainder of the microscopic underlying structure.

3.2.4 Host deformations

We now consider that the host lattice undergoes small deformations induced by the lithium intercalation at the interstitial lattice sites. Such small deformations exclude any drastic changes of the crystalline host structure assumed cubic independently of the lithium concentration state being either homogeneous or phase-segregated. Instead of starting with a microscopic Hamiltonian to describe the interaction between the intercalated lithium ions and the host material, as it is done in Ref. [99], we directly make use of a mesoscopic approach treating the host crystalline structure as a continuous elastic medium.

In this context, the host deformations are assumed to be small. They arise as a consequence of a small applied perturbation and thus depend linearly on this perturbation. Basically the crystalline cathodic particle material undergoes deformations due to the lithium intercalation. In the considered particle system, these deformations have two origins: the former is directly induced by the lithium insertion into and extraction from the host material. As it will be demonstrated in the next chapter, Chp. 4, this kind of deformations generate stress-free deformations provided that the equilibrium lithium concentration state is homogeneous over the entire crystalline particle. Otherwise, for phase-segregated stresses, stress-free states are not allowed. Such deformations are represented by a strain tensor referred to as $\boldsymbol{\varepsilon}^{\text{Li}}$. The latter is due to stresses that are possibly induced in order to fulfill the constraint of a continuous particle. The corresponding strain tensor is referred to as $\boldsymbol{\varepsilon}^{\text{el}}$. In linear response theory, the total deformations, mathematically represented by the strain tensor $\boldsymbol{\varepsilon}$, are expressed as a superposition of both the lithium-induced deformations and the stress induced elastic deformations,

$$\boldsymbol{\varepsilon} = \boldsymbol{\varepsilon}^{\text{Li}} + \boldsymbol{\varepsilon}^{\text{el}}. \quad (3.34)$$

The relationship between the components of elastic strain tensor $\boldsymbol{\varepsilon}^{\text{el}}$ and the components of the stress tensor $\boldsymbol{\sigma}$ is linear [109] and given by

$$\varepsilon_{ij}^{\text{el}} = S_{ijkl} \sigma_{kl} \quad (3.35)$$

where S_{ijkl} are the components of the fourth-rank compliance tensor. This tensor governs the response of the host material in terms of deformations as a reaction to applied mechanical stresses expressed via the stress tensor. Intrinsically, since both the elastic strain tensor and the stress tensor are symmetric [110], the compliance tensor always fulfills the relationships

$$S_{ijkl} = S_{jikl} = S_{ijlk}$$

which allows for reducing its total number of independent components from 81 to 36. Further the elastic strain energy, that will be defined in Eq. (3.39), should not change when interchanging ij and kl [110]. This leads to

$$S_{ijkl} = S_{klij}.$$

By this relation, the total number of independent stiffness tensor components finally reduces to 21. Additionally, depending on the material symmetries, the number of independent compliance tensor components may be further reduced. The material symmetries strongly depend on the crystalline structure of the host material. However, due to the presence of grain boundaries and other defects of the crystalline structure, the considered cathodic material is rarely monocrystalline. For this reason, it is possible to assume that even a crystalline material with intrinsic preferred orientations is isotropic at the mesoscopic scale. Under the assumption of isotropy the compliance tensor S remains invariant under arbitrary rotations. In Voigt notation this tensor is formally written as

$$S = \begin{pmatrix} S_{11} & S_{12} & S_{12} & 0 & 0 & 0 \\ S_{12} & S_{11} & S_{12} & 0 & 0 & 0 \\ S_{12} & S_{12} & S_{11} & 0 & 0 & 0 \\ 0 & 0 & 0 & 2(S_{11} - S_{12}) & 0 & 0 \\ 0 & 0 & 0 & 0 & 2(S_{11} - S_{12}) & 0 \\ 0 & 0 & 0 & 0 & 0 & 2(S_{11} - S_{12}) \end{pmatrix}$$

where $S_{11} = 1/E$ and $S_{12} = -\nu/E$, E and ν being the Young's modulus and the Poisson coefficient of the host material, respectively.

Further, using a thermo-mechanical analogy [111], the components of the lithium-induced strain tensor ε^{Li} are given by

$$\varepsilon_{ij}^{\text{Li}} = \frac{\tilde{\Omega}}{3} \delta_{ij} (n - n_0)$$

where n_0 is a homogeneous reference lithium concentration. As for the elastic deformations, the lithium-induced deformations linearly depend on the quantity that gives rise to them, namely the local lithium concentration change $(n - n_0)$. Moreover, the tensor $(\tilde{\Omega}/3)\mathbb{1}$, which governs the response of the host material to lithium concentration changes, is proportional to the unit tensor, and is hence invariant under rotation. Thus lithium intercalation by itself does not break the ‘‘local’’ isotropy of the host material.

We now turn to the evaluation of the elastic strain energy Ψ^{es} that corresponds to the energy of deforming the host material provided that the host deformations are linear elastic. Its expression is given by [112]

$$\Psi^{\text{es}} = \frac{1}{2} \int_{V_0} dV \varepsilon_{ij}^{\text{el}} \sigma_{ij} \quad (3.36)$$

where V_0 is the volume of the host material being in the stress-free reference state, which is related to the homogeneous lithium concentration n_0 . We define the stiffness tensor C as the ‘‘inverse’’ of the compliance tensor S ,

$$\sigma_{ij} = C_{ijkl} \varepsilon_{kl}^{\text{el}}.$$

It has the same symmetries as the compliance tensor S . In case of an isotropic host material the

stiffness tensor expressed in Voigt notation is given by

$$C = \begin{pmatrix} C_{11} & C_{12} & C_{12} & 0 & 0 & 0 \\ C_{12} & C_{11} & C_{12} & 0 & 0 & 0 \\ C_{12} & C_{12} & C_{11} & 0 & 0 & 0 \\ 0 & 0 & 0 & (C_{11} - C_{12})/2 & 0 & 0 \\ 0 & 0 & 0 & 0 & (C_{11} - C_{12})/2 & 0 \\ 0 & 0 & 0 & 0 & 0 & (C_{11} - C_{12})/2 \end{pmatrix}$$

where $C_{11} = \lambda_1 + 2\lambda_2$ and $C_{12} = \lambda_1$, λ_1 and λ_2 being the Lamé's first and second parameters, respectively as defined in Eq. (2.12) and Eq. (2.13).

Using Eq. (3.34) the elastic strain tensor,

$$\boldsymbol{\varepsilon}^{\text{el}} = \boldsymbol{\varepsilon} - \boldsymbol{\varepsilon}^{\text{Li}}, \quad (3.37)$$

is related to both the lithium-induced strain tensor and the total strain tensor. Further, under the assumption of small host deformations, the components of the total strain tensor simply read

$$\varepsilon_{ij} = \frac{1}{2} (u_{i,j} + u_{j,i}). \quad (3.38)$$

where u_i is the i -component of the mechanical displacement \mathbf{u} . Inserting Eq. (3.37) into the elastic strain energy functional, Eq. (3.36), we obtain

$$\Psi^{\text{es}} = \int_{V_0} dV \frac{1}{2} (\varepsilon_{ij} - \varepsilon_{ij}^{\text{Li}}) C_{ijkl} (\varepsilon_{kl} - \varepsilon_{kl}^{\text{Li}}) \quad (3.39)$$

We further define the mechanical energy density

$$\psi^{\text{me}} = \frac{1}{2} \varepsilon_{ij} C_{ijkl} \varepsilon_{kl}$$

and the coupling energy density

$$\psi^{\text{cp}} = \frac{1}{2} (\varepsilon_{ij}^{\text{Li}} C_{ijkl} \varepsilon_{kl}^{\text{Li}} - \varepsilon_{ij}^{\text{Li}} C_{ijkl} \varepsilon_{kl} - \varepsilon_{ij} C_{ijkl} \varepsilon_{kl}^{\text{Li}})$$

so that

$$\Psi^{\text{es}} = \int_{V_0} dV (\psi^{\text{me}} + \psi^{\text{cp}}). \quad (3.40)$$

In case of an isotropic material the different contributions to the elastic strain energy density,

$$\psi^{\text{es}} = \psi^{\text{me}} + \psi^{\text{cp}}, \quad (3.41)$$

are respectively given by

$$\psi^{\text{me}} = \frac{1}{2} \left(\lambda_2 \text{Tr}^2(\boldsymbol{\varepsilon}) + 2\lambda_1 \text{Tr}(\boldsymbol{\varepsilon}^2) + 4\lambda_1 (\varepsilon_{12}^2 + \varepsilon_{23}^2 + \varepsilon_{31}^2) \right), \quad (3.42)$$

$$\psi^{\text{cp}} = -\frac{1}{2} \tilde{\Omega} \lambda (n - n_0) \left(2\text{Tr}(\boldsymbol{\varepsilon}) - \tilde{\Omega} (n - n_0) \right). \quad (3.43)$$

Finally, we can note that the elastic strain energy functional of Eq. (3.39), valid in case of small linear elastic host deformations, can be seen as the coarse-graining formulation of the microscopic Hamiltonian $\Delta\mathcal{H}_{\text{host}}\{n_\alpha, \mathbf{u}_\alpha\}$ of Eq. (3.2).

3.2.5 Total free energy of the system

When considering nonzero lithium-induced host deformations, the total system free energy becomes a sum of two contributions represented by Eq. (3.32) and Eq. (3.39). The system free energy, initially denoted by Ψ in Sec. 3.2.3 in a context where the macroscopic elastic strain energy of the host material induced by the lithium intercalation was neglected, is now referred to as Ψ^{ch} . The total system free energy, now denoted by Ψ , is equal to

$$\Psi = \Psi^{\text{ch}} + \Psi^{\text{es}} = \int_{V_0} dV \psi \quad (3.44)$$

with $\psi = \psi^{\text{ch}} + \psi^{\text{es}}$ being the total free energy density. According to Eq. (3.32) the chemical free energy density ψ^{ch} related to the chemical free energy Ψ^{ch} by

$$\Psi^{\text{ch}} = \int_{V_0} dV \psi^{\text{ch}}$$

reads

$$a_0^3 \psi^{\text{ch}} = U_0 n + \frac{U\Gamma}{2} n^2 + \frac{\kappa}{2} |\nabla n|^2 + k_B T (n \ln n + (1-n) \ln(1-n)). \quad (3.45)$$

and can be further separated into two different contributions

$$\psi^{\text{ch}} = \psi^{\text{mf}} + \psi^{\text{gd}}$$

where

$$\begin{aligned} a_0^3 \psi^{\text{mf}} &= U_0 n + \frac{U\Gamma}{2} n^2 + k_B T (n \ln n + (1-n) \ln(1-n)), \\ a_0^3 \psi^{\text{gd}} &= \frac{\kappa}{2} |\nabla n|^2. \end{aligned}$$

At this place, we will derive expressions for the conjugate quantities of the independent variables — the local lithium concentration n and the local mechanical displacement \mathbf{u} — of the system free energy functional that are further needed to describe the lithium intercalation into and the release from the LMO crystalline cathodic particle.

Chemical potential

The conjugate quantity of the local lithium concentration n is the local chemical potential μ appearing, in phase-field modeling, as a superposition of three terms,

$$\mu = \frac{\delta \Psi}{\delta (n/a_0^3)} = \mu^{\text{mf}} + \mu^{\text{gd}} + \mu^{\text{cp}} \quad (3.46)$$

with

$$\mu^{\text{mf}} = \frac{\partial \psi^{\text{mf}}}{\partial (n/a_0^3)} = U_0 + U\Gamma n + k_B T \ln \left(\frac{n}{1-n} \right) \quad (3.47)$$

$$\mu^{\text{gd}} = -\nabla \cdot \left(\frac{\partial \psi^{\text{gd}}}{\partial (n_i/a_0^3)} \mathbf{e}_i \right) = -\kappa \nabla \cdot (\nabla n) \quad (3.48)$$

$$\mu^{\text{cp}} = \frac{\partial \psi^{\text{cp}}}{\partial (n/a_0^3)} = -\tilde{\Omega} a_0^3 \sigma_h. \quad (3.49)$$

Here \mathbf{e}_i denotes a basis of the three-dimensional space and σ_h the hydrostatic stress. In phase-field modeling, the chemical potential

$$\begin{aligned} \mu^{\text{ch}} &= \mu^{\text{mf}} + \mu^{\text{gd}} \\ &= U_0 + U\Gamma n + k_B T \ln \left(\frac{n}{1-n} \right) - \kappa \nabla \cdot (\nabla n) \end{aligned} \quad (3.50)$$

that is induced by lithium concentration variation only, is rather different from the one obtained by means of the dilute solution approximation and defined in Eq. (2.7) of Sec. 2.2.1.

In fact, the dilute solution approximation relies on the fact that the total number of lithium ions present in the system, i.e. the LMO particle, is very small compared to the total number of available interstitial sites, $n \ll 1$. Under this assumption, the chemical free energy, Eq. (3.32), can be expanded up to the leading order in n ,

$$\Psi^{\text{ch}} \approx \int_{V_0} \frac{dV}{a_0^3} \left(U_0 n + k_B T n \ln n \right). \quad (3.51)$$

In the following we briefly demonstrate how to obtain Eq. (3.51) starting from the free energy density Eq. (3.32). Strictly speaking, the procedure that will be introduced here is not a Taylor expansion because a functional (the chemical free energy of the system) — and not a function — is expanded with respect to its variable being a function (the local lithium concentration n). In the limit $n \rightarrow 0$, we will see that this method exactly corresponds to the dilute solution model introduced in Sec. 2.2.1.

At this place, the term

$$\int_{V_0} \frac{dV}{a_0^3} k_B T \left(n \ln n + (1-n) \ln(1-n) \right)$$

in Eq. (3.45) has been approximated by

$$\begin{aligned} &\int_{V_0} \frac{dV}{a_0^3} k_B T \left(n \ln n + (1-n) \ln(1-n) \right) \\ &= k_B T \int_{V_0} \frac{dV}{a_0^3} \left(n \ln n + (1-n) \underbrace{\ln(1-n)}_{\approx -n} \right) \\ &\quad \underbrace{\approx -n + n^2 \approx -n}_{\approx n(\ln n - 1) \approx n \ln n} \\ &\approx k_B T \int_{V_0} \frac{dV}{a_0^3} n \ln n. \end{aligned}$$

Regarding the term

$$\int_{V_0} \frac{dV}{a_0^3} \left(U_0 n + \frac{U\Gamma}{2} n^2 + \frac{\kappa}{2} |\nabla n|^2 \right),$$

in Eq. (3.45), it is simply approximated by

$$\int_{V_0} \frac{dV}{a_0^3} \left(U_0 n + \frac{U\Gamma}{2} n^2 + \frac{\kappa}{2} |\nabla n|^2 \right) \approx \int_{V_0} \frac{dV}{a_0^3} U_0 n.$$

Here the second order term in n has been neglected meaning that the lithium-lithium interactions are no longer accounted for. In this context, no phase segregation can arise and it is then possible to neglect the gradient term in Eq. (3.45). Finally, the chemical potential μ^{ch} obtained from the chemical free energy functional, Eq. (3.51), reads

$$\mu^{\text{ch}} = U_0 + k_B T (1 + \ln n) \approx U_0 + k_B T \ln n \quad (3.52)$$

which is identical to the chemical potential μ^{ch} defined Eq. (2.7) for the purpose of describing the lithium intercalation by means of the dilute solution approach.

In phase-field modeling, the stress induced chemical potential of Eq. (3.49) has exactly the same expression (see Eq. (2.8)) as the one defined in the dilute solution approximation. Indeed, this chemical potential is calculated from the elastic strain free energy functional only. This is due to the fact that the dilute solution model relies on the same form of the elastic strain free energy functional as the phase-field model.

Mechanical stresses

The conjugate quantity of the local mechanical displacement \mathbf{u} is the force density \mathbf{f} , whose components f_i in any cartesian basis \mathbf{e}_i are given by

$$f_i = \frac{\delta \Psi}{\delta u_i} = -\nabla \cdot \left(\frac{\partial \psi^{\text{es}}}{\partial u_{i,j}} \mathbf{e}_j \right). \quad (3.53)$$

Since the elastic strain free energy functional does not explicitly depend on the component u_i of the mechanical displacement, the term $\partial \psi / \partial u_i$ that should appear in Eq. (3.53) is simply zero. Further, the quantity $\partial \psi^{\text{es}} / \partial u_{i,j}$ can be related to $\partial \psi^{\text{es}} / \partial \varepsilon_{ij}$ by

$$\begin{aligned} \frac{\partial \psi^{\text{es}}}{\partial u_{i,j}} &= \frac{\partial \psi^{\text{es}}}{\partial \varepsilon_{ij}} \frac{\partial \varepsilon_{ij}}{\partial u_{i,j}} + \frac{\partial \psi^{\text{es}}}{\partial \varepsilon_{ji}} \frac{\partial \varepsilon_{ji}}{\partial u_{i,j}} \\ &= \frac{1}{2} \left(\frac{\partial \psi^{\text{es}}}{\partial \varepsilon_{ij}} + \frac{\partial \psi^{\text{es}}}{\partial \varepsilon_{ji}} \right), \end{aligned} \quad (3.54)$$

according to Eq. (3.38). Since the total strain tensor is symmetric, i.e. $\varepsilon_{ij} = \varepsilon_{ji}$, Eq. (3.54) reduces to

$$\frac{\partial \psi^{\text{es}}}{\partial u_{i,j}} = \frac{\partial \psi^{\text{es}}}{\partial \varepsilon_{ij}}.$$

At this place, the component of the stress tensor $\boldsymbol{\sigma}$,

$$\sigma_{ij} = \frac{\partial \psi^{\text{es}}}{\partial \varepsilon_{ij}}, \quad (3.55)$$

are recognized and the conjugate variable of the mechanical displacement, Eq. (3.53), reads

$$f_i = -\nabla \cdot (\sigma_{ij} \mathbf{e}_j)$$

with

$$\sigma_{ij} = 2\lambda_1 \varepsilon_{ij} + (\lambda_2 \text{Tr}(\boldsymbol{\varepsilon}) - \tilde{\Omega} \lambda (n - n_0)) \delta_{ij},$$

according to Eq. (3.41) and Eq. (3.55). Thus, similarly to the stress-induced chemical potential μ^{cp} of Eq. (3.49), the expression of the stresses obtained in phase-field modeling is exactly the same as the one introduced in the dilute solution approach, see Eq. (2.11).

3.3 Near to equilibrium

3.3.1 Equilibrium conditions

At equilibrium the average internal energy of the cathodic particle as well as the total number of lithium ions N are maintained constant. The first constraint concerning the internal energy is always ensured provided that the temperature of the system remains fixed to a given but arbitrary constant value. The total number of lithium ions present in the cathodic particle is related to the local lithium concentration n by

$$N = \int_{V_0} \frac{dV}{a_0^3} n \quad (3.56)$$

which represents a constraint for the lithium concentration n since $N = \text{cst}$. Further, at equilibrium, the particle momentum referred to as \mathbf{P} is also a conserved quantity. In the absence of volumetric force acting in the particle system, this condition is simply expressed as

$$\oint_{\partial V_0} dS (-\boldsymbol{\sigma} \cdot \mathbf{n}) = 0. \quad (3.57)$$

Under these constraints, the equilibrium lithium concentration and mechanical displacement being the unknown functions of the problem minimize the following functional

$$\Psi' = \Psi - \zeta \left(\int_{V_0} \frac{dV}{a_0^3} n - N \right) - \xi \left(\oint_{\partial V_0} dS (-\boldsymbol{\sigma} \cdot \mathbf{n}) \right) \quad (3.58)$$

where ζ and ξ are two Lagrange parameters introduced to ensure that the constraints Eq. (3.56) and Eq. (3.57) are satisfied. The functional Ψ denotes the total system free energy as it has been defined in Eq. (3.44). Minimizing the functional represented by Eq. (3.58) with respect to its independent

variables, n , \mathbf{u} , ζ and ξ , leads to a set of six differential equations given by

$$\frac{\delta\Psi'}{\delta n} = \frac{\delta\Psi}{\delta n} - \zeta \stackrel{!}{=} 0, \quad (3.59)$$

$$\frac{\delta\Psi'}{\delta u_i} = \frac{\delta\Psi}{\delta u_i} \stackrel{!}{=} 0, \quad (3.60)$$

$$\frac{\delta\Psi'}{\delta\zeta} = \int_{V_0} \frac{dV}{a_0^3} n - N \stackrel{!}{=} 0, \quad (3.61)$$

$$\frac{\delta\Psi'}{\delta\xi} = \oint_{\partial V_0} dS (-\boldsymbol{\sigma} \cdot \mathbf{n}) \stackrel{!}{=} 0. \quad (3.62)$$

The first equation, Eq. (3.59), of this set of equations states, that, at equilibrium, the local chemical potential

$$\mu \equiv \frac{\delta\Psi}{\delta(n/a_0^3)} = a_0^3 \zeta$$

is spatially constant, here equal to the Lagrange parameter ζ . The second equation, Eq. (3.60) reads

$$\nabla \cdot \boldsymbol{\sigma}_{ij} = 0,$$

and represents the local mechanical equilibrium as it has been introduced in Sec. 2.2.1. At this place, we refer to Eq. (2.3). The two remaining equations, Eq. (3.61) and Eq. (3.62) stand for the constraints, Eq. (3.56) and Eq. (3.57) that are specifically applied to the considered system.

When the mechanics is neglected and in case of weak phase separation⁵, analytical expressions for the lithium concentration profile solving the system of equations represented by Eq. (3.59) and Eq. (3.61) only can be found. A detailed description of the mathematical method used to obtain these solutions is given in Ref. [114] for a one-dimensional cartesian system and in Ref. [115] for a two-dimensional cartesian system. Moreover, under specific assumptions, D. Bettinson and G. Rowlands [116] also exhibit a semi-analytical solution valid in case of a three-dimensional system of spherical symmetry.

3.3.2 Evolution equations

In reality, during battery charging and discharging, the lithium amount present in the host material of a particular particle at the cathode of a porous LIB varies. Thus, the equilibrium formalism represented by the set of Eq. (3.59) - (3.62) becomes invalid and an extended formalism has to be considered. In single particle modeling, the total number of lithium ions $N(t)$ present in the cathodic particle is a time-dependent quantity that is varied by application of a flux \mathbf{J}_a at the particle surface. This flux drives the system out of equilibrium and allows for lithium injection into or extraction from the particle. The total number of lithium ions present in the cathodic particle at time t , is a conserved quantity which hence satisfies

$$\frac{dN(t)}{dt} = - \oint_{\partial V_0} dS \mathbf{J}_a \cdot \mathbf{n} \quad (3.63)$$

⁵In case of weak phase separation, the chemical free energy density is represented by a polynom being usually of degree 4 with respect to the local lithium concentration n [113]. Such an expression is valid when the externally fixed temperature is close to but below the critical temperature T_c defined in Sec. 3.2.2.

in the absence of lithium sources inside the particle.

In a static approximation, it is assumed that the injected or extracted lithium ions do not carry any momentum⁶ and, thus, do not contribute to the kinetic energy of the entire particle system. In this approximation, the total momentum of the cathodic particle, referred to as $\mathbf{P}(t)$, is entirely carried by the host material. It is also a conserved quantity and hence fulfills

$$\frac{d\mathbf{P}(t)}{dt} = - \oint_{\partial V_0} dS \boldsymbol{\sigma}_a \cdot \mathbf{n} \quad (3.64)$$

in the absence of a momentum source inside of the particle. The quantity $\boldsymbol{\sigma}_a$ stands for external stress tensor possibly applied at the particle surface. In the present case, the particle momentum $\mathbf{P}(t) = \mathbf{0}$ because the considered particle is assumed to be located at a fixed spatial location in the cathode of a LIB. This further implies that $d\mathbf{P}(t)/dt = 0$ and leads to

$$\oint_{\partial V_0} dS \boldsymbol{\sigma}_a \cdot \mathbf{n} = \mathbf{0} \quad (3.65)$$

in Eq. (3.64). This last condition does not necessary imply that the stresses holding at the particle surface are identical to zero. It means the stress vector, $\boldsymbol{\sigma}_a \cdot \mathbf{n}$, integrated over the particle surface is zero meaning that the total force exerted by the applied stresses on the particle vanishes.

The global conservation laws, Eq. (3.63) and Eq. (3.64), can be deduced from their local formulations valid inside of the particle,

$$\frac{\partial}{\partial t} \left(\frac{n}{a_0^3} \right) + \nabla \cdot \mathbf{J} = 0, \quad (3.66)$$

$$\frac{\partial \mathbf{p}}{\partial t} + \nabla \cdot \boldsymbol{\sigma} = \mathbf{0}, \quad (3.67)$$

in combination with the following two additional boundary conditions

$$-\mathbf{J} \cdot \mathbf{n} \Big|_{\partial V_0} = -\mathbf{J}_a \cdot \mathbf{n}, \quad (3.68)$$

$$-\boldsymbol{\sigma} \cdot \mathbf{n} \Big|_{\partial V_0} = -\boldsymbol{\sigma}_a \cdot \mathbf{n}, \quad (3.69)$$

where $\boldsymbol{\sigma}_a$ fulfills Eq. (3.65). In Eq. (3.66) and Eq. (3.67), n/a_0^3 and \mathbf{p} denote the volumetric lithium ion density and the volumetric host material momentum density, respectively. As usual, \mathbf{n} denotes the outgoing vector perpendicular to the surface area of the cathodic particle. The global conservation laws, Eq. (3.63) and Eq. (3.64), are obtained from the local formulation of the problem represented by the set of equations Eq. (3.66) - (3.69) by means of the Gauss theorem. Additionally, two “nonequilibrium” quantities, \mathbf{J} and $\boldsymbol{\sigma}$, have been introduced. They represent local fluxes of lithium ions and of host momentum, respectively. In continuum mechanics, the local flux of host momentum is called the stress tensor.

Differently from the equilibrium formalism, introduced in the previous sections of this chapter, where both the lithium concentration and the mechanical displacement were implicitly assumed to be static quantities, they are treated here as dynamic quantities allowed to vary in time. In this nonequilibrium formalism, lithium ion transport represented by the (nonzero) lithium flux \mathbf{J} occurs to ensure

⁶The lithium ions that are not part of the host material are assumed to be massless. Note that Eq. (3.63) formally expresses the conservation of the total number of lithium ions and not the conservation of the lithium ion mass.

the relaxation of the system towards an equilibrium state. This transport occurs via diffusion where no momentum transfer may occur. At the microscopic scale, “diffusion” is governed by diverse deterministic reversible processes like the collisions between the different species as well as with (randomly distributed) defects. At the mesoscopic scale, the underlying microscopic origin for diffusion is not accounted for in detail but only in a stochastic manner and diffusion appears as an irreversible process [50]. An usual expression for the lithium flux \mathbf{J} driven by diffusion is given by the Onsager relation,

$$\mathbf{J} = -L \nabla \mu, \quad (3.70)$$

where μ is the chemical potential obtained from the free energy functional Eq. (3.44) in an *equilibrium formalism*, see Eq. (3.46). To ensure the relaxation of the system towards the thermal equilibrium the proportionality constant between the lithium flux and the gradient of the chemical potential must be non-negative, i.e. $L \geq 0$, as will be demonstrated in Eq. (3.74).

Another assumption of the current lithium intercalation model is that the host material instantaneously deforms as a consequence of the local lithium intercalation in order to maintain mechanical equilibrium. That means, at each instant, it holds

$$\nabla \cdot \boldsymbol{\sigma} = \mathbf{0}. \quad (3.71)$$

According to Eq. (3.67), the local momentum density \mathbf{p} is hence time-independent, $\partial \mathbf{p} / \partial t = \mathbf{0}$, and retains its initial value,

$$\mathbf{p}(\mathbf{r}, t) = \mathbf{0}, \quad (3.72)$$

at any instant t and position \mathbf{r} .

The relaxation of the system towards the thermal equilibrium after the system has been disturbed from equilibrium is described by the time evolution of the free energy functional $\Psi = \int_{V_0} dV \psi$. Its density ψ is a function of the local lithium occupation n , its spatial derivatives $n_{,j}$ and the local derivatives of the displacements $u_{i,j}$ such that the chain rule [117] yields

$$\frac{d\Psi}{dt} = \int_{V_0} dV \left(\frac{\partial \psi}{\partial n} \frac{\partial n}{\partial t} + \frac{\partial \psi}{\partial n_{,j}} \frac{\partial n_{,j}}{\partial t} + \frac{\partial \psi}{\partial u_{i,j}} \frac{\partial u_{i,j}}{\partial t} \right). \quad (3.73)$$

Gauss’s theorem enables us to perform integration by parts in three dimensions:

$$\begin{aligned} \int_{V_0} dV \frac{\partial \psi}{\partial n_{,j}} \frac{\partial n_{,j}}{\partial t} &= \int_{V_0} dV \frac{\partial \psi}{\partial n_{,j}} \mathbf{e}_j \cdot \nabla \frac{\partial n}{\partial t} \\ &= \int_{V_0} dV \left[\nabla \cdot \left(\frac{\partial \psi}{\partial n_{,j}} \mathbf{e}_j \frac{\partial n}{\partial t} \right) - \left(\nabla \cdot \frac{\partial \psi}{\partial n_{,j}} \mathbf{e}_j \right) \frac{\partial n}{\partial t} \right] \\ &= \oint_{\partial V_0} dS \mathbf{n} \cdot \frac{\partial \psi}{\partial n_{,j}} \mathbf{e}_j \frac{\partial n}{\partial t} - \int_{V_0} dV \left(\nabla \cdot \frac{\partial \psi}{\partial n_{,j}} \mathbf{e}_j \right) \frac{\partial n}{\partial t}. \end{aligned}$$

In a fully analogous manner we obtain

$$\int_{V_0} dV \frac{\partial \psi}{\partial u_{i,j}} \frac{\partial u_{i,j}}{\partial t} = \oint_{\partial V_0} dS \mathbf{n} \cdot \frac{\partial \psi}{\partial u_{i,j}} \mathbf{e}_j \frac{\partial u_i}{\partial t} - \int_{V_0} dV \left(\nabla \cdot \frac{\partial \psi}{\partial u_{i,j}} \mathbf{e}_j \right) \frac{\partial u_i}{\partial t}.$$

Substituting above expressions into Eq. (3.73) gives

$$\begin{aligned} \frac{d\Psi}{dt} = & \int_{V_0} dV \underbrace{\left(\frac{\partial\psi}{\partial n} - \nabla \cdot \frac{\partial\psi}{\partial n_{,j}} \mathbf{e}_j \right)}_{=\delta\Psi/\delta n \equiv \mu/a_0^3} \frac{\partial n}{\partial t} - \int_{V_0} dV \underbrace{\left(\nabla \cdot \frac{\partial\psi}{\partial u_{i,j}} \mathbf{e}_j \right)}_{=\nabla \cdot \sigma_{ij} \mathbf{e}_j = \nabla \cdot \sigma_i = 0} \frac{\partial u_i}{\partial t} \\ & + \oint_{\partial V_0} dS \mathbf{n} \cdot \left[\frac{\partial\psi}{\partial n_{,j}} \mathbf{e}_j \frac{\partial n}{\partial t} + \underbrace{\frac{\partial\psi}{\partial u_{i,j}} \mathbf{e}_j}_{=\sigma_i} \frac{\partial u_i}{\partial t} \right]. \end{aligned}$$

Note that mechanical equilibrium, $\nabla \cdot \sigma_i = 0$, and the absence of external stress, $\mathbf{n} \cdot \sigma_i \big|_{\partial V_0} = 0$, leads to the vanishing of all mechanical contributions, containing $\partial\psi/\partial u_{i,j}$, in above equation. The first term can be dealt with using the local lithium number conservation $\partial n/\partial t = -a_0^3 \nabla \cdot \mathbf{J}$ and integration by parts:

$$\int_{V_0} dV \mu \frac{\partial n/a_0^3}{\partial t} = - \int_{V_0} dV \mu \nabla \cdot \mathbf{J} = - \oint_{\partial V_0} dS \mathbf{n} \cdot \mu \mathbf{J} + \int_{V_0} dV \mathbf{J} \cdot \nabla \mu.$$

During pure relaxation applied flux is absent, i.e. $\mathbf{n} \cdot \mathbf{J} \big|_{\partial V_0} = 0$, and we conclude that the time derivative of the free energy

$$\frac{d\Psi}{dt} = \int_{V_0} dV \mathbf{J} \cdot \nabla \mu + \oint_{\partial V_0} dS \mathbf{n} \cdot \frac{\partial\psi}{\partial n_{,j}} \mathbf{e}_j \frac{\partial n}{\partial t}$$

has both a bulk and a surface contribution. It is natural to assume that during relaxation the free energy decreases (according to the second law of thermodynamics). This requires at least the bulk term to be negative. It is easy to see that Onsager's phenomenological relation $\mathbf{J} = -L \nabla \mu$ with $L \geq 0$ is sufficient to satisfy this requirement:

$$\frac{d\Psi}{dt} = - \underbrace{\int_{V_0} L (\nabla \mu)^2}_{<0} + \oint_{\partial V_0} dS \mathbf{n} \cdot \frac{\partial\psi}{\partial n_{,j}} \mathbf{e}_j \frac{\partial n}{\partial t}. \quad (3.74)$$

While the negativity of the surface contribution is by no means ensured, we have numerically checked in all simulations that in total the free energy decreases during pure relaxation.

In the dilute solution model of Sec. 2.2, the coefficient L was expressed as

$$L = \frac{D_0 n}{a_0^3 k_B T},$$

see Eq. (2.5). In phase-field modeling, we use the phenomenological expression

$$L = \frac{D_0 n(1-n)}{a_0^3 k_B T} \quad (3.75)$$

which prevents the lithium flux from diverging when n locally approaches its maximal value, $n_{\max} = 1$ ⁷. Both expressions are indeed positive due to $0 < n < 1$. Some considerations about the way Eq. (3.75) is obtained are given in Ref. [118].

⁷The gradient of the chemical potential contains a term proportional to $1/(n(1-n))$ which diverges when n approaches, at some spatial locations, the value 1. Thus, by choosing L proportional to $n(1-n)$, a divergence of the lithium flux may be prevented, see Eq. (3.76).

Similarly to the formalism introduced in Sec. 2.2.2 regarding the dilute solution approach and in order to distinguish between the different effects leading to lithium transport within the particle, the total lithium flux \mathbf{J} is further separated into two different contributions: The lithium flux driven by the lithium concentration gradients, \mathbf{J}^{ch} , on the one hand, and the lithium flux driven by the hydrostatic stress gradients, \mathbf{J}^{cp} , on the other hand. It holds

$$\mathbf{J} = \mathbf{J}^{\text{ch}} + \mathbf{J}^{\text{cp}}.$$

Using the linearity (with respect to μ) of the Onsager relation, Eq. (3.70), we define

$$\begin{aligned} \mathbf{J}^{\text{ch}} &= -L \nabla \mu^{\text{ch}} \\ &= -\frac{D_0 n(1-n)}{a_0^3} \nabla \left(\underbrace{\frac{U_0}{k_B T} + \frac{U \Gamma n}{k_B T} - \frac{\kappa}{k_B T} \nabla \cdot (\nabla n)}_{\text{energetic term}} + \underbrace{\ln \left(\frac{n}{1-n} \right)}_{\text{entropic term}} \right) \end{aligned} \quad (3.76)$$

$$\begin{aligned} &= -\frac{D_0 n(1-n)}{a_0^3} \nabla \left(\frac{U \Gamma n}{k_B T} + \ln \left(\frac{n}{1-n} \right) - \frac{\kappa}{k_B T} \nabla \cdot (\nabla n) \right), \\ \mathbf{J}^{\text{cp}} &= -L \nabla \mu^{\text{cp}} \\ &= \frac{D_0 \tilde{\Omega}_0 n(1-n)}{k_B T} \nabla \sigma_h, \end{aligned} \quad (3.77)$$

according to the definition of L represented by Eq. (3.75) and to Eqs. (3.47) - (3.49) regarding the definition of the chemical potentials. We also introduce

$$\begin{aligned} \mathbf{J}^{\text{mf}} &= -L \nabla \mu^{\text{mf}} \\ &= -\frac{D_0 n(1-n)}{a_0^3} \nabla \left(\underbrace{\frac{U \Gamma n}{k_B T}}_{\text{energetic term}} + \underbrace{\ln \left(\frac{n}{1-n} \right)}_{\text{entropic term}} \right), \end{aligned} \quad (3.78)$$

$$\begin{aligned} \mathbf{J}^{\text{gd}} &= -L \nabla \mu^{\text{gd}} \\ &= \frac{D_0 \kappa n(1-n)}{a_0^3 k_B T} \nabla \left(\nabla \cdot (\nabla n) \right) \end{aligned} \quad (3.79)$$

so that

$$\mathbf{J}^{\text{ch}} = \mathbf{J}^{\text{mf}} + \mathbf{J}^{\text{gd}}.$$

Let us make some explanatory remarks regarding the different contributions to the total lithium flux \mathbf{J} . In the dilute solution approach, the lithium flux induced by gradients in the lithium concentration, \mathbf{J}^{ch} , only contains the entropic term that has been further approximated in the limit of small lithium content, see Eq. (3.52). The absence of the energetic term — derived from the system internal energy — explains why this flux acts such that the lithium ions become homogeneously distributed over the particle.

In contrast, in phase-field modeling, this flux, represented by Eq. (3.76), contains both entropic and energetic terms which may act in two opposite directions. While the entropic term enhances the system “disordering” and thus the lithium ion homogenization, the energetic term may favor phase segregation and hence the “ordering” of the lithium ions.

The stress-induced lithium flux \mathbf{J}^{cp} derived in phase-field modeling, Eq. (3.77), is similar to the one used in the dilute solution approach and is thus expected to enhance the lithium ion homogenization over the particle, according to Sec. 2.2.2. For a better understanding of the effect of the diffuse phase boundary on lithium ion transport, the lithium flux induced by the interfacial energy term only, referred to as \mathbf{J}^{gd} , has been further introduced in Eq. (3.79). This term is related to the energetic term of Eq. (3.76).

3.3.3 Mathematical formulation

In this technical part, the problem of inserting (extracting) lithium into (from) a crystalline cathodic particle made of LMO — whose states may exhibit phase segregation — is mathematically formulated. Similarly to the dilute solution approach, to avoid costly three-dimensional simulations, it is, here, assumed that the unknown functions of the problem, the lithium concentration n and the mechanical displacement \mathbf{u} , are either of spherical or of ellipsoidal symmetry. Thus only particles of spherical or ellipsoidal shapes can be considered.

In this part, we will first treat the case of spherically symmetric particles. For such particles, the expression of the different contributions to the lithium flux as well as the conservation laws will be formulated using the spherical coordinates with radial dependence only. In a similar manner, the same quantities for particles exhibiting an ellipsoidal symmetry will be given in cylindrical coordinates.

Particles of spherical symmetry

We here consider a particle model of spherical symmetry, as it is depicted in Fig. 2.2 of Sec. 2.2.2. In spherical coordinates with radial dependence only, the different contributions to the lithium flux are given by

$$\begin{aligned} \mathbf{J}^{\text{mf}} &= J_r^{\text{mf}} \mathbf{e}_r = -\frac{D_0 n(1-n)}{a_0^3 k_B T} \frac{\partial \mu^{\text{mf}}}{\partial r} \mathbf{e}_r \\ &= -\frac{D_0}{a_0^3} \left(\frac{U\Gamma}{k_B T} n(1-n) + 1 \right) \frac{\partial n}{\partial r} \mathbf{e}_r \\ &= -\frac{D_0}{a_0^3} \left(\alpha_2 \frac{T_{\text{ref}}}{T} n(1-n) + 1 \right) \frac{\partial n}{\partial r} \mathbf{e}_r \end{aligned} \quad (3.80)$$

$$\begin{aligned} \mathbf{J}^{\text{gd}} &= J_r^{\text{gd}} \mathbf{e}_r = -\frac{D_0 n(1-n)}{a_0^3 k_B T} \frac{\partial \mu^{\text{gd}}}{\partial r} \mathbf{e}_r \\ &= \frac{D_0 \kappa n(1-n)}{a_0^3 k_B T} \left(-\frac{2}{r^2} \frac{\partial n}{\partial r} + \frac{2}{r} \frac{\partial^2 n}{\partial r^2} + \frac{\partial^3 n}{\partial r^3} \right) \mathbf{e}_r \end{aligned} \quad (3.81)$$

$$\begin{aligned} \mathbf{J}^{\text{cp}} &= J_r^{\text{cp}} \mathbf{e}_r = -\frac{D_0 n(1-n)}{a_0^3 k_B T} \frac{\partial \mu^{\text{cp}}}{\partial r} \mathbf{e}_r \\ &= \frac{D_0 \tilde{\Omega}_0 n(1-n)}{k_B T} \frac{\partial \sigma_{\text{h}}}{\partial r} \mathbf{e}_r, \end{aligned} \quad (3.82)$$

according to Eqs. (3.78), (3.79) and (3.77), respectively.

As already pointed out in Sec. 3.2.5, the strain and stress tensors obtained in Sec. 2.2.2 in the context of the dilute solution approach are also valid in the context of phase-field modeling. At this place, the

components of the stress tensor as a function of the radial mechanical displacement u_r are rewritten and read

$$\sigma_r = 2\lambda_1 \frac{\partial u_r}{\partial r} + \lambda_2 \left(\frac{\partial u_r}{\partial r} + 2\frac{u_r}{r} \right) - \lambda \tilde{\Omega}_0 (n - n_0), \quad (3.83)$$

$$\sigma_t = 2\lambda_1 \frac{u_r}{r} + \lambda_2 \left(\frac{\partial u_r}{\partial r} + 2\frac{u_r}{r} \right) - \lambda \tilde{\Omega}_0 (n - n_0), \quad (3.84)$$

see Eqs. (2.26) - (2.27).

Under the assumption of spherical symmetry, the conservation of lithium matter, Eq. (3.66), as well as the mechanical equilibrium, Eq. (3.71), read

$$\frac{\partial(r^2 n)}{\partial t} + \frac{\partial}{\partial r} \left(a_0^3 r^2 \left(J_r^{\text{mf}} + J_r^{\text{gd}} + J_r^{\text{cp}} \right) \right) = 0, \quad (3.85)$$

$$\frac{\partial \sigma_r}{\partial r} + \frac{2}{r} (\sigma_r - \sigma_t) = 0. \quad (3.86)$$

Note that, due to the term \mathbf{J}^{gd} , the differential equation, Eq. (3.85), representing the conservation of lithium in phase-field modeling, is of fourth order whereas Eq. (2.28), standing for the lithium conservation in the dilute solution approach, is of second order, only.

At the particle boundary surface and center, it still holds, in phase-field modeling, Eqs. (2.30) - (2.33). But in order to ensure the uniqueness of the solution of Eq. (3.85), that is of higher order than Eq. (2.28), additional boundary conditions are required. Because of the assumption of spherical symmetry, the odd derivatives of the lithium concentration n with respect to the radial component r all must be zero at the particle center, see App. A. Thus, at the particle center the boundary conditions

$$\left. \frac{\partial n}{\partial r} \right|_{r=0} = 0 \quad (3.87)$$

$$\left. \frac{\partial^3 n}{\partial r^3} \right|_{r=0} = 0 \quad (3.88)$$

$$\left. u_r \right|_{r=0} = 0 \quad (3.89)$$

have to be satisfied.

For completeness of the mathematical formulation of this problem, initial conditions have to be specified. They are the same as for the dilute solution model and are given by Eqs. (2.34) - (2.35).

Particles of ellipsoidal symmetry

We here consider a particle model of ellipsoidal symmetry, as it is depicted in Fig. 2.7 of Sec. 2.2.3. In cylindrical coordinates with ϑ -invariance, the different contributions to the lithium flux are given by

$$\begin{aligned} \mathbf{J}^{\text{mf}} &= J_{\varrho}^{\text{mf}} \mathbf{e}_{\varrho} + J_z^{\text{mf}} \mathbf{e}_z = -\frac{D_0 n(1-n)}{a_0^3 k_B T} \left(\frac{\partial \mu^{\text{mf}}}{\partial \varrho} \mathbf{e}_{\varrho} + \frac{\partial \mu^{\text{mf}}}{\partial z} \mathbf{e}_z \right) \\ &= -\frac{D_0}{a_0^3} \left(\frac{U\Gamma}{k_B T} n(1-n) + 1 \right) \left(\frac{\partial n}{\partial \varrho} \mathbf{e}_{\varrho} + \frac{\partial n}{\partial z} \mathbf{e}_z \right) \\ &= -\frac{D_0}{a_0^3} \left(\alpha_2 \frac{T_{\text{ref}}}{T} n(1-n) + 1 \right) \left(\frac{\partial n}{\partial \varrho} \mathbf{e}_{\varrho} + \frac{\partial n}{\partial z} \mathbf{e}_z \right), \end{aligned} \quad (3.90)$$

$$\begin{aligned} \mathbf{J}^{\text{gd}} &= J_{\varrho}^{\text{gd}} \mathbf{e}_{\varrho} + J_z^{\text{gd}} \mathbf{e}_z = -\frac{D_0 n(1-n)}{a_0^3 k_B T} \left(\frac{\partial \mu^{\text{gd}}}{\partial \varrho} \mathbf{e}_{\varrho} + \frac{\partial \mu^{\text{gd}}}{\partial z} \mathbf{e}_z \right) \\ &= \frac{D_0 \kappa n(1-n)}{a_0^3 k_B T} \left(\left(-\frac{1}{\varrho^2} \frac{\partial n}{\partial \varrho} + \frac{1}{\varrho} \frac{\partial^2 n}{\partial \varrho^2} + \frac{\partial^3 n}{\partial \varrho^3} + \frac{\partial^3 n}{\partial z^2 \partial \varrho} \right) \mathbf{e}_{\varrho} \right. \\ &\quad \left. + \left(\frac{1}{\varrho} \frac{\partial^2 n}{\partial z \partial \varrho} + \frac{\partial^3 n}{\partial z \partial \varrho^2} + \frac{\partial^3 n}{\partial z^3} \right) \mathbf{e}_z \right), \end{aligned} \quad (3.91)$$

$$\begin{aligned} \mathbf{J}^{\text{cp}} &= J_{\varrho}^{\text{cp}} \mathbf{e}_{\varrho} + J_z^{\text{cp}} \mathbf{e}_z = -\frac{D_0 n(1-n)}{a_0^3 k_B T} \left(\frac{\partial \mu^{\text{cp}}}{\partial \varrho} \mathbf{e}_{\varrho} + \frac{\partial \mu^{\text{cp}}}{\partial z} \mathbf{e}_z \right) \\ &= \frac{D_0 \tilde{\Omega}_0 n(1-n)}{k_B T} \left(\frac{\partial \sigma_{\text{h}}}{\partial \varrho} \mathbf{e}_{\varrho} + \frac{\partial \sigma_{\text{h}}}{\partial z} \mathbf{e}_z \right), \end{aligned} \quad (3.92)$$

according to Eqs. (3.78), (3.79) and (3.77), respectively.

The components of both the strain and stress tensors are identical to those obtained in the dilute solution approach, see Eqs. (2.46) - (2.49). At this place, the components of the stress tensor expressed in terms of the components of the mechanical displacement, u_{ϱ} and u_z , are given by

$$\sigma_{\varrho\varrho} = 2\lambda_1 \frac{\partial u_{\varrho}}{\partial \varrho} + \lambda_2 \left(\frac{\partial u_{\varrho}}{\partial \varrho} + \frac{u_{\varrho}}{\varrho} + \frac{\partial u_z}{\partial z} \right) - \lambda \tilde{\Omega}_0 (n - n_0), \quad (3.93)$$

$$\sigma_{\theta\theta} = 2\lambda_1 \frac{u_{\varrho}}{\varrho} + \lambda_2 \left(\frac{\partial u_{\varrho}}{\partial \varrho} + \frac{u_{\varrho}}{\varrho} + \frac{\partial u_z}{\partial z} \right) - \lambda \tilde{\Omega}_0 (n - n_0), \quad (3.94)$$

$$\sigma_{zz} = 2\lambda_1 \frac{\partial u_z}{\partial z} + \lambda_2 \left(\frac{\partial u_{\varrho}}{\partial \varrho} + \frac{u_{\varrho}}{\varrho} + \frac{\partial u_z}{\partial z} \right) - \lambda \tilde{\Omega}_0 (n - n_0), \quad (3.95)$$

$$\sigma_{\varrho z} = \sigma_{z\varrho} = \lambda_1 \left(\frac{\partial u_z}{\partial \varrho} + \frac{\partial u_{\varrho}}{\partial z} \right). \quad (3.96)$$

Under the assumption of ellipsoidal symmetry, the conservation of lithium matter, Eq. (3.66), as well

as the mechanical equilibrium, Eq. (3.71), read

$$\frac{\partial}{\partial t} (\varrho n) + \frac{\partial}{\partial \varrho} \left(a_0^3 \varrho \left(J_\varrho^{\text{mf}} + J_\varrho^{\text{gd}} + J_\varrho^{\text{cp}} \right) \right) + \frac{\partial}{\partial z} \left(a_0^3 \varrho \left(J_z^{\text{mf}} + J_z^{\text{gd}} + J_z^{\text{cp}} \right) \right) = 0, \quad (3.97)$$

$$\frac{\partial \sigma_{\varrho\varrho}}{\partial \varrho} + \frac{\partial \sigma_{\varrho z}}{\partial z} + \frac{1}{\varrho} \left(\sigma_{\varrho\varrho} - \sigma_{\theta\theta} \right) = 0, \quad (3.98)$$

$$\frac{\partial \sigma_{\varrho z}}{\partial \varrho} + \frac{\partial \sigma_{zz}}{\partial z} + \frac{\sigma_{\varrho z}}{\varrho} = 0. \quad (3.99)$$

To ensure the uniqueness of the solution of this set of equations, Eqs. (3.97) - (3.99), both boundary and initial conditions have to be precised. They are given by Eqs. (2.56) - (2.61) and Eqs. (2.62) - (2.64), respectively, as in the dilute solution model.

Because the differential equation, Eq. (3.97), representing the lithium conservation in phase-field modeling, is of higher order as compared to the dilute solution model, we further require that

$$\left. \frac{\partial^3 n}{\partial \varrho^3} \right|_{\varrho=0} = 0,$$

$$\left. \frac{\partial^3 n}{\partial z^3} \right|_{z=0} = 0$$

are satisfied. Similarly to particles of spherical symmetry, such artificial boundary conditions are obtained by means of symmetry arguments, see App. A.

Conclusion

In this chapter, by means of a very simple classical microscopic Hamiltonian, we reminded of the microscopic origin of phase segregation arising in cathodic particles of LMO: Due to an effective attractive interaction between nearest neighboring lithium ions and provided that the externally fixed temperature remains below the critical temperature, phase segregation is always expected when varying the particle state of charge between 0 and 1.

Using a coarse-graining approach, we could replace the discrete Hamiltonian by an equilibrium free energy functional depending on the lithium concentration as well as the mechanical displacement. Under the assumption that the system is slightly disturbed from equilibrium when intercalating lithium ions into the crystalline cathodic particle, we related the derivatives of the free energy functional, being the chemical potential and the stresses, to the local lithium concentration and momentum fluxes, respectively, by means of a phenomenological Onsager's relation as well as by elasticity laws.

Since both the number of lithium ions and the particle momentum are conserved quantities in the considered system, we make use of these fluxes for being inserted into two time-dependent conservation equations being the local governing equations describing the lithium intercalation into cathodic particles.

Similarly to the dilute solution model of Chp. 2, these local equations have been implemented for both spherical and ellipsoidal particles. To take care of the electrochemical coupling that arises between particles embedded at the cathode of a porous LIB, a dualfoil model with microscopic particles where phase segregation is accounted for has also been implemented. These results are all summarized in the following chapters, Chps. 4 - 5.

4

Chapter 4

Phase-segregated states of the spherically symmetric particle model

Introduction

In the previous chapter (Chp. 3) we introduced the theory related to lithium intercalation into a crystalline cathodic particle where phase segregation possibly occurs during particle loading or unloading, depending on the average lithium concentration. To account for the lithium-induced stresses, an elastic strain energy functional was motivated which led to the same linear elastic constitutive law as the one introduced in Chp. 2 and related to the dilute solution model. In that context the occurrence of phase segregation is still assumed to give rise to small reversible deformations.

In this chapter we study the impact of the phase segregation on the stresses arising in cathodic particles of spherical symmetry and made of LMO. The next chapter (Chp. 5) will be devoted to the analysis of the phase-segregated states arising in cathodic particles without the assumption of spherical symmetry. In Chp. 2 we demonstrated, using the dilute solution model, that large stresses occur as a consequence of large lithium concentration gradients which were induced by large flux magnitudes applied at the particle surface. Differently from the dilute solution model where elevated stresses arise only if the system is significantly driven far away from equilibrium, the phase-field model exhibits equilibrium phase-segregated states where a smooth but very narrow interface separates regions of different lithium concentration. At this place, the gradient in the lithium concentration is very large. Thus, in the context of phase-field modeling, even the equilibrium states exhibit large stress magnitudes.

For this reason, the present chapter is first devoted to the understanding of the equilibrium states obtained using the phase-field model. Such an analysis has not been performed in dilute solution modeling where the equilibrium states are trivially homogeneous and stress-free. In a second part, the stresses arising under particle charging or discharging at constant applied flux magnitude are analyzed. As for the dilute solution, single cathodic particles that are in reality embedded in the cathode of a porous LIB, all couple with each other and, by means of the dualfoil model, this coupling is additionally taken into account. Finally, we study the influence of several quantities as, for instance, the effect of concentration-dependent material parameters or, as it will be done later in Chp. 5, the impact of the particle symmetry on both the equilibrium and dynamical states.

4.1 Equilibrium states

4.1.1 Origin of the phase separation and system relaxation

To begin with, we focus on a cathodic particle that satisfies the condition of spherical symmetry and first neglect the lithium-induced deformations. At equilibrium, the average lithium concentration \bar{n} is a fixed quantity. However, at finite temperatures $T > 0$, the local lithium concentration n exhibits thermal fluctuations that may spontaneously drive the system into a phase-segregated state.

In the considered model, the thermal fluctuations are however not accounted for. To account for them, a thermal noise inducing randomly distributed fluctuations of the lithium concentration over the system should have been considered in the expression of the free energy functional [119]. In our implementation, due to the absence of thermal noise, the impact of the thermal fluctuations on the formation of phase-segregated states cannot be properly analyzed. Nevertheless, by generating initial nonhomogeneous lithium concentration profiles of varying amplitude and given average lithium concentration \bar{n} , the role of the thermal fluctuations on the occurrence or absence of phase segregation may be roughly understood.

For the study of the influence of the thermal fluctuations on the system equilibrium states, the parameters related to the mean-field free energy, shown in Fig. 4.1, are chosen equal to $\alpha_1 = 2.5$ and $\alpha_2 = -4.2$. This last value differs from its usually chosen value, $\alpha_2 = -5.2$. Fig. 4.2 shows, at different

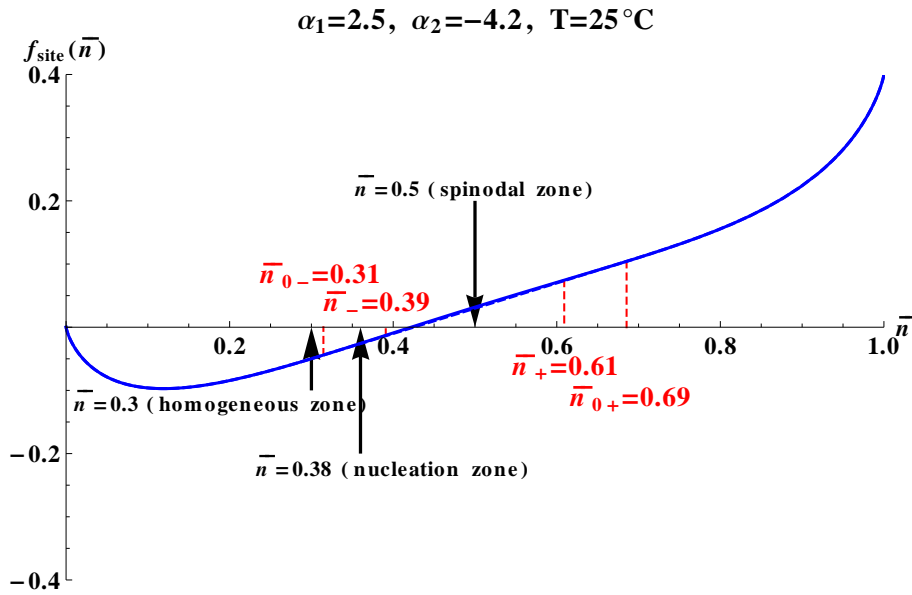
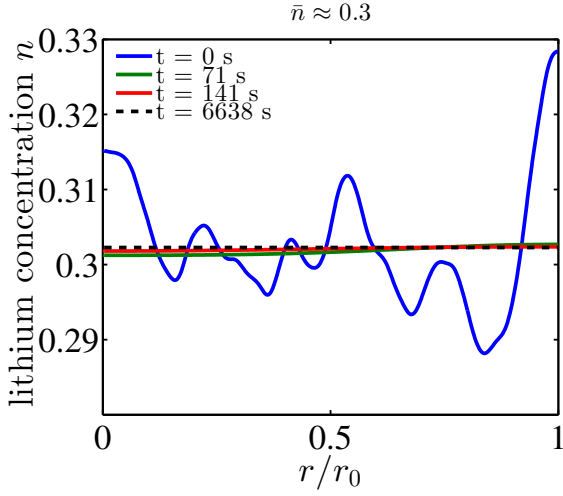


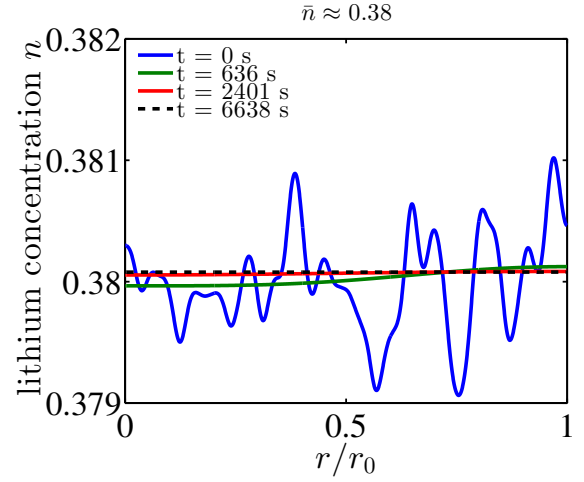
Figure 4.1: Mean-field free energy as function of the average lithium concentration \bar{n} at fixed temperature, $T = 25^\circ\text{C}$. With $\alpha_1 = 2.5$ and $\alpha_2 = -4.2$, the exemplary average values, $\bar{n} = 0.3$, $\bar{n} = 0.38$ and $\bar{n} = 0.5$, belong to the “homogeneous”, “nucleation” and “spinodal zones” of the mean-field free energy, respectively.

times during the system relaxation, e.g. with vanishing surface lithium flux, the lithium concentration profile until the equilibrium state is reached¹.

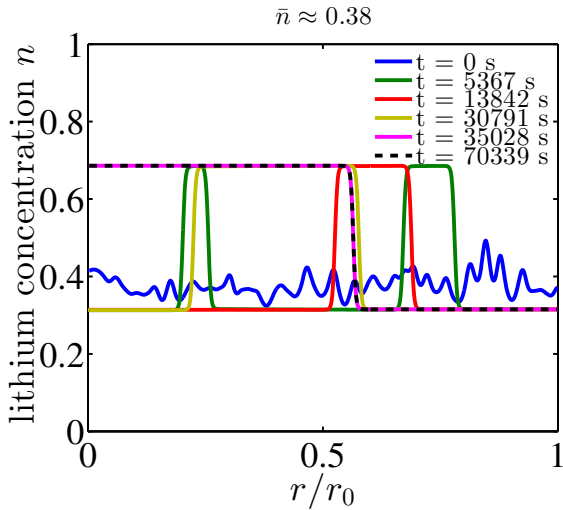
¹The equilibrium state is the state holding at time equals infinity. The simulations, however, cannot be performed during an infinitely long time. Hence, they are stopped until the unknown variable of the system, the lithium concentration, does not vary any more in time. At such time, the equilibrium state is assumed to be reached.



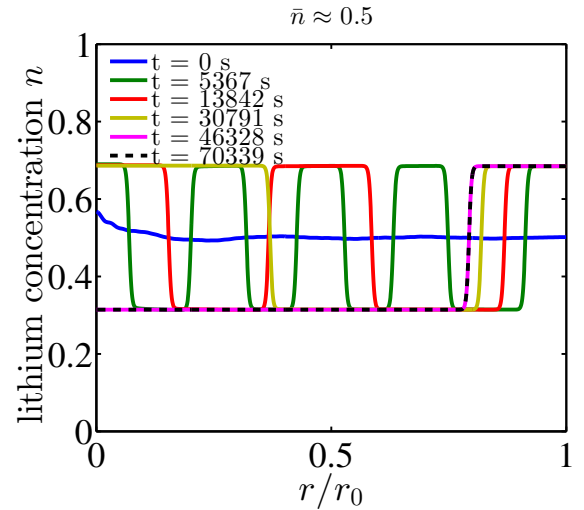
(a) The initial lithium ion configuration exhibits *large fluctuations* around its average value, $\bar{n} \approx 0.3$ and corresponds to a state located in the *homogeneous zone* of the mean-field free energy.



(b) The initial lithium ion configuration exhibits *small fluctuations* around its average value, $\bar{n} \approx 0.38$ and corresponds to a state located in the *nucleation zone* of the mean-field free energy.



(c) The initial lithium ion configuration exhibits *large fluctuations* around its average value, $\bar{n} \approx 0.38$ and corresponds to a state located in the *nucleation zone* of the mean-field free energy.



(d) The initial lithium ion configuration exhibits *small fluctuations* around its average value, $\bar{n} \approx 0.5$ and corresponds to a state located in the *spinodal zone* of the mean-field free energy.

Figure 4.2: Profile of the lithium concentration at different times during the system relaxation obtained for different initial lithium ion configurations. The solid blue lines correspond to the initial lithium concentration profile whereas the dashed black lines are the reached equilibrium states obtained at the end of the simulations.

As expected from the mean-field free energy profile of Fig. 4.1, four different regimes could be observed: The first regime, shown in Fig. 4.2(a), has been obtained from an initial lithium concentration state of fixed average lithium concentration $\bar{n} \approx 0.3$ with large fluctuations around the average value. Since this initial state corresponds to the “homogeneous zone” of the mean-field free energy, as depicted in Fig. 4.1, the reached equilibrium state is homogeneous.

The second and third regimes, shown in Fig. 4.2(b) and Fig. 4.2(c), respectively, both have been obtained at fixed average lithium concentration $\bar{n} \approx 0.38$ located in the “nucleation zone” of the mean-field free energy. In the second regime with small fluctuations $\delta n = |n - \bar{n}| < |\bar{n}_\pm - \bar{n}|$, the system relaxes towards a homogeneous lithium state (see Fig. 4.2(b)). On the contrary, in the third regime where the fluctuations of the lithium concentration are large, $\delta n = |n - \bar{n}| > |\bar{n}_\pm - \bar{n}|$, the system relaxes towards a phase-segregated state (see Fig. 4.2(c)). These two different behaviors illustrate the role of the thermal fluctuations in the phase segregation process. In the “nucleation zone”, the (mean-field) free energy of the homogeneous lithium concentration states is higher than the free energy of the phase-segregated states whose value is obtained from the Maxwell construction. Nevertheless, in this zone, the mean-field free energy, which is still a convex function of the average lithium concentration \bar{n} , leads to homogeneous metastable states. As a consequence, phase segregation arises only if the fluctuations in the lithium concentration are large enough and locally drive the system into the “spinodal zone” of the mean-field free energy. The fourth regime, shown in Fig. 4.2(d) for $\bar{n} \approx 0.5$, is related to this “spinodal zone”. Here, even infinitesimal (but nonzero) fluctuations drive the system into a phase-segregated state. Indeed, in this zone, the mean-field free energy is not a convex function of the average lithium concentration \bar{n} indicating that the homogenous lithium concentration states, on the contrary to the phase-segregated states, are unstable.

Another way to drive the system into a phase-segregated state is to apply, at the particle surface, a lithium flux. Such a flux acts in a similar manner as thermal fluctuations because it locally (at the particle surface) enforces a variation in the lithium concentration. But, differently from thermal fluctuations, applying a flux at the particle surface also induces a change in the average lithium concentration \bar{n} . Thus, to study the equilibrium states, after the system has been disturbed from equilibrium by application of a nonzero surface flux, it is allowed for relaxing towards equilibrium while the applied flux is set equal to zero.

Fig. 4.3 shows the time-dependent lithium flux magnitude $|J_{an}|$ applied at the particle surface as well as the system free energy as function of time. The system free energy shown here is in fact the system free energy per interstitial site, $\mathcal{N} = V_0/a_0^3$, and per unit of $k_B T$. It is denoted by $\tilde{\Psi}$ and is related to the “real” system free energy Ψ , defined in Eq. (3.32), by

$$\tilde{\Psi} \equiv \frac{\Psi}{\mathcal{N}k_B T} = \frac{a_0^3}{V_0 k_B T} \Psi.$$

For the particular case of a spherically symmetric particle model, it is equal to

$$\begin{aligned} \tilde{\Psi} &= \frac{3a_0^3}{4\pi r_0^3 k_B T} \Psi \\ &= \frac{3a_0^3}{4\pi r_0^3 k_B T} \int_0^{r_0} \frac{dr}{a_0^3} 4\pi r^2 \psi \\ &= \frac{3}{r_0^3 k_B T} \int_0^{r_0} dr r^2 \psi \\ &= \frac{3}{k_B T} \int_0^1 d\tilde{r} \tilde{r}^2 \psi, \end{aligned} \tag{4.1}$$

with $\tilde{r} = r/r_0$, r_0 being the particle radius.

The flux magnitude shown in Fig. 4.3 can be applied during both lithium insertion and extraction, however with opposite flux directions and starting either from an initial homogeneous lithium concentration $\bar{n} = 0.05$ (lithium insertion) or $\bar{n} = 0.95$ (lithium extraction). In order to disturb the spherical

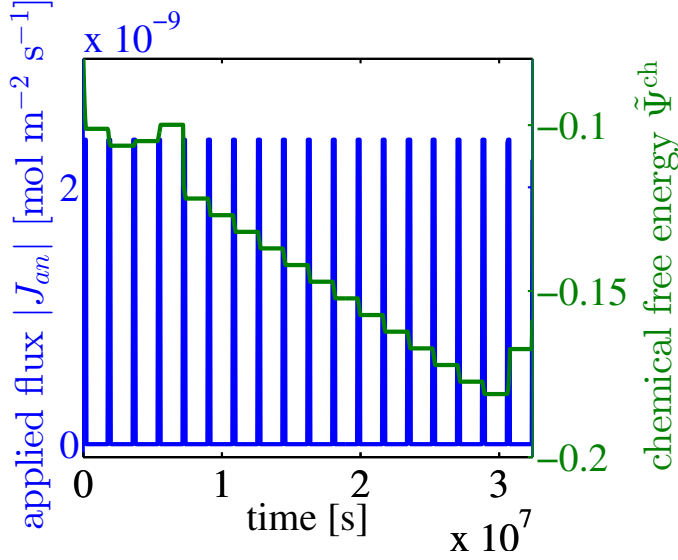


Figure 4.3: Applied lithium flux (blue curve) and system free energy (green curve) as function of time during lithium intercalation into the cathodic particle.

cathodic particle not too far away from equilibrium, the applied C -rate related to the applied flux magnitude $|J_{an}|$ by

$$|J_{an}| = \frac{C}{t_0} \frac{r_0}{3a_0^3},$$

according to Eq. (2.1), must satisfy

$$Cr_0^2 \ll t_0 D_0.$$

In the present study of the system equilibrium states, we choose $C = 0.001$ ($t_0 = 3600$ s) relatively to a particle of radius $r_0 = 1 \mu\text{m}$. During the hold times, the system relaxes towards equilibrium and the system free energy decreases to become constant at the end of each hold time meaning the system has reached an equilibrium state.

The equilibrium values of the system free energy — here equal to the chemical free energy Ψ^{ch} since the host deformations induced by the lithium intercalation are, for the first, not considered — as function of the average lithium concentration \bar{n} are represented in Fig. 4.4(a). Up to now and for all simulations discussed in the following if not specified otherwise, the parameters of the corresponding mean-field free energy are chosen equal to

$$\begin{aligned} \alpha_1 &= 2.5, \\ \alpha_2 &= -5.2. \end{aligned}$$

The temperature T is maintained constant equal to

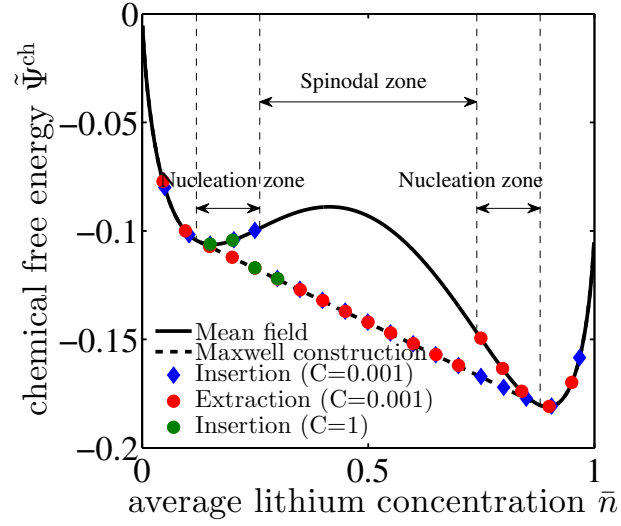
$$T = T_{\text{ref}} = 25^\circ\text{C}.$$

Regarding the parameter κ related to the thickness of the boundary layer between the two different lithium concentration phases, it is taken equal to

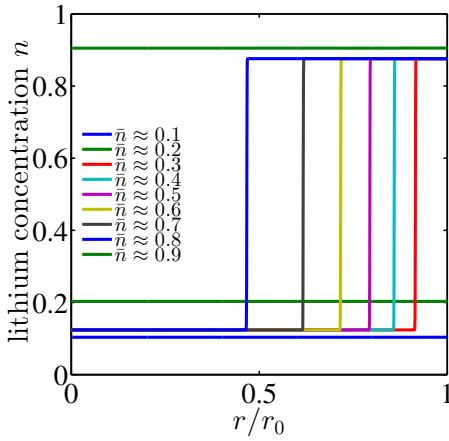
$$\kappa = -2Ua_0^2 = -2\frac{\alpha_2 k_B T_{\text{ref}}}{\Gamma} a_0^2, \quad (4.2)$$

according to the calculation performed in App. C and to the definition of α_2 , Eq. (3.19). As illustrated in Fig. 4.4(b) - 4.4(c), values of the system free energy that fit the mean-field free energy curve correspond to homogeneous lithium concentration states whereas values of the system free energy that match the Maxwell construction correspond to phase-segregated lithium concentration states.

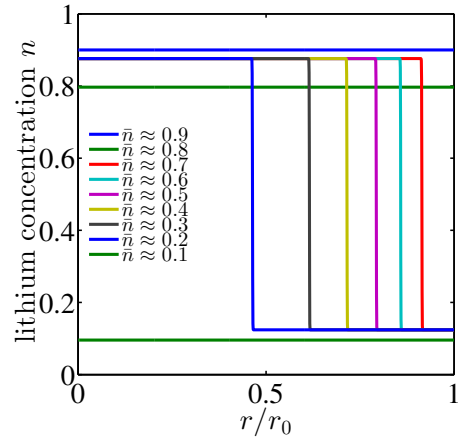
The system free energy exhibits an hysteresis-like behavior to be linked with the magnitude of the applied lithium flux. In the “nucleation zone” of the mean-field free energy where the homogeneous states are metastable, the system does not undergo the phase segregation unless the lithium concentration locally reaches a value located in the “spinodal zone”. Such a situation may however arise if the applied flux magnitude $|J_{an}|$ is sufficiently large (as compared to the lithium flux magnitude $|\mathbf{J}|$ holding within the particle) and drives the lithium concentration at the particle boundary surface $n(r_0, t)$ into the “spinodal zone” of the mean-field free energy, e.g. if $n_- < n(r_0, t) < n_+$ at some particular time t . In contrast, in the “spinodal zone”, even infinitesimal applied flux magnitudes lead to phase segregation since the mean-field free energy is not convex with respect to the average lithium concentration \bar{n} .



(a) Equilibrium free energy as function of the average lithium concentration \bar{n} .



(b) Profiles of the lithium concentration n at equilibrium obtained during lithium insertion.



(c) Profiles of the lithium concentration n at equilibrium obtained during lithium extraction.

Figure 4.4: Free energy and corresponding lithium concentration profiles at equilibrium obtained during both lithium insertion and extraction.

4.1.2 Effect of the interfacial energy

In order to analyze the effect of the interfacial energy Ψ^{gd} , the contribution of the elastic strain energy to the total system free energy is still neglected. The interfacial energy contributes to the total system free energy by

$$\Psi^{\text{gd}} = \frac{\kappa}{2} \int_{V_0} \frac{dV}{a_0^3} |\nabla n|^2,$$

which is inserted into Eq. (4.1) to obtain the interfacial free energy per interstitial site and per unit of $k_B T$,

$$\tilde{\Psi}^{\text{gd}} = \frac{3}{k_B T} \frac{\kappa}{r_0^2} \int_0^1 d\tilde{r} \tilde{r}^2 \left| \frac{\partial n}{\partial \tilde{r}} \right|^2.$$

With

$$\tilde{\kappa} = \frac{\kappa}{k_B T r_0^2},$$

the interfacial free energy $\tilde{\Psi}^{\text{gd}}$ reduces to

$$\tilde{\Psi}^{\text{gd}} = 3\tilde{\kappa} \int_0^1 d\tilde{r} \tilde{r}^2 \left| \frac{\partial n}{\partial \tilde{r}} \right|^2. \quad (4.3)$$

For a system of attractively interacting lithium ions, $\tilde{\kappa} > 0$. Thus, according to Eq. (4.3), if the lithium concentration profile exhibits nonvanishing gradients, the interfacial free energy becomes strictly positive (nonzero) and increases with increasing values of $\tilde{\kappa}$. As reference value for the parameter $\tilde{\kappa}$, we define

$$\tilde{\kappa}_0 = \frac{\kappa_0}{k_B T r_0^2},$$

where

$$\kappa_0 = -2 \frac{\alpha_2 k_B T_{\text{ref}}}{\Gamma} a_0^2,$$

according to Eq. (4.2). Note that, at this place, the particle radius is considered as a fixed quantity equal to $r_0 = 1 \mu\text{m}$. Then, at given temperature T , the parameter $\tilde{\kappa}_0$ appears as constant of the model.

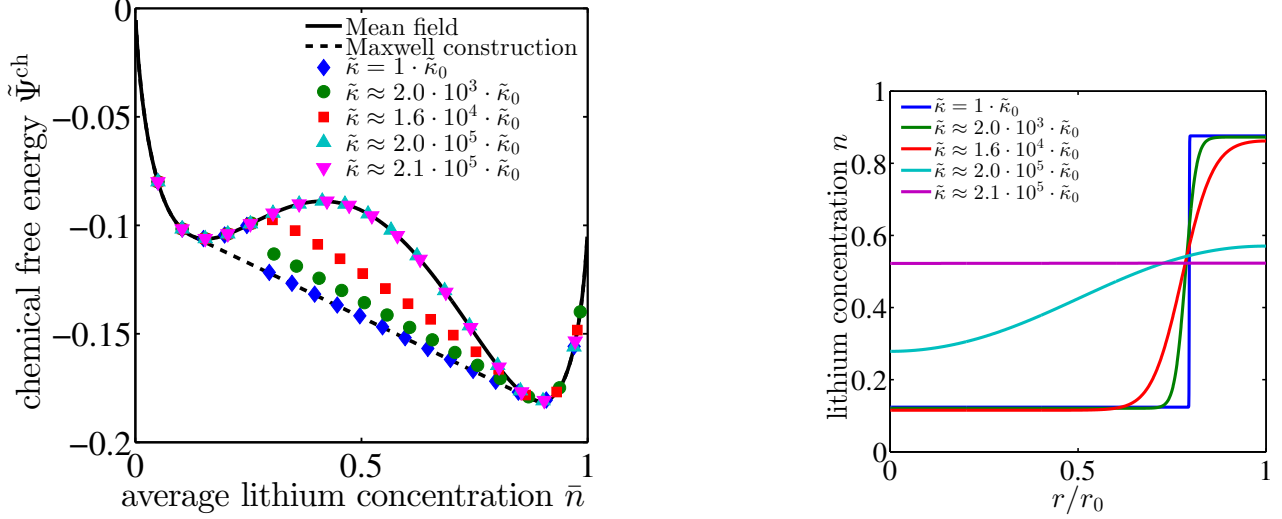
To analyze the influence of the interfacial energy on the phase segregation, the parameter $\tilde{\kappa}$ is allowed to vary according to

$$\begin{aligned} \tilde{\kappa} &= \alpha \tilde{\kappa}_0 = \frac{\alpha \kappa_0}{k_B T r_0^2} \\ &= \frac{\kappa}{k_B T} \frac{1}{r_0^2} \text{ with } \kappa = \alpha \kappa_0, \end{aligned} \quad (4.4)$$

where $\alpha > 0$ will be varied in order to study the energetic cost of building an interface between the two different lithium concentration phases. Because the particle radius r_0 is here maintained constant, a change of the value of α represents a modification of the interfacial energy term², solely.

²We here modify the interfacial energy term κ without changing the value of α_2 . This may be questioned because it has been motivated that κ depends on α_2 . Nevertheless, it allows for the understanding of the sole effect of the interfacial energy on the phase segregation.

Fig. 4.5 shows the system free energy, here equal to the chemical free energy since the elastic strain energy is not considered, for different values of $\tilde{\kappa}$, as well as the corresponding lithium concentration profiles in the spinodal zone of the system free energy when the average lithium concentration $\bar{n} \approx 0.5$. As expected, increasing value of $\tilde{\kappa}$ increases the total system free energy and broadens the interfacial



(a) Equilibrium free energy as function of the average lithium concentration \bar{n} for different values of $\tilde{\kappa}$.

(b) Lithium concentration profiles n for different values of $\tilde{\kappa}$ when $\bar{n} \approx 0.5$.

Figure 4.5: Influence of the parameter $\tilde{\kappa}$ on the system free energy as well as on the lithium concentration profiles at equilibrium.

layer between the two different lithium concentration phases. For the chosen mean-field free energy parameters, $\alpha_1 = 2.5$ and $\alpha_2 = -5.2$, the phase segregation is even suppressed when

$$\tilde{\kappa} > \tilde{\kappa}_c = \alpha_c \tilde{\kappa}_0 = \frac{\alpha_c \kappa_0}{k_B T} \frac{1}{r_0^2} \quad (4.5)$$

$$(4.6)$$

where α_c is a numerical value found to be equal to $\alpha_c \approx 2.1 \cdot 10^5$. In fact, for $\tilde{\kappa}$ -values above the critical interfacial energy term $\tilde{\kappa}_c$, building a phase boundary costs the system more energy than remaining in a homogeneous lithium concentration state.

At fixed temperature and given value of $\kappa = \alpha \kappa_0$, the occurrence or absence of phase segregation appears to be solely governed by the particle radius r_0 , according to Eq. (4.4). Hence, the critical interfacial energy term $\tilde{\kappa}_c$ introduced in Eq. (4.5) can be related to a critical particle radius defined as

$$r_c = \sqrt{\frac{\kappa}{k_B T \tilde{\kappa}_c}}.$$

The critical particle radius r_c specifies a length scale below which phase segregation cannot arise in the spherical particle. Its representation as function of $\kappa/k_B T$ is shown in Fig. 4.6. Indeed, in particles of radius smaller than the critical radius, the proportion of interfacial layers becomes too important compared to the homogeneous regions so that the free energy of the phase-segregated states is always larger than the free energy of the homogeneous states related to the same average lithium

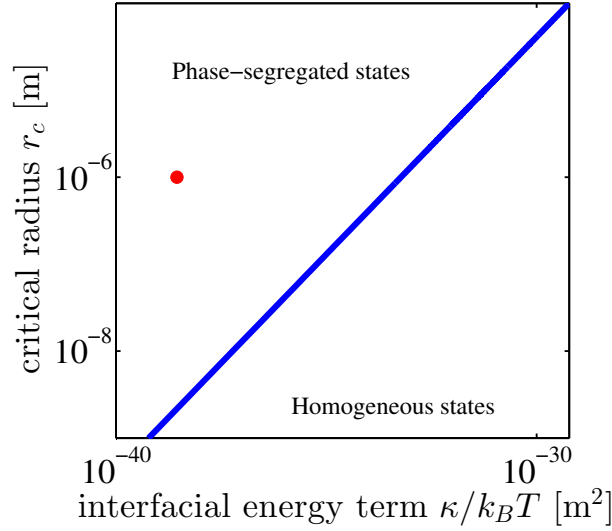


Figure 4.6: Critical radius r_c as function of the interfacial parameter $\kappa/k_B T$. The red point represents a cathodic particle of radius $r_0 = 1 \mu\text{m}$ and of interfacial parameter equals $\kappa_0/k_B T$.

concentration, that consequently hold in the system. With $\kappa = \kappa_0$ as realistic value, a critical radius of some nanometers is obtained.

4.1.3 Effect of the elastic strain energy term

The elastic strain energy Ψ^{es} contributes to the total system free energy by

$$\Psi^{\text{es}} = \int_{V_0} \frac{dV}{a_0^3} \frac{a_0^3}{2} \varepsilon_{ij}^{\text{el}} C_{ijkl} \varepsilon_{ij}^{\text{el}}$$

which is inserted into Eq. (4.1) to obtain the elastic strain energy per interstitial site and per unit of $k_B T$,

$$\tilde{\Psi}^{\text{es}} = \frac{3a_0^3}{2k_B T} \int_0^1 d\tilde{r} \varepsilon_{ij}^{\text{el}} C_{ijkl} \varepsilon_{ij}^{\text{el}}. \quad (4.7)$$

For an isotropic material, according to Eqs. (3.42) - (3.43) and to Eq. (3.40), the above equation reads

$$\tilde{\Psi}^{\text{es}} = \frac{3a_0^3}{2k_B T} \int_0^1 d\tilde{r} \left(\lambda_2 \text{Tr}^2(\varepsilon) + 2\lambda_1 \text{Tr}(\varepsilon^2) + 4\lambda_1 (\varepsilon_{12}^2 + \varepsilon_{23}^2 + \varepsilon_{31}^2) - \tilde{\Omega}_0 \lambda (n - n_0) (2 \text{Tr}(\varepsilon) - \tilde{\Omega}_0 (n - n_0)) \right),$$

which simplifies to

$$\tilde{\Psi}^{\text{es}} = \frac{3a_0^3}{2k_B T} \int_0^1 d\tilde{r} \left(\lambda_2 (\varepsilon_r + 2\varepsilon_t)^2 + 2\lambda_1 (\varepsilon_r^2 + 2\varepsilon_t^2) - \tilde{\Omega}_0 \lambda (n - n_0) \left(2(\varepsilon_r + 2\varepsilon_t) - \tilde{\Omega}_0 (n - n_0) \right) \right),$$

for a spherically symmetric particle model. Using the definitions, Eqs. (3.83) - (3.84), the elastic strain energy $\tilde{\Psi}^{\text{es}}$ is then given by

$$\tilde{\Psi}^{\text{es}} = \frac{3a_0^3}{2k_B T} E \int_0^1 d\tilde{r} \left(\frac{\nu (\varepsilon_r + 2\varepsilon_t)^2}{(1 - 2\nu)(1 + \nu)} + \frac{(\varepsilon_r^2 + 2\varepsilon_t^2)}{(1 + \nu)} - \frac{\tilde{\Omega}_0 (\nu + 1) (n - n_0)}{3(1 - 2\nu)(1 + \nu)} \left(2(\varepsilon_r + 2\varepsilon_t) - \tilde{\Omega}_0 (n - n_0) \right) \right). \quad (4.8)$$

From Eq. (4.7) it clearly appears that, due the positive definiteness of the stiffness tensor \mathbf{C} , the elastic strain energy is a quadratic form in the elastic strains $\varepsilon_{ij}^{\text{el}} = \varepsilon_{ij} - \varepsilon_{ij}^{\text{Li}}$. It means that the elastic strain energy is always positive and vanishes only if

$$\varepsilon_{ij} = \varepsilon_{ij}^{\text{Li}}.$$

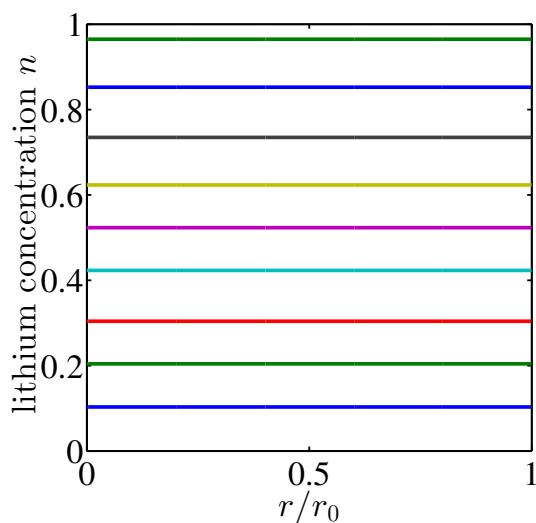
In a system of spherical symmetry, this condition is equivalent to a set of three equalities,

$$\varepsilon_r(r) = \varepsilon_t(r) = \varepsilon^{\text{Li}}(r) \equiv \frac{\tilde{\Omega}_0}{3} (n(r) - n_0), \text{ for } 0 \leq r \leq 1, \quad (4.9)$$

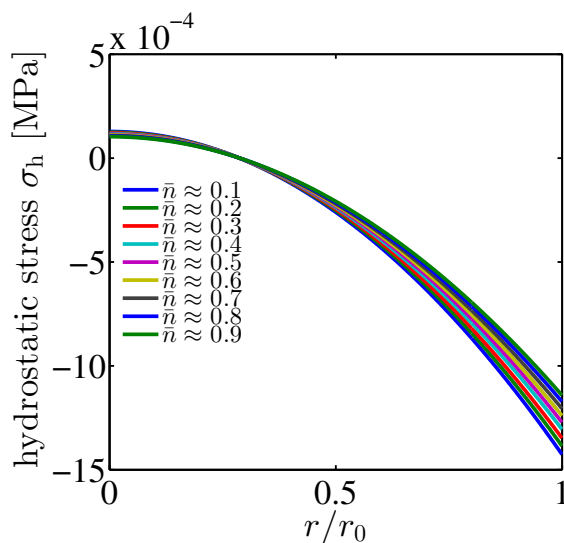
which can be fulfilled at equilibrium provided that the lithium concentration is homogeneous over the entire system. Otherwise, in equilibrium phase-segregated states, the equalities represented by Eq. (4.9) are not compatible. As a consequence, the elastic strain energy becomes strictly positive and prevents the system from relaxing towards a stress-free state.

For comparison, we show in Fig. 4.7 the profiles of both the lithium concentration n and the hydrostatic stress σ_h obtained at equilibrium using the dilute solution model. At this place, we can see that, as expected, the system states are homogeneous and almost stress-free.

From Eq. (4.8), we can conclude that, at fixed temperature T and given lithium concentration and strain profiles, the elastic strain energy is proportionnal to the Young's modulus E of the material. Thus, at given nonhomogeneous lithium concentration profile, the elastic strain energy increases with increasing values of the Young's modulus. In a certain manner, varying the Young's modulus E as the same effect as varying the interfacial energy term $\tilde{\kappa}$. Indeed, the interfacial energy $\tilde{\Psi}^{\text{gd}}$ and the elastic strain energy $\tilde{\Psi}^{\text{es}}$ are both quadratic forms proportional to $\tilde{\kappa}$ and E , respectively. If the lithium concentration is homogeneous over the particle, their contributions to the total system free energy vanish, and are otherwise strictly positive. Hence the energetic cost of building a phase boundary increases with increasing values of the interfacial energy term $\tilde{\kappa}$ and the Young's modulus E (see Fig. 4.8), respectively. As a consequence, elevated values of these quantities suppress the phase segregation.

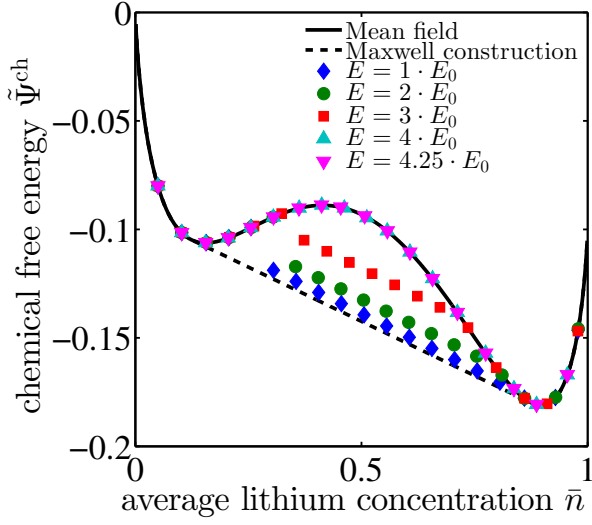


(a) Profile of the lithium concentration n at equilibrium for different average lithium concentration \bar{n} .

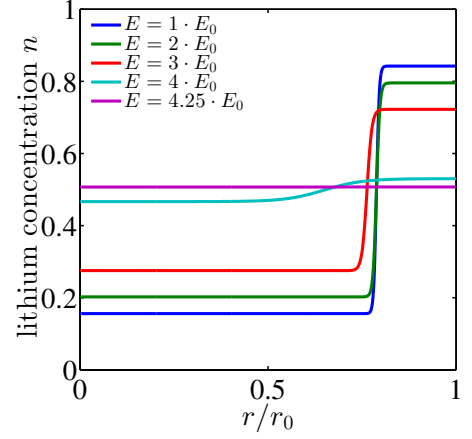


(b) Profile of the hydrostatic stress σ_h at equilibrium for different average lithium concentration \bar{n} .

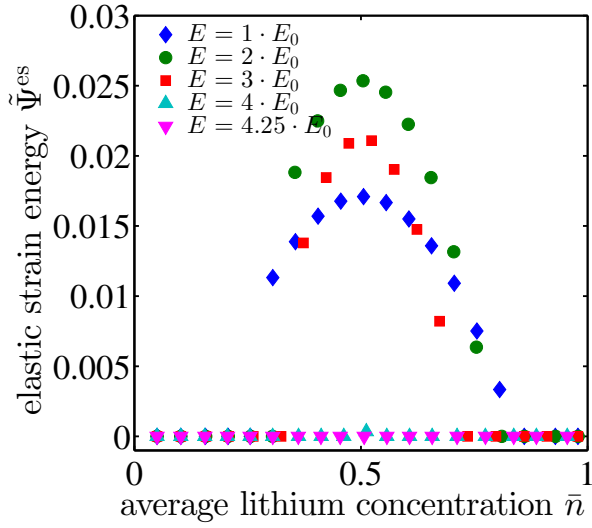
Figure 4.7: *Lithium concentration and hydrostatic stress profiles obtained at equilibrium in the dilute solution approximation. The hydrostatic stress exhibits, independently of the average lithium concentration \bar{n} , a quasi-vanishing profile indicating that the elastic strain energy is almost zero.*



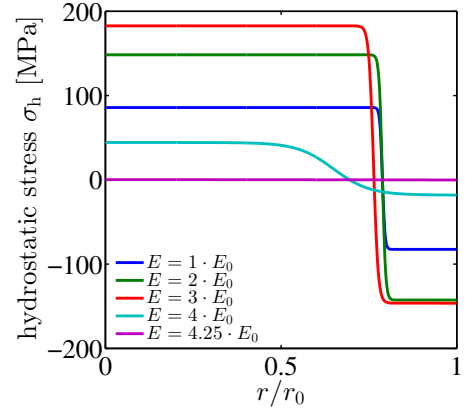
(a) Equilibrium chemical free energy as function of the average lithium concentration for different Young's modulus values E .



(b) Lithium concentration profiles n for different Young's modulus values when $\bar{n} \approx 0.5$.



(c) Equilibrium elastic strain energy as function of the average lithium concentration for different Young's modulus values E .



(d) Hydrostatic stress profile σ_h for different Young's modulus values when $\bar{n} \approx 0.5$.

Figure 4.8: Influence of the Young's modulus E on the different contributions to the system free energy as well as on the lithium concentration and hydrostatic stress profile.

Differently from the effect of the interfacial energy term $\tilde{\kappa}$, varying the Young's modulus E does not change the thickness of the interfacial layer between the two different lithium concentration phases, but modifies the values of the lithium concentration reached in these phases. Increasing the Young's modulus acts so that the discrepancy in the lithium concentration between the low- and high-concentration phases shrinks, the former increasing and the later decreasing. With

$$\begin{aligned}\alpha_1 &= 2.5, \\ \alpha_2 &= -5.2, \\ \tilde{\kappa} &= 100 \cdot \tilde{\kappa}_0, \\ \nu &= 0.3,\end{aligned}$$

this discrepancy becomes zero when

$$E > E_c \approx 4.0 \cdot E_0.$$

Above the critical Young's modulus E_c , building the phase boundary costs, the system, more (elastic strain) energy than the chemical energy gained when undergoing the phase segregation. Hence, for $E > E_c$, the system always remains in a homogeneous lithium concentration state.

In contrast to the critical interfacial energy term κ_c , the critical Young's modulus E_c was found to be independent of the particle size, but strongly dependent on the form of double-well chemical free energy which is determined, at given temperature T , by the values of α_1 and α_2 , solely. Fig. 4.9 demonstrates

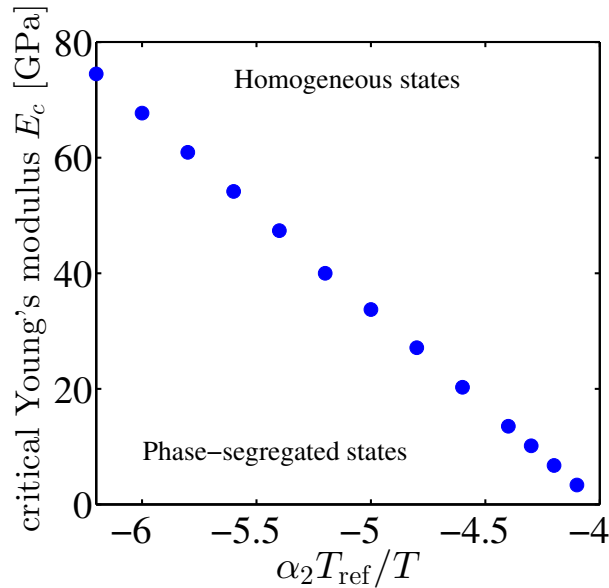


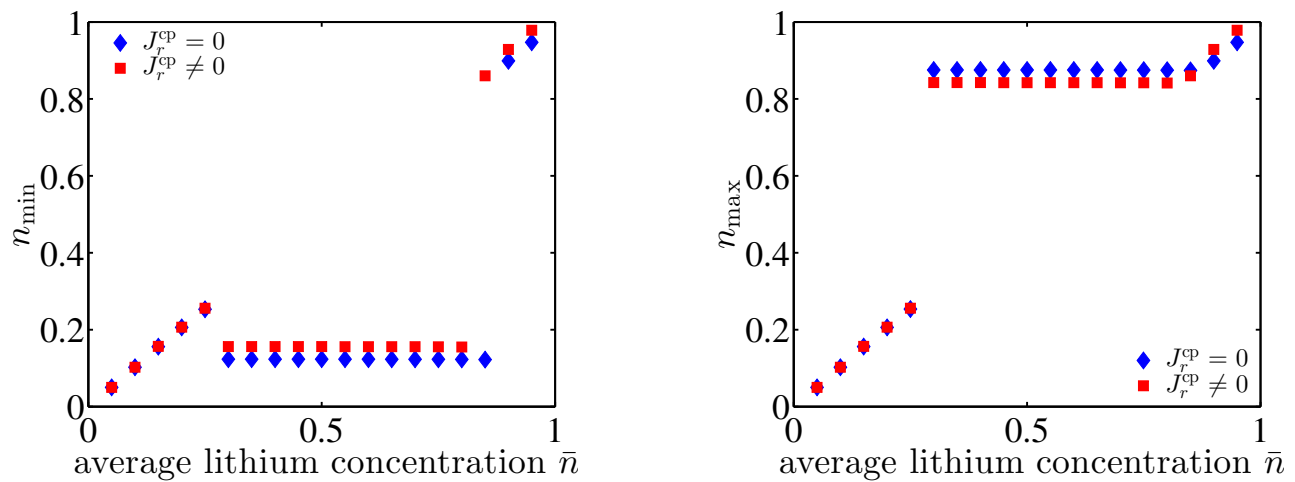
Figure 4.9: Curve representing the numerically obtained critical Young's modulus E_c in dependency of the quantity $\alpha_2 T_{\text{ref}}/T$ at constant temperature $T = T_{\text{ref}}$ and for $\alpha_1 = 2.5$. Above this curve, the lithium concentration state is homogeneous because building the phase boundary costs the system more energy than being in a homogeneous state. Below this curve, the lithium concentration state is phase-segregated.

that the critical Young's modulus E_c decreases when α_2 grows towards $\alpha_2 = -4$, where, even without consideration of the lithium-induced deformations, the phase-segregated states all are suppressed. It

is due to the fact that, for $T = T_{\text{ref}}$, the concavity zone of the mean-field free energy disappears when $\alpha_2 > -4^3$.

In the dilute solution model introduced in Chp. 2, we analyzed in Sec. 2.2.2 the effect of the stress-induced lithium flux J_r^{cp} as compared to the case where this flux is neglected by setting $J_r^{\text{cp}} = 0$. Within this model, we demonstrated that the stress-induced lithium flux acts in the same way as the lithium flux induced by gradients in the lithium concentration J_r^{ch} and thus contributes to a better lithium ion distribution inside of the particle. In this study we saw that large stresses were induced by large lithium concentration gradients. Thus it was also found that the hydrostatic stress was larger when neglecting the stress-induced lithium flux.

At this place, we analyze, at equilibrium, the effect of considering or neglecting the stress-induced lithium flux on the phase segregated states. For these two cases, Fig. 4.10 shows, at equilibrium, the value of lithium-concentration reached in both the low- and high-lithium concentration phases. As



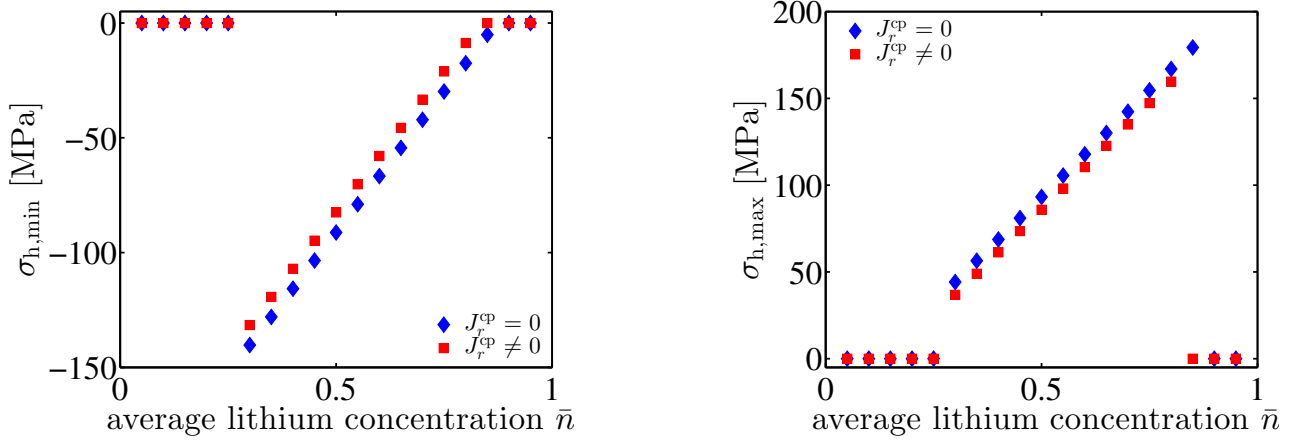
(a) Minimum of the lithium concentration n at equilibrium in dependency of the average lithium concentration \bar{n} .

(b) Maximum of the lithium concentration n at equilibrium in dependency of the average lithium concentration \bar{n} .

Figure 4.10: *Extrema of the lithium concentration n at equilibrium as function of the average lithium concentration \bar{n} . These values have been obtained after lithium insertion followed by relaxation times. The minima of the lithium concentration are located at the particle center and its maxima at the particle surface.*

expected, the discrepancy between these two values is smaller when the stress-induced lithium flux is not neglected. As for the dilute solution model, we here also argue that this flux enhances the lithium diffusion and thus contributes to a better lithium ion distribution inside of the particle. Consequently, as illustrated in Fig. 4.11, the hydrostatic stresses obtained when neglecting the stress-induced lithium flux are larger than those obtained when this flux is different from zero.

³For a working temperature $T = T_{\text{ref}} < T_c$, phase segregation always takes place. However, according to Eq. (3.21) of Sec. 3.2.2, this last condition reduces to $\alpha_2 > -4$.



(a) Minimum of the hydrostatic stress σ_h at equilibrium in dependency of the average lithium concentration \bar{n} .

(b) Maximum of the hydrostatic stress σ_h at equilibrium in dependency of the average lithium concentration \bar{n} .

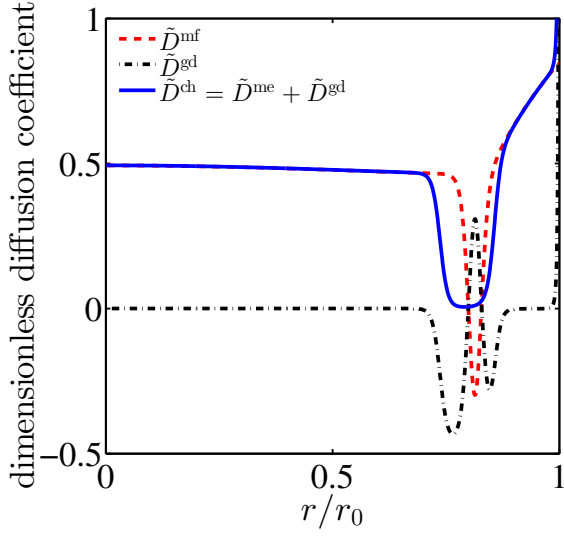
Figure 4.11: *Extrema of the hydrostatic stress σ_h at equilibrium as function of the average lithium concentration \bar{n} . These values have been obtained after lithium insertion followed by relaxation times. The minima of the hydrostatic stresses are located at the particle surface and the maxima at the particle center.*

4.2 Dynamical behavior

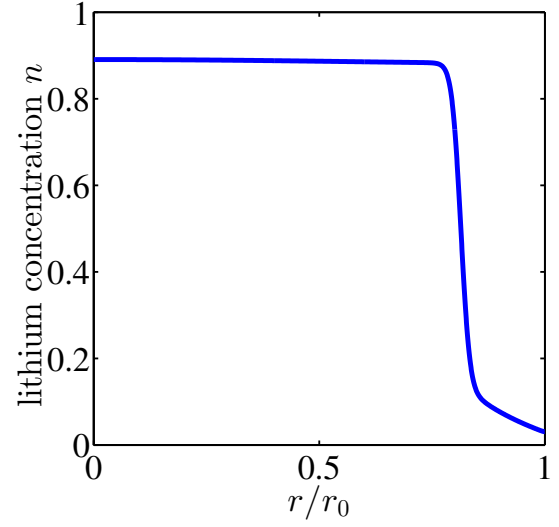
4.2.1 Different contributions to the flux

In the previous section, Sec. 4.1, devoted to the study of the equilibrium states of a cathodic particle of spherical symmetry, we argued by means of energetic considerations at equilibrium that the interfacial and elastic strain energies, both positive quantities, equal to zero in the homogeneous lithium concentration states, become strictly positive when the system undergoes phase segregation. Moreover, if their contributions to the total system free energy become too important, it has been demonstrated that phase segregation is suppressed.

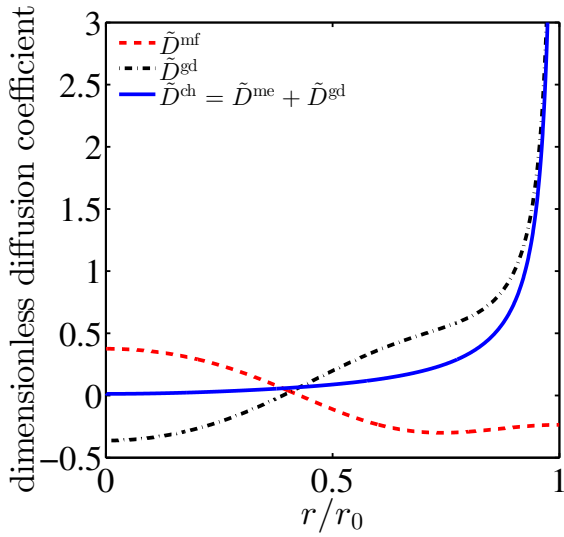
In contrast to the last section where the occurrence of phase segregation was analyzed at equilibrium, we here examine the formation of phase-segregated states under dynamical particle unloading, e.g. during lithium extraction at constant applied flux magnitude related to a given particle C -rate. Phase segregation arises when the lithium flux within the particle is “anomalous”. This means that the lithium flux instead of dragging the lithium ions from the high lithium concentration regions to the low lithium concentration regions, acts in the opposite direction. In Sec. 2.2.2 related to the dilute solution model, it is obvious that the proportionality constant between the conventional diffusion flux J_r^{cp} — equal to D_0/a_0^3 (see Eq. (2.39)) — and the opposite of the lithium concentration gradient $-\partial n/\partial r$ is positive. On the contrary, when phase segregation arises, this proportionality constant becomes negative. In that sense the occurrence of phase segregation can be viewed in terms of a “negative diffusion coefficient”.



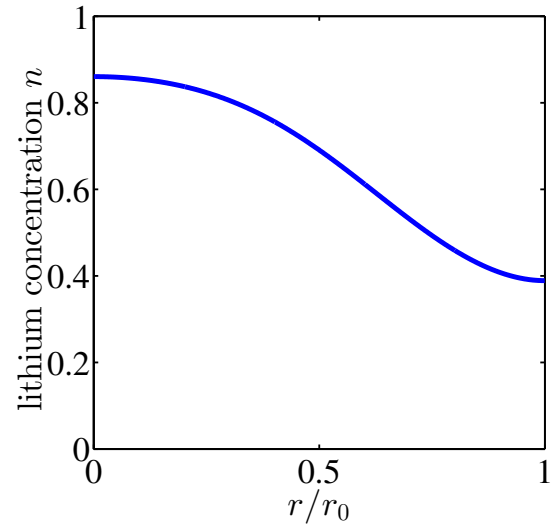
(a) Profile of the different contributions to the dimensionless diffusion coefficient \tilde{D}^{ch} for $\tilde{\kappa} \approx 1.0 \cdot 10^3 \cdot \tilde{\kappa}_0$ at fixed average lithium concentration $\bar{n} \approx 0.5$.



(b) Profile of the lithium concentration n for $\tilde{\kappa} \approx 1.0 \cdot 10^3 \cdot \tilde{\kappa}_0$ at $\bar{n} \approx 0.5$.



(c) Profile of the different contributions to the dimensionless diffusion coefficient \tilde{D}^{ch} for $\tilde{\kappa} \approx 2.9 \cdot 10^5 \cdot \tilde{\kappa}_0$ at fixed average lithium concentration $\bar{n} \approx 0.5$.



(d) Profile of the lithium concentration n for $\tilde{\kappa} \approx 2.9 \cdot 10^5 \cdot \tilde{\kappa}_0$ at $\bar{n} \approx 0.5$.

Figure 4.12: Profiles of the dimensionless diffusion coefficients, \tilde{D}^{mf} , \tilde{D}^{gd} and $\tilde{D}^{\text{ch}} = \tilde{D}^{\text{mf}} + \tilde{D}^{\text{gd}}$ and of the lithium concentration at given average lithium concentration $\bar{n} \approx 0.5$ obtained during lithium extraction at $C = 25$ and for two different values of $\tilde{\kappa}$: a relatively small value $\tilde{\kappa} \approx 1.0 \cdot 10^3 \cdot \tilde{\kappa}_0$ and a large value, $\tilde{\kappa} \approx 2.9 \cdot 10^5 \cdot \tilde{\kappa}_0$.

In order to separate the effect of the different flux contributions on the occurrence of phase segregation, we define

$$J_r^{\text{mf}} = -\tilde{D}^{\text{mf}} \frac{\partial n}{\partial r}, \quad (4.10)$$

$$J_r^{\text{gd}} = -\tilde{D}^{\text{gd}} \frac{\partial n}{\partial r}, \quad (4.11)$$

$$J_r^{\text{ch}} = J_r^{\text{mf}} + J_r^{\text{gd}} = -\tilde{D}^{\text{ch}} \frac{\partial n}{\partial r} \quad (4.12)$$

with $\tilde{D}^{\text{ch}} = \tilde{D}^{\text{mf}} + \tilde{D}^{\text{gd}}$,

$$J_r^{\text{cp}} = -\tilde{D}^{\text{cp}} \frac{\partial n}{\partial r}. \quad (4.13)$$

With these notations, the radial component J_r of the total lithium flux, $\mathbf{J} = J_r \mathbf{e}_r$, is equal to

$$J_r = J_r^{\text{ch}} + J_r^{\text{cp}} = -\tilde{D} \frac{\partial n}{\partial r} \quad (4.14)$$

with $\tilde{D} = \tilde{D}^{\text{cp}} + \tilde{D}^{\text{ch}}$.

Note that, at equilibrium, the total lithium flux vanishes. Hence, the analysis of the effect of the different contributions to the total lithium flux on the occurrence of phase segregation has to be done out of equilibrium. We here first neglect the effect of the stress-induced lithium flux and set $J_r^{\text{cp}} = 0$.

Fig. 4.12 shows, for two different $\tilde{\kappa}$ -values, the profile of both \tilde{D}^{mf} and \tilde{D}^{gd} as well as of $\tilde{D}^{\text{ch}} = \tilde{D}^{\text{mf}} + \tilde{D}^{\text{gd}}$ at the particular time when the average lithium concentration $\bar{n} \approx 0.5$ is located in the “spinodal zone” of the mean-field free energy. For the smallest value of $\tilde{\kappa}$, e.g. $\tilde{\kappa} \approx 1.0 \cdot 10^3 \cdot \tilde{\kappa}_0$, the obtained lithium concentration state (Fig. 4.12(b)) is phase-segregated whereas, for the largest value of $\tilde{\kappa}$, e.g. $\tilde{\kappa} \approx 2.9 \cdot 10^5 \cdot \tilde{\kappa}_0$, the obtained lithium concentration state (Fig. 4.12(d)) is almost homogeneous⁴. These $\tilde{\kappa}$ -values have been chosen large enough to ensure that the phase boundary between the low- and large-concentration phases are not too thin, hence preventing from the occurrence of numerical problems.

The dimensionless diffusion coefficient \tilde{D}^{mf} , derived from the mean-field free energy Ψ^{mf} , is at the origin of phase segregation. Indeed, this term given by

$$\tilde{D}^{\text{mf}} = \alpha_2 \frac{T_{\text{ref}}}{T} n(1-n) + 1,$$

according to Eq. (3.80) and the definition of Eq. (4.10), is negative when

$$n(1-n) > -\frac{1}{\alpha_2} \frac{T}{T_{\text{ref}}}.$$

From the theoretical considerations of Sec. 3.2.2, it is clear that the values of n which fulfill this inequality would be located in the unstable “spinodal zone” of the mean-field free energy if the lithium concentration state could be homogeneous over the entire system. In Fig. 4.12(a) as well as in Fig. 4.12(c), it can be shown that, as expected, negative local values of the dimensionless diffusion coefficient \tilde{D}^{mf} solely arises in the region where the phase boundary is built. There, the lithium concentration profile smoothly varies from its low lithium concentration state to its high lithium concentration state and,

⁴The lithium concentration profile shown here does not correspond to an equilibrium state. But it is worth noting that such a state would relax towards a homogeneous state.

consequently, at this place the dimensionless diffusion coefficient \tilde{D}^{mf} exhibits negative values. As seen in Sec. 4.1.2 and as also illustrated in Fig. 4.12(b) - 4.12(d), for large values of $\tilde{\kappa}$, the phase boundary is more extended than for small values of $\tilde{\kappa}$. Thus, the proportion of regions with negative dimensionless diffusion coefficient \tilde{D}^{mf} is more important for $\tilde{\kappa} = 2.9 \cdot 10^5$ than for $\tilde{\kappa} = 1.0 \cdot 10^3$, as it can be seen in a comparison between Fig. 4.12(a) and Fig. 4.12(c).

We then turn to the analysis of the sign of the dimensionless diffusion coefficient \tilde{D}^{gd} equal to

$$\tilde{D}^{\text{gd}} = -\tilde{\kappa}n(1-n) \left(-\frac{2}{r^2} \frac{\partial n}{\partial r} + \frac{1}{r} \frac{\partial^2 n}{\partial r^2} + \frac{\partial^3 n}{\partial r^3} \right) \left(\frac{\partial n}{\partial r} \right)^{-1},$$

according to Eq. (3.81) and to the definition of Eq. (4.11). The analytical study of the sign of \tilde{D}^{gd} is not straightforward. Nevertheless, from this expression, we can conclude that \tilde{D}^{gd} has to vanish in the regions where the lithium concentration gradients vanish, e.g. far away from the phase boundary. The \tilde{D}^{gd} -profiles shown in Fig. 4.12(a) and Fig. 4.12(c) corroborate this assertion. In Sec. 4.1.2, we demonstrate that the interfacial energy term Ψ^{gd} acts to suppress phase segregation because building lithium concentration gradients into the particle adds to the total system free energy Ψ an energetic penalty. Thus it is expected that the dimensionless diffusion coefficient \tilde{D}^{gd} contributes to the suppression of phase segregation. Indeed, the curves of \tilde{D}^{gd} shown in Fig. 4.12(a) and Fig. 4.12(c) exhibit positive values in the region where the phase boundary is built. Note that, towards relaxation, the lithium flux,

$$\mathbf{J}^{\text{gd}} = \underbrace{\tilde{\kappa}n(1-n)}_{>0} \nabla (\Delta n),$$

according to Eq. (3.79) and to Eq. (4.11), acts in order to diminish the curvature of the lithium concentration profile and not to diminish the lithium concentration gradient as it could be intuitively thought at the first glance. For large $\tilde{\kappa}$ -values the phase boundary is more extended than for small $\tilde{\kappa}$ -values, thus the proportion of regions where the dimensionless diffusion coefficient \tilde{D}^{gd} is strictly positive (significantly above zero) is more important for $\tilde{\kappa} = 2.9 \cdot 10^5$ than for $\tilde{\kappa} = 1.0 \cdot 10^3$, as illustrated in Fig. 4.12(a) and in Fig. 4.12(c).

We then consider a nonvanishing stress-induced lithium flux, i.e. $J_r^{\text{cp}} \neq 0$. At this place, we analyze the effect of this flux on the dynamical phase-segregated states. In the dilute solution approach, it was demonstrated that $\tilde{D}^{\text{cp}} > 0$ (see Sec. 2.2.2). We thus concluded that the stress-induced lithium flux enhanced lithium diffusion from the high lithium concentration regions to the low lithium concentration regions. Because, the dimensionless diffusion coefficient \tilde{D}^{cp} has the same expression in phase-field modeling as in the dilute solution model, it is expected that, also in phase-field modeling, the stress-induced lithium flux contributes to the lithium ion homogenization over the particle.

Figs. 4.13(a) - 4.13(c) show at fixed average lithium concentration $\bar{n} \approx 0.5$ located in the “spinodal zone” of the mean-field free energy, the profiles of dimensionless diffusion coefficient \tilde{D}^{cp} for two different Young’s modulus values. For the smallest Young’s modulus value, i.e. $E = 1.0 \cdot E_0$, the lithium concentration state is phase-segregated whereas, for the largest Young’s modulus value, i.e. $E = 5.0 \cdot E_0$, the lithium concentration state is almost homogeneous⁵. As expected, for both values of the Young’s modulus, the dimensionless diffusion coefficient \tilde{D}^{cp} is strictly positive over the entire particle. Such a behavior is consistent with the results obtained using the dilute solution model (see Sec. 2.2.2), but also with the results obtained in Sec. 4.1.3 where we found that the elastic strain energy Ψ^{es} , in case

⁵The lithium concentration profile shown here does not correspond to an equilibrium state. But it is worth noting that such a state would relax towards a homogeneous state.

of phase segregation, always adds to the system free energy Ψ an energetic penalty and thus acts to homogenize the lithium concentration state over the entire particle.

As compared to the case where $J_r^{\text{CP}} = 0$ from Fig. 4.12(a), considering a nonvanishing stress-induced lithium flux, as illustrated in Fig. 4.13(a), diminishes the amplitude of the variation of the dimensionless diffusion coefficient \tilde{D}^{gd} . This is also a possible explanation why the discrepancy between the lithium concentration values reached in the two different phases decreases for nonvanishing stress-induced lithium flux as compared to the case where $J_r^{\text{CP}} = 0$. Note that, within the phase boundary, for $E = 5.0 \cdot E_0$, the total dimensionless diffusion coefficient \tilde{D} becomes significantly positive, whereas, for $E = 1.0 \cdot E_0$, it is almost zero. This may indicate that, for $E = 5.0 \cdot E_0$, the system would relax towards a homogeneous state instead of a phase-segregated state like it would be the case for $E = 1.0 \cdot E_0$ (see Sec. 4.1.3).

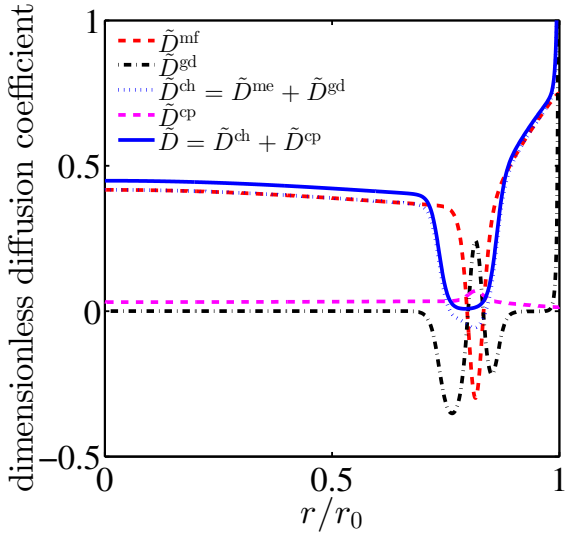
The profiles of the dimensionless diffusion coefficients shown in the previous part of this section all have been obtained during lithium extraction at a relatively large applied flux magnitude ($C = 25$) which presents the advantage of avoiding too small lithium concentration gradients and consequently allows for the numerical evaluation of the different dimensionless diffusion coefficient contributions⁶. Nevertheless, large applied flux magnitudes may override the fact that the total dimensionless coefficient $\tilde{D} = \tilde{D}^{\text{ch}} + \tilde{D}^{\text{cp}}$ has the possibility to become equal to zero, especially at the particular time when the phase boundary separating the two different lithium-concentration phases is about to be built.

Fig. 4.14(a) and Fig. 4.14(c) show, at fixed average lithium concentration $\bar{n} \approx 0.5$, for varying applied flux magnitudes, the profiles of the total dimensionless coefficient \tilde{D} in two different cases regarding the values of α_2 . For $\alpha_2 = -4.2$ and $E = E_0 > E_c(\alpha_2 T_{\text{ref}}/T)$ (see Fig. 4.9 of Sec. 4.1.3), even at low applied flux magnitudes, $\tilde{D} = \tilde{D}^{\text{ch}} + \tilde{D}^{\text{cp}}$ never reaches zero. This suggests that the phase-segregated states are not stable and may explain why the system, instead of relaxing towards a phase-segregated state, will relax towards a homogeneous state.

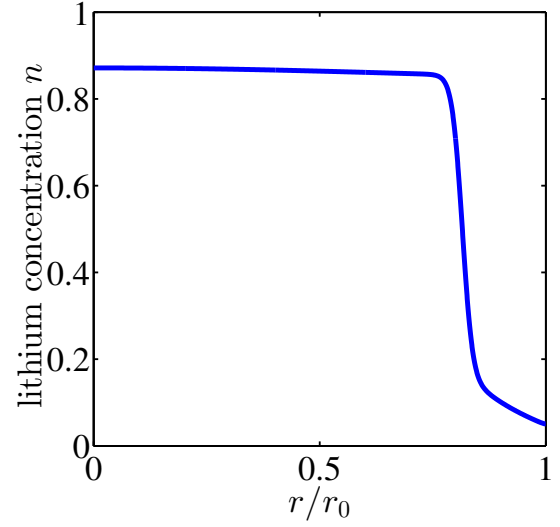
On the contrary, for $\alpha_2 = -5.2$ and $E = E_0 < E_c(\alpha_2 T_{\text{ref}}/T)$ (see Fig. 4.9 of Sec. 4.1.3), at low applied flux magnitude, the dimensionless diffusion coefficient \tilde{D} becomes equal to zero indicating the fact that the phase-segregated states are stable states. The lithium concentration states obtained for $\alpha_2 = -4.2$ reveal under particle unloading at large applied flux magnitudes, phase-segregated-like profiles, as illustrated in Fig. 4.14(b). This behavior is correlated with the minimum of the dimensionless diffusion coefficient \tilde{D} that locally hinders lithium diffusion. Because this minimum is strictly positive, it does not prevent the lithium ions from diffusing from the high lithium concentration regions towards the low lithium concentration regions but only makes this diffusion slower because, at this place, the diffusion coefficient becomes smaller.

Thus, as illustrated in Fig. 4.14(a), at low applied flux magnitudes, this minimum tends to disappear and, as seen in Sec. 4.1.3, in the limit case of equilibrium, the lithium ion distribution is completely homogeneous over the entire particle. Note that, at relatively low applied flux magnitude, the diffusion coefficient \tilde{D} seems to be divergent (see Fig. 4.14(c)). This divergence is obviously not physical and is due to the fact that, at some spatial location, the lithium flux J_r and the lithium concentration gradient $\partial n/\partial r$ are both almost zero which makes the evaluation of the dimensionless diffusion coefficient, equal to the ratio of this two quantities, numerically unstable.

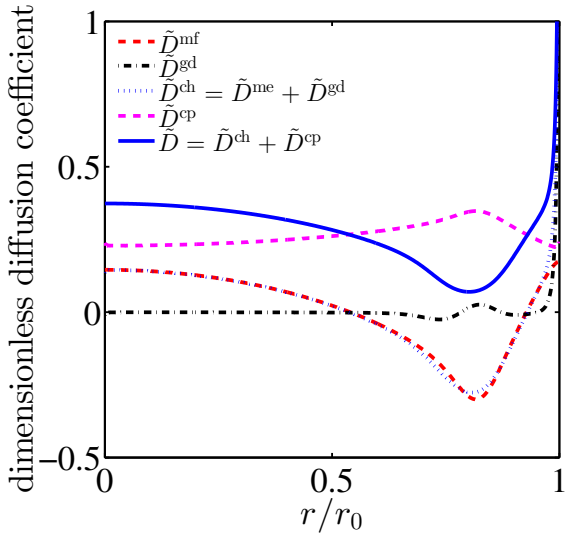
⁶Note that, at this place, the dimensionless diffusion coefficient are numerically evaluated through division of the considered flux contribution by the lithium concentration gradient.



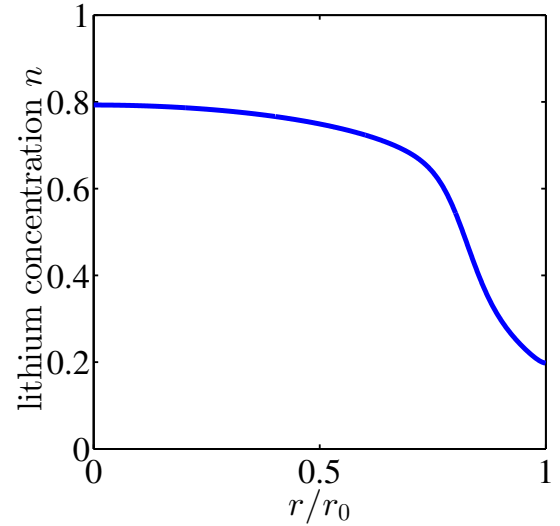
(a) Profile of the the different contributions to the total dimensionless diffusion coefficient \tilde{D} for $E = 1.0 \cdot E_0$ at fixed average lithium concentration $\bar{n} \approx 0.5$.



(b) Profile of the lithium concentration n for $E = 1.0 \cdot E_0$ at $\bar{n} \approx 0.5$.

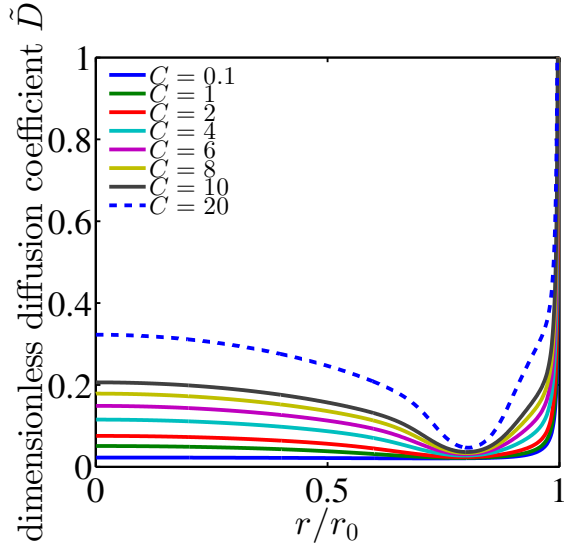


(c) Profile of the the different contributions to the total dimensionless diffusion coefficient \tilde{D} for $E = 5.0 \cdot E_0$ at fixed average lithium concentration $\bar{n} \approx 0.5$.

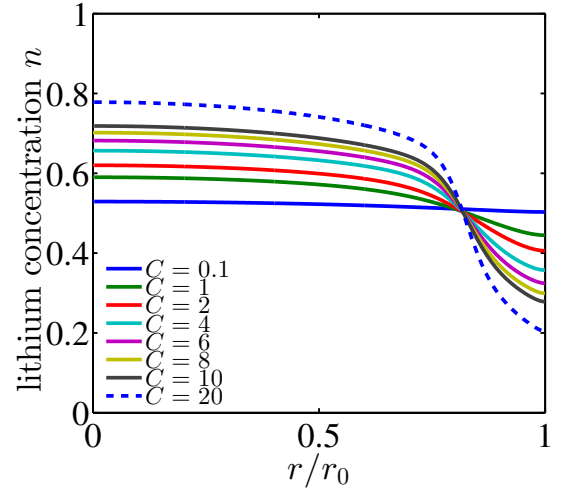


(d) Profile of the lithium concentration n for $E = 5.0 \cdot E_0$ at $\bar{n} \approx 0.5$.

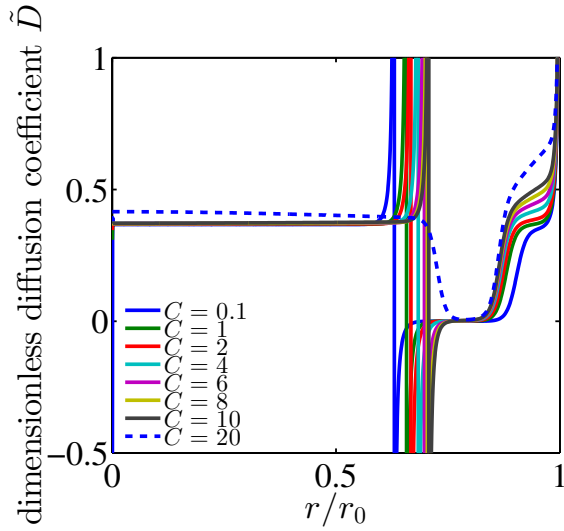
Figure 4.13: Profiles of the dimensionless diffusion coefficients, \tilde{D}^{mf} , \tilde{D}^{gd} , $\tilde{D}^{\text{ch}} = \tilde{D}^{\text{mf}} + \tilde{D}^{\text{gd}}$, \tilde{D}^{cp} , $\tilde{D} = \tilde{D}^{\text{ch}} + \tilde{D}^{\text{cp}}$ and of the lithium concentration n at given average lithium concentration $\bar{n} \approx 0.5$ obtained during lithium extraction at $C = 25$ and for two different values of the Young's modulus: $E = 1.0 \cdot E_0$ and $E = 5.0 \cdot E_0$. The interfacial energy term has been chosen equal to $\tilde{\kappa} \approx 1.0 \cdot 10^3 \cdot \tilde{\kappa}_0$ to enable the occurrence of phase segregation from the “chemical point of view”.



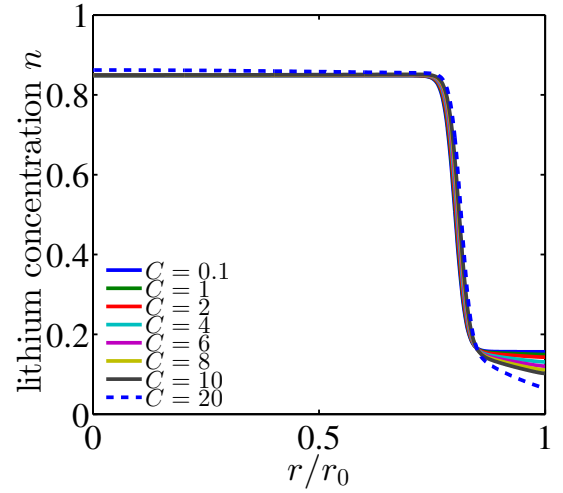
(a) Profiles of the dimensionless diffusion coefficient \tilde{D} at given average lithium concentration $\bar{n} \approx 0.5$ for $\alpha_2 = -4.2$.



(b) Lithium concentration profiles n at given average lithium concentration $\bar{n} \approx 0.5$ for $\alpha_2 = -4.2$.



(c) Profiles of the dimensionless diffusion coefficient \tilde{D} at given average lithium concentration $\bar{n} \approx 0.5$ for $\alpha_2 = -5.2$.



(d) Lithium concentration profiles n at given average lithium concentration $\bar{n} \approx 0.5$ for $\alpha_2 = -5.2$.

Figure 4.14: Profiles of the dimensionless diffusion coefficient \tilde{D} and of the lithium concentration n at given average lithium concentration $\bar{n} \approx 0.5$ for two different values of α_2 , $\alpha_2 = -4.2$ and $\alpha_2 = -5.2$. These profiles are shown for varying applied flux magnitude corresponding to different C -rates.

4.2.2 Effect of the phase segregation on the stresses

In Sec. 2.2.2 we analyze, in the dilute solution approach, the effect of a nonvanishing stress-induced lithium flux, $J_r^{\text{CP}} \neq 0$, on both the lithium concentration and hydrostatic stress profiles. The same study was performed in Sec. 4.1.3 regarding the equilibrium states obtained using the phase-field model. As compared to the case where this flux is neglected, $J_r^{\text{CP}} = 0$, we found that the stress-induced lithium flux enhances the lithium diffusion from the high lithium concentration regions to the low lithium concentration regions and thus acts “against” phase-segregation.

The consideration of this flux may also influence the phase-segregated states obtained under dynamical particle unloading, as illustrated in Fig. 4.15.

In Fig. 4.15(a), we observe that the discrepancy between the high-concentration phase in the particle core and the low-concentration phase in the outer shell of the particle is lower in the case where $J_r^{\text{CP}} \neq 0$ than in the case where $J_r^{\text{CP}} = 0$. We further note that the high-concentration phase located in the particle core does not feel the effect of the lithium flux applied at the particle surface, on the contrary to the low-concentration phase which is located in the outer shell of the particle and is more influenced by the applied lithium flux. Indeed, while the lithium concentration is almost homogeneous in the high-concentration phase, it exhibits a nonnegligible gradient in the low-concentration phase. At this place, we remark that the nonzero applied lithium flux at the particle surface contributes to move the phase boundary towards the particle center.

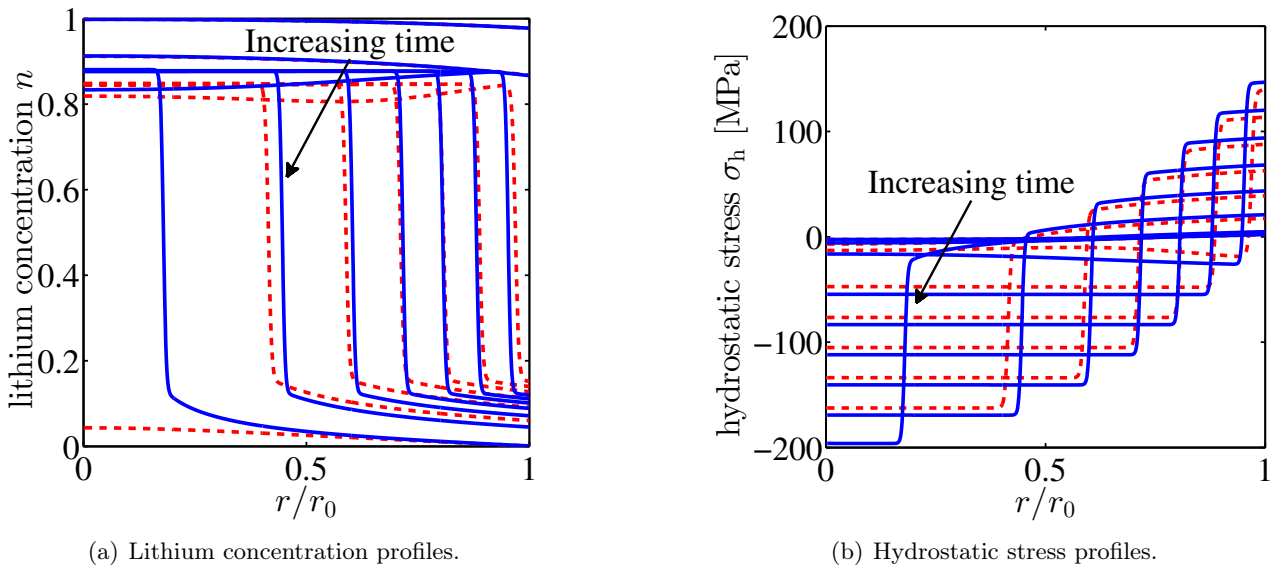


Figure 4.15: Profiles of the lithium concentration n and of the hydrostatic stress σ_h obtained during lithium extraction at $C = 3.8$. The solid blue lines and the dashed red lines have been obtained using a phase-field model ($\alpha_2 = -5.2$) with $J_r^{\text{CP}} = 0$ and $J_r^{\text{CP}} \neq 0$, respectively.

Regarding the hydrostatic stresses, shown in Fig. 4.15(b), it is not surprising to observe that they are more elevated when $J_r^{\text{CP}} = 0$ than in case of a nonvanishing stress-induced lithium flux, $J_r^{\text{CP}} \neq 0$. We also demonstrate in Fig. 4.16 that, independently of the applied flux magnitude, the maximum of the hydrostatic stress magnitude obtained during both lithium extraction and insertion is always higher when the stress-induced lithium flux is zero than when it is different from zero. Note that, for these

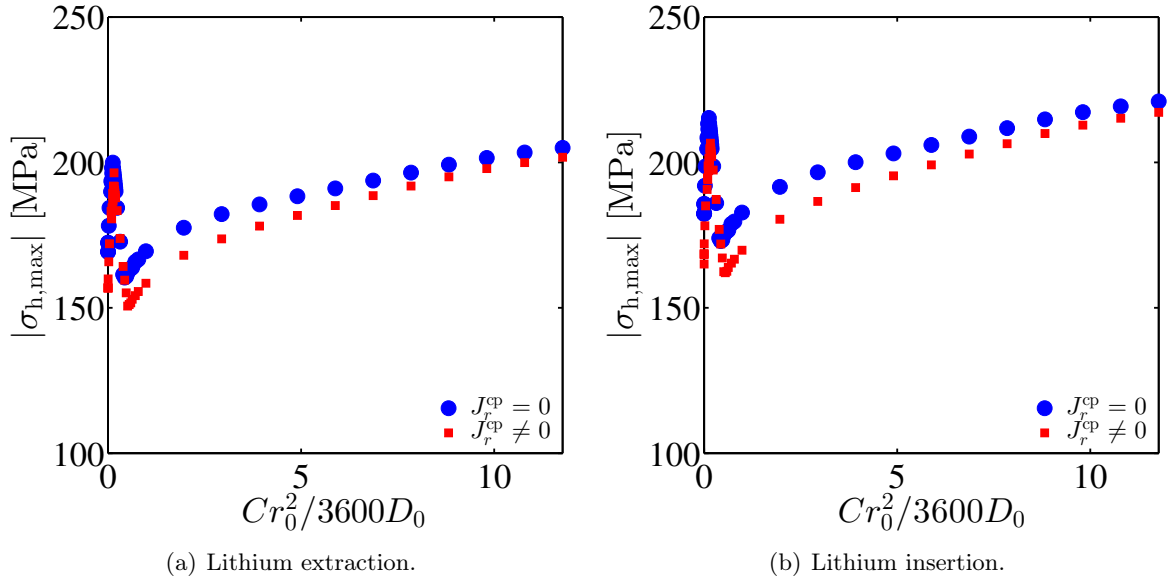
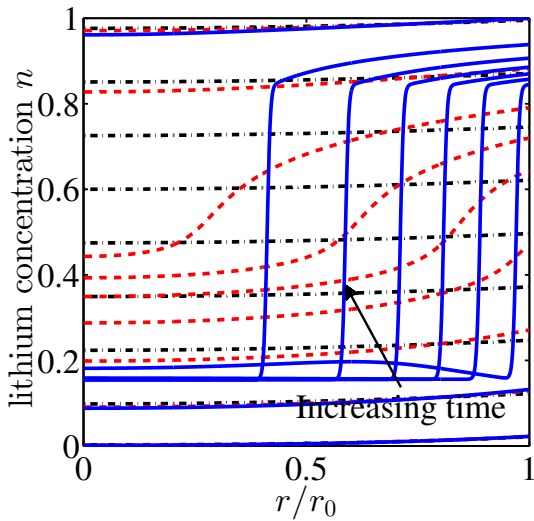


Figure 4.16: Maximum values of the hydrostatic stress magnitude reached during lithium extraction and insertion as a function of the ratio $Cr_0^2/3600D_0$ at given particle radius $r_0 = 1 \mu\text{m}$. These curves have been obtained using the phase-field model with fixed interaction term $\alpha_2 = -5.2$. For $J_r^{\text{cp}} = 0$, the obtained hydrostatic stress magnitudes are larger than for $J_r^{\text{cp}} \neq 0$.

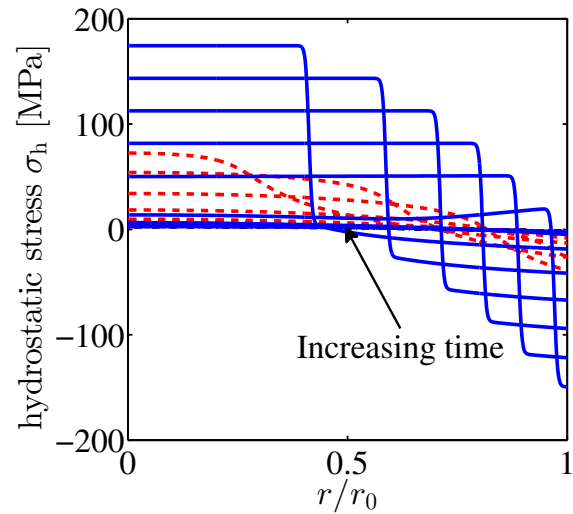
two cases, the behavior of the hydrostatic stress maximum is qualitatively the same. The analysis of this behavior in dependency of the applied flux magnitude follows at the end of this section.

In Sec. 4.1.3, we demonstrate that, at given $\tilde{\kappa}$ -value, the occurrence of equilibrium phase-segregated states strongly depends on the Young's modulus E of the host material as well as on the term α_2 representing the strength of the attractive interaction between two nearest-neighboring lithium ions. At given Young's modulus $E = E_0$, we show that, for $\alpha_2 = -5.2$, $E_c(\alpha_2 T/T_{\text{ref}}) > E_0$ whereas, for $\alpha_2 = -4.2$, $E_c(\alpha_2 T/T_{\text{ref}}) < E_0$. Thus, for $\alpha_2 = -5.2$, there exist equilibrium (stable) phase-segregated states, whereas, for $\alpha_2 = -4.2$, the equilibrium (stable) system states all are homogeneous. Nevertheless, in Sec. 4.2.1, for $\alpha_2 = -4.2$, phase-segregated-like states could be exhibited. These states were obtained during dynamical particle unloading at relatively large applied flux magnitude. Their lithium concentration profiles present a gradient significantly different from zero. Hence such phase-segregated-like states may also give rise to large stresses within the particle. In Fig. 4.17, we show, for $\alpha_2 = -5.2$ as well as for $\alpha_2 = -4.2$, the profiles of the lithium concentration n and of hydrostatic stress σ_h obtained during both lithium insertion and extraction at constant applied flux magnitude, $C = 3.8$. For comparison, the results obtained by means of the dilute solution model also are shown.

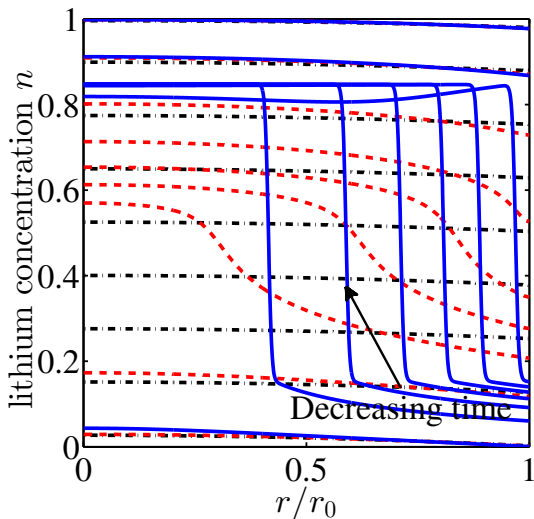
As expected, far away from the nucleation and spinodal zones of the mean-field free energy when $\bar{n} \ll 1$ or $1 - \bar{n} \ll 1$, both the lithium concentration and hydrostatic stress profiles obtained using the phase-field model show a good agreement with those obtained by means of the dilute solution model. However, in the spinodal zone and even in the nucleation zone, these profiles exhibit significant discrepancies depending on the considered model.



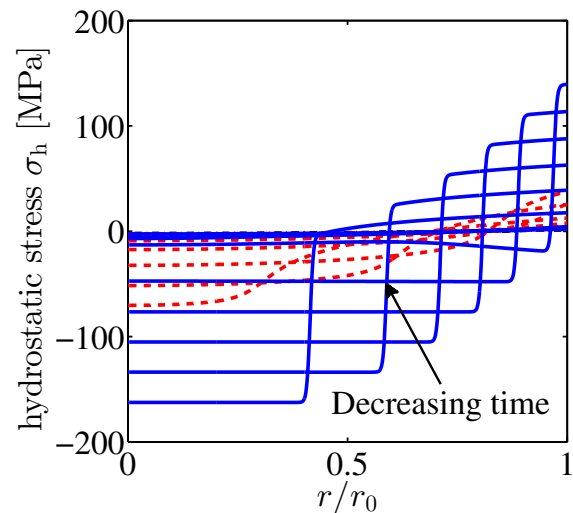
(a) Lithium concentration profiles obtained during lithium insertion.



(b) Hydrostatic stress profiles obtained during lithium insertion.



(c) Lithium concentration profiles obtained during lithium extraction.



(d) Hydrostatic stress profiles obtained during lithium extraction.

Figure 4.17: Profiles of the lithium concentration n and of the hydrostatic stress σ_h obtained during both lithium insertion and extraction at $C = 3.8$ at fixed particle radius $r_0 = 1 \mu\text{m}$. The solid blue lines and the dashed red lines are related to the phase-field model with $\alpha_2 = -5.2$ and $\alpha_2 = -4.2$, respectively. The dash-dotted black lines correspond to the dilute solution model. Compared to the hydrostatic stresses reached in phase-field modeling, the hydrostatic stresses reached in the dilute solution model, are very low. Thus their representations are overlapped by the curves belonging to the homogeneous states obtained using the phase-field model.

In the dilute solution approach, it has been demonstrated in Sec. 2.2.2 that only large applied flux magnitudes, i.e. $Cr_0^2/3600D_0 > 8.8$, which drive the system significantly far away from equilibrium, give rise to large concentration gradients and consequently, to large stress magnitudes. The curves shown in Fig. 4.17 all have been obtained at given C -rate, $C = 3.8$. For the considered particle radius, $r_0 = 1 \mu\text{m}$, the ratio $Cr_0^2/3600D_0 \approx 0.15 \ll 8.8$. In that case, both the flux driven by gradient in the chemical potential and the stress-induced lithium flux act in the same direction rapidly enough to homogenize the lithium ion distribution within the particle. Thus, the lithium concentration profiles do not present large concentration gradients and, consequently, the hydrostatic stress profiles exhibit relatively low magnitude values.

In contrast to the dilute solution model, it was shown in the previous section (Sec. 4.2.1) that the phase-field model with $\alpha_2 = -4.2$ exhibits, under dynamical particle loading and unloading at relatively large applied flux magnitude, phase-segregated-like lithium concentration states. Such a behavior was linked to the minimum of the dimensionless diffusion coefficient \tilde{D} which locally slows down the lithium ion diffusion from the high to the low lithium concentration regions. Near to this minimum, the gradient in the lithium concentration becomes maximal which explains the fact that the hydrostatic stress magnitudes reach larger values than those obtained by means of the dilute solution model.

Finally, as expected from the computation of the equilibrium states the lithium concentration profiles obtained using the phase-field model with $\alpha_2 = -5.2$, exhibit phase segregation since the average lithium concentration attains the nucleation and spinodal zones of the mean-field free energy. In these zones, the lithium concentration gradients, higher than in the two other models, give rise to much larger stress magnitudes than those obtained using the dilute solution model and the phase-field model with $\alpha_2 = -4.2$, respectively. Due to the α_2 -value, the dimensionless diffusion coefficient \tilde{D} may vanish when, at least, the spinodal zone of the mean-field free energy is reached, and consequently always drives the system in phase-segregated states even at equilibrium, on the contrary to the phase-field model with $\alpha_2 = -4.2$. For this reason, as also illustrated in Fig. 4.18, even at low applied flux magnitudes, the stress magnitudes present values that are significantly larger than those obtained using the dilute solution model and the phase-field model with $\alpha_2 = -4.2$, respectively.

Fig. 4.18 shows, during both lithium extraction and insertion, for the two different phase-field models ($\alpha_2 = -4.2$ and $\alpha_2 = -5.2$) as well as for the dilute solution model, the maximum hydrostatic stress magnitude reached at some position in the cathodic particle during lithium extraction versus the ratio $Cr_0^2/3600D_0$. These curves have been computed for two different particle radii and when varying the applied flux magnitude corresponding to a given C -rate. Like for the dilute solution model, the maximum value of the hydrostatic stress magnitude is a function of the ratio $Cr_0^2/3600D_0$ only⁷. Both phase-field models exhibit three different regimes.

In the first one, referred to as regimes ① and ①', respectively, depending on the considered phase-field model, the applied flux magnitude is low and the maximum value of the hydrostatic stress magnitude grows when increasing the applied C -rate. In this regime, the maximum hydrostatic stress magnitude is reached, for both phase-field models, at the particle center at the end of the phase segregation just before the system transforms back to the homogeneous state.

In the second regime, denoted by regimes ② and ②', respectively, the increase of the product Cr_0^2 in comparison with the diffusion coefficient D_0 induces, during lithium extraction from the particle, the complete lithium depletion near the surface of the particle before the system has arrived back at the

⁷This is true provided that the interfacial energy contributes to the total system free energy as a negligible quantity compared to the other energetic contributions.

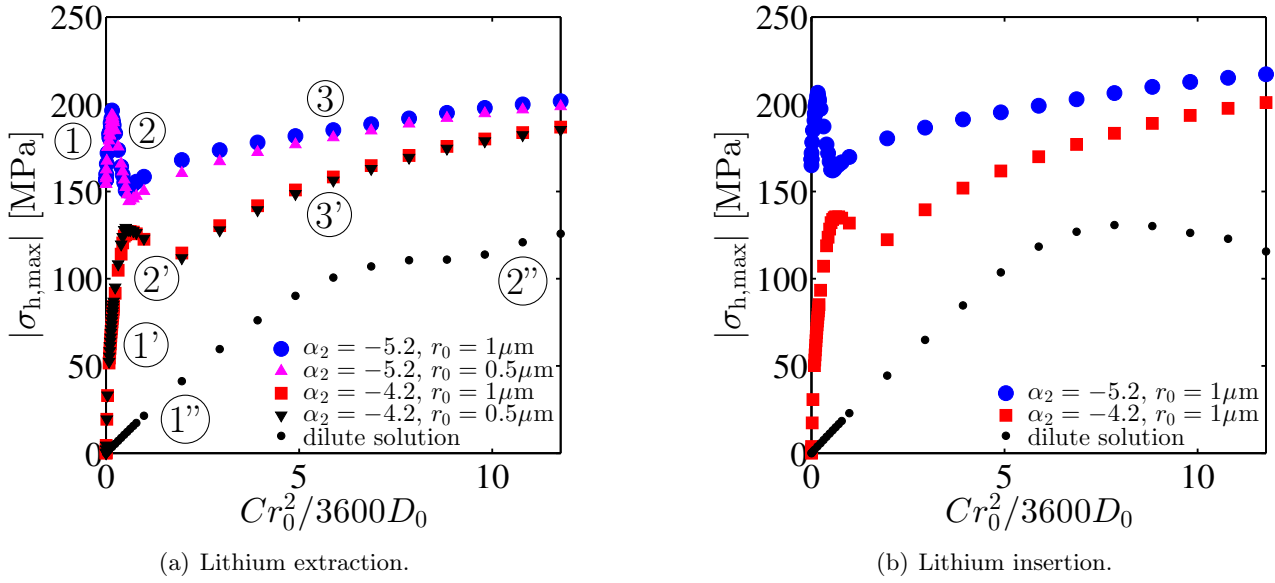


Figure 4.18: Comparison of the maximum values of the hydrostatic stress magnitude reached during both lithium extraction and insertion as a function of the ratio $Cr_0^2/3600D_0$ for two different particle radii. The curves shown here are related to both the dilute solution model and to the phase-field model ($\alpha_2 = -5.2$ and $\alpha_2 = -4.2$).

homogeneous state and the maximum value of the hydrostatic stress is attained at the time when the stop condition⁸ is reached at the particle surface.

Finally, in the last regimes referred to as (3) and (3'), respectively, at high applied flux magnitudes, the maximum value of the hydrostatic stress is not attained at the particle center like in the two other regimes, but at the surface of the particle, just after the phase segregation happened. Indeed, during lithium extraction, near the particle surface, due to the phase segregation, as well as to the large applied C -rate, the lithium concentration reaches its minimum allowed value before the high-concentration phase has been formed in the core of the particle. As a consequence, concentration and, thus, stresses in the core have not changed much compared to before phase segregation was initiated. The system state is so that the particle core made of high-concentration phase is in mechanical equilibrium with a very thin shell made of low-concentration phase located near the particle boundary. Thus, in the core, the arising stresses, spatially better distributed than in the shell, are lower than in the shell.

4.2.3 Coupling with the dualfoil model

Similarly to Sec. 2.3.1, instead of considering one single cathodic particle entirely decoupled from the battery, we now consider an assembly of spherical particles that represent the cathodic material. These particles couple with each other via the flux holding at their surface whose component normal to the particle surface satisfies the Butler-Volmer relation, Eq. (2.73).

But, differently from the dualfoil model introduced in Sec. 2.3.1 where the lithium diffusion into the anodic and cathodic particles is described by means of the dilute solution theory, the cathodic particles

⁸The stop condition is fulfilled when $n|_{r=r_0} = 0$, according to Eq. (2.21).

here possibly undergo phase segregation.

Nonconstant lithium flux at the cathodic particle surface

Fig. 4.19 shows the time-dependent lithium flux magnitude that enters three particles located at different positions in the cathode, as well as their constant values averaged over time.

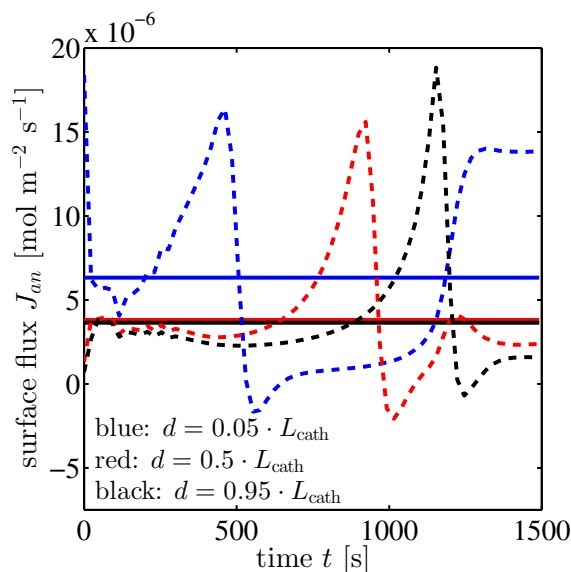


Figure 4.19: Surface flux over time during battery discharging ($C = 2$) at three different spatial locations: near the separator (blue curves), at the middle of the cathode (red curves) and close to the current collector (black curves). The parameter d refers to the distance of the considered cathodic particle to the separator region expressed relatively to the cathode dimension $L_{\text{cath}} = 183 \mu\text{m}$. The dashed and solid lines respectively are the time-dependent normal flux J_{an} at the particle surface and its value averaged over time.

The time-dependent flux magnitudes holding at the surface of these particles are similar in that they all exhibit a peak that however occurs at different times depending on the particle locations. This peak first concerns the particle near to the separator region, then the particle in the middle of the cathode and, finally, the particle close to the current collector at the interface between the cathode and the external circuit. When the flux magnitude peak arises, it can be shown that the cathodic particle starts the phase segregation. The lithium flux magnitude peak is followed by a minimum where the lithium flux at the particle surface becomes, during a short time, negative. It means that just after phase segregation has begun within a particle, lithium ions are released from the particle. This flux then slowly decreases to stabilize around a small but positive value indicating that lithium ions are inserted again into the particle.

This result may be explained by the Butler-Volmer relation that governs the lithium flux holding at

the particle surface,

$$\begin{aligned}
 J_{an} &= -\mathbf{J}_a \cdot \mathbf{n} = -J_0 \left(\exp\left(\frac{e\eta}{2k_B T}\right) - \exp\left(-\frac{e\eta}{2k_B T}\right) \right) \\
 &\approx -J_0 \left(\frac{e\eta}{k_B T} \right) \text{ if } \frac{e\eta}{2k_B T} \ll 1 \text{ (fulfilled in our model),}
 \end{aligned} \tag{4.15}$$

which further implies that the lithium flux magnitude at the particle surface is determined by the product of the exchange flux magnitude J_0 and of the overpotential η .

Fig. 4.20 shows, over time, the variation of these two quantities for different cathodic particles. From

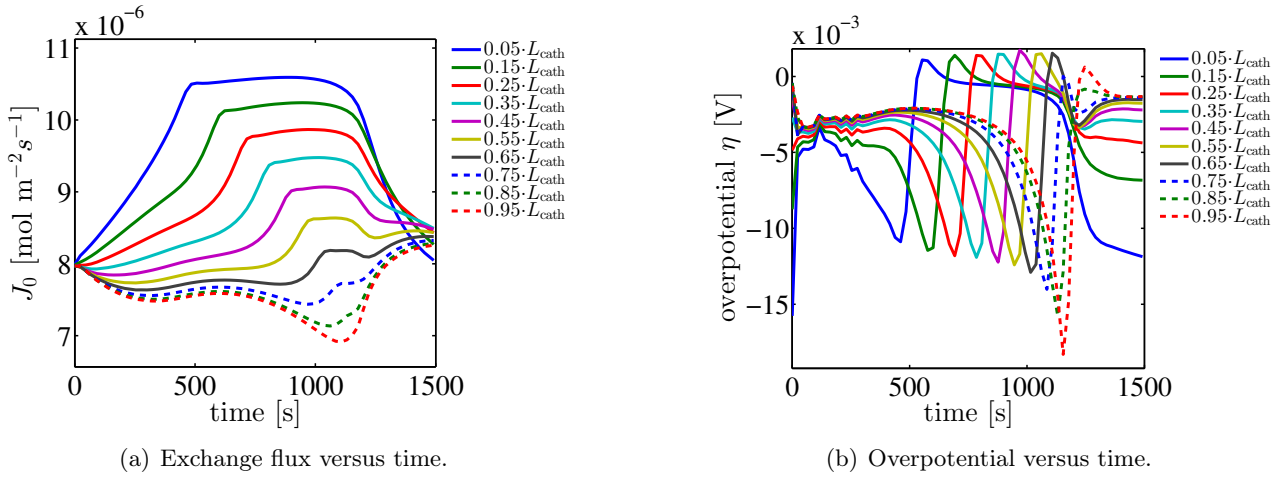


Figure 4.20: Exchange flux J_0 and overpotential η over time at different spatial locations in the cathode during battery discharging at $C = 2$. The negative of the overpotential, $-\eta$, exhibits the same variation as the flux J_{an} holding at the particle surface, see Fig. 4.19 for comparison.

these curves, it appears that the behavior of the lithium flux J_{an} holding at the particle surface is governed by the overpotential η , defined as

$$\eta = \phi_s - \phi_l - E_{\text{oc,cath}}, \tag{4.16}$$

according to Eq. (2.74). Indeed, as seen by comparing Fig. 4.20(b) to Fig. 4.19, the negative of the overpotential, $-\eta$, exhibits the same profile as the lithium flux magnitude J_{an} .

Before the beginning of phase segregation in a given particle at the cathode, the overpotential $\eta < 0$ at the cathode exhibits a decrease. Once phase segregation has been initiated, the overpotential rapidly increases to become (anomalously) positive. It finally decreases and becomes almost constant equal to a small negative value.

The understanding of the time-dependent behavior of η is complicated. In correlation with the formation of a phase-segregated state within a given cathodic particle, the voltage ϕ_s obtained in the solid phase of the cathode, as we shall see in the following, drastically diminishes. It may be due to the fact that, for the macroscopic battery model, the relevant microscopic quantity is the lithium

concentration at the surface of the particles⁹. During battery discharging, the phase-segregated state is such that the cathodic particle outer shell is made of high-concentration phase. At the macroscopic battery scale, such a state is analogous to a homogeneous high-lithium-concentration state. Thus, the voltage holding there has the same value as the one corresponding to a particle with homogeneous lithium concentration equal to the value of the lithium concentration holding in the high-concentration phase. In that sense, at the macroscopic battery scale, the cathodic particle seems to contain more lithium than it contains in reality.

This may qualitatively explain why the voltage ϕ_s significantly drops just after the initialization of phase segregation within the cathodic particles but it does not completely account for the sudden increase of the overpotential η occurring at the same time. Let us, at this place, remark that the system is at equilibrium if, at the surface of each particle, $\eta = 0$ is satisfied. Once this relation is fulfilled, the system remains in the corresponding state. According to Eq. (4.16), this equilibrium condition indicates that the voltage ϕ_s in the solid phase will follow the same behavior as the sum of the voltage ϕ_l in the liquid phase and the open-circuit voltage $E_{oc,cath}$ that depends on the lithium concentration at the particle surface. One can see in Fig. 2.10(b) that the open-circuit voltage $E_{oc,cath}$ at the cathode exhibits a sudden drop when the lithium state of charge, also equal to the lithium concentration at the particle surface, $x \approx 0.5$. Once phase segregation is initiated within a given particle, the lithium concentration at its surface rapidly increases. When the surface concentration $n_s \approx 0.5$, the open-circuit voltage $E_{oc,cath}$ strongly drops. In order to reestablish a situation as near as possible to the “equilibrium” situation of the system, the voltages in both the solid and liquid phases are modified such that this drop becomes compensated. The response of the system however occurs with a certain delay during which the overpotential η is governed by the negative of the open-circuit voltage $-E_{oc,cath}$. This may explain why the overpotential η strongly increases. After this delay, the voltage ϕ_s in the solid phase has significantly dropped and the overpotential η becomes negative again.

We finally analyze the effect of a realistic time-dependent flux applied at the surface of a single particle, as compared to the case of a constant applied flux. Fig. 4.21 shows both the lithium concentration and hydrostatic stress profiles within a spherical cathodic particle located in the middle of the cathode where, on the one hand, the time-dependent lithium flux magnitude (dashed red lines of Fig. 4.21) holds at its surface, and, on the other hand, an averaged constant flux magnitude (solid blue lines of Fig. 4.21) is applied there. A comparison between these two cases has demonstrated (not shown here) that, once the lithium concentration, due to the initialization of the phase segregation, reaches at the particle surface $n_s \approx 0.5$, the possibility to insert lithium ions into the cathodic particle becomes very limited. Due to the Butler-Volmer relation, the time-dependent flux holding at the particle surface rapidly decreases to become almost zero allowing for the formation of a quasi-equilibrium phase-segregated state in the single cathodic particle.

As a consequence and differently from the dualfoil model based on the dilute solution theory for the lithium ion diffusion into the single cathodic particles, as seen in Fig. 4.21(b), the hydrostatic stress magnitudes reached, during the battery discharging, in a single particle embedded in the cathode, becomes not as elevated as those attained when applying the constant average flux magnitude at the particle surface.

⁹The sole microscopic quantity that explicitly appears in the macroscopic model is the lithium concentration at the surface of the particle. This quantity enters in the macroscopic model via both the open-circuit voltage E_{oc} and the exchange flux J_0 , see Eq. (2.75) and Fig. 2.10 of Sec. 2.3.1.

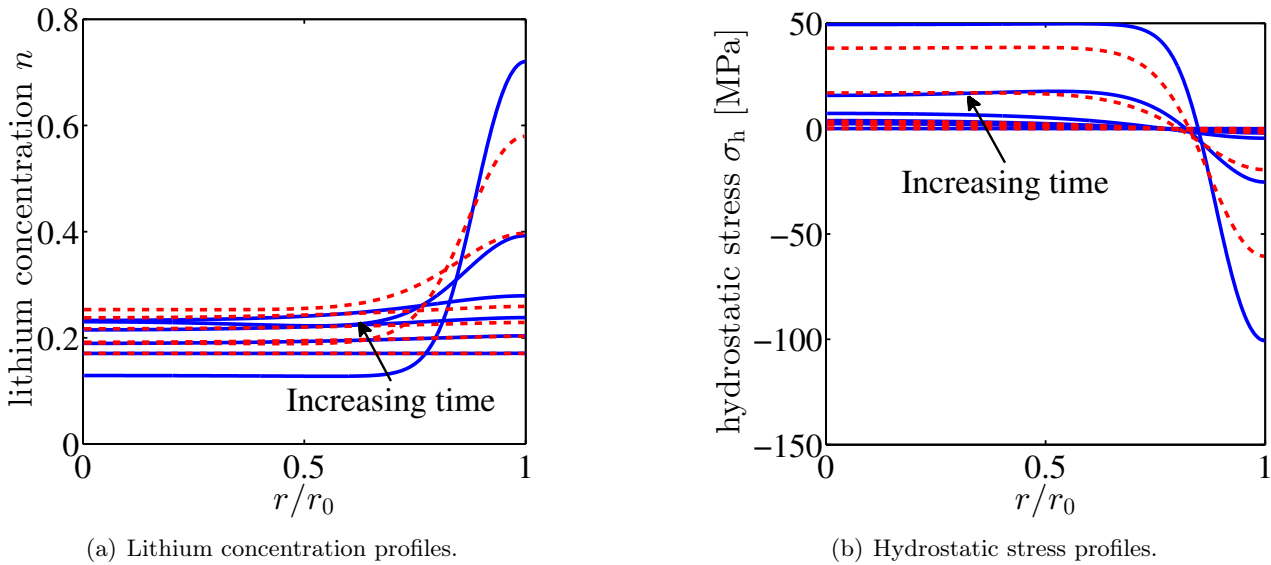


Figure 4.21: *Lithium concentration and hydrostatic stress profiles within a cathodic particle located in the middle of the cathode ($d = 0.5 \cdot L_{\text{cath}}$) during battery discharging at $C = 2$. The dashed red lines correspond to the case where a time-dependent flux, obtained through the Butler-Volmer relation Eq. (2.73) by means of the dualfoil model, holds at the single particle surface. On the contrary, the solid blue lines are obtained by application of a constant lithium flux at the particle surface corresponding to the average value of the time-dependent lithium flux.*

Many-particle states

As illustrated in Fig. 4.19, during battery discharging, once a cathodic particle has undergone phase segregation, the flux magnitude at its surface rapidly decreases to increase at the surface of a neighboring particle located closer to the current collector and so on until all cathodic particles have undergone the phase segregation.

Thus, combined with the Butler-Volmer relation as flux boundary condition for the single particles, using the phase-field model to describe the lithium ion diffusion into the cathodic particles leads to a behavior where the phase segregation is successively initiated in all these particles. Such a many-particle behavior is however at the opposite of the behavior reported in Ref. [120] where a conservation law of Fokker-Planck type is used to describe the time-evolution of the granular cathode. This aspect of the model response needs further investigations.

We then conclude that, due to the Butler-Volmer relation, the lithium insertion into particles that already exhibit a phase-segregated state is hindered once particles still exist in the cathode that have not undergone phase segregation. Consequently, as shown in Fig. 4.22, after all the cathodic particles have reached a phase-segregated state, they may relax towards the same equilibrium phase-segregated state. This many-particle equilibrium state is rather different from the equilibrium cathodic state obtained using the dilute solution model to describe the lithium intercalation into the single cathodic particles where, at the end of the battery discharge, different homogeneous single particle states are reached as illustrated in Fig. 2.17(c) of Sec. 2.3.3.

Further, the analysis of the Butler-Volmer relation previously done in this section has shown that the

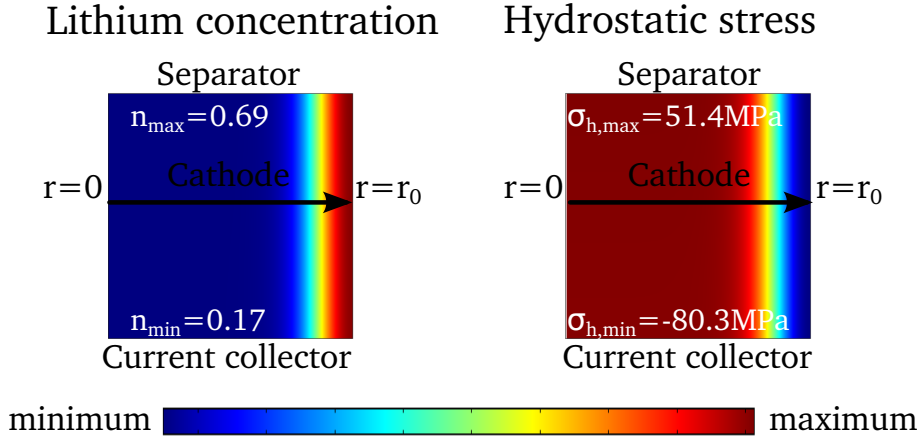


Figure 4.22: *Lithium concentration and hydrostatic stresses profiles in the cathode at the end of the relaxation time when the cathodic state of charge $x \approx 0.35$. The many-particle state shown here has been obtained during the battery discharging process at $C = 1$.*

occurrence of phase segregation is correlated with a drop of the overpotential η which was suggested to be induced by the decrease of the voltage ϕ_s at the cathode. This is confirmed by Fig. 4.23 which shows the time-dependent battery voltage (see Fig. 4.23(a))— equal to the voltage ϕ_s at the interface between the cathode and the current collector¹⁰— as well as the equilibrium battery voltage also referred to as open-circuit voltage (see Fig. 4.23(b)).

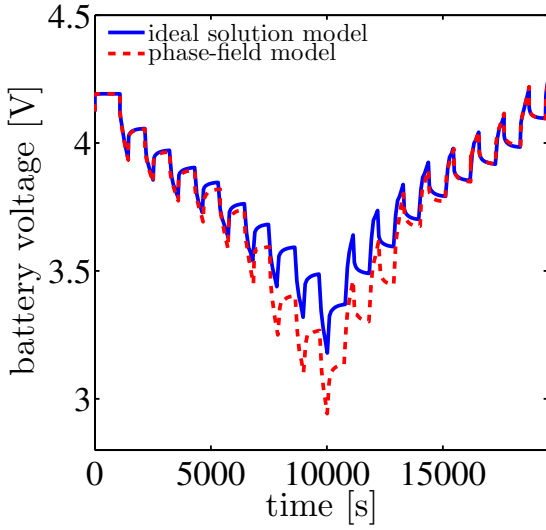
4.3 Concentration-dependent material parameters

4.3.1 Motivation

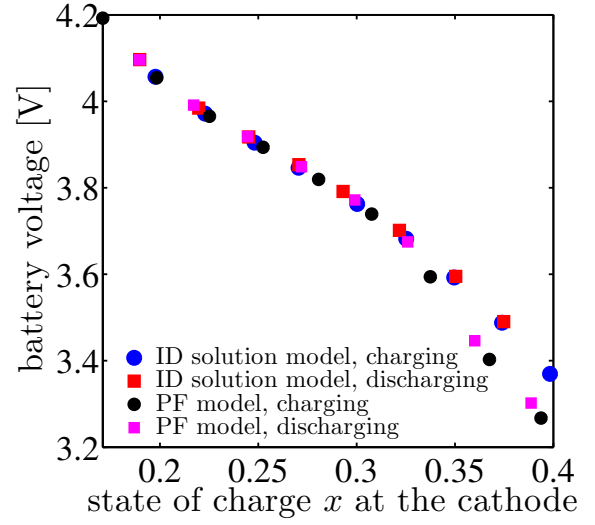
Until now, it has been assumed that intercalating lithium ions into the host material does not have any influence on the material parameters related to the host crystalline structure. Indeed, in all previous simulations, not only the dimensionless partial volume $\tilde{\Omega}$ has been considered as a material constant equal to $\tilde{\Omega}_0$, according to Eq. (2.20) of Sec. 2.2.1, but also the Young’s modulus E_0 and the Poisson ratio ν .

Indeed, in Sec. 3.1.2, we pointed out that the lithium ions were treated as guest species that do not induce drastic modifications of the host crystalline structure. Using this assumption, it was possible to treat the deformations of the host material— here, solely induced by the variation in the lithium amount— in a perturbative manner, e.g. using the linear elasticity theory. In the context of small elastic lithium-induced deformations, we assumed that the host material parameters remain unchanged under lithium insertion and extraction. Nevertheless, in order to account for a coupling between the intercalated lithium ions and the host material, a constant dimensionless partial volume $\tilde{\Omega}_0$ was introduced allowing for a linear volumetric expansion or contraction with varying lithium amount in the host material. Further, all other host material parameters, being the Young’s modulus E_0 and the Poisson ratio ν , were assumed to be independent of the lithium concentration n .

¹⁰According to Eq. (2.76), the electronic potential ϕ_s is set equal to zero at the interface between the anode and the current collector. Note that the electronic diffusion in the electrodes is very fast as compared to the lithium ion diffusion within both the electrolyte and the electrode particles. As a consequence the electronic potential ϕ_s exhibits a very weak spatial dependence.



(a) Battery voltage over time during one cycle of battery charging and discharging ($C = 1$) with hold times during which the current delivered by the battery is set equals zero in order to enable the system relaxation.



(b) Battery voltage versus the cathodic state of charge x at equilibrium during both battery discharging and charging ($C = 1$).

Figure 4.23: *Transient and equilibrium battery voltages obtained during both battery discharging and charging. In the dilute solution model, lithium diffusion in the particle is modeled by the usual Fick's law whereas, in the phase-field model with mechanics, lithium diffusion is described by a flux derived from the free energy functional represented by Eq. (3.44).*

However, both ab-initio calculations [121] and experimental measurements [90, 122] demonstrate that these parameters (except for the Poisson ratio whose variation in dependency with the lithium ion concentration is not known) are slightly dependent on the lithium amount. In this part, based on the free energy functional formalism developed in Sec. 3.3.3, we will account for this dependence. In the next, the concentration-dependent dimensionless partial volume and Young's modulus are referred to as $\tilde{\Omega}[n]$ and $E[n]$, respectively.

Concentration-dependent dimensionless partial volume

At this place, based on theoretical calculations [74] as well as on experimental measurements [52], the functional $\tilde{\Omega}[n]$, describing the dependence of the dimensionless partial volume with the lithium amount in the host material, will be specified.

According to Eq. (2.19) of Sec. 2.2.1, the relationship between the dimensionless partial volume and the concentration-dependent lattice parameter referred to as $a[n]$ reads

$$\tilde{\Omega}[n] = \frac{1}{a_0^3} \frac{\partial a^3[n]}{\partial n}. \quad (4.17)$$

When the volume of the sublattice unit cell available for *one* lithium ion, denoted by $a^3[n]$, linearly expands with the lithium concentration n , the dimensionless partial volume is constant equal to $\tilde{\Omega}_0$ and

fulfills Eq. (2.20) of Sec. 2.2.1. It means that the concentration-dependent term of the lattice parameter is proportional to $\sqrt[3]{n}$. Indeed, for $\tilde{\Omega} = \tilde{\Omega}_0$, we insert Eq. (2.20) into Eq. (2.19) and obtain for the lattice parameter,

$$a_{\text{cst}}[n] = \sqrt[3]{a_i^3 + \left(\frac{a_f^3 - a_i^3}{n_f - n_i}\right)(n - n_i)}.$$

But experimental measurements [52] demonstrate that the lattice parameter expressed as a function of the lithium concentration n is rather given by

$$a_{\text{fit}}[n] = \frac{1}{2} \left(8.158435 + 0.033912 \tanh [7.5434(n - 0.42606)] \right. \\ \left. + 0.061423 \tanh [3.1809(n - 0.78435)] \right), \quad (4.18)$$

according to Ref. [31] where a fit of these experimental measurements¹¹ was realized.

In our model, rather than assuming the dependence represented by Eq. (4.18), we assume in a first step that the lattice parameter $a[n]$ linearly depends on the lithium concentration n and fit this dependence to the experimentally measured values at $n_i = 0.2$ and $n_f = 0.995$ — $a_i = 4.0341 \text{ \AA}$ and $a_f = 4.1141 \text{ \AA}$, according to the values reported in Tab. 2.1. It then formally holds

$$a[n] = \left(\frac{a_f - a_i}{n_f - n_i}\right)(n - n_i) + a_i. \quad (4.19)$$

From this expression, it obviously appears that the volume of the unit cell where the lithium ions can sit, $a^3[n]$, is cubic with respect to the lithium concentration n . Then, according to Eq. (4.17), the dimensionless partial volume, $\tilde{\Omega}[n]$, becomes quadratic in n . Inserting Eq. (4.19) into Eq. (4.17), we obtain

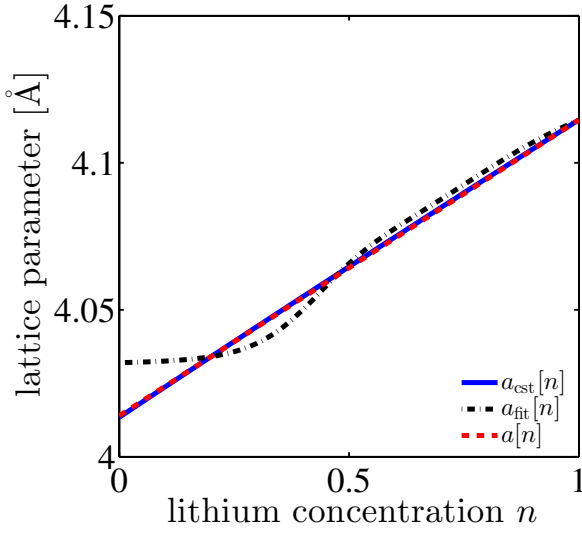
$$\tilde{\Omega}[n] = \frac{3}{a_0^3} \left(\frac{a_f - a_i}{n_f - n_i}\right) \left(\left(\frac{a_f - a_i}{n_f - n_i}\right)(n - n_i) + a_i\right)^2. \quad (4.20)$$

Fig. 4.24 shows for varying lithium content in the host material both the lattice parameter (see Fig. 4.24(a)) and the dimensionless partial volume (see Fig. 4.24(b)) obtained under the three mentioned assumptions regarding the dependence of the lattice parameter with the lithium concentration: The $\sqrt[3]{n}$ -dependence that leads to a constant dimensionless partial volume, the dependence represented by Eq. (4.18) as it is done in Ref. [31] and the linear dependence represented by Eq. (4.19), as we shall assume it in the present work.

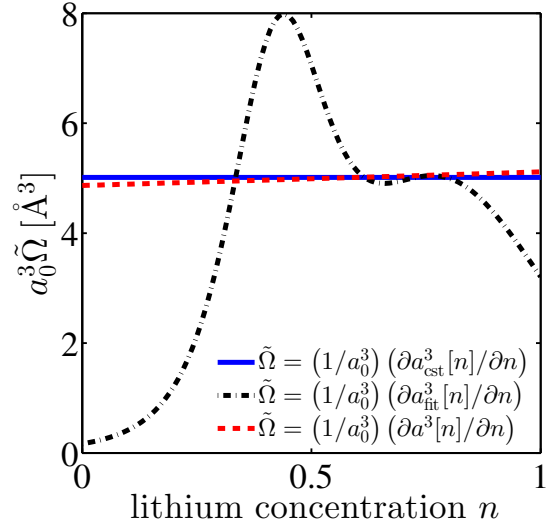
Concentration-dependent Young's modulus

Ab-initio calculations performed on LMO show a very slight dependence of the Young's modulus with varying lithium amount in the host material [121]. However, different experimental measurements

¹¹As compared to Eq. (25) of Ref. [31], there is a multiplicative factor 1/2 in Eq. (4.18) because the authors of Ref. [31] consider the lattice parameter of the crystalline spinel structure equal to $2a$ (see Fig. 3.4(b) of Sec. 3.1.1) whereas, in this work, the considered lattice parameter, equal to a , is the one corresponding to the approximated cubic sublattice where the lithium ions have the possibility to sit, see Fig. 3.5 of Sec. 3.1.1.



(a) Lattice parameter a versus the the local lithium concentration n .



(b) Representation of the quantity $a_0^3 \tilde{\Omega}$ — which is proportional to the dimensionless partial volume $\tilde{\Omega}$ — versus the lithium concentration n .

Figure 4.24: Representation of the lattice parameter a as well as of the quantity $a_0^3 \tilde{\Omega}$ in dependency of the lithium concentration n in three different cases: For a constant dimensionless partial volume, $\tilde{\Omega} = (1/a_0^3) (\partial a_{\text{cst}}^3[n]/\partial n) = \tilde{\Omega}_0$, for a concentration-dependent dimensionless partial volume obtained from a lattice parameter $a = a_{\text{fit}}[n]$ and for a concentration-dependent dimensionless partial volume obtained from a lattice parameter $a = a[n]$ assumed to be linearly dependent on the lithium concentration n .

of the Young's modulus exhibit significant discrepancies possibly attributed to different lithium contents in the host material [9]. This discrepancy may indicate that the Young's modulus depends on the lithium concentration n . Furthermore, theoretical calculations performed on other intercalation materials, Li_xC_6 [123] as well as on various forms of Li-Si alloys [124], could establish a relationship (approximately linear) between the Young's modulus of the host material and the lithium amount present inside of it. Additionally, in Ref. [125], it could be verified that the variation of the lithium amount in Li_xFePO_4 changes the elastic properties of this material which may be either isotropic or anisotropic depending on the lithium content.

Regarding LMO, it could not be found in the literature whether or not the Young's modulus depends on the lithium concentration n . Thus, a fortiori, there was no indication on how this dependence may appear. Nevertheless, based on the results obtained for the other intercalation materials (Li_xC_6 and Li-Si alloys) and according to Ref. [126, 127], we may assume that the Young's modulus of the host material linearly depends on the lithium concentration,

$$E[n] = E_0 (1 + k_e n). \quad (4.21)$$

Here E_0 , as usual, denotes the concentration-independent Young's modulus of the pure host material

whose value is reported in Tab. 2.1 of Sec. 2.2.1. In Eq. (4.21), the constant parameter k_e must fulfill

$$k_e > -1$$

in order to ensure the positivity of the concentration-dependent Young's modulus.

Under lithium insertion, depending on the sign of k_e , the host material may be either softened if $-1 < k_e < 0$ or stiffened if $k_e > 0$. For a given k_e -value, this behavior is reversed if lithium ions are extracted instead of being inserted. If $k_e = 0$, the Young's modulus becomes independent of the lithium concentration and the variations of the lithium amount into the cathodic particle has no effect on elastic properties of the host material. Since the concentration dependence of Young's modulus remains controversial, no value for the parameter k_e could be found in the literature. At this place, a numerical study of the effect of k_e on the system states will be performed.

4.3.2 Theory

In this part, we briefly introduce the basis of a formalism that accounts for any arbitrary dependence of the dimensionless partial volume $\tilde{\Omega}[n]$ and the Young's modulus $E[n]$ on the lithium concentration n , provided that these two quantities both are possibly expressed as functions of the lithium concentration. Both Eqs. (4.20) - (4.21) that specify the dependence of both the dimensionless partial volume and Young's modulus, respectively, are related to particular cases of the formalism introduced here.

This formalism relies on the functional form of the system free energy, Eq. (3.44), and more specifically, on the elastic strain energy functional of the system, Eq. (3.40), that exclusively contains both the $\tilde{\Omega}$ - and E -dependences. According to Eq. (3.40), the elastic strain energy of the particle, Ψ^{es} , is given by

$$\Psi^{\text{es}} = \int_{V_0} dV (\psi^{\text{me}} + \psi^{\text{cp}}).$$

With both the $\tilde{\Omega}$ - and E -dependences, according to Eqs. (3.42) - (3.43), the energy densities, ψ^{me} and ψ^{cp} , read

$$\psi^{\text{me}} = \frac{1}{2} \left(\lambda_2[n] \text{Tr}^2(\varepsilon) + 2 \lambda_1[n] \text{Tr}(\varepsilon^2) + 4 \lambda_1[n] (\varepsilon_{12}^2 + \varepsilon_{23}^2 + \varepsilon_{31}^2) \right), \quad (4.22)$$

$$\psi^{\text{cp}} = -\frac{1}{2} \tilde{\Omega}[n] \lambda[n] (n - n_0) \left(2 \text{Tr}(\varepsilon) - \tilde{\Omega}[n] (n - n_0) \right) \quad (4.23)$$

where, upon the concentration-dependent Young's modulus, the two Lamé's coefficients, $\lambda_1[n]$ and $\lambda_2[n]$ as well as the quantity $\lambda[n]$ now depend on the lithium concentration n . According to Eqs. (2.12) - (2.14), these three parameters read

$$\begin{aligned} \lambda_1[n] &= \frac{E[n]}{2(1+\nu)}, \\ \lambda_2[n] &= \frac{2\nu \lambda_1[n]}{1-2\nu}, \\ \lambda[n] &= \frac{3\lambda_2[n] + 2\lambda_1[n]}{3}. \end{aligned}$$

Following the notations of Eqs. (3.47), (3.48), (3.50) as well as of Eq. (3.49), we have

$$\mu^{\text{ch}} = a_0^3 \frac{\partial \psi^{\text{ch}}}{\partial n}, \quad (4.24)$$

$$\mu^{\text{me}} = a_0^3 \frac{\partial \psi^{\text{me}}}{\partial n}, \quad (4.25)$$

$$\mu^{\text{cp}} = a_0^3 \frac{\partial \psi^{\text{cp}}}{\partial n}. \quad (4.26)$$

With these notations, the chemical potential defined as

$$\mu = a_0^3 \frac{\partial \psi}{\partial n},$$

according to Eq. (3.46), is equal to

$$\mu = \mu^{\text{ch}} + \mu^{\text{me}} + \mu^{\text{cp}}. \quad (4.27)$$

Let us make some explanatory remarks regarding Eq. (4.27): According to Eq. (4.24), the chemical potential μ^{ch} is obtained from the chemical free energy density ψ^{ch} , solely. Since this free energy density term depends neither on $\tilde{\Omega}[n]$ nor on $E[n]$, the expression of μ^{ch} remains unchanged as compared to Eq. (3.50) obtained in a *concentration-independent* formalism where both the dimensionless partial volume and the Young's modulus have been assumed to be independent of the lithium concentration. In phase-field modeling, its expression is given by

$$\mu^{\text{ch}} = E + U\Gamma n + k_B T \ln \left(\frac{n}{1-n} \right) - \kappa \nabla \cdot (\nabla n),$$

according to Eq. (3.50) whereas, in the dilute solution approach where no phase segregation is accounted for, it reads

$$\mu^{\text{ch}} = E + k_B T \ln n,$$

according to Eq. (3.52).

The chemical potential μ^{me} derived from the energy density ψ^{me} , according to Eq. (4.25), was not present in the concentration-independent formalism because this kind of energy density was not dependent on the lithium concentration n . After insertion of Eq. (3.42) into Eq. (4.25), we obtain

$$\mu^{\text{me}} = \frac{1}{2} \left(\frac{\partial \lambda_2[n]}{\partial n} \text{Tr}^2(\varepsilon) + 2 \frac{\partial \lambda_1[n]}{\partial n} \text{Tr}(\varepsilon^2) + 4 \frac{\partial \lambda_1[n]}{\partial n} (\varepsilon_{12}^2 + \varepsilon_{23}^2 + \varepsilon_{31}^2) \right).$$

Because both $\tilde{\Omega}$ and λ are now concentration-dependent, the chemical potential μ^{cp} becomes modified as compared to Eq. (3.49). For clarity, we define

$$\begin{aligned} \mu^{\text{cp, ch}} &= -\frac{\partial \tilde{\Omega}[n]}{\partial n} a_0^3 \lambda[n] (n - n_0) \left(\text{Tr}(\varepsilon) - \tilde{\Omega}[n] (n - n_0) \right), \\ \mu^{\text{cp, me}} &= -\frac{1}{2} \tilde{\Omega}[n] a_0^3 \frac{\partial \lambda[n]}{\partial n} (n - n_0) \left(2 \text{Tr}(\varepsilon) - \tilde{\Omega}[n] (n - n_0) \right), \\ \mu^{\text{cp, cp}} &= -\tilde{\Omega}[n] a_0^3 \lambda[n] \left(\text{Tr}(\varepsilon) - \tilde{\Omega}[n] (n - n_0) \right) \\ &= -\tilde{\Omega}[n] a_0^3 \sigma_h[n] \end{aligned}$$

where the hydrostatic stress σ_h now reads

$$\sigma_h [n] = \lambda [n] \left(\text{Tr} (\varepsilon) - \tilde{\Omega} [n] (n - n_0) \right). \quad (4.28)$$

At this place, we recognize that

$$\mu^{\text{cp}} = \mu^{\text{cp, ch}} + \mu^{\text{cp, me}} + \mu^{\text{cp, cp}}. \quad (4.29)$$

Note that the term $\mu^{\text{cp, cp}}$ is identical to the chemical potential μ^{cp} defined in Eq. (3.49) of Sec. 3.49, introduced in a concentration-independent formalism. Inserting Eq. (4.29) into Eq. (4.27), we finally obtain

$$\mu = \mu^{\text{ch}} + \mu^{\text{me}} + \left(\mu^{\text{cp, ch}} + \mu^{\text{cp, me}} + \mu^{\text{cp, cp}} \right). \quad (4.30)$$

In relation to these five different contributions to the total chemical potential μ (see Eq. (4.30)) and based on the linearity of the Onsager relation, Eq. (3.70), we define five contributions to the total lithium flux \mathbf{J} . These different contributions read

$$\begin{aligned} \mathbf{J}^{\text{ch}} &= -L \nabla \mu^{\text{ch}}, \\ \mathbf{J}^{\text{me}} &= -L \nabla \mu^{\text{me}}, \\ \mathbf{J}^{\text{cp, ch}} &= -L \nabla \mu^{\text{cp, ch}}, \\ \mathbf{J}^{\text{cp, me}} &= -L \nabla \mu^{\text{cp, me}}, \\ \mathbf{J}^{\text{cp, cp}} &= -L \nabla \mu^{\text{cp, cp}} \end{aligned}$$

where

$$L = \frac{D_0 n (1 - n)}{a_0^3 k_B T}$$

in phase-field modeling, or

$$L = \frac{D_0 n}{a_0^3 k_B T}$$

in the dilute solution approach. With these definitions, the total lithium flux \mathbf{J} reads

$$\begin{aligned} \mathbf{J} &= -L \nabla \mu \\ &= -L \nabla \left(\mu^{\text{ch}} + \mu^{\text{me}} + \mu^{\text{cp, ch}} + \mu^{\text{cp, me}} + \mu^{\text{cp, cp}} \right) \\ &= \mathbf{J}^{\text{ch}} + \mathbf{J}^{\text{me}} + \mathbf{J}^{\text{cp, ch}} + \mathbf{J}^{\text{cp, me}} + \mathbf{J}^{\text{cp, cp}}. \end{aligned}$$

For spherically symmetric particle model where the spherical coordinates may be used, the conservation of lithium matter as well as the mechanical equilibrium are given by

$$\frac{\partial}{\partial t} (r^2 n) + \frac{\partial}{\partial r} \left(a_0^3 r^2 \left(J_r^{\text{ch}} + J_r^{\text{me}} + J_r^{\text{cp, ch}} + J_r^{\text{cp, me}} + J_r^{\text{cp, cp}} \right) \right) = 0, \quad (4.31)$$

$$\frac{\partial \sigma_r [n]}{\partial r} + \frac{2}{r} (\sigma_r [n] - \sigma_t [n]) = 0. \quad (4.32)$$

Note that, as compared to Eqs. (3.83) - (3.84), both the radial and tangential stresses exhibit an additional dependence on the lithium concentration contained in the Lamé's coefficients as well as in the dimensionless partial volume,

$$\begin{aligned}\sigma_r [n] &= 2 \lambda_1 [n] \varepsilon_r + \lambda_2 [n] (\varepsilon_r + 2\varepsilon_t) - \lambda [n] \tilde{\Omega} [n] (n - n_0), \\ \sigma_t [n] &= 2 \lambda_1 [n] \varepsilon_t + \lambda_2 [n] (\varepsilon_r + 2\varepsilon_t) - \lambda [n] \tilde{\Omega} [n] (n - n_0).\end{aligned}$$

Using this formalism applied to the particular case where

$$\tilde{\Omega} [n] = \frac{3}{a_0^3} \left(\frac{a_f - a_i}{n_f - n_i} \right) \left(\left(\frac{a_f - a_i}{n_f - n_i} \right) (n - n_i) + a_i \right)^2,$$

according to Eq. (4.20) and

$$E = E_0(1 + k_e n),$$

according to Eq. (4.21), the calculations of the different contributions to the total lithium flux \mathbf{J} , ie. \mathbf{J}^{ch} , \mathbf{J}^{me} , $\mathbf{J}^{\text{cp,ch}}$, $\mathbf{J}^{\text{cp,me}}$, $\mathbf{J}^{\text{cp,cp}}$, upon the corresponding contributions to the total chemical potential μ , ie. μ^{ch} , μ^{me} , $\mu^{\text{cp,ch}}$, $\mu^{\text{cp,me}}$, $\mu^{\text{cp,cp}}$, is straightforward and is not shown in details here.

4.3.3 Influence of the concentration-dependent material parameters in the dilute solution approach

For a better understanding of the effect of both the concentration-dependent dimensionless partial volume $\tilde{\Omega} [n]$ and the concentration-dependent Young's modulus $E [n]$, we first analyze the system states obtained by means of the dilute solution approach introduced in Sec. 2.2.

Influence of the concentration-dependent partial volume

The effect of the concentration-dependent dimensionless partial volume on the system states of a spherical cathodic particle of radius $r_0 = 1 \mu\text{m}$ in dilute solution modeling is illustrated in Fig. 4.25. At this place, the lithium concentration and hydrostatic stress profiles obtained during lithium extraction with a concentration-dependent dimensionless partial volume $\tilde{\Omega} [n]$ are compared to those performed at constant dimensionless partial volume equals $\tilde{\Omega}_0$. Both Fig. 4.25(a) and Fig. 4.25(b) demonstrate that, as compared to the case of a constant dimensionless partial volume, considering a concentration-dependent dimensionless partial volume has neither a significant effect on the lithium concentration profiles nor on the hydrostatic stress profiles. This is not so surprising since the variation of the concentration-dependent dimensionless partial volume are relatively small as compared to the constant dimensionless partial volume,

$$\left| \frac{\tilde{\Omega} [n]}{\tilde{\Omega}_0} \right| \leq 1.02 \%.$$

The lithium concentration profiles obtained at both concentration-dependent and constant dimensionless partial volume are exactly the same. Regarding the hydrostatic stress profiles, there is a very good agreement between these two cases, especially at the beginning of the lithium extraction. Nevertheless, over lithium extraction, when the average lithium concentration in the particle becomes lower,

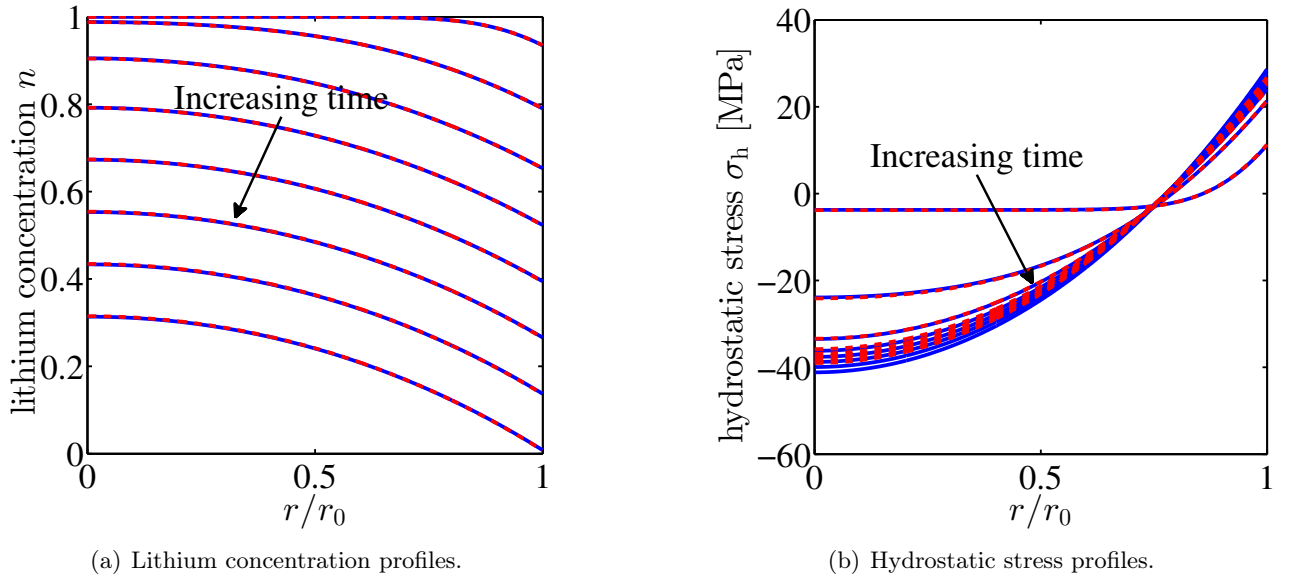


Figure 4.25: Profiles of the lithium concentration n and of the hydrostatic stress σ_h obtained during lithium extraction at $C = 50$ for a cathodic particle of radius $r_0 = 1 \mu\text{m}$ using the dilute solution model. The blue solid lines have been obtained with a constant dimensionless partial volume $\tilde{\Omega}_0$ whereas the red dashed lines are related to the case of a concentration-dependent partial volume $\tilde{\Omega}[n]$.

it appears a slight discrepancy between these two cases: The hydrostatic stresses are slightly smaller in case of a nonconstant dimensionless partial volume. Such a behavior is confirmed by Fig. 4.26(a) which shows the maximum of the hydrostatic stresses reached during lithium extraction in dependency with the applied flux magnitude linearly related to the applied C -rate.

Note that, in contrast to lithium extraction, the hydrostatic stresses obtained over lithium insertion (see Fig. 4.26(b)) are slightly larger in case of a concentration-dependent dimensionless partial volume. The discrepancy between constant and nonconstant dimensionless partial volume becomes more significant at large applied flux magnitude. The asymmetry between lithium extraction and insertion is probably due to the fact that the maximum of the hydrostatic stress is reached at the end of the particle unloading and loading, respectively. Thus, during lithium extraction, this maximum is attained when the lithium concentration in the particle is quite low. In this case, according to Fig. 4.24(b), the concentration-dependent dimensionless partial volume is lower than the constant corresponding one, which further leads to lower hydrostatic stress values. During lithium insertion, this situation is reversed: The maximum of the hydrostatic stress is attained when the lithium concentration in the particle is quite high. Thus, considering a constant dimensionless partial volume leads to larger stress values than those obtained at constant dimensionless partial volume.

Influence of the concentration-dependent Young's modulus

The influence of the concentration-dependent Young's modulus $E[n]$ is illustrated in Fig. 4.27. This figure shows both the lithium concentration and hydrostatic stress profiles obtained during lithium extraction from a spherical particle of radius $r_0 = 1 \mu\text{m}$ for different k_e -values which are related to the

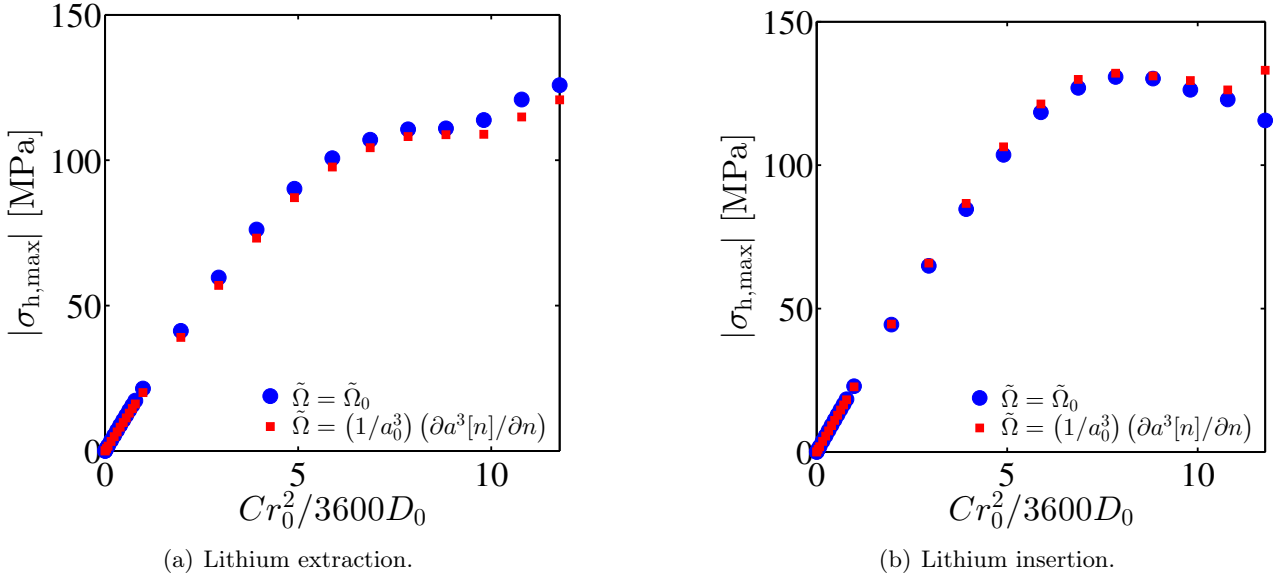


Figure 4.26: Maximum of the hydrostatic stress magnitude reached during both lithium extraction and insertion as a function of the ratio $Cr_0^2/3600D_0$ and for the two different cases corresponding to a constant dimensionless partial volume equal to $\tilde{\Omega}_0$, on the one hand and to a concentration-dependent dimensionless partial volume $\tilde{\Omega}[n]$.

concentration-dependent Young’s modulus by Eq. (4.21).

Fig. 4.27(a) demonstrates that increasing the value of k_e leads to an enhanced lithium ion homogenization in the particle. Furthermore, as shown in Fig. 4.27(b), increasing the value of k_e induces an increase of the hydrostatic stress magnitude. A possible explanation for this behavior is that, during particle loading and unloading, the concentration-dependent Young’s modulus averaged over the particle,

$$\bar{E}[n] = E_0(1 + k_e \bar{n}),$$

effectively enlarges when the parameter k_e grows. Indeed, we saw in Sec. 2.2.2 that the stress-induced lithium flux — proportional to the particle Young’s modulus — enhances the lithium ion diffusion, thus contributing to a better lithium ion distribution over the cathodic particle. It is also not surprising that the increase of the “effective” Young’s modulus, $\bar{E}[n]$, upon the parameter k_e , leads to an enhanced lithium ion homogenization in the particle.

Moreover, as it is well-known from the stress-strain relation (see for example Eq. (4.28)), the stresses are proportional to the particle Young’s modulus and thus may increase when the “effective” Young’s modulus, $\bar{E}[n]$, becomes larger.

Indeed, as shown in Fig. 4.28, the maximum of the hydrostatic stress magnitude reached during both lithium extraction and insertion always enlarges with growing value of the parameter k_e . Similarly to the results obtained in Sec. 2.2.2, the maximum of the hydrostatic stress magnitude reached during lithium insertion is significantly larger than the one reached during lithium extraction. For larger value of k_e , the discrepancy between lithium insertion and extraction becomes more flagrant than for smaller value of k_e : The maximum of the hydrostatic stress magnitude reached during lithium insertion is significantly larger than the one reached during lithium extraction.

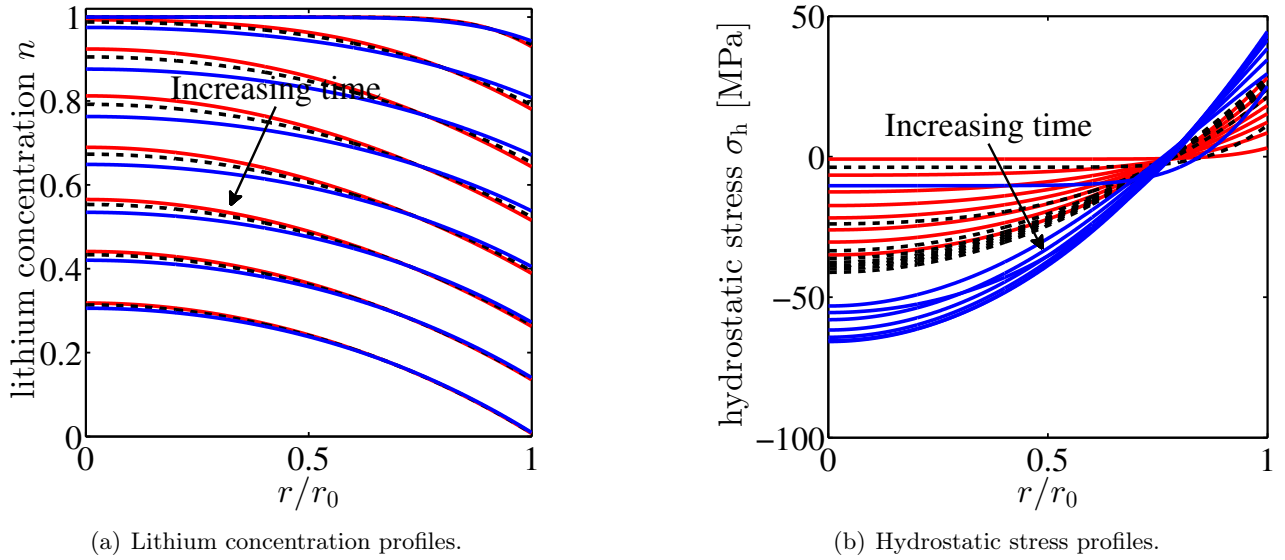


Figure 4.27: *Lithium concentration and hydrostatic stress profiles obtained during lithium extraction at $C = 50$. The dashed black lines are related to the case of a constant Young's modulus equal to E_0 ($k_e = 0$). The solid lines of different colors correspond to different values of k_e : The red and blue lines represent models computed with $k_e = -0.8$ and $k_e = 1.8$, respectively.*

4.3.4 Influence of the concentration-dependent material parameters in phase-field modeling

We here analyze by means of the phase-field model the influence of the concentration-dependent dimensionless partial volume $\tilde{\Omega}[n]$ and Young's modulus $E[n]$, respectively. We study their effect on the equilibrium as well as on the dynamical system states. For both situations, the system consists of a spherically symmetric particle of radius $r_0 = 1 \mu\text{m}$. Since the consideration of concentration-dependent material parameters only affect the elastic-strain energy and not the chemical free energy, we here qualitatively expect the same behaviors as those obtained in the previous section, Sec. 4.3.3 and related to dilute solution modeling.

Influence of the concentration-dependent partial volume

As for the dilute solution model, Fig. 4.29 demonstrates that the effect of the concentration-dependent dimensionless partial volume $\tilde{\Omega}[n]$ on the equilibrium phase-segregated states (obtained by means of a lithium insertion process) is insignificant, as compared to the case where the dimensionless partial volume is constant equal to $\tilde{\Omega}_0$.

Indeed, in both cases, the chemical and elastic-strain energy (see Figs. 4.29(a) - 4.29(c), respectively) are almost identical. The same observation can be done for the lithium concentration and hydrostatic stress profiles (see Figs. 4.29(b) - 4.29(d), respectively). In order to explain such similarities, we may invoke the same reason as the one invoked in Sec. 4.3.3 related to the dilute solution model, namely the fact that the variations of concentration-dependent dimensionless partial volume are small as compared to the case of a constant dimensionless partial volume.

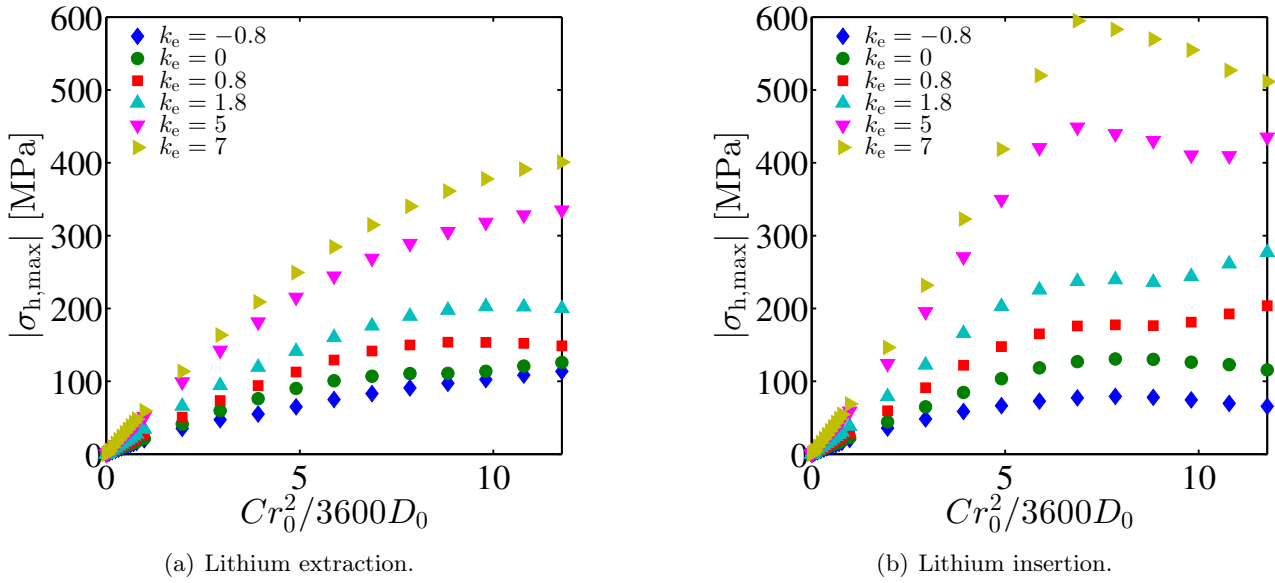


Figure 4.28: Maximum of the hydrostatic stress magnitude reached during both lithium extraction and insertion as a function of the ratio $Cr_0^2/3600D_0$ for different values of the parameter k_e .

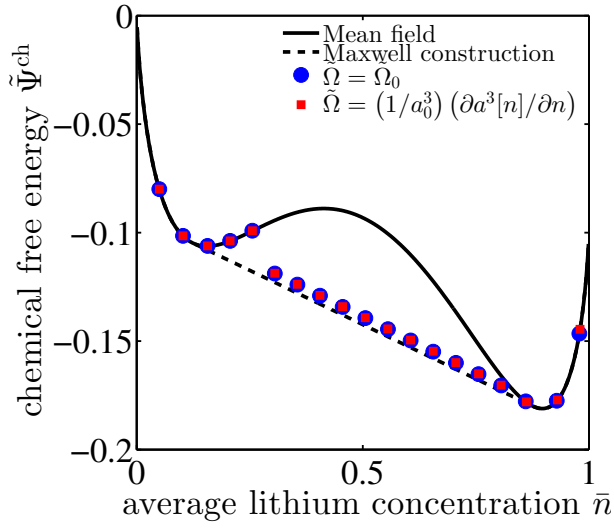
Fig. 4.30 compares, under dynamical particle unloading, the lithium concentration and hydrostatic stress profiles obtained for a nonconstant dimensionless partial volume, $\tilde{\Omega}[n]$, on the one hand, and, at constant dimensionless partial volume equal to $\tilde{\Omega}_0$, on the other hand. As for the dilute solution model, one can notice that, from the lithium concentration profiles, there is no possibility to distinguish one case from the other. As expected from the results obtained in dilute solution modeling, the hydrostatic stress magnitudes at nonconstant dimensionless partial volume are slightly smaller than those obtained at constant dimensionless partial volume. If, instead of extracting lithium ions from the particle, one would consider lithium insertion, the hydrostatic stress magnitudes obtained at nonconstant dimensionless partial volume would be larger than those obtained in case of a constant dimensionless partial volume.

Such a behavior is also illustrated in Fig. 4.31 where the maximum of the hydrostatic stress magnitude reached during both lithium extraction and insertion is represented as a function of the applied flux magnitude at both constant and non constant dimensionless partial volume.

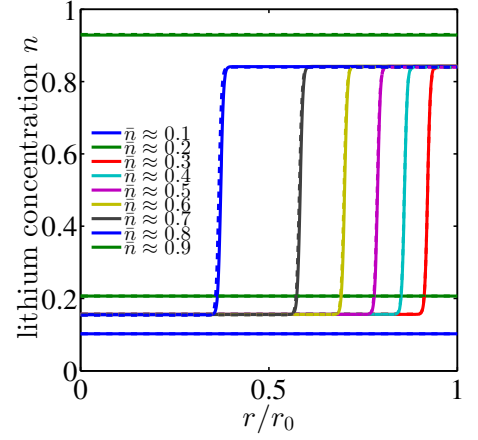
Influence of the concentration-dependent Young's modulus

We further analyze, at constant partial volume equals $\tilde{\Omega}_0$, the effect of varying the parameter k_e on the equilibrium states of the system. As illustrated in Fig. 4.32, increasing the value of k_e suppresses the phase segregation.

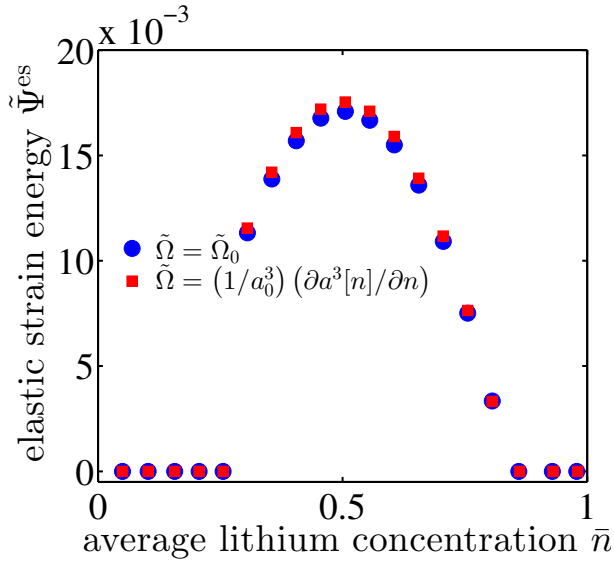
Note that, in Sec. 4.3.3, we argue, that increasing the value of k_e is equivalent to an increase of the effective Young's modulus $\bar{E}[n]$, standing for the particle Young's modulus averaged over the entire particle. Under this consideration, we may easily understand why the phase-segregated states are suppressed when the parameter k_e becomes larger. At this place, we refer to Sec. 4.1.3 where the analysis of the equilibrium states of a spherically symmetric particle as function of the particle Young's modulus was done: We saw that, with increasing values of the particle Young's modulus,



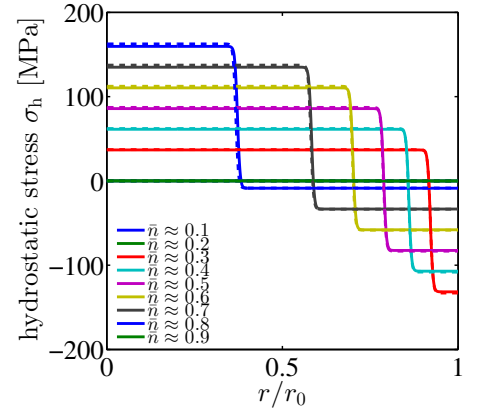
(a) Equilibrium chemical free energy as function of the average lithium concentration \bar{n} .



(b) Lithium concentration profiles n . The dashed and solid lines are obtained at concentration-dependent partial volume $\tilde{\Omega}$ and at constant partial volume equals $\tilde{\Omega}_0$, respectively.



(c) Equilibrium elastic strain energy as function of the average lithium concentration \bar{n} .



(d) Hydrostatic stress profiles σ_h . The dashed and solid lines are obtained at concentration-dependent partial volume $\tilde{\Omega}$ and at constant partial volume equals $\tilde{\Omega}_0$, respectively.

Figure 4.29: Influence of the concentration-dependent partial volume $\tilde{\Omega}$ as compared to the case of a constant partial volume equals $\tilde{\Omega}_0$ on the different contributions to the system free energy ($\alpha_2 = -5.2$) as well as on the lithium concentration and hydrostatic stress profiles. These curves have been obtained at equilibrium during the process of lithium insertion at constant applied flux magnitude, $C = 0.001$.

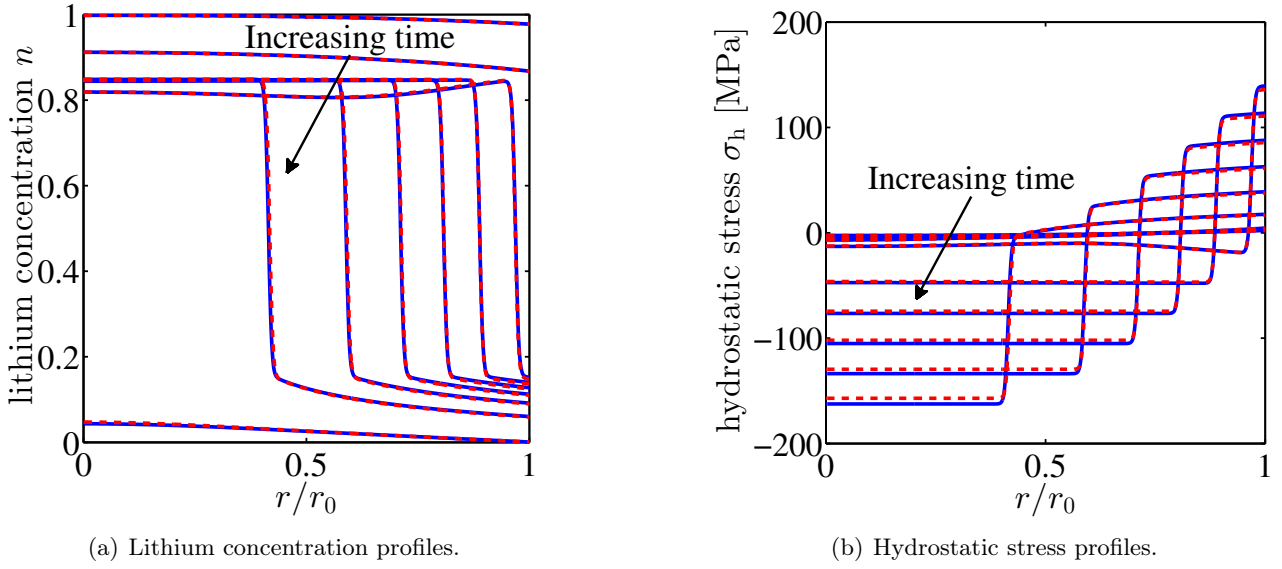


Figure 4.30: Profiles of the lithium concentration n and of the hydrostatic stress σ_h obtained during lithium extraction at $C = 3.8$. The solid blue lines and the dashed red lines have been obtained using a phase-field model ($\alpha_2 = -5.2$) with constant and nonconstant dimensionless partial volume, respectively.

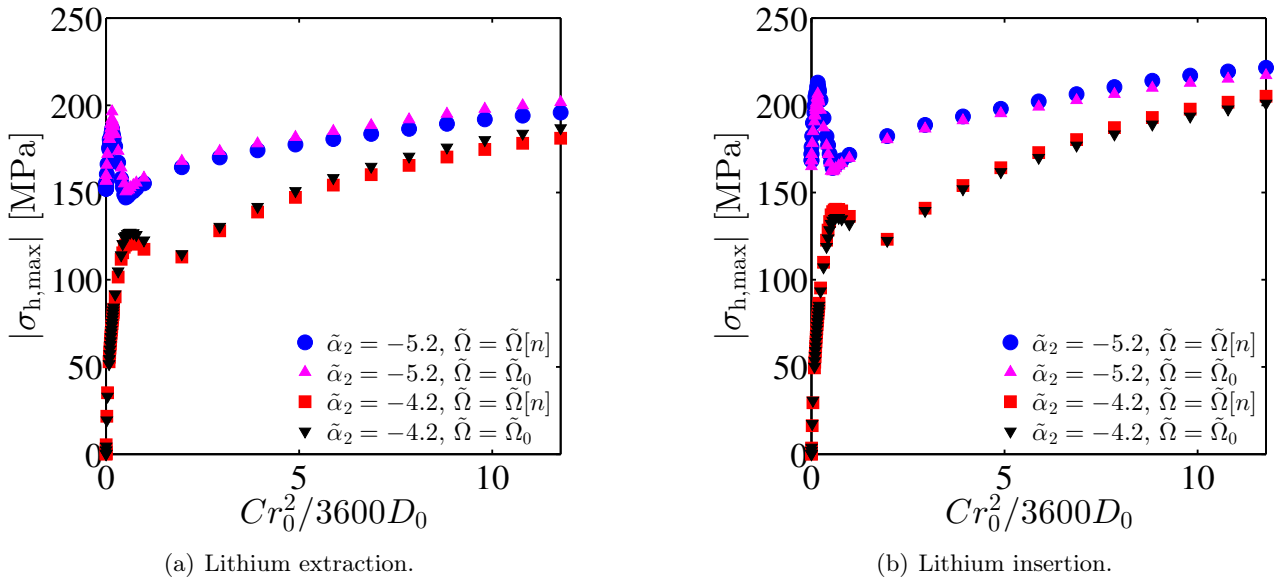
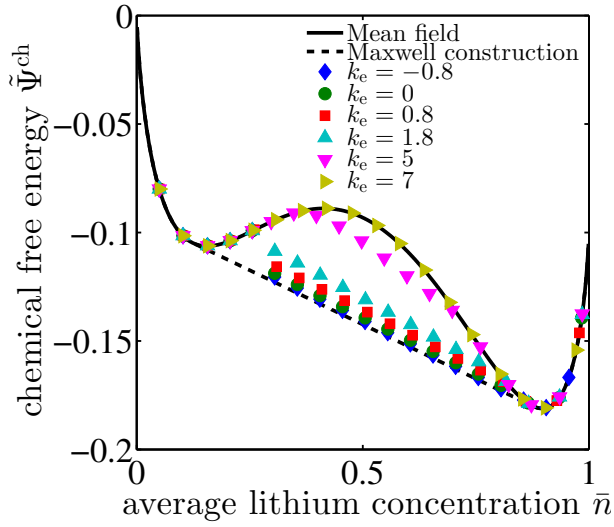
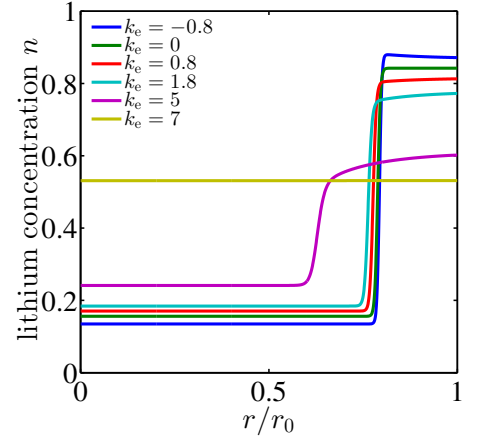


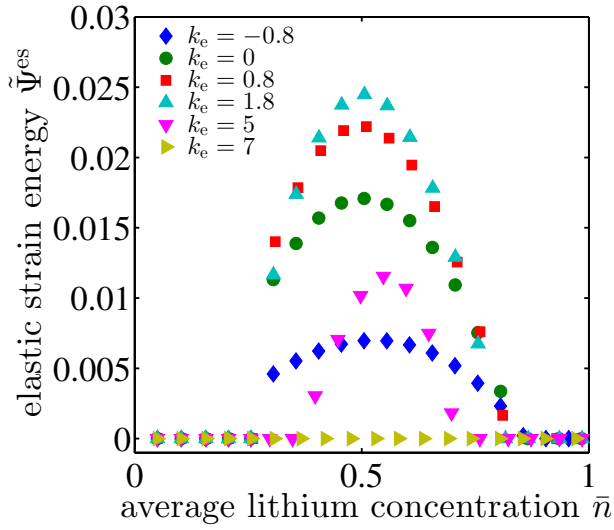
Figure 4.31: Maximum values of the hydrostatic stress magnitude reached during lithium extraction and insertion as a function of the ratio $Cr_0/3600D_0$ at given particle radius $r_0 = 1 \mu\text{m}$. The influence on the stresses of the nonconstant dimensionless partial volume as compared to the case of a constant dimensionless partial volume for two different values of the interacting term α_2 is shown.



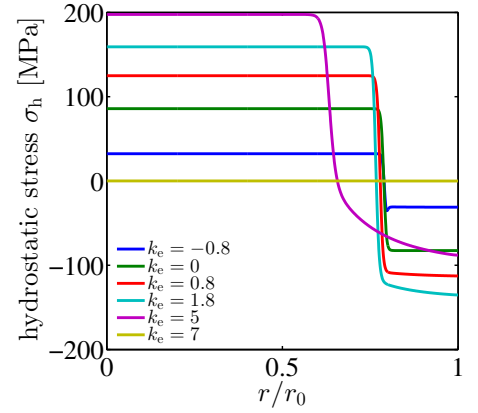
(a) Equilibrium chemical free energy as function of the average lithium concentration for different values of k_e .



(b) Lithium concentration profiles n for different k_e -values when $\bar{n} \approx 0.5$.



(c) Equilibrium elastic strain energy as function of the average lithium concentration for different values of k_e .



(d) Hydrostatic stress profiles σ_h for different k_e -values when $\bar{n} \approx 0.5$.

Figure 4.32: Influence of the parameter k_e on the different contributions to the system free energy ($\alpha_2 = -5.2$) as well as on the lithium concentration and hydrostatic stress profiles. These curves have been obtained at equilibrium during the process of lithium insertion at constant applied flux magnitude, $C = 0.001$.

the discrepancy in the lithium concentration between the low- and high-concentration phases diminishes. We also demonstrate that, for Young's modulus larger than a critical value, denoted by $E_c(\alpha_2 T/T_{\text{ref}})$, the phase-segregated states are completely suppressed leading to homogeneous lithium concentration states. As it is shown in Fig. 4.32(b), by increasing the value of k_e a similar behavior is observed. Moreover, as seen in Fig. 4.32(d), provided that phase segregation still may arise in the particle, we observe that increasing the value of k_e leads to increasing hydrostatic stress magnitude. Once the equilibrium states of the system are homogeneous, the stresses in the particle however vanish.

Fig. 4.33 compares, under dynamical particle unloading, the lithium concentration and hydrostatic stress profiles obtained for different values of k_e . As for the dilute solution model, we observe in

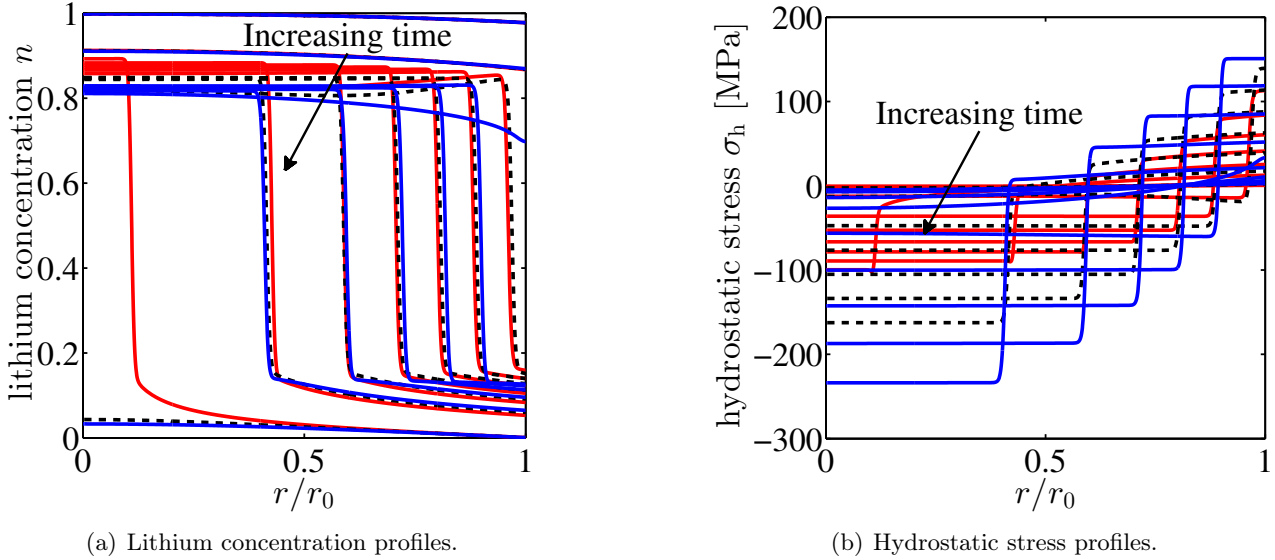


Figure 4.33: Profiles of the lithium concentration n and of the hydrostatic stress σ_h obtained during lithium extraction at $C = 3.8$. The dashed black lines are related to the case of a constant Young's modulus equals E_0 ($k_e = 0$). The solid red and blue lines have been obtained in cases of $k_e = -0.8$ and $k_e = 1.8$, respectively.

Fig. 4.33(a) that, for the largest value of k_e , e.g. $k_e = 1.8$, the lithium ions within both the high- and low-concentration phases are more homogeneously distributed than for smaller values of k_e . Furthermore, as previously pointed out in the study of the influence of the k_e -value on the equilibrium states of the system, the discrepancy in the lithium concentration between the low- and high-concentration regions becomes smaller when the value of k_e grows. In the same time, as illustrated in Fig. 4.33(b), the magnitude of the hydrostatic stresses enlarges with increasing value of k_e . Such a behavior is confirmed in Fig. 4.34 which shows, for different values of k_e as well as for two different values of the interacting term α_2 , the maximum of the hydrostatic stress magnitude reached during both lithium extraction and insertion as function of the applied flux magnitude.

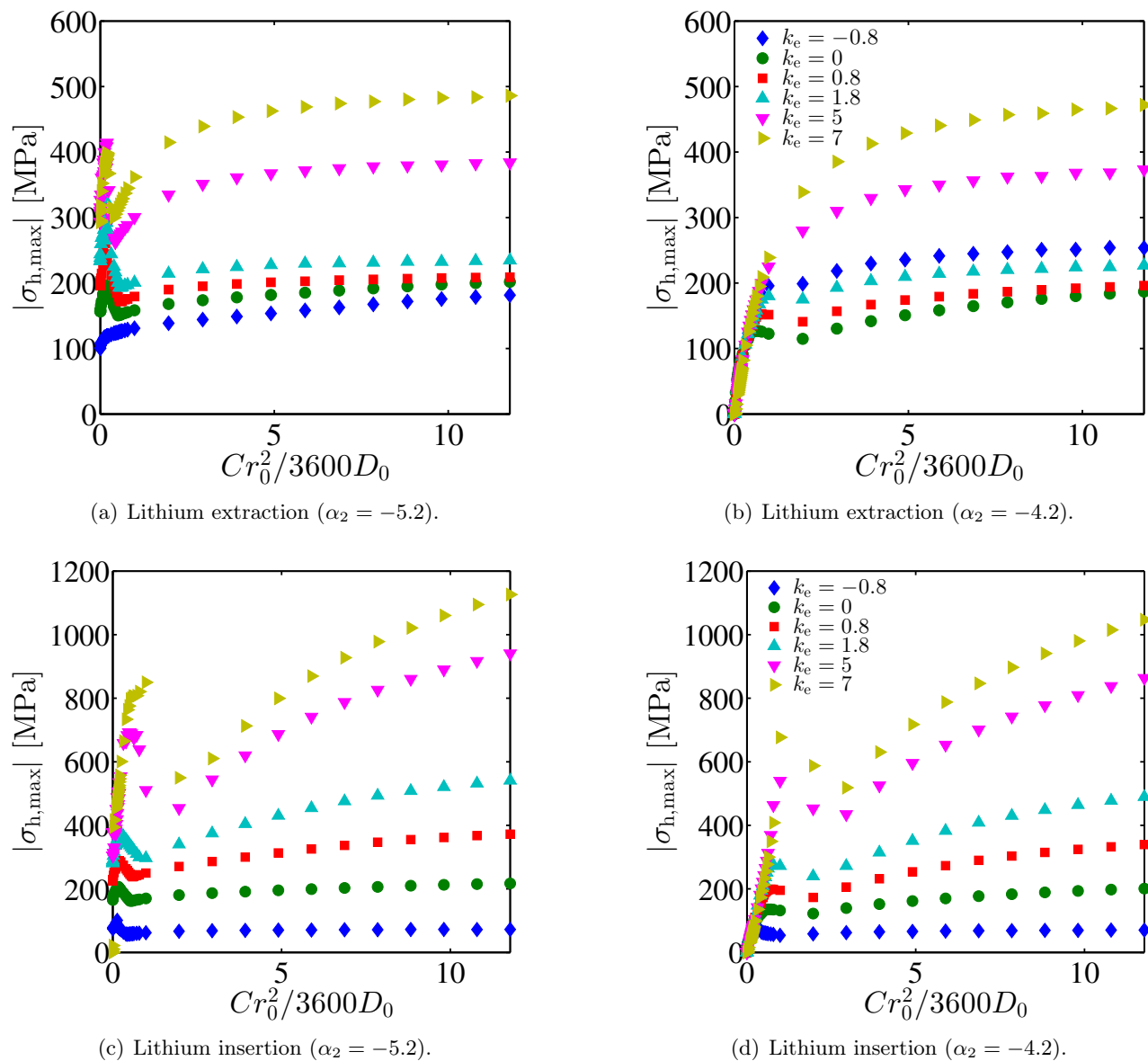


Figure 4.34: Maximum of the hydrostatic stress magnitude reached during both lithium extraction and insertion as a function of the ratio $Cr_0^2/3600D_0$ for different values of the parameter k_e and for two different values of the interaction term α_2 .

Conclusion

In this chapter, using a phase-field model coupled to mechanics, we could account for the occurrence of phase segregation arising during lithium insertion into or extraction from a particle made of LMO that is located at the cathode of a porous LIB.

Considering the simplified case of a spherically symmetric particle, the analysis of the influence of several material parameters on the system equilibrium states was performed. At this place, we demonstrate that the interfacial energy term κ related to the effective interaction strength between two nearest-neighboring lithium ions as well as the Young's modulus of the host material play an important role in the occurrence or the absence of phase segregation: It was especially of interest to note that large values of these parameters suppress phase segregation.

A dynamical study of the system states in phase-field modeling was also performed. Both a constant and a time-dependent flux, obtained from the dualfoil model where the entire macroscopic battery is taken into account. In contrast to the results obtained in the dilute solution approach of Chp. 2 where only large applied flux magnitudes that significantly drive the system out of equilibrium, lead to large stresses, we here demonstrate that, due the occurrence of phase segregation, even low applied flux magnitudes induce large stresses in the particle.

Finally, based on experimental measurements as well as on ab-initio calculations, we allow both the lattice parameter a and Young's modulus E of the host material for being dependent on the local lithium concentration. For both parameters, a linear dependence was assumed. The obtained results are not surprising: As compared to the case of a constant partial volume, the concentration-dependent partial volume derived from the linear dependence of the lattice parameter with respect to the lithium concentration, has an insignificant effect on the system states only. On the contrary, for large values of the parameter k_e may significantly increase the effective Young's modulus $\bar{E}[n]$ of the host material which consequently may lead to the suppression of the phase-segregated states of the system.

Note that, until now, we exclusively consider a particle model of spherical symmetry. But, in reality, the cathode of a LIB is made of an assembly of particles that exhibit various shapes, as illustrated in Fig. 2.1. Using a spherically symmetric particle model, there is however no possibility to take into account particles of other shapes than the spherical shape. Moreover, even for particles of spherical shapes, it is not obvious that the system states are of spherical symmetry. In the next chapter (Chp. 5), we will focus on the influence of the system symmetries on both the concentration and stress states within the particle. Similarly to the analysis performed in Sec. 2.2.3 by means of the dilute solution model, a study of the influence of the particle aspect ratio on the system states will also be performed in phase-field modeling, by means of an ellipsoidal symmetric particle model.

5

Chapter 5

Influence of the particle geometry on the phase-segregated states

Introduction

In the previous chapter (Chp.4), we solely analyze the system states of a cathodic LMO particle that exhibits the spherical symmetry. Under the assumption of spherical symmetry, it was possible to model the three-dimensional particle by means of a one-dimensional particle model using spherical coordinates. With this assumption, the simulation time could be drastically reduced. Nevertheless, in reality, there is no need for this assumption to be satisfied.

First, as illustrated in Fig. 2.1 of Sec. 2.1.1, the LMO particles embedded in the cathode do not have spherical shapes. Moreover, for such particles, there is no reason why the lithium flux at their surface, should be isotropic with respect to the particle surface. Secondly, even for spherical particles with isotropically applied lithium flux at their surface, it is not obvious that the lithium concentration and the mechanical displacement are of spherical symmetry. It is the case only if such spherically symmetric states possess among all other possible states the lowest free energy.

In the first part of this chapter (Sec. 5.1), we analyze without the assumption of spherical symmetry the system states of a spherical particle with isotropically applied lithium flux at its surface. We will show that the system states obtained by means of the dilute solution model are intrinsically of spherical symmetry whereas it is not the case for the states obtained using the phase-field modeling. Here, depending on the initial state as well as on the system history, various particle states may arise. At this place, we will also analyze the effect on the stress-induced lithium flux on the arising system states.

In the second and third parts of this chapter (Sec. 5.2 and Sec. 5.3), we will analyze, in phase-field modeling, the system states of particles of ellipsoidal symmetry. This study will be performed by means of the two-dimensional particle model introduced in Sec. 2.2.3 for the dilute solution approach.

5.1 System states of the spherical particle

5.1.1 Influence of the model dimensionality

As illustrated in Fig. 5.1, a cathodic particle of spherical shape with vanishing stress and isotropically applied lithium flux at its surface may be represented by different particle models depending on whether

symmetries regarding the unknown functions of the problem being the lithium concentration and the mechanical displacement are assumed or not.

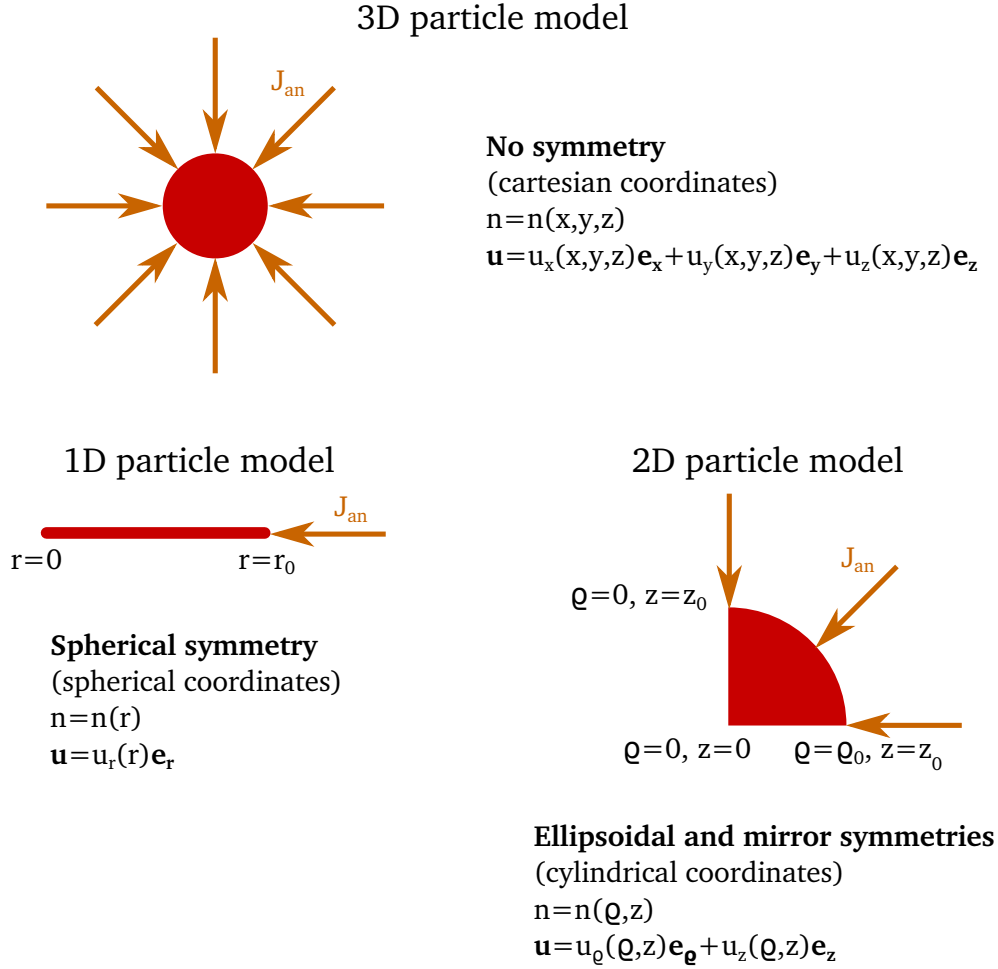


Figure 5.1: Different coordinate systems corresponding to different assumptions regarding the symmetries of the system states.

Until now and without further justifications we have assumed that both the local lithium concentration n and the local mechanical displacement \mathbf{u} exhibit the same symmetry as the particle geometry. Hence, for a spherical particle, we could postulate that

$$n(x, y, z) = n(r), \tag{5.1}$$

$$\mathbf{u}(x, y, z) = u_r(r) \mathbf{e}_r, \tag{5.2}$$

where $r = \sqrt{x^2 + y^2 + z^2}$ is the radial coordinate of the usual spherical coordinate system (r, ϑ, φ) with local orthonormal basis $(\mathbf{e}_r, \mathbf{e}_\vartheta, \mathbf{e}_\varphi)$. Under this assumption, the dimensionality of the particle model could be reduced to one (see Fig. 5.1) which further significantly lowers the computation time.

In a similar way, using the usual cylindrical coordinate system (ϱ, ϑ, z) with local orthonormal basis $(\mathbf{e}_\varrho, \mathbf{e}_\vartheta, \mathbf{e}_z)$ the local lithium concentration n and the local mechanical displacement \mathbf{u} within an

ellipsoidal particle of two equal semi-axis were assumed to satisfy

$$n(x, y, z) = n(\varrho, z), \quad (5.3)$$

$$\mathbf{u}(x, y, z) = u_\varrho(\varrho, z) \mathbf{e}_\varrho + u_z(\varrho, z) \mathbf{e}_z, \quad (5.4)$$

with $\varrho = \sqrt{x^2 + y^2}$. Under these conditions, it was possible to represent an ellipsoidal particle by a particle model of dimensionality equals two, as illustrated in Fig. 5.1. In this section, this two-dimensional particle model will also be used to represent spherical particles.

These assumptions (Eqs. (5.1) - (5.1) and Eqs. (5.3) - (5.4)) regarding the symmetry of both the lithium concentration and mechanical displacement are obviously not related to any physical properties of the system. They only were considered for the purpose of gaining time when performing the simulations. Note that, even if it always was possible to find numerical solutions fulfilling these artificial conditions of symmetries, it is not ensured that the exhibited solutions are those that will arise in reality. Indeed, from the physics, there is no need that the lithium concentration and the mechanical displacement satisfy any constraints of symmetry. The sole constraint induced by the physics is that the free energy has to diminish when the system relaxes towards equilibrium.

We first analyze the system states of a spherical particle obtained using the one-, two- and three-dimensional particle models as they are depicted in Fig. 5.1.

Fig. 5.2 shows lithium concentration and hydrostatic stress profiles obtained in the dilute solution approach using these three different kinds of models. This figure demonstrates that the system states computed in the context of dilute solution modeling have the same symmetry as the particle geometry even if no particular condition of symmetry are artificially required, as it is the case when using the three-dimensional particle model.

A similar study performed at equilibrium was carried out using the phase-field model. At this place, the lithium-induced deformations were neglected. We did so in order to reduce the computation time when performing simulations by means of the three-dimensional particle model. In this model, the total number of unknown functions is equal to 7 which is significantly larger than the one in the dilute solution approach equal to 4¹. Furthermore, the number of mesh elements needed to resolve the phase boundary in phase-field modeling is higher than the one needed in the context of dilute solution modeling where no phase segregation is accounted for. Thus, using the phase-field model, it was not possible to compute the system states by means of the three-dimensional particle model without neglecting the lithium-induced deformations within a reasonable time.

As shown in Fig. 5.3, the phase-segregated lithium concentration states obtained in this context are not of spherical symmetry meaning that they do not exhibit the same symmetry as the particle geometry any more. Indeed, as compared to the states of spherical symmetry obtained using the one-dimensional particle model, such asymmetric states possess a lower free energy, as it is reported in Fig. 5.3. As compared to the one-dimensional particle model, in the two- and three-dimensional particle models, there is the additional possibility to modify the path followed by the boundary such that its proportion in the particle becomes as low as possible. This additional degree of freedom in particle models of higher dimensionality explains why the free energy diminishes when the dimensionality of the considered particle model increases.

¹The finite-element software COMSOL, used here, does not account for third and fourth derivatives of the unknown functions with respect to the spatial coordinates. Such derivatives however appear in the local conservation of lithium matter. To overcome this problem, the second derivatives of the lithium concentration, $\partial^2 n / \partial x^2$, $\partial^2 n / \partial y^2$ and $\partial^2 n / \partial z^2$, have been defined by additional differential equations and hence become unknown functions of the problem. As a consequence, the three-dimensional particle model accounting for phase segregation represents a mathematical problem with a set of seven unknown functions, as opposed to the four unknown functions of the dilute solution model.

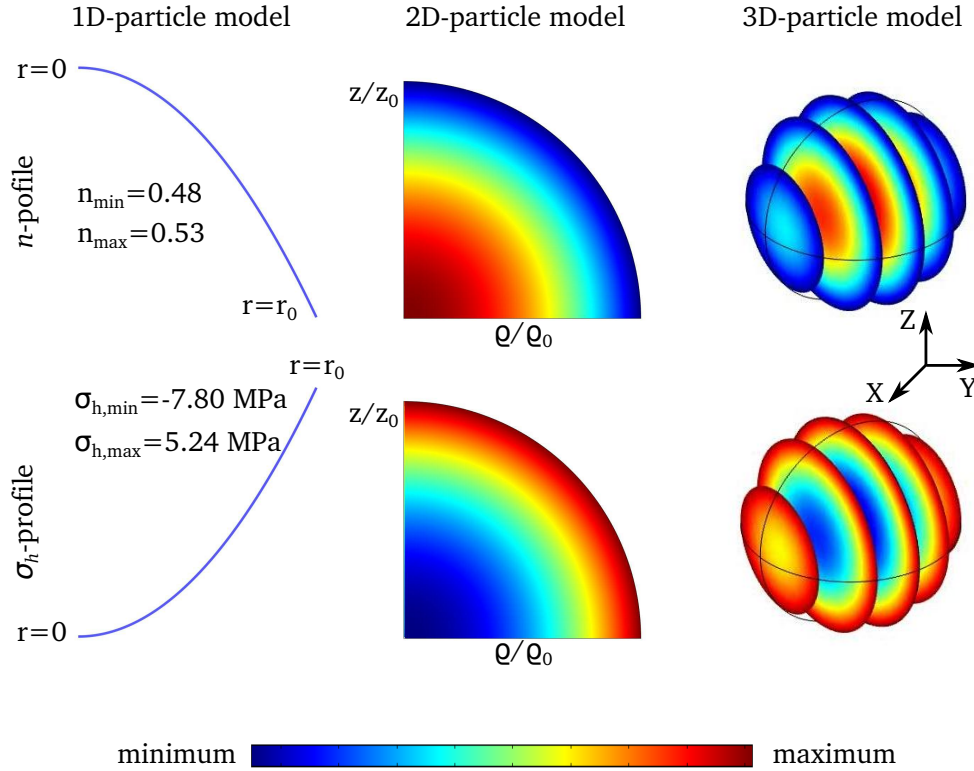


Figure 5.2: System states at $\bar{n} = 0.5$ obtained in the dilute solution approach by means of the one-, two- and three-dimensional particle models. The lithium concentration and hydrostatic stress profiles shown here are those of a spherical particle of radius $r_0 = 1 \mu\text{m}$ where a constant isotropic flux (of spherical symmetry) has been applied at the particle surface to extract lithium at $C = 10$. Independently of the dimensionality of the considered particle model, these states all are equal.

The lithium flux applied at the particle surface to obtain the equilibrium states shown in Fig. 5.3 has a similar profile as the one shown in Fig. 4.3 of Sec. 4.1.1. Its variation over time as well the time-dependent system free energy are shown in Fig. 5.4 for the three different kinds of models (one-, two- and three-dimensional particle models).

The lithium flux applied at the particle surface exhibits hold times where it is equal to zero to enable the system relaxation towards an equilibrium state. As expected, during the system relaxation, the computed system free energy decreases.

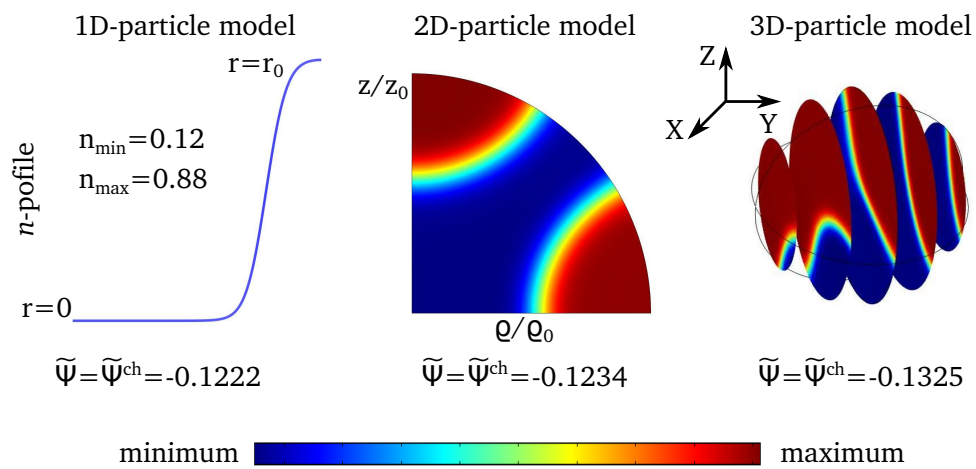


Figure 5.3: *Equilibrium states and related free energy of a spherical cathodic particle of radius $r_0 = 1 \mu\text{m}$ at $\bar{n} = 0.5$ obtained in phase-field modeling by means of the one-, two- and three-dimensional particle model. Depending on the dimensionality of the considered particle model, the obtained system states are different.*

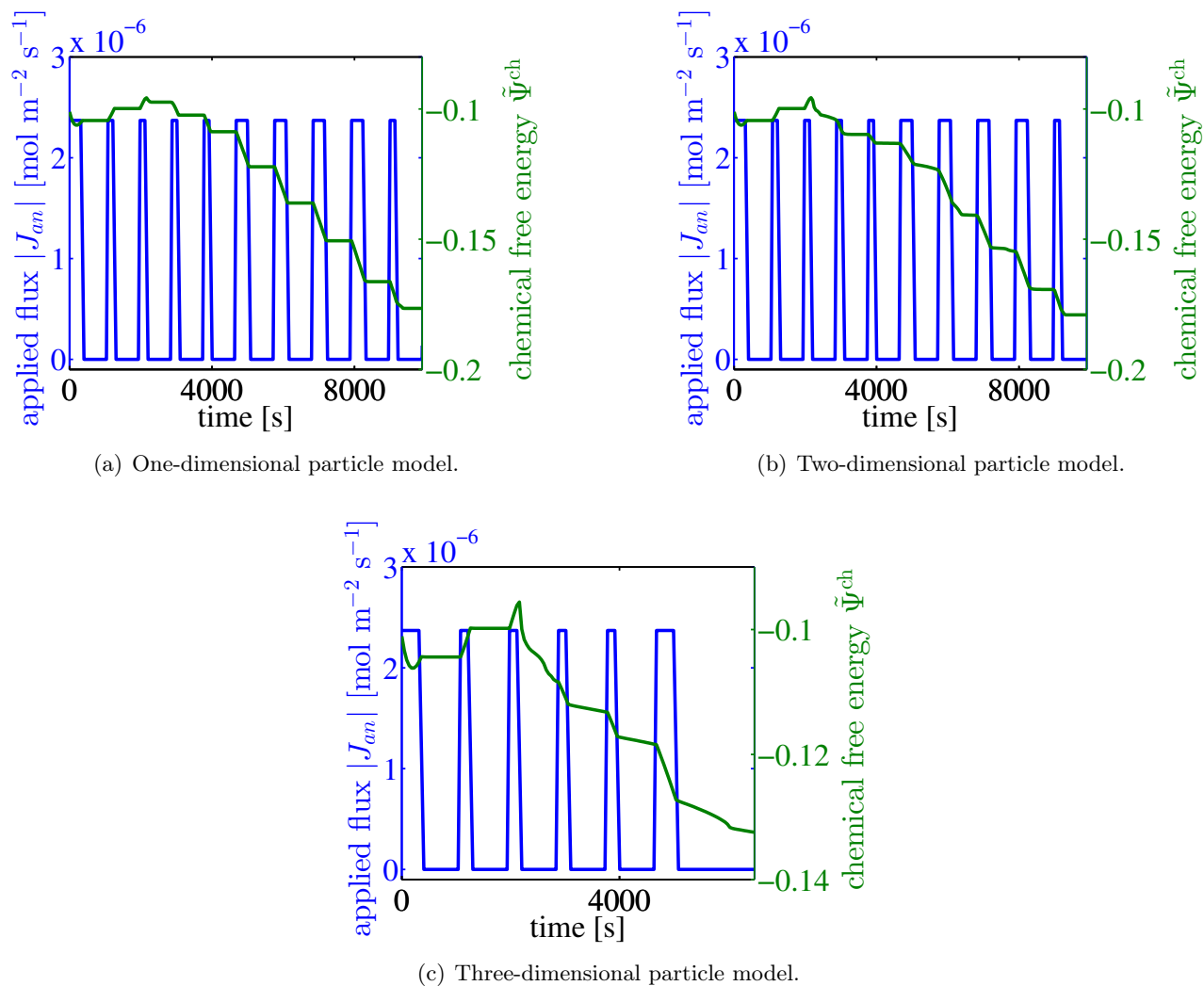
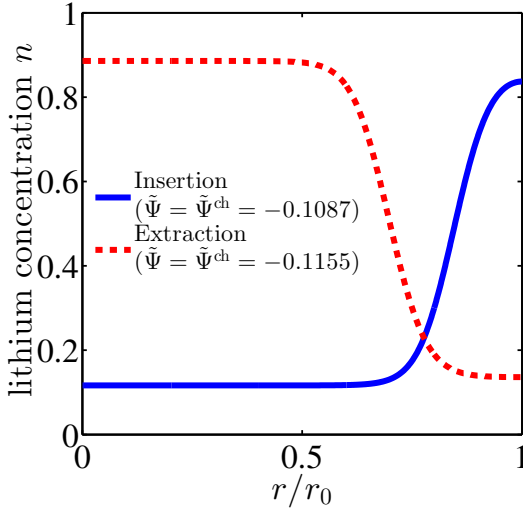


Figure 5.4: Applied lithium flux (blue curves) and system free energy (green curves) as function of time during lithium intercalation into the cathodic particle. The curves shown here are related to a spherical particle of radius $r_0 = 1 \mu\text{m}$ modeled by means of the one-, two- and three-dimensional particle model, respectively. In these three different cases, the applied flux corresponds to a C-rate $C = 1$. During the hold times, the system relaxes and, as expected, the system free energy decreases.

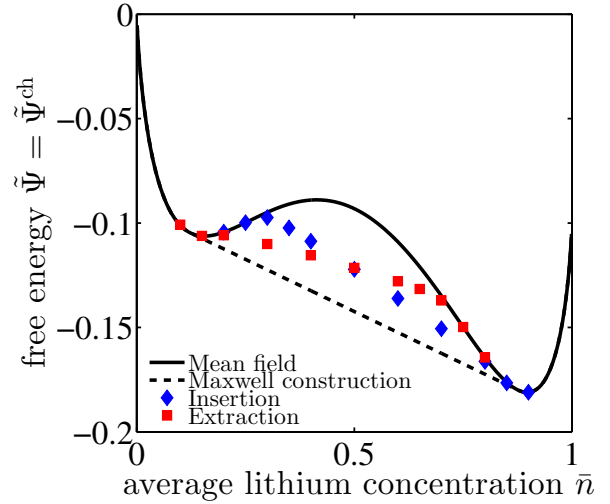
5.1.2 Influence of the system history

At this place it is worth noting that not only the particle symmetry but also the system history, meaning the way the system has been driven into a given equilibrium state, may influence the profile of the obtained system equilibrium states. We here still neglect the lithium-induced deformations.

Fig. 5.5(a) shows, for the one-dimensional particle model, at equal average lithium concentration, $\bar{n} \approx 0.4$, two possible equilibrium states obtained using the phase-field model. These two different



(a) Lithium concentration profiles at average lithium concentration $\bar{n} \approx 0.4$ for two different equilibrium situations. The blue solid line has been obtained during the process of lithium insertion into the particle. Thus the high lithium concentration phase is located in the particle outer shell whereas the low lithium concentration phase takes place in the inner core of the particle. The situation is reversed during the process of lithium extraction from the particle (dashed red line).



(b) Equilibrium system free energy in dependency with the average lithium concentration. During the process of lithium insertion, the high lithium concentration phase is always located in the outer particle shell, the low lithium concentration phase taking place in the inner particle core. The situation is reversed during the process of lithium extraction where the outer particle shell corresponds to low-lithium concentration phase whereas the inner particle core corresponds to high-lithium concentration phase.

Figure 5.5: *Equilibrium states computed by means of the one-dimensional particle model using the phase-field model. The equilibrium situations shown here have been obtained using two different processes: Lithium insertion ($C = 1$), on the one hand and lithium extraction ($C = 1$), on the other hand.*

equilibrium states have been obtained by means of two different processes being lithium insertion on the one hand, and lithium extraction on the other hand, starting from a homogeneous high- and low-lithium concentration, respectively. Moreover, as indicated in Fig. 5.5(a) and as also illustrated in Fig. 5.5(b), these two states do not have the same energy.

The state obtained during the process of lithium extraction has a lower energy than the state obtained during the process of lithium insertion. This observation has to be linked with the position of the phase boundary which is less eccentric for the state obtained by means of lithium extraction than for the one obtained by means of lithium insertion. Indeed, in the one-dimensional particle model representing a particle of spherical symmetry, a phase boundary near to the particle center has less surface area than

a phase boundary far away from the particle center. This explains why, despite equal average lithium concentration, the state obtained during the process of lithium extraction has a lower energy than the state obtained during the process of lithium insertion.

More generally, when phase segregation arises — except when $\bar{n} = 0.5$ for which there is only one position available for the phase boundary — the phase boundary has the possibility to form at two different spatial locations depending on the system state holding before the system goes into relaxation. As shown in Fig. 5.5(b), when $\bar{n} < 0.5$, the energetically favorable lithium concentration profile is the one where the low-lithium concentration phase is located in the outer particle shell, the high-lithium concentration phase taking place in the inner particle core. This situation is reversed when $\bar{n} > 0.5$.

The influence of the system history on the equilibrium states has also been studied using the two-dimensional particle model. Here, at equal average lithium concentration, various lithium concentration profiles could be obtained. As illustrated in Fig. 5.6, these states do not simply depend on whether lithium ions are inserted or extracted — like it is the case using the one-dimensional particle model — but they also depend on the magnitude of the flux that has been applied at the particle surface before the system goes into relaxation.

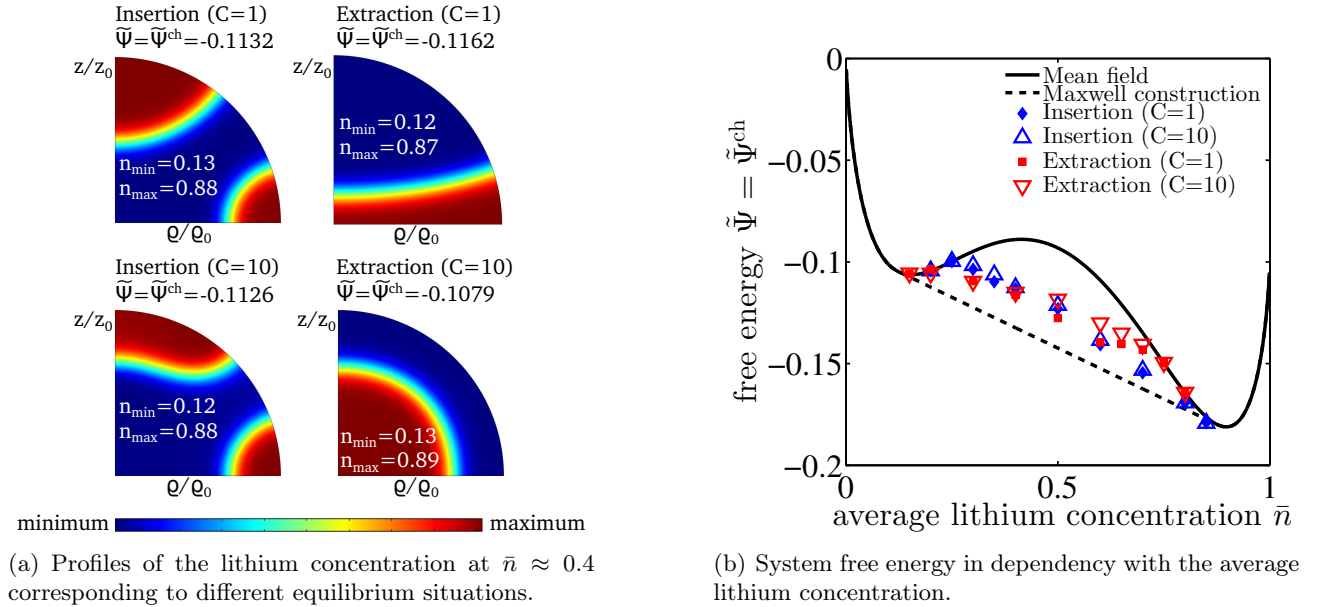


Figure 5.6: Different equilibrium states of a spherical particle modeled using the two-dimensional particle model. These states have been obtained at the end of the relaxation time after differently applied perturbations to the system (lithium insertion/extraction at low/large applied flux magnitude).

5.1.3 Effect of the lithium induced deformations

In Sec. 4.1.3 the effect of the stress-induced lithium flux on the equilibrium states of a spherical particle was analyzed. At this place, we demonstrated that considering a nonzero stress-induced lithium flux leads to smaller hydrostatic stresses than in the case where this flux was neglected. This effect was due to the stress-induced lithium flux that contributes to a better lithium homogenization inside of the particle.

In this part, we perform a similar study by means of the two-dimensional particle model. Compared to the one-dimensional model, the system has here the additional possibility to change the path followed by the phase boundary — which is not assumed to be of spherical symmetry any more — in order to lower the system free energy. Thus we may expect that considering the stress-induced lithium flux leads to a significant modification of the path followed by the phase boundary as it is confirmed in Fig. 5.7 where the lithium concentration profile obtained with both $\mathbf{J}^{\text{cp}} = \mathbf{0}$ and $\mathbf{J}^{\text{cp}} \neq \mathbf{0}$ are shown. Note that, differently from the one-dimensional particle model related to spherically symmetric particle particles, the extrema of the hydrostatic stress obtained by means of the two-dimensional particle model, are neither attained at the particle center nor at the particle surface when the lithium concentration profiles do not exhibit the spherical symmetry.

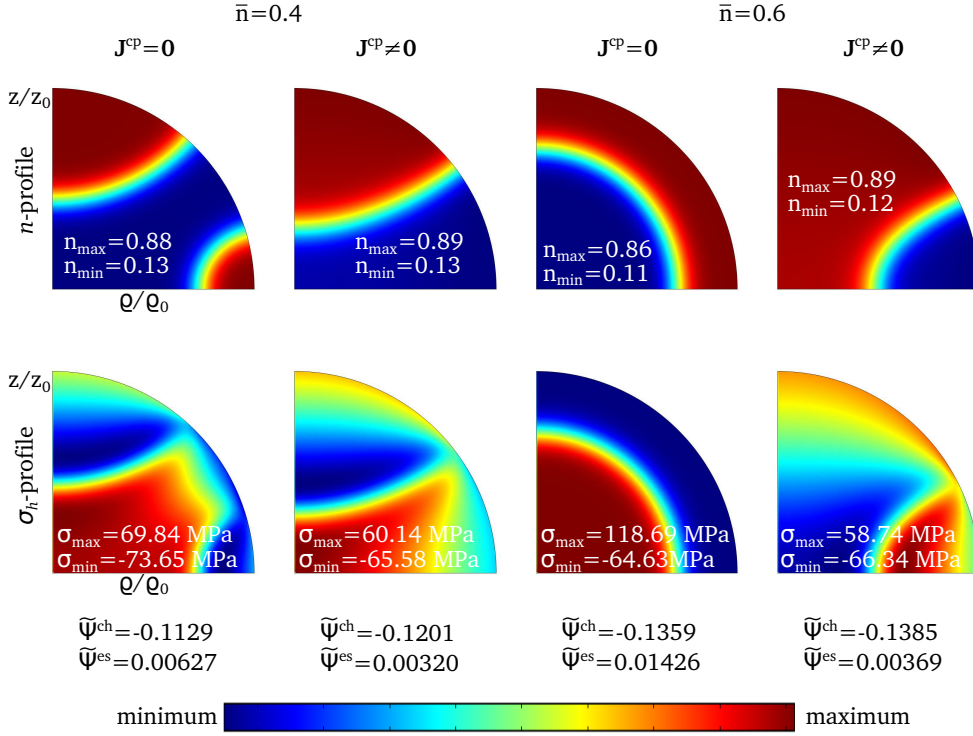


Figure 5.7: Lithium concentration and hydrostatic stress profiles at $\bar{n} \approx 0.4$ and $\bar{n} \approx 0.6$ with and without neglect of the lithium induced deformations. These two different cases are referred to as $\mathbf{J}^{\text{cp}} = \mathbf{0}$ and $\mathbf{J}^{\text{cp}} \neq \mathbf{0}$, respectively. All the profiles shown here have been obtained at equilibrium during the process of lithium insertion at $C = 1$.

For a better understanding of the effect of the stress-induced lithium flux at equilibrium, the contributions of the chemical and elastic strain free energies to the total system free energy as well as the minimal and maximal values of both the local lithium concentration and hydrostatic stress for both the one- and two-dimensional particle models are shown in Fig. 5.8 and 5.9.

As expected both the chemical and elastic strain free energies obtained by means of the two-dimensional particle model are lower than those obtained using the one-dimensional particle model. Moreover, for both the one- and two-dimensional particle models, separately considered, the chemical free energy as well as the elastic strain energy are lower when the lithium induced deformations are not neglected, see Figs. 5.8(a) - 5.8(b).

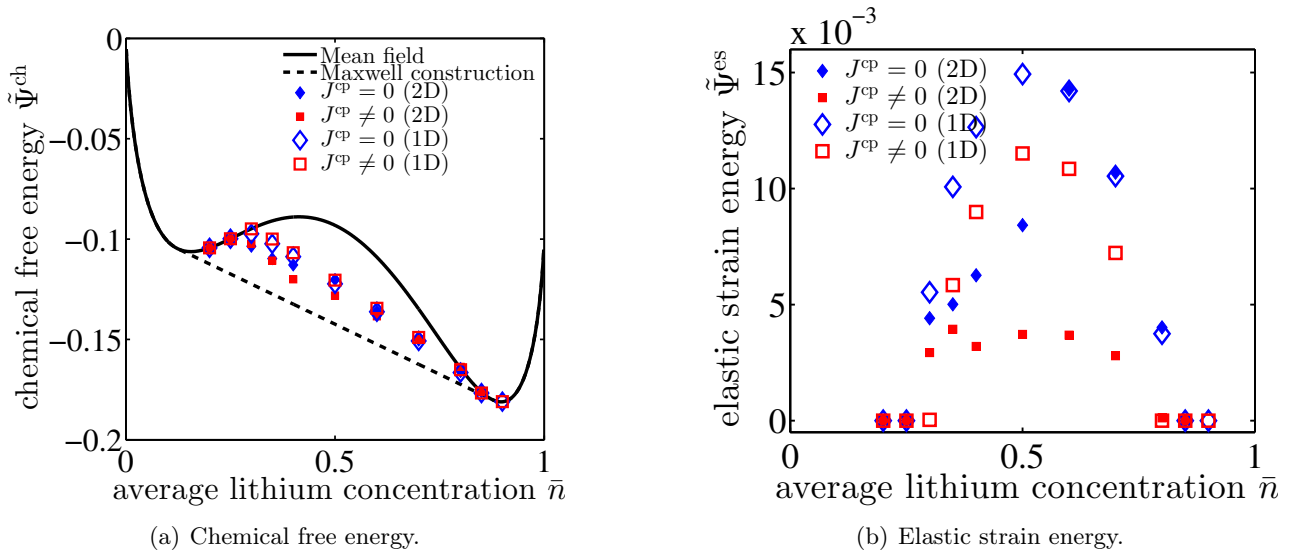


Figure 5.8: Chemical free energy and elastic strain energy at equilibrium in dependency of the average lithium concentration \bar{n} . The curves shown here are related to the one- and two-dimensional particle model as well as to the cases $\mathbf{J}^{\text{cp}} = 0$ and $\mathbf{J}^{\text{cp}} \neq 0$, respectively. They have been obtained during the process of lithium insertion at $C = 1$.

As illustrated in Figs. 5.9(a) - 5.9(b), the model dimensionality has a slight influence on the extrema of the lithium concentration n obtained at equilibrium, especially when the stress-induced flux $\mathbf{J}^{\text{cp}} \neq 0$. In this case, the discrepancy between the maxima and the minima of the equilibrium lithium concentration at equal average lithium concentration is lower for the one-dimensional particle model than for the two-dimensional particle model.

In Figs. 5.9(c) - 5.9(d), we can notice that the model dimensionality has a nonnegligible effect on the extrema of the hydrostatic stress σ_{h} . The curves shown in these figures demonstrate that the equilibrium hydrostatic stresses obtained by means of the two-dimensional particle model are generally lower than those obtained using the one-dimensional particle model. This result is consistent with the equilibrium elastic strain energy shown in Fig. 5.8(b) whose values evaluated at different average lithium concentration \bar{n} are generally lower in case of a two-dimensional particle model than in case of a one-dimensional particle model.

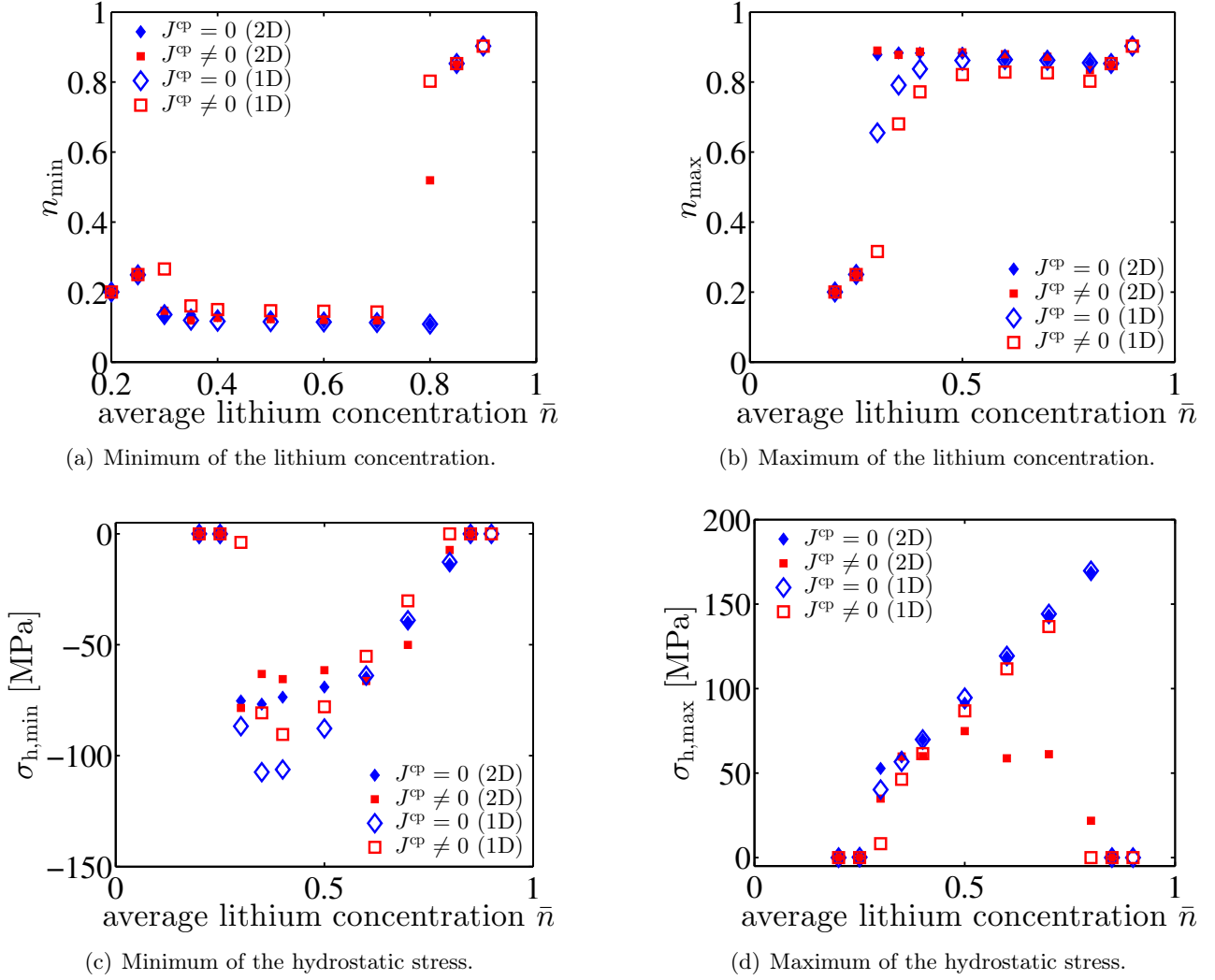


Figure 5.9: Extrema of the lithium concentration and of the hydrostatic stress at equilibrium in dependency of the average lithium concentration \bar{n} . These curves have been obtained during the process of lithium insertion at $C = 1$.

5.2 Equilibrium states of a particle of ellipsoidal symmetry

5.2.1 Influence of the particle aspect ratio

We here analyze the influence of the particle aspect ratio γ on the equilibrium phase-segregated states. To perform such a study, we make use of the two-dimensional particle model shown in Fig. 5.1 where both ellipsoidal and mirror symmetries are assumed.

For a better understanding of the influence of the particle aspect ratio γ on the system equilibrium states, we first neglect the lithium induced deformations and set $\mathbf{J}^{\text{cp}} = \mathbf{0}$. Fig. 5.10 shows, for different particle aspect ratios but constant particle volume equals $V_0 = (4/3)\pi(1\mu\text{m})^3$, the equilibrium phase-segregated states at $\bar{n} \approx 0.4$ obtained during both the processes of lithium insertion and extraction at $C = 1$. The applied flux at the particle surface has the same profile as the one shown in Fig. 5.4(b)

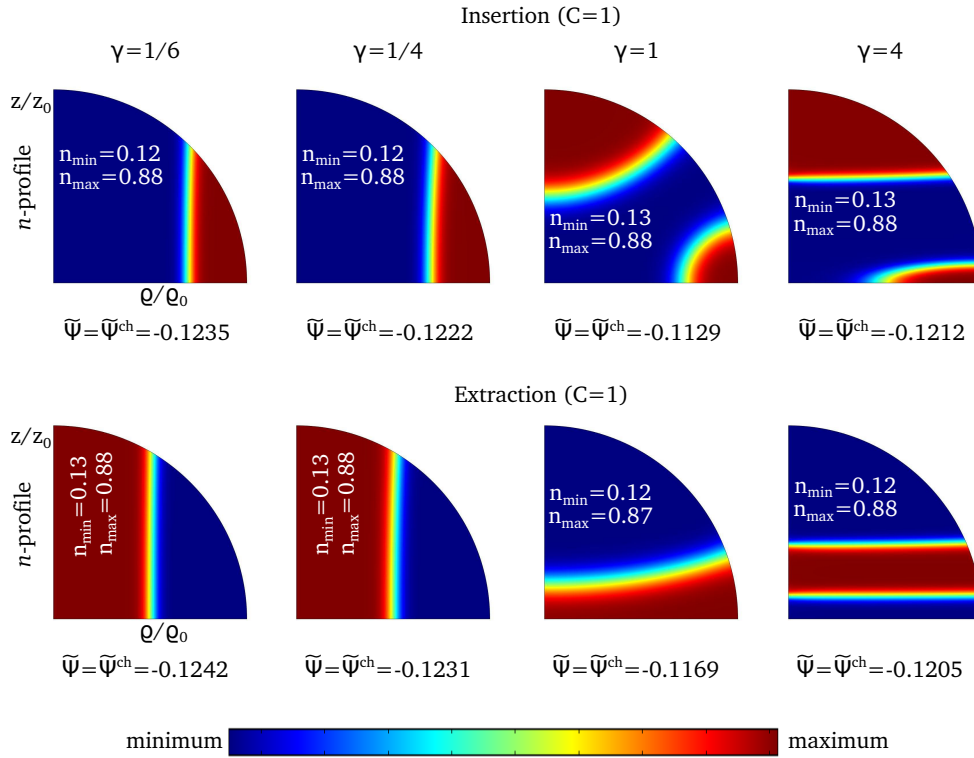


Figure 5.10: *Lithium concentration profiles and corresponding system free energy at equilibrium within particles of ellipsoidal symmetry and of different aspect ratios. By varying the particle aspect ratio γ , the volume of the particle was kept constant at $V_0 = (4/3)\pi\mu\text{m}^3$. The profiles shown here correspond to an average lithium concentration $\bar{n} \approx 0.4$ and have been obtained during the processes of lithium insertion and extraction at $C = 1$.*

where, during the hold times, the system relaxes towards equilibrium.

As for the spherical particle modeled by means of the two-dimensional particle model, see Sec. 5.1.2, the arising equilibrium states in particles of ellipsoidal symmetry with different aspect ratios strongly depend on the way the system has been driven into equilibrium. Indeed, as illustrated in Fig. 5.10, the equilibrium states obtained during the process of lithium insertion are different from those obtained

during the process of lithium extraction. Further, as indicated in Fig. 5.10 for the particular case where the average lithium concentration $\bar{n} \approx 0.4$, at given particle aspect ratio γ , the system free energy of two states with equal average lithium concentration \bar{n} do not necessary exhibit the same value.

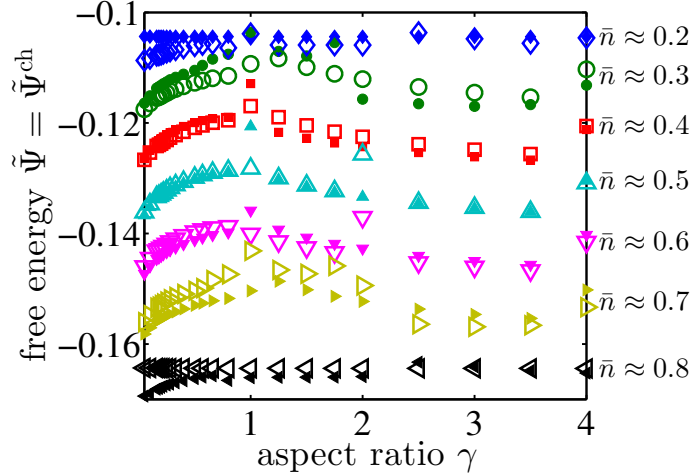


Figure 5.11: *Equilibrium system free energy as a function of the particle aspect ratio γ at different values of the average lithium concentration \bar{n} . These curves have been obtained at equilibrium during both the processes of lithium insertion and extraction at $C = 1$. The filled markers are related to the process of lithium insertion whereas the empty markers correspond to the process of lithium extraction. At $\bar{n} \approx 0.2$ during the process of lithium insertion as well as at $\bar{n} \approx 0.8$, during the process of lithium extraction the lithium concentration state is homogeneous which explains why the system free energy is independent of the particle aspect ratio.*

This is also illustrated in Fig. 5.11 which represents the system free energy at equilibrium in dependency of the particle aspect ratio γ for different fixed values of the average lithium concentration \bar{n} . These curves have been obtained during the processes of both lithium insertion and extraction.

From these curves, it can be shown that, at given average lithium concentration \bar{n} , the system free energy exhibits a relatively weak dependence on the particle aspect ratio γ . Depending on the average lithium concentration, the manner in which the system free energy depends on the particle aspect ratio may vary a little bit. By trend, we observe that the system free energy of the phase-segregated states exhibits a local maximum at around $\gamma \approx 1$. Note that this value may slightly differ depending on the average lithium concentration value as well as on whether lithium ions have been previously inserted or extracted. In general, we observe that, for flat-shaped particles ($\gamma < 1$), the system free energy decreases when the particle aspect ratio decreases. Differently, for elongated particles ($\gamma > 1$), with increasing values of the particle aspect ratio, the system free energy first decreases, reaches a local minimum and then increases.

We now analyze the influence of the particle aspect ratio γ on the path followed by the phase boundary. In the dilute solution approach, we saw that both the lithium concentration and the hydrostatic stress have the same symmetry as the particle geometry, as seen in Fig. 2.8 of Sec. 2.2.3.

In contrast to the dilute solution model, the equilibrium phase-segregated states obtained by means of the phase-field model do not exhibit such a symmetry, as it is illustrated in Fig. 5.10. Here, we observe that, for elongated particles with aspect ratio $\gamma > 1$, the phase boundary surface is almost

perpendicular to the rotation axis of the particles, i.e. the z -axis, whereas for flat-shaped particles with aspect ratio $\gamma < 1$, the phase boundary surface is almost parallel to this axis.

Such a behavior may have two different origins: First, we can invoke a history argument. In order to drive the system from one equilibrium situation to the other, a lithium flux has been applied at the particle surface which is such that its component normal to the boundary surface of the particle is constant. In Sec. 2.2.3 related to the dilute solution model, we saw that, due to their geometry, elongated particles ($\gamma > 1$) have more surface per unit of particle volume in the vicinity of the “pole”, ($\varrho = 0, z = z_0$), as compared to the “equator” region, ($\varrho = \varrho_0, z = 0$). Thus, during lithium insertion, there is an enhanced lithium accumulation in the pole regions as compared to the equator region. As a consequence, when phase segregation arises, the phase nucleation takes place in the vicinity of the particle “pole” which may enforce the formation of the phase boundary almost perpendicularly to the z -axis. For flat-shaped particles ($\gamma < 1$), analogous arguments hold, but with reversed role regarding the “pole” and the “equator”, explaining the formation of the phase boundary parallel to the z -axis.

Another possible explanation to justify the formation of such lithium concentration profiles is to invoke an energy argument. Due to the particle geometry, in very elongated particles ($\gamma \gg 1$), the proportion of phase boundary in the particle is minimal when the phase boundary is located perpendicularly to the z -axis. In contrast, for very flat-shaped particles ($\gamma \ll 1$), the proportion of phase boundary in the particle is minimal when the phase boundary is parallel to the z -axis. In Sec. 4.1.2 related to the equilibrium states of spherically symmetric particles, we saw, that the free energy of the equilibrium phase-segregated states increases when the proportion of phase boundary in the particle increases, provided that the lithium induced deformations are neglected. In this case, the system free energy is minimal when the the proportion of phase boundary in the particle is as low as possible which may explain why the lithium concentration profiles are such that the phase boundary forms almost perpendicularly to the z -axis in elongated particles ($\gamma > 1$) and almost parallel to this axis in flat-shaped particles ($\gamma < 1$).

From these arguments, it follows that, in many cases, the phase boundary does not remain confined inside of the particle like it is the case for spherical particles modeled by means of the one-dimensional particle model. This remark is also true for spherical particles ($\gamma = 1$), see Sec. 5.1. Using the two-dimensional particle model, we observed that numerous equilibrium phase-segregated states exhibit a phase boundary going across the particle boundary surface, independently of the particle aspect ratio γ and of the average lithium concentration \bar{n} . Note that, after formation of a particular lithium concentration profile, it becomes difficult, due to the low applied flux magnitude, to drive the system into another equilibrium situation even if, upon change of the average lithium concentration \bar{n} , another lithium concentration profile would be energetically favorable.

At this place, we should note that the equilibrium position of a phase boundary going across the boundary surface of the particle is not arbitrary. At equilibrium, the conservation of matter, Eq. (3.97), is ensured provided that the local lithium flux $\mathbf{J} = \mathbf{J}^{\text{ch}}$ satisfies

$$\mathbf{J} \cdot \mathbf{n} \Big|_{\partial V_0} = \mathbf{J}^{\text{ch}} \cdot \mathbf{n} \Big|_{\partial V_0} = 0, \quad (5.5)$$

at the particle boundary surface ∂V_0 oriented, as usual, by the outgoing normal \mathbf{n} . Eq. (5.5) represents a constraint, e.g. a differential equation for n , to be fulfilled at the particle boundary surface. Combined with the local law of lithium conservation matter, this constraint may play an important role regarding the orientation of the phase boundary layer going across the particle boundary surface.

5.2.2 Effect of the lithium induced deformations

In this part, we study the effect of the lithium-induced deformations, neglected until now, on the equilibrium phase-segregated states arising in particles of ellipsoidal symmetry with different particle aspect ratios. The influence of the particle aspect ratio γ on the stresses arising at equilibrium is also analyzed.

Fig. 5.12 shows, for different particle aspect ratio and constant average lithium concentration $\bar{n} \approx 0.4$, both the equilibrium lithium concentration and hydrostatic stress profiles obtained when neglecting the stress-induced lithium flux, e.g. $\mathbf{J}^{\text{cp}} = \mathbf{0}$, on the one hand, and when considering it, e.g. $\mathbf{J}^{\text{cp}} \neq \mathbf{0}$, on the other hand.

At the first glance, considering the stress-induced lithium flux does not engender significant modifications regarding the position of the phase boundary except for nearby spherical particles ($\gamma \approx 1$). We here invoke the same history and energy arguments as those invoked in the previous section, Sec. 5.2.1, in order to explain the obtained equilibrium lithium concentration profiles in a context where the lithium-induced deformations were neglected: The history argument is that the phase nucleation arises at the spatial location where the lithium concentration deviates at the most from its average value, i.e. in the “pole” regions for elongated particles ($\gamma > 1$) or in the “equator” region for flat-shaped particles ($\gamma < 1$).

The energy argument is that the equilibrium profiles of the lithium concentration n and of the mechanical displacement \mathbf{u} are such that the system free energy, being the sum of the chemical free energy and the elastic strain energy, is minimal. In the previous section (Sec. 5.2.1), we pointed out that the chemical free energy of the system reaches a minimum when the proportion of phase boundary in the particle is as low as possible.

In the one-dimensional particle model related to particles of spherical symmetry, only homogeneous lithium concentration profiles lead to a minimal elastic strain energy value, i.e. equals zero. Thus, for phase-segregated states with large lithium concentration gradients at the phase boundary, the contribution of the elastic strain energy to the total free energy of the system becomes (strictly) positive and stresses are induced in the particle, see in Sec. 4.1.3. This is due to the fact that, for spherically symmetric particles, the relation,

$$\varepsilon_{ij} = \varepsilon_{ij}^{\text{Li}}, \quad (5.6)$$

between the total strains ε_{ij} and the lithium-induced strains $\varepsilon_{ij}^{\text{Li}}$ cannot be satisfied when the lithium concentration n is not equal to a constant value, see Eq. (4.9) of Sec. 4.1.3.

In the two-dimensional particle model related to particles of ellipsoidal symmetry, we demonstrated in the dilute solution approach, see Sec. 2.2.3, that the diagonal, i.e. $(\rho\rho)$ -, $(\theta\theta)$ -, (zz) -components of Eq. (5.6) can be fulfilled provided that the lithium concentration n depends on the z -coordinate only,

$$n(\rho, z) = n(z),$$

see Eqs. (2.69) - (2.70) of Sec. 2.2.3. As a consequence, we conclude that, in the two-dimensional particle model, the phase-segregated states minimizing the elastic strain energy are those for which the phase boundary is perpendicular to the z -axis without ρ -dependence for the lithium concentration n .

When considering nonvanishing lithium-induced deformations, the energetically favorable states are those that minimize the sum of the chemical free energy and the elastic strain energy. Such states generally do not minimize at the same time both the chemical free energy and the elastic strain energy, separately considered. In combination with the history reason, this may explain why the equilibrium

phase-segregated states obtained for $\mathbf{J}^{\text{cp}} \neq \mathbf{0}$, shown in Fig. 5.12 do not necessary exhibit a phase boundary which is always oriented perpendicularly to the z -axis.

Note that at equilibrium the lithium flux $\mathbf{J} = \mathbf{J}^{\text{ch}} + \mathbf{J}^{\text{cp}}$ must satisfy

$$\mathbf{J} \cdot \mathbf{n} \Big|_{\partial V_0} = \left(\mathbf{J}^{\text{ch}} + \mathbf{J}^{\text{cp}} \right) \cdot \mathbf{n} \Big|_{\partial V_0} = 0, \quad (5.7)$$

at the particle boundary surface ∂V_0 in order to ensure the conservation of lithium matter within the particle, Eq. (3.97). Eq. (5.7) represents a constraint which, combined with the local conservation of matter, may have an influence on the orientation of the phase boundary layer going across the particle boundary surface. For $\mathbf{J}^{\text{cp}} \neq \mathbf{0}$, this condition is different from Eq. (5.5) where the stress-induced lithium flux is neglected, $\mathbf{J}^{\text{cp}} = \mathbf{0}$. Thus, depending on whether $\mathbf{J}^{\text{cp}} = \mathbf{0}$ or $\mathbf{J}^{\text{cp}} \neq \mathbf{0}$, Eq. (5.7) may also play a role regarding the obtained equilibrium states of the system.

Fig. 5.13 represents, at equilibrium, the chemical free energy as well as the elastic strain energy in dependency of the particle aspect ratio γ for different values of the average lithium concentration \bar{n} . Two different cases are considered: the case where $\mathbf{J}^{\text{cp}} = \mathbf{0}$ on the one hand and the case where $\mathbf{J}^{\text{cp}} \neq \mathbf{0}$ on the other hand.

Fig. 5.13(a) demonstrates that, at given particle aspect ratio and average lithium concentration, considering the stress-induced lithium flux does not have a significant influence on the values of the chemical free energy at equilibrium.

As seen in Figs. 5.13(b) - 5.13(c), the effect of the stress-induced flux on the equilibrium elastic strain energy is more significant than its effect on the equilibrium chemical free energy. Here, we observe that the elastic strain energy is generally significantly lower when considering a nonvanishing stress-induced flux than when neglecting it. This is particularly true for flat-shaped particles ($\gamma < 1$). Indeed, in such particles, due to the history reason, the phase boundary forms almost parallel to the z -axis. This corresponds to a situation where the elastic strain energy is higher than in the situation where the phase boundary is almost perpendicular to this axis. Differently, for elongated particles ($\gamma \gg 1$), also due to the history reason, the phase boundary forms almost perpendicular to the z -axis. Such a situation corresponds to a situation where the elastic strain energy is nearby to its minimum. Thus, for elongated particles ($\gamma > 1$), the discrepancy between the case where $\mathbf{J}^{\text{cp}} = \mathbf{0}$ and the case $\mathbf{J}^{\text{cp}} \neq \mathbf{0}$ is not such important than for flat-shaped particles ($\gamma < 1$).

Fig. 5.14 shows at equilibrium the extrema of the lithium concentration n as a function of the particle aspect ratio γ for different values of the average lithium concentration \bar{n} in the case where $\mathbf{J}^{\text{cp}} = \mathbf{0}$, on the one hand, and in the case where $\mathbf{J}^{\text{cp}} \neq \mathbf{0}$, on the other hand. This figure demonstrates that the particle aspect ratio as well as the average lithium concentration only have a very slight influence on both the minima and the maxima of the equilibrium lithium concentration. In contrast, as it has also been shown in Sec. 5.1.3 related to particles of spherical symmetry, the consideration of the stress-induced lithium flux has a more significant influence on the values of these extrema whose discrepancy, at given particle aspect ratio and average lithium concentration, becomes smaller when the stress-induced flux does not vanish.

Differently, we can see in Fig. 5.15 that the particle aspect ratio γ as well as the average lithium concentration \bar{n} strongly influence the arising stresses at equilibrium. By trend, independently of the particle aspect ratio, we observe that the hydrostatic stress magnitude becomes larger when the average lithium concentration increases. Further, at fixed average lithium concentration \bar{n} , both the minima and the maxima of the hydrostatic stress reach their extremum when the particle aspect ratio is about $\gamma \approx 1$. When the stress-induced lithium flux is nonzero, the hydrostatic stresses are generally lower as

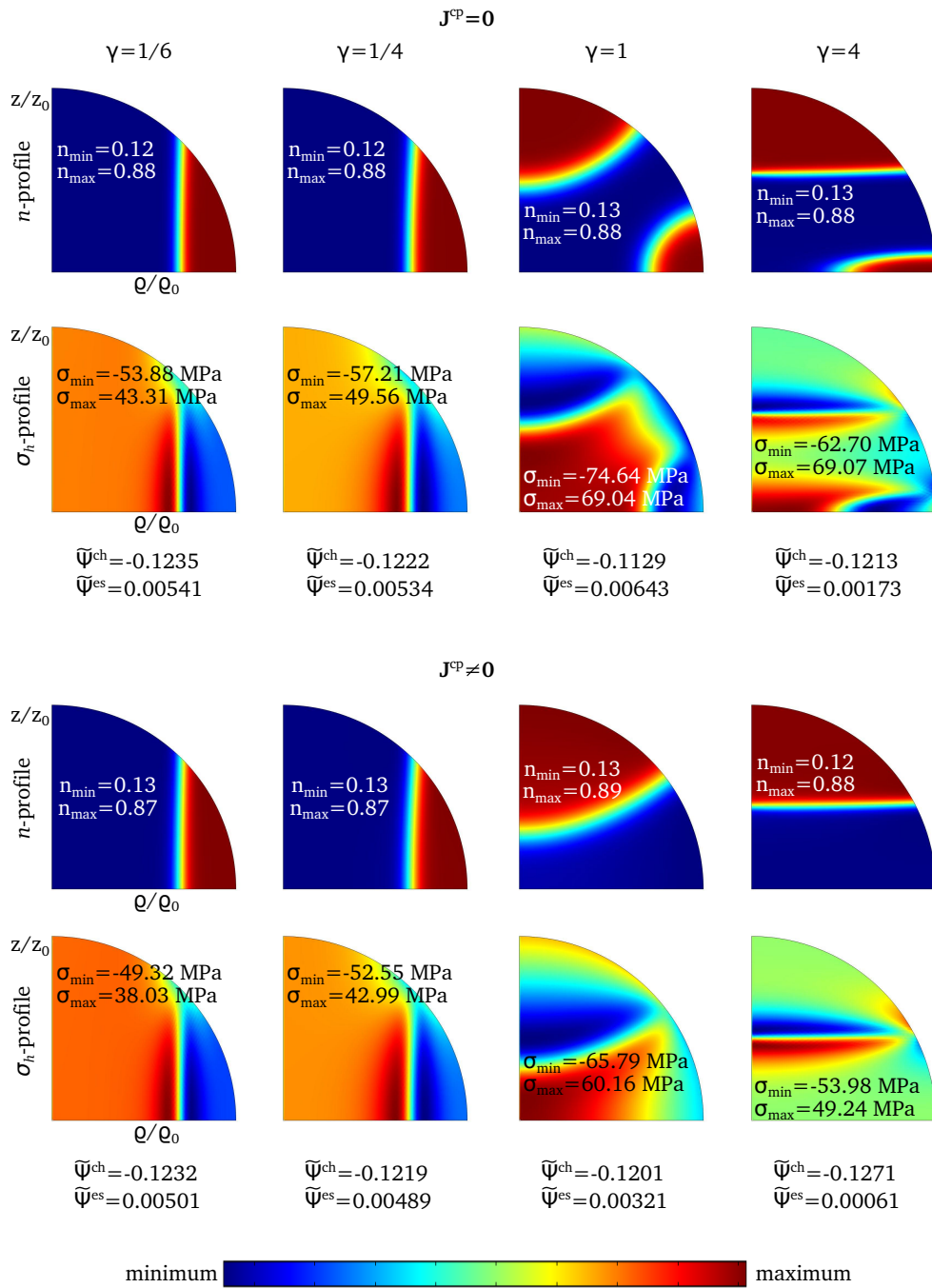


Figure 5.12: Lithium concentration and hydrostatic profiles obtained at equilibrium when $\bar{n} \approx 0.4$ for different values of particle aspect ratio γ . The profiles shown here have been obtained during the process of lithium insertion at $C = 1$. They are related to two different cases corresponding to $J^{\text{cp}} = 0$, on the one hand, and $J^{\text{cp}} \neq 0$, on the other hand.

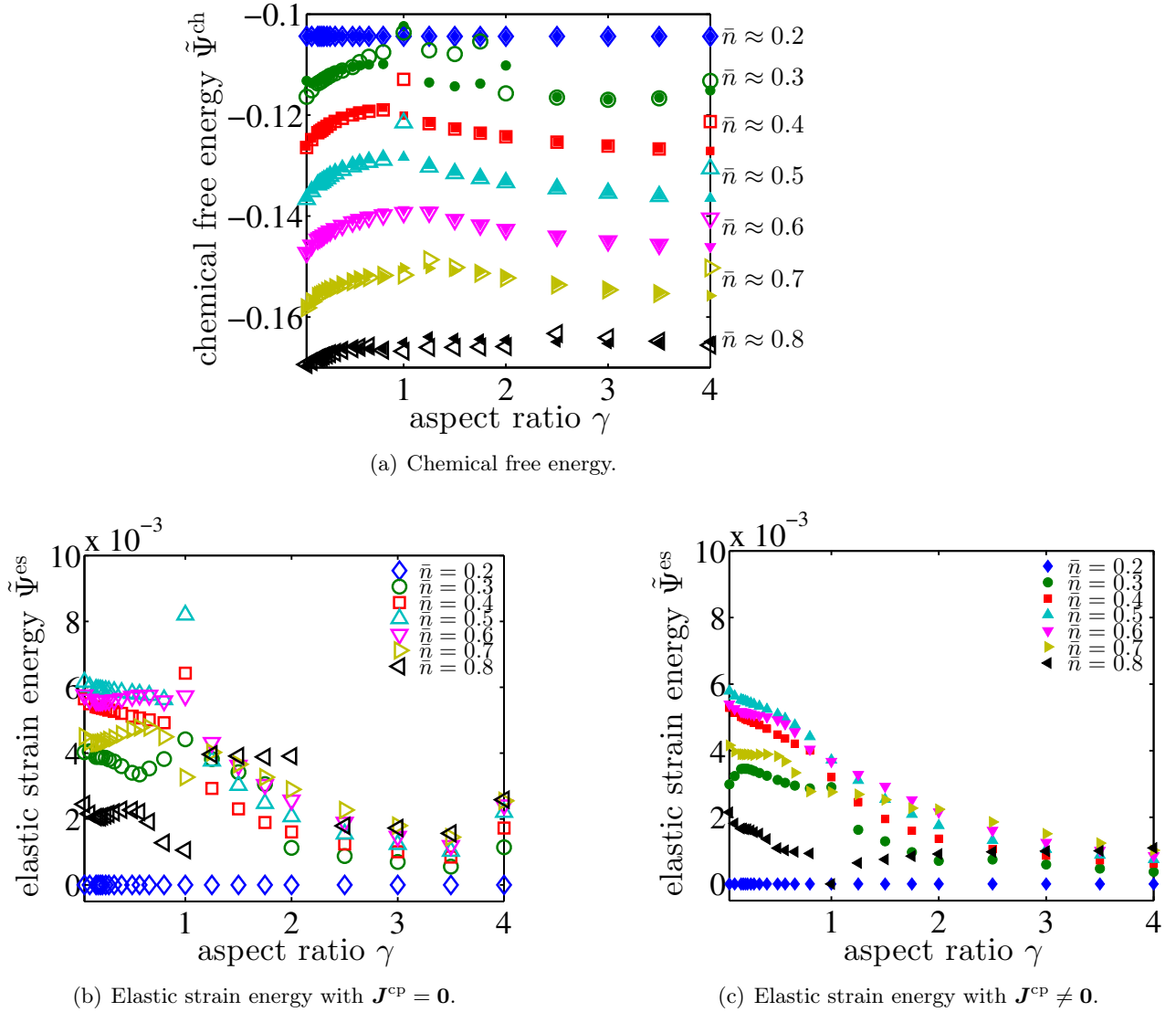


Figure 5.13: Chemical free energy and elastic strain energy at equilibrium in dependency of the particle aspect ratio γ for different values of the average lithium concentration \bar{n} . These curves have been obtained during the process of lithium insertion at $C = 1$ and illustrate the influence of the consideration or not of the stress-induced lithium flux on both the chemical and elastic contributions to the total system free energy. The filled markers are related to the case where $\mathbf{J}^{\text{cp}} = \mathbf{0}$ whereas the empty markers correspond to the case where $\mathbf{J}^{\text{cp}} \neq \mathbf{0}$.

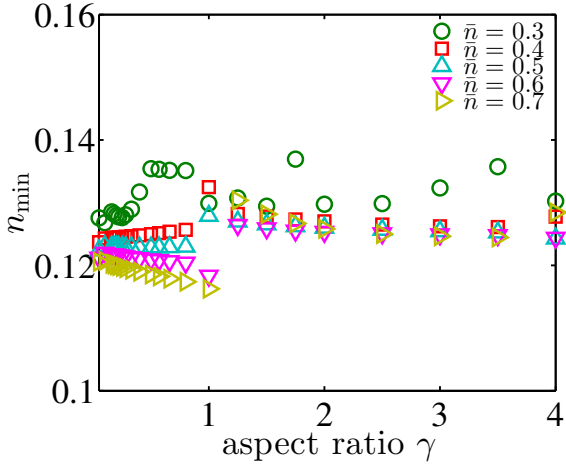
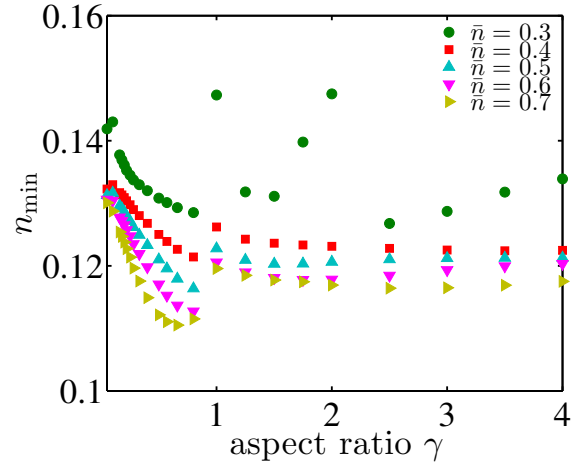
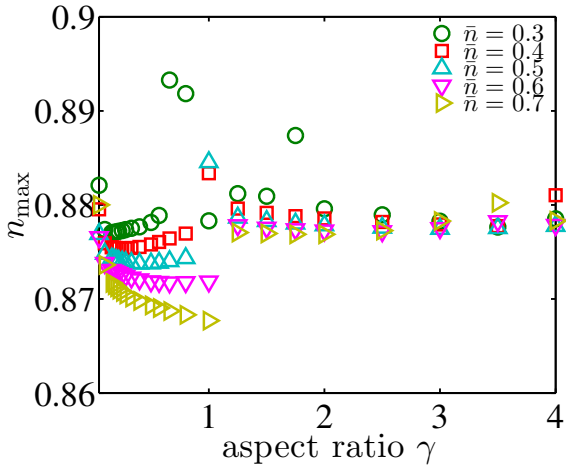
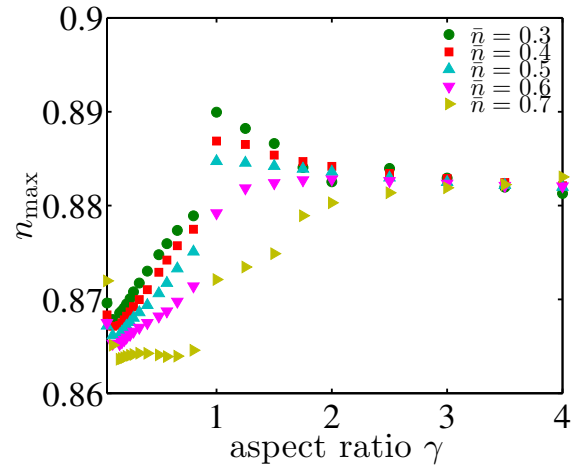

 (a) Minima of the lithium concentration with $\mathbf{J}^{\text{cp}} = \mathbf{0}$.

 (b) Minima of the lithium concentration with $\mathbf{J}^{\text{cp}} \neq \mathbf{0}$.

 (c) Maxima of the lithium concentration with $\mathbf{J}^{\text{cp}} = \mathbf{0}$.

 (d) Maxima of the lithium concentration with $\mathbf{J}^{\text{cp}} \neq \mathbf{0}$.

Figure 5.14: Extrema of the lithium concentration at equilibrium in dependency of the particle aspect ratio γ for phase-segregated states of different average lithium concentration \bar{n} . These curves have been obtained during the process of lithium insertion at $C = 1$. The filled markers are related to the case where $\mathbf{J}^{\text{cp}} = \mathbf{0}$ whereas the empty markers correspond to the case where $\mathbf{J}^{\text{cp}} \neq \mathbf{0}$.

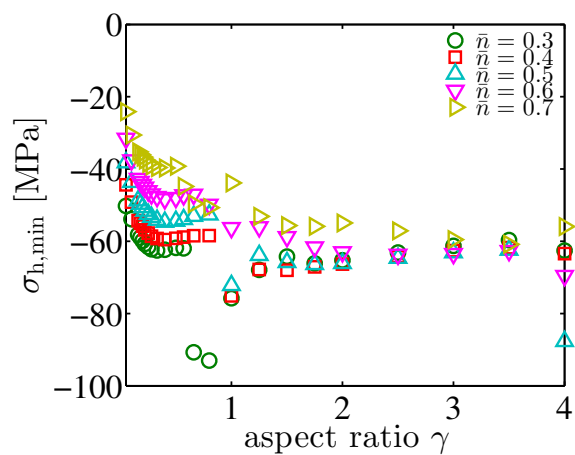
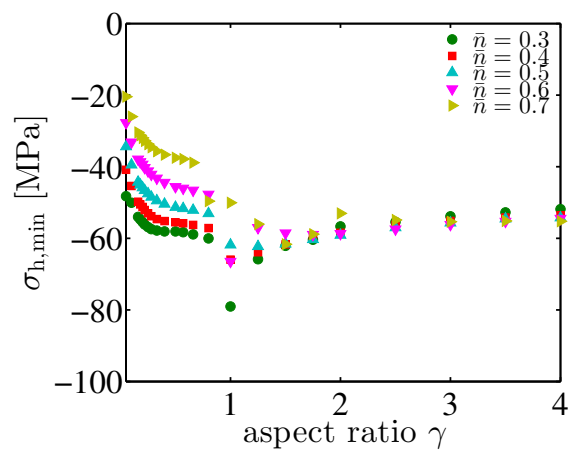
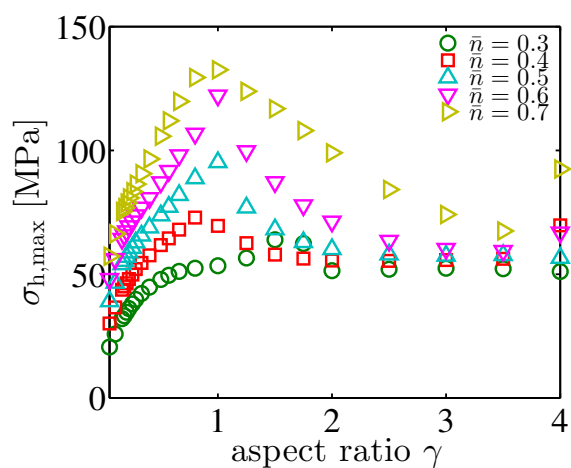
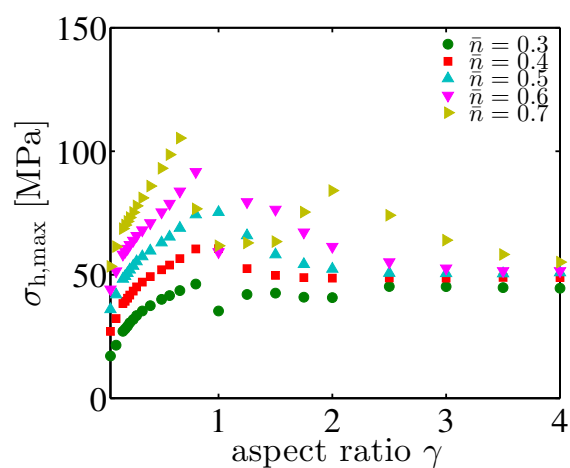
(a) Minima of the hydrostatic stress with $J^{\text{cp}} = \mathbf{0}$.(b) Minima of the hydrostatic stress with $J^{\text{cp}} \neq \mathbf{0}$.(c) Maxima of the hydrostatic stress with $J^{\text{cp}} = \mathbf{0}$.(d) Maxima of the hydrostatic stress with $J^{\text{cp}} \neq \mathbf{0}$.

Figure 5.15: Extrema of the hydrostatic stress at equilibrium in dependency of the particle aspect ratio γ for phase-segregated states of different average lithium concentration \bar{n} . These curves have been obtained during the process of lithium insertion at $C = 1$. The filled markers are related to the case where $J^{\text{cp}} = \mathbf{0}$ whereas the empty markers correspond to the case where $J^{\text{cp}} \neq \mathbf{0}$.

compared to the case where this flux is set equal to zero. As compared to elongated particles ($\gamma > 1$), this behavior is enhanced for flat-shaped particles ($\gamma < 1$). Indeed, in case of flat-shaped particles ($\gamma < 1$), the phase boundary forms almost parallel to the z -axis which corresponds to a situation where the elastic strain energy is higher than in the situation where the phase boundary is almost perpendicular to this axis, like it is the case for elongated particles ($\gamma > 1$).

In Fig. 5.16, the extrema of the hydrostatic stress reached at equilibrium during the whole process of lithium insertion are shown as a function of the particle aspect ratio γ . At this place, we can see that, differently from the one-dimensional particle model related to spherically symmetric particles, the maximum of the hydrostatic stress magnitude corresponds to a positive stress. From this figure, it appears that the minimum of the hydrostatic stress is attained when the particle aspect ratio is about $\gamma \approx 1$. Regarding the maximum of the hydrostatic stress, its variation as a function of the particle aspect ratio exhibits oscillations which are difficult to be properly interpreted.

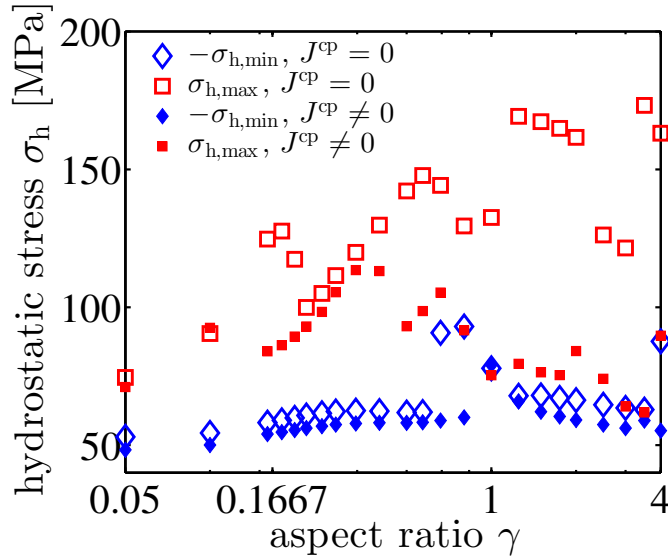


Figure 5.16: Maximum of the hydrostatic stress magnitude reached at equilibrium during the whole process of lithium insertion at $C = 1$ in dependency of the particle aspect ratio γ .

5.3 Dynamical states of a particle of ellipsoidal symmetry

In this part, we analyse the influence of the particle aspect ratio on the dynamical states of the system. To achieve that purpose, a lithium flux of constant magnitude is applied at the surface of the particle without hold times. We here restrict our study to the states obtained during lithium extraction starting from a homogenous high lithium concentration state whose average value $\bar{n} = 1$.

Figs. 5.17 - 5.18 show, for particles of ellipsoidal symmetry with different aspect ratios, the lithium concentration and hydrostatic stress profiles reached at the particular time when the average lithium concentration $\bar{n} \approx 0.5$. The profiles shown in Fig. 5.17 have been obtained at a relatively low applied flux magnitude corresponding to $C = 1$ whereas, the profiles shown in Fig. 5.18 have been obtained at a relatively large applied flux magnitude, $C = 20$. For these two different applied flux magnitudes, we further compare the profiles obtained when the stress-induced lithium flux J^{cp} is neglected to those obtained when this flux is different from zero.

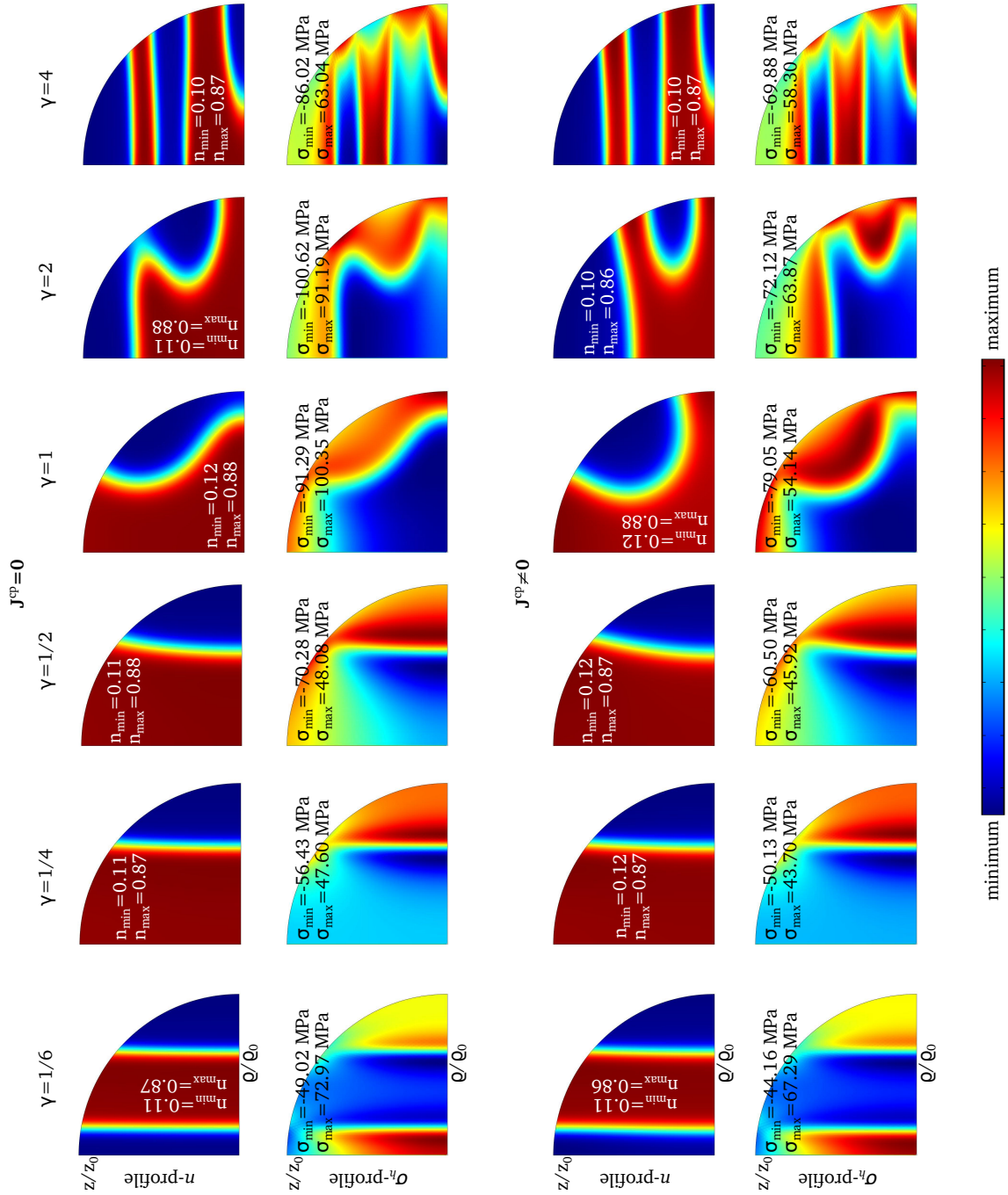


Figure 5.17: Lithium concentration and hydrostatic profiles obtained during lithium extraction at constant applied flux magnitude when $\bar{n} \approx 0.5$ for different values of the particle aspect ratio γ . The extraction rate at the particle surface is relatively low, $C = 1$. The profiles shown here are related to the case where $\mathbf{J}^{\text{cp}} = \mathbf{0}$, on the one hand, and to the case where $\mathbf{J}^{\text{cp}} \neq \mathbf{0}$, on the other hand.

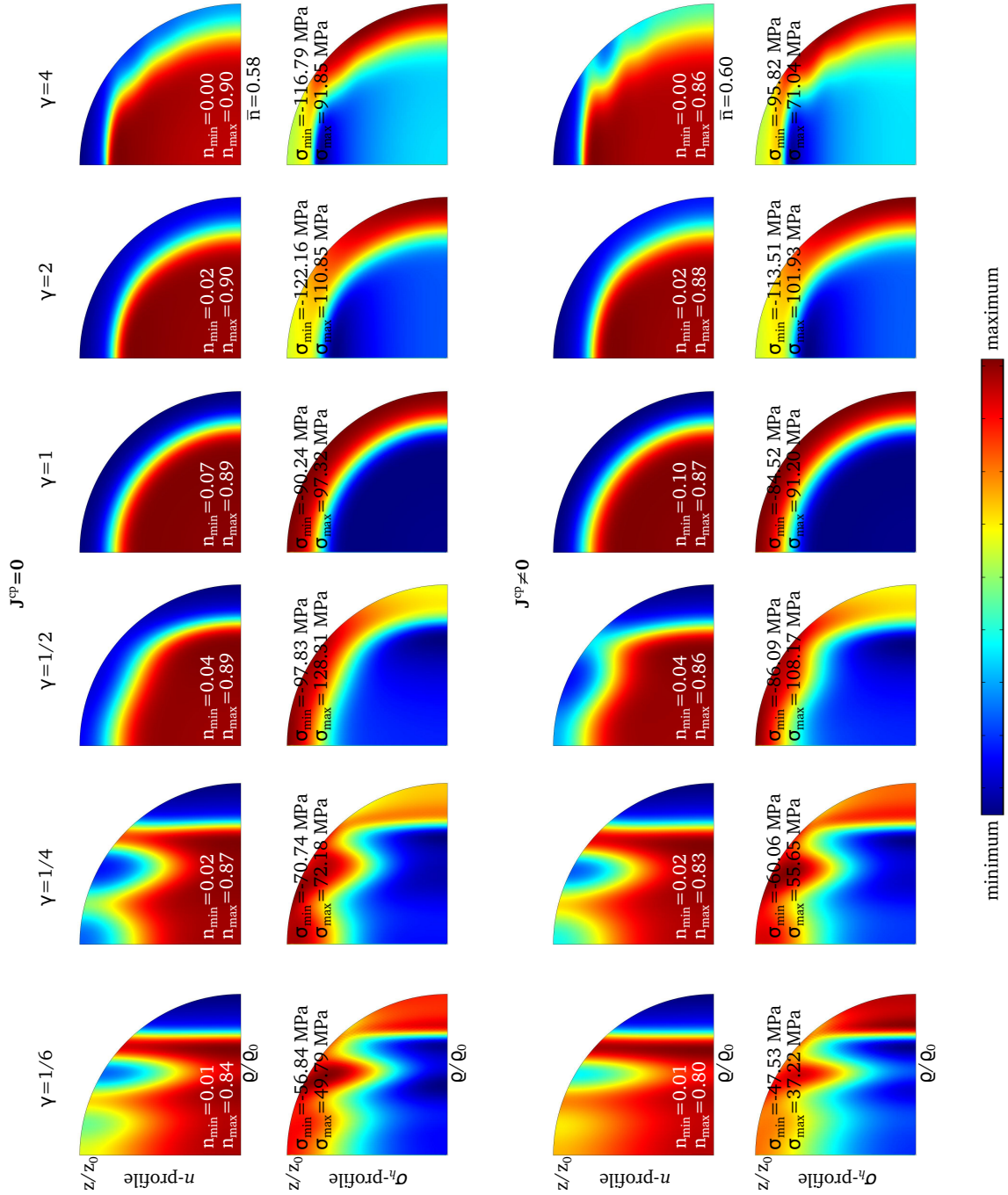


Figure 5.18: *Lithium concentration and hydrostatic profiles obtained during lithium extraction at constant applied flux magnitude when $\bar{n} \approx 0.5$ for different values of the particle aspect ratio γ . The extraction rate at the particle surface is relatively large, $C = 20$. The profiles shown here are related to the case where $\mathbf{J}^{\text{cp}} = \mathbf{0}$, on the one hand, and to the case where $\mathbf{J}^{\text{cp}} \neq \mathbf{0}$, on the other hand.*

Here, we can see that, as expected, considering the stress-induced lithium flux does not lead to drastic modifications of the lithium concentration and hydrostatic stress profiles. In agreement with the results related to the equilibrium situation analyzed in the previous section, Sec. 5.2.2, we observe that, independently of the particle aspect ratio γ , the hydrostatic stress are larger for $\mathbf{J}^{\text{cp}} = \mathbf{0}$ than for $\mathbf{J}^{\text{cp}} \neq \mathbf{0}$.

Differently than for the dilute solution model, see Sec. 2.2.3, we notice that, in phase-field modeling, the applied flux magnitude play an important role regarding the obtained lithium concentration and hydrostatic stress profiles.

For the lower applied flux magnitude, e.g. $C = 1$, the lithium concentration and hydrostatic stress profiles, shown in Fig. 5.17, exhibit similarities with those obtained at equilibrium, see Fig. 5.12 for comparison. For elongated particles ($\gamma > 1$), the phase boundary is almost perpendicular to the z -axis whereas, for flat-shaped particles ($\gamma < 1$), the phase boundary is almost parallel to this axis. Independently of the particle aspect ratio, we see that the particle states do not exhibit the same symmetry as the particle geometry.

The situation is rather different for the higher applied flux magnitude, e.g. $C = 20$ (see Fig. 5.18). Here, similarly to the states obtained at equilibrium, very flat-shaped particles, e.g. $\gamma = 1/6$ and $\gamma = 1/4$, exhibit a phase boundary which is almost parallel to the z -axis. In contrast, for nearly spherical particles, e.g. $\gamma = 1/2$, $\gamma = 1$ and $\gamma = 2$ as well as for very elongated particles, $\gamma = 4$, the obtained system states have approximately the same symmetry as the particle geometry.

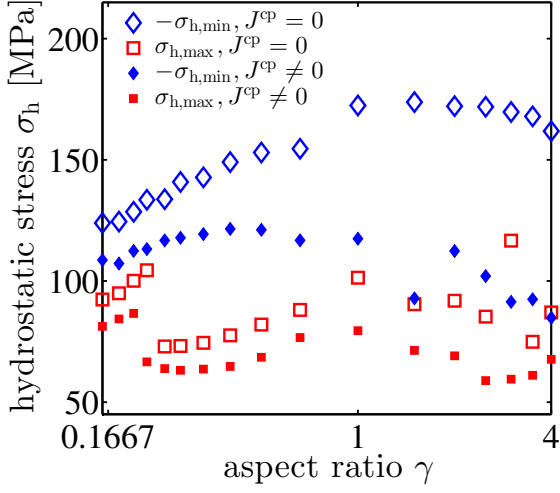
In order to understand the influence of the applied flux magnitude on the phase-segregated states that form during particle unloading, we may consider the time when phase segregation occurs. At this time, the average lithium concentration \bar{n} in the particle is such that the “nucleation zone” of the mean-field free energy is reached and, within the particle, there is at least one spatial location where the lithium concentration attains a value corresponding to the “spinodal zone” of the mean-field free energy.

For particles whose aspect ratio strongly deviates from one, at both low and large applied flux magnitudes, there is a large lithium concentration gradient between the “pole” regions and the “equator” region. Thus, depending on whether the aspect ratio $\gamma \gg 1$ or $\gamma \ll 1$, the “spinodal zone” of the mean-field free energy is reached either in the “pole” regions or in the “equator” region, respectively.

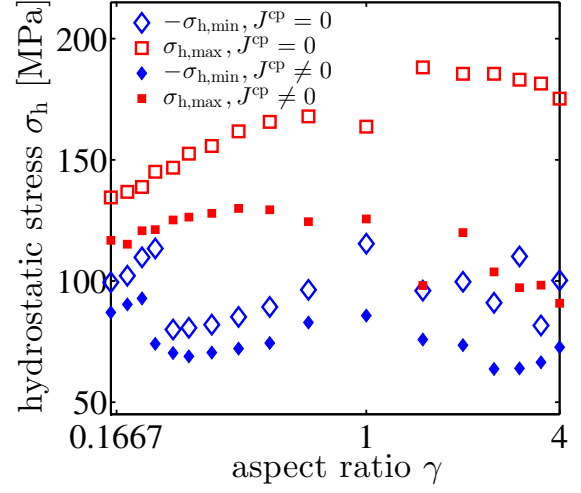
Differently, for nearly spherical particles ($\gamma \approx 1$), the lithium concentration gradient between the “pole” and the “equator” regions is not as high as the one that holds in very elongated or very flat-shaped particles. In that case, at low applied flux magnitude, the “spinodal zone” of the free energy is reached either in the “pole” or in the “equator” regions, whereas, at large applied flux magnitude, this zone is simultaneously reached in both the “pole” and the “equator” regions.

To conclude this part, we show in Fig. 5.19, the extrema of the hydrostatic stress as a function of the particle aspect ratio γ . The curves shown in Figs. 5.19(a) - 5.19(c) and in Figs. 5.19(b) - 5.19(d) have been obtained during lithium extraction from and insertion into the particle, respectively. Figs. 5.19(a) - 5.19(b) and Figs. 5.19(c) - 5.19(d) correspond to a constant applied flux magnitude equal to $C = 1$ and $C = 20$, respectively. In each of these figures, two different cases have been considered: the case where the stress-induced lithium flux is neglected, i.e. $\mathbf{J}^{\text{cp}} = \mathbf{0}$ and the case where this flux does not vanish, i.e. $\mathbf{J}^{\text{cp}} \neq \mathbf{0}$.

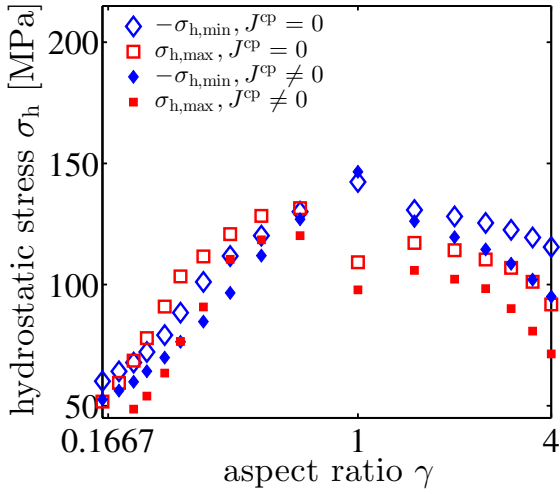
For the lower applied flux magnitude, e.g. $C = 1$, during lithium extraction, the maximum of the hydrostatic stress is reached at the time when phase segregation arises whereas the minimum of the hydrostatic stress is attained at the end of the phase segregation just before the particle state transforms back to a homogeneous state. This behavior is reversed if lithium ions are inserted instead of being



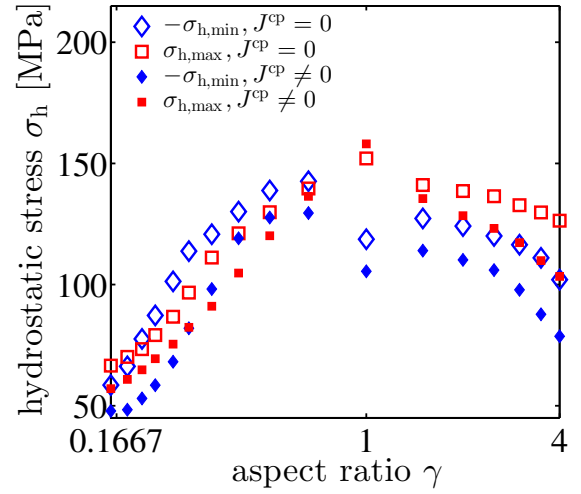
(a) Extrema of the hydrostatic stress obtained during lithium extraction at constant applied flux magnitude $C = 1$.



(b) Extrema of the hydrostatic stress obtained during lithium insertion at constant applied flux magnitude $C = 1$.



(c) Extrema of the hydrostatic stress obtained during lithium extraction at constant applied flux magnitude $C = 20$.



(d) Extrema of the hydrostatic stress obtained during lithium insertion at constant applied flux magnitude $C = 20$.

Figure 5.19: Extrema of the hydrostatic stress obtained for different applied flux magnitude during both lithium extraction from and insertion into ellipsoidal particles in dependency of the particle aspect ratio γ .

extracted. Differently, for the larger applied flux magnitude, e.g. $C = 20$, during both lithium insertion and extraction, the stop condition at the particle surface, see Eq. (2.21), is reached at a time which is significantly before the system has arrived back at the homogeneous state. In this case, both the maximum and minimum values of the hydrostatic stress are attained at the time when the stop condition is fulfilled. At this place, we refer to Sec. 4.2.2 where the variation of the maximum of the hydrostatic stress magnitude in dependency with the applied flux magnitude for a particle of spherical symmetry has been analysed. From this study, we may easily understand why the maximum of the hydrostatic stress magnitude is remarkably higher for the lower applied flux magnitude: The case where $C = 1$ corresponds to the regime ① of Fig. 4.18 whereas the case where $C = 20$ corresponds to the regime ② of this figure.

The curves shown in Fig. 5.19 demonstrate that the extrema of the hydrostatic stress strongly depend on the particle aspect ratio γ . The manner that the extrema of the hydrostatic stress depend on the particle aspect ratio is however also strongly dependent on the value of the applied flux magnitude as well as on whether lithium is inserted into or extracted from the particle, which indicates the importance of the system history on the arising states of the system.

At low applied flux magnitude, the variation of the extrema of the hydrostatic stress in dependency of the particle aspect ratio γ exhibit some oscillations which are similar to those obtained at equilibrium, see Fig. 5.16. At large applied flux magnitude, we observe that, during lithium extraction, the quantity $-\sigma_{h,\min}$ exhibits a maximum at $\gamma = 1$. For particles of aspect ratio $\gamma < 1$, this quantity increases with increasing values of the particle aspect ratio, whereas, for particles of aspect ratio $\gamma > 1$, it decreases with increasing values of the particle aspect ratio. The hydrostatic stress maximum $\sigma_{h,\max}$ as a function of the particle aspect ratio shows two local maxima located in the neighborhood of $\gamma = 1$, at $\gamma \lesssim 1$ and at $\gamma \gtrsim 1$, as well as a minimum at $\gamma = 1$. During lithium insertion the behaviors of $-\sigma_{h,\min}$ and $\sigma_{h,\max}$ are reversed.

Conclusion

In this chapter we focussed on the study of the system states using the two-dimensional particle model where the unknown functions of the problem, the lithium concentration and the mechanical displacement, exhibit a lower symmetry than in the one-dimensional particle.

Differently from the dilute solution approach, it was found that, in the phase-field model, the system states obtained by means of the two-dimensional particle model do not have the same symmetry as the particle geometry, especially at low applied flux magnitude. From this observation, we conclude that the assumption that both the lithium concentration and the mechanical displacement fulfill several conditions of symmetry is not completely justified for the purpose of modeling a particle located at the cathode of a porous LIB, even in the case that the considered cathodic particle exhibits a perfectly spherical shape with a homogeneous applied normal lithium flux at its surface.

In this part, we showed that the system states of a spherical particle obtained using the two-dimensional particle model are significantly different from those obtained by means of the one-dimensional particle model. Further, we demonstrated that the stresses obtained in the particle model of spherical symmetry are always larger than those obtained in the particle model of ellipsoidal symmetry.

By means of the two-dimensional particle model, an analysis of the influence of the particle aspect ratio on both the equilibrium and dynamical states was performed. At equilibrium, we saw that the system history, i.e. the way to drive the system from an equilibrium state to another equilibrium state, plays an important role for the arising equilibrium state which is somehow more significant than the

role played by the system free energy of the corresponding equilibrium state. For the same history reason, we found that the dynamical states exhibited by particles of ellipsoidal symmetry were strongly dependent on the applied flux magnitude.

Finally, we performed at equilibrium as well as under dynamical particle loading and unloading, a study of the arising stresses in the particle, which were found to be strongly dependent on the particle aspect ratio.

6 Chapter 6

Conclusion

This work was devoted to the understanding of the mechanical behavior of a particle made of LMO that is located in the cathode of a porous LIB. Differently from many existing particle models that account for lithium-induced deformations in the dilute solution approach solely, we here used a phase-field model coupled to mechanics.

Indeed, there exist numerous experimental measurements as well as ab-initio calculations indicating that two distinguishable cubic phases coexist in the cathodic material, $\text{Li}_x\text{Mn}_2\text{O}_4$, when the state of charge $0 < x < 1$. During battery charging and discharging the state of charge is usually varied between zero and one. Thus, over battery charging and discharging, phase segregation may arise within the particle. The occurrence of phase segregation was thought as a possible explanation for the battery capacity fade which is considered as a consequence of large mechanical stresses arising within cathodic particles.

By means of a phase-field model coupled to mechanics, it was possible to account for the phase-segregated lithium-concentration states as well as for the deformations induced by the lithium intercalation. At this place, we demonstrated that, the existence of an interfacial boundary layer, which separates regions with different lithium concentrations, leads to large stresses in the particle. Thus, in case of phase segregation, the equilibrium situations obtained in phase-field modeling were found to be completely different from those obtained in the commonly used dilute solution approach where the equilibrium lithium-concentration states are homogeneous and hence stress-free.

Using the dilute solution model, we perform a dynamical study from which we concluded that the occurrence of large stresses within the particle is a consequence of large lithium concentration gradients. In this approach, large lithium concentration gradients arise only if the particle is driven significantly far away from equilibrium. Such a situation results for example from the application of a large lithium flux at the particle surface. Here we found that with increasing values of the applied flux magnitude, the stresses within the particle increase. For very small applied lithium flux at the particle surface, the particle is in a quasi-equilibrium state and the arising stresses were almost vanishing.

In phase-field modeling, we also obtained that the increase of the lithium flux applied at the particle surface induces an increase of the stresses arising in the particle. However, in this context, the resulting stresses were found to be about hundred times larger than those obtained in the dilute solution model. Further, due to the occurrence of phase-segregation, the quasi-equilibrium phase-segregated states did not lead to insignificantly small stresses in the particle.

Another part of this work was to analyze the effect of the stress-induced lithium flux which is derived from the coupling system free energy. We found that this flux enhances the lithium ion homogenization

over the particle. Thus, as compared to the case where this flux was neglected, the arising stresses obtained in a context where the stress-induced lithium flux was nonzero were smaller. As a consequence, we found that this flux contributes together with the gradient term suppressing the phase segregation. We obtained that the consideration of nonvanishing lithium-induced deformations reduces the discrepancy between the lithium concentration values in the two different lithium-concentration phases, as compared to the case where the lithium-induced deformations were neglected.

We also study by means of a battery model, the so-called dualfoil model, the many-particle states occurring over battery charging and discharging. At this place, the coupling between the microscopic particles and the macroscopic battery is done via the Butler-Volmer relation which determines the kinetics of the lithium intercalation into the particles. Also in the dualfoil model, the occurrence of phase segregation in the cathodic particles leads to battery and particle states which are drastically different from those obtained using the dilute solution approach.

In a first approximation, the cathodic particles were assumed to be of spherical symmetry. The main advantage of this assumption was to avoid costly three-dimensional simulations. Nevertheless, from the physics, such an assumption is not justified. Thus, by means of a two-dimensional particle model, we performed a study to analyze the system states in a context where the particles do not fulfill the condition of spherical symmetry. Differently from the states obtained using the dilute solution model, we found that, in phase-field modeling, the phase-segregated states do not necessarily have the same symmetry as the particle geometry. This is due to the fact that such asymmetric states possess a lower free energy than the symmetric one. In this context, we found that there exist numerous possible equilibrium states which indicates the strong influence of the system history on the arising system states.

Finally, by means of the two-dimensional particle model, we could consider particles of ellipsoidal shape and study, at this place, the influence of the particle aspect ratio on the arising system states. This study reveals that the stresses arising in nearly spherical particles are larger than those arising in both elongated and flat-shaped particles.

A

Flux boundary condition at the inner particle boundaries

A.1 One-dimensional particle model

In the one-dimensional particle model introduced in Sec. 2.2.2 for the dilute solution approach and in Sec. 3.3.3 for the phase-field approach, it is assumed that both the particle geometry as well as the unknown functions of the problem — the lithium concentration n and the mechanical displacement \mathbf{u} — are of spherical symmetry.

Using spherical coordinates with radial dependence only to describe such a system, boundary conditions at the particle center (see Eqs. (2.32) - (2.33) for dilute solution modeling and Eqs. (3.87) - (3.89) for phase-field modeling) were artificially introduced to mathematically ensure the uniqueness of the solutions.

In this appendix, we will demonstrate that these artificial boundary conditions also ensure that the lithium flux holding at the particle center is zero which is a physical condition that has to be satisfied in order to guarantee the conservation of lithium matter within the cathodic particle.

In the dilute solution model these artificial boundary conditions are given by

$$\left. \frac{\partial n}{\partial r} \right|_{r=0^+} = 0, \quad (\text{A.1})$$

$$u_r \Big|_{r=0^+} = 0, \quad (\text{A.2})$$

whereas, in the phase-field model, they read

$$\left. \frac{\partial n}{\partial r} \right|_{r=0^+} = 0, \quad (\text{A.3})$$

$$\left. \frac{\partial^3 n}{\partial r^3} \right|_{r=0^+} = 0, \quad (\text{A.4})$$

$$u_r \Big|_{r=0^+} = 0, \quad (\text{A.5})$$

where u_r denotes the radial component of the mechanical displacement, $\mathbf{u} = u_r \mathbf{e}_r$, expressed as usual with respect to the local orthonormal basis $(\mathbf{e}_r, \mathbf{e}_\vartheta, \mathbf{e}_\varphi)$.

A.1.1 Boundary conditions at the particle center

For a particle model of spherical symmetry, provided that the unknown functions of the problem, the lithium concentration n and the mechanical displacement \mathbf{u} , are analytic, it holds, at the particle center, the following set of boundary conditions,

$$\left. \frac{\partial^{(2p+1)} n}{\partial r^{2p+1}} \right|_{r=0^+} = 0 \quad (p \in \mathbb{N}), \quad (\text{A.6})$$

$$\left. \frac{\partial^{(2p)} u_r}{\partial r^{2p}} \right|_{r=0^+} = 0 \quad (p \in \mathbb{N}). \quad (\text{A.7})$$

These conditions are however stronger than the boundary conditions, Eqs. (A.1) - (A.2) for the dilute solution model and Eqs. (A.3) - (A.5) for the phase-field model, that are indeed required.

In the following, we will demonstrate, in the dilute solution approach, that, in combination with the two local conservation laws, see Eqs. (2.28) - (2.29), Eqs. (A.1) - (A.2) imply that Eqs. (A.6) - (A.7) are fulfilled. The proof that Eqs. (A.3) - (A.5) imply Eqs. (A.6) - (A.7), in the phase-field modeling, can be done in a similar manner.

Assumptions of the proof

We assume that the unknown functions of the problem, the lithium concentration n and the radial displacement u_r , are analytic and that they fulfill, at the particle center, the following relationships:

$$\left. \frac{\partial n}{\partial r} \right|_{r=0^+} = 0, \quad (\text{A.8})$$

$$\left. u_r \right|_{r=0^+} = 0. \quad (\text{A.9})$$

Further, we assume that the local conservation laws within the particle are satisfied, i.e.

$$\frac{\partial(r^2 n)}{\partial t} + \frac{\partial}{\partial r} \left(a_0^3 r^2 (J_r^{\text{ch}} + J_r^{\text{cp}}) \right) = 0, \quad (\text{A.10})$$

$$\frac{\partial \sigma_r}{\partial r} + \frac{2}{r} (\sigma_r - \sigma_t) = 0. \quad (\text{A.11})$$

Preliminary calculations

After insertion of Eqs. (2.24) - (2.25) into Eqs. (2.26) - (2.27), we obtain

$$\sigma_r = 2\lambda_1 \frac{\partial u_r}{\partial r} + \lambda_2 \left(\frac{\partial u_r}{\partial r} + 2 \frac{u_r}{r} \right) - \lambda \tilde{\Omega}_0 (n - n_0), \quad (\text{A.12})$$

$$\sigma_t = 2\lambda_1 \frac{u_r}{r} + \lambda_2 \left(\frac{\partial u_r}{\partial r} + 2 \frac{u_r}{r} \right) - \lambda \tilde{\Omega}_0 (n - n_0). \quad (\text{A.13})$$

With $\sigma_h = 1/3(\sigma_r + 2\sigma_t)$, the two different flux contributions read

$$J_r^{\text{ch}} = -\frac{D_0}{a_0^3} \frac{\partial n}{\partial r}, \quad (\text{A.14})$$

$$J_r^{\text{cp}} = \frac{D_0 \tilde{\Omega}_0 n}{k_B T} \frac{\partial \sigma_h}{\partial r} = \frac{D_0 \tilde{\Omega}_0 \lambda n}{k_B T} \left(\frac{\partial^2 u_r}{\partial r^2} + \frac{2}{r} \frac{\partial u_r}{\partial r} - \frac{2}{r^2} u_r - \tilde{\Omega}_0 \frac{\partial n}{\partial r} \right), \quad (\text{A.15})$$

according to Eqs. (2.22) - (2.23).

Proof

Because the lithium concentration n and the radial displacement u_r are analytic, we have

$$n(r, t) = \sum_{k=0}^{+\infty} \frac{n^{(k)}(0, t)}{k!} r^k, \quad (\text{A.16})$$

$$u_r(r, t) = \sum_{k=0}^{+\infty} \frac{u_r^{(k)}(0, t)}{k!} r^k, \quad (\text{A.17})$$

with

$$n^{(k)}(0, t) = \left. \frac{\partial^{(k)} n}{\partial r^k} \right|_{r=0^+}, \quad (\text{A.18})$$

$$u_r^{(k)}(0, t) = \left. \frac{\partial^{(k)} u_r}{\partial r^k} \right|_{r=0^+}. \quad (\text{A.19})$$

We first insert Eqs. (A.12) - (A.13) into Eq. (A.11) which gives

$$2\lambda_1 \frac{\partial^2 u_r}{\partial r^2} + \lambda_2 \left(\frac{\partial^2 u_r}{\partial r^2} + \frac{2}{r} \frac{\partial u_r}{\partial r} - \frac{2}{r^2} u_r \right) - \lambda \tilde{\Omega}_0 \frac{\partial n}{\partial r} + \frac{4}{r} \lambda_1 \left(\frac{\partial u_r}{\partial r} - \frac{u_r}{r} \right) = 0. \quad (\text{A.20})$$

After insertion of Eqs. (A.16) - (A.17) into the above equation, Eq. (A.20), we obtain

$$\sum_{k=0}^{+\infty} \frac{r^k}{k!} \left(\left(\frac{k+4}{k+2} \right) (2\lambda_1 + \lambda_2) u_r^{(k+2)}(0, t) - \lambda \tilde{\Omega}_0 n^{(k+1)}(0, t) \right) - \frac{2}{r^2} (2\lambda_1 + \lambda_2) u_r^{(0)}(0, t) = 0 \quad (\text{A.21})$$

which simplifies to

$$\sum_{k=0}^{+\infty} \frac{r^k}{k!} \left(\left(\frac{k+4}{k+2} \right) (2\lambda_1 + \lambda_2) u_r^{(k+2)}(0, t) - \lambda \tilde{\Omega}_0 n^{(k+1)}(0, t) \right) = 0, \quad (\text{A.22})$$

according to Eq. (A.9). This leads to the following recurrence relation

$$\forall k \in \mathbb{N}, u_r^{(k+2)}(0, t) = \left(\frac{k+2}{k+4} \right) \frac{\lambda \tilde{\Omega}_0}{2\lambda_1 + \lambda_2} n^{(k+1)}(0, t). \quad (\text{A.23})$$

We then insert Eqs. (A.14) - (A.15) into Eq. (A.10),

$$\frac{\partial n}{\partial t} - \frac{D_0}{r^2} \frac{\partial}{\partial r} \left(r^2 \frac{\partial n}{\partial r} - \frac{a_0^3 \tilde{\Omega}_0 \lambda}{k_B T} n \left(r^2 \frac{\partial^2 u_r}{\partial r^2} + 2r \frac{\partial u_r}{\partial r} - 2u_r \right) + \frac{a_0^3 \tilde{\Omega}_0^2 \lambda}{k_B T} r^2 n \frac{\partial n}{\partial r} \right) = 0 \quad (\text{A.24})$$

With

$$\tilde{\beta}_0 \equiv \frac{a_0^3 \tilde{\Omega}_0 \lambda}{k_B T}, \quad (\text{A.25})$$

Eq. (A.24) simplifies to

$$\frac{\partial n}{\partial t} - \frac{D_0}{r^2} \frac{\partial}{\partial r} \left(r^2 \frac{\partial n}{\partial r} \right) + \frac{D_0 \tilde{\beta}_0}{r^2} \frac{\partial}{\partial r} \left(n \left(r^2 \frac{\partial^2 u_r}{\partial r^2} + 2r \frac{\partial u_r}{\partial r} - 2u_r \right) - \frac{D_0 \tilde{\beta}_0 \tilde{\Omega}_0}{r^2} \frac{\partial}{\partial r} \left(r^2 n \frac{\partial n}{\partial r} \right) \right) = 0. \quad (\text{A.26})$$

According to Eqs. (A.16) - (A.17), the first two terms appearing in the above equation, Eq. (A.26), read

$$\frac{\partial n}{\partial t} = \sum_{k=0}^{+\infty} \frac{r^k}{k!} \frac{\partial n^{(k)}}{\partial t}(0, t) \quad (\text{A.27})$$

$$\begin{aligned} \frac{1}{r^2} \frac{\partial}{\partial r} \left(r^2 \frac{\partial n}{\partial r} \right) &= \sum_{k=0}^{+\infty} \frac{r^k}{k!} \left(\frac{k+3}{k+1} \right) n^{(k+2)}(0, t) + \frac{2}{r} n^{(1)}(0, t) \\ &= \sum_{k=0}^{+\infty} \frac{r^k}{k!} \left(\frac{k+3}{k+1} \right) n^{(k+2)}(0, t) \end{aligned} \quad (\text{A.28})$$

The calculation of the two remaining terms is a bit more complicated since they contain a product of two series. Here we use the Cauchy product rule.

The third term of Eq. (A.26) reads

$$\begin{aligned}
& \frac{1}{r^2} \frac{\partial}{\partial r} \left(n \left(r^2 \frac{\partial^2 u_r}{\partial r^2} + 2r \frac{\partial u_r}{\partial r} - 2u_r \right) \right) \\
&= \frac{1}{r^2} \frac{\partial}{\partial r} \left(\left(\sum_{q=0}^{+\infty} \frac{r^q}{q!} n^{(q)}(0, t) \right) \left(\sum_{k=2}^{+\infty} \frac{r^k}{k!} (k-1)(k+2) u_r^{(k)}(0, t) - \underbrace{2u_r^{(0)}(0, t)}_{=0, \text{ see Eq. (A.9)}} \right) \right) \\
&= \frac{1}{r^2} \frac{\partial}{\partial r} \left(\left(\sum_{q=0}^{+\infty} \frac{r^q}{q!} n^{(q)}(0, t) \right) \left(\sum_{k=2}^{+\infty} \frac{r^k}{k!} (k-1)(k+2) u_r^{(k)}(0, t) \right) \right) \\
&= \frac{1}{r^2} \frac{\partial}{\partial r} \left(\sum_{k=2}^{+\infty} r^k \sum_{q=0}^{k-2} \frac{n^{(q)}(0, t) u_r^{(k-q)}(0, t)}{q! (k-q)!} (k-q-1)(k-q+2) \right)
\end{aligned}$$

With

$$\forall k \geq 2, A_k(0, t) \equiv \sum_{q=0}^{k-2} \frac{n^{(q)}(0, t) u_r^{(k-q)}(0, t)}{q! (k-q)!} (k-q-1)(k-q+2), \quad (\text{A.29})$$

we obtain

$$\begin{aligned}
\frac{1}{r^2} \frac{\partial}{\partial r} \left(n \left(r^2 \frac{\partial^2 u_r}{\partial r^2} + 2r \frac{\partial u_r}{\partial r} - 2u_r \right) \right) &= \frac{1}{r^2} \frac{\partial}{\partial r} \left(\sum_{k=2}^{+\infty} r^k A_k(0, t) \right) \\
&= \sum_{k=0}^{+\infty} r^k (k+3) A_{k+3}(0, t) + \frac{2}{r} A_2(0, t), \quad (\text{A.30})
\end{aligned}$$

where, according to Eq. (A.29),

$$A_2(0, t) = 2n^{(0)}(0, t)u_r^{(2)}(0, t).$$

From Eq. (A.23), for the particular case $k = 0$, it holds

$$u_r^{(2)}(0, t) = \frac{\lambda \tilde{\Omega}_0}{2(2\lambda_1 + \lambda_2)} n^{(1)}(0, t) = 0, \quad (\text{A.31})$$

according to Eq. (A.8). This means that

$$A_2(0, t) = 0.$$

Thus, Eq. (A.30) reduces to

$$\frac{1}{r^2} \frac{\partial}{\partial r} \left(n \left(r^2 \frac{\partial^2 u_r}{\partial r^2} + 2r \frac{\partial u_r}{\partial r} - 2u_r \right) \right) = \sum_{k=0}^{+\infty} r^k (k+3) A_{k+3}(0, t). \quad (\text{A.32})$$

We then treat the fourth term of Eq. (A.26),

$$\frac{1}{r^2} \frac{\partial}{\partial r} \left(r^2 n \frac{\partial n}{\partial r} \right) = \frac{1}{r^2} \frac{\partial}{\partial r} \left(\sum_{k=0}^{+\infty} r^{k+2} \sum_{q=0}^k \frac{n^{(q)}(0, t)}{q!} \frac{n^{(k-q+1)}(0, t)}{(k-q)!} \right).$$

With

$$\forall k \in \mathbb{N}, B_k(0, t) \equiv \sum_{q=0}^k \frac{n^{(q)}(0, t)}{q!} \frac{n^{(k-q+1)}(0, t)}{(k-q)!}, \quad (\text{A.33})$$

we obtain

$$\begin{aligned} \frac{1}{r^2} \frac{\partial}{\partial r} \left(r^2 n \frac{\partial n}{\partial r} \right) &= \frac{1}{r^2} \frac{\partial}{\partial r} \left(\sum_{k=0}^{+\infty} r^{k+2} B_k(0, t) \right) \\ &= \sum_{k=0}^{+\infty} r^k (k+3) B_{k+1}(0, t) + \underbrace{\frac{2}{r} B_0(0, t)}_{=0, \text{ see Eq. (A.8)}} \\ &= \sum_{k=0}^{+\infty} r^k (k+3) B_{k+1}(0, t). \end{aligned} \quad (\text{A.34})$$

We put Eqs.(A.27), (A.28), (A.32) and (A.34) into Eq. (A.26) and obtain

$$\sum_{k=0}^{+\infty} \frac{r^k}{k!} \left[\frac{\partial n^{(k)}}{\partial t}(0, t) - D_0(k+3) \left(\frac{n^{(k+2)}(0, t)}{k+1} - \tilde{\beta}_0 k! A_{k+3}(0, t) + \tilde{\beta}_0 \tilde{\Omega}_0 k! B_{k+1}(0, t) \right) \right] = 0 \quad (\text{A.35})$$

which implies that

$$\forall k \in \mathbb{N}, \frac{\partial n^{(k)}}{\partial t}(0, t) - D_0(k+3) \left(\frac{n^{(k+2)}(0, t)}{k+1} - \tilde{\beta}_0 k! A_{k+3}(0, t) + \tilde{\beta}_0 \tilde{\Omega}_0 k! B_{k+1}(0, t) \right) = 0. \quad (\text{A.36})$$

We will now demonstrate that

$$\forall k \in \mathbb{N}, k \text{ odd}, n^{(k)}(0, t) = 0, \quad (\text{A.37})$$

$$\forall k \in \mathbb{N}, k \text{ even}, u_r^{(k)}(0, t) = 0. \quad (\text{A.38})$$

Eq. (A.37) is equivalent to

$$\forall k \in \mathbb{N}, k \text{ odd}, \forall j \leq k, j \text{ odd}, n^{(j)}(0, t) = 0. \quad (\text{A.39})$$

In order to prove Eq. (A.39), we make a mathematical induction.

For $k = 1$, Eq. (A.40) is fulfilled according to Eq. (A.8).

We suppose that, for a particular $k \in \mathbb{N}$, k odd, Eq. (A.40) is satisfied, i.e. it holds

$$\forall j \leq k, j \text{ odd}, n^{(j)}(0, t) = 0. \quad (\text{A.40})$$

This is the induction hypothesis. We then have to prove that

$$n^{(k+2)}(0, t) = 0. \quad (\text{A.41})$$

For this particular $k \in \mathbb{N}$, k odd, we have

$$\frac{\partial n^{(k)}}{\partial t}(0, t) = 0, \quad (\text{A.42})$$

according to Eq. (A.8). Further, according to Eq. (A.29), it holds

$$A_{k+3}(0, t) = \sum_{q=0}^{k+1} \frac{n^{(q)}(0, t)}{q!} \frac{u_r^{(k+3-q)}(0, t)}{(k+3-q)!} (k+2-q)(k+5-q) \quad (\text{A.43})$$

where

$$u_r^{(k+3-q)}(0, t) = \left(\frac{k+3-q}{k+5-q} \right) \frac{\lambda \tilde{\Omega}_0}{2\lambda_1 + \lambda_2} n^{(k+2-q)}(0, t),$$

according to Eq. (A.23). Inserting this last equation into Eq. (A.43) we obtain

$$A_{k+3}(0, t) = \frac{\lambda \tilde{\Omega}_0}{2\lambda_1 + \lambda_2} \sum_{q=0}^{k+1} \frac{n^{(q)}(0, t)}{q!} \frac{n^{(k+2-q)}(0, t)}{(k+1-q)!}. \quad (\text{A.44})$$

We analyze the terms appearing in this sum.

If q is odd then $q \leq k$ (k is supposed to be odd, then $k+1$ is even) and, according to the induction hypothesis, Eq. (A.40), $n^{(q)}(0, t) = 0$. Thus, only the terms corresponding to an even value of q do not vanish in the sum of Eq. (A.44).

If q is even, then $k+2-q$ is odd (k is supposed to be odd) and it holds $1 \leq k+2-q \leq k+2$ (since $0 \leq q \leq k+1$). According to the induction hypothesis, Eq. (A.40), for all $q \leq k$, it holds $n^{(q)}(0, t) = 0$. Thus, only the term $q = 0$ is not vanishing in the sum of Eq. (A.44) which is equal to

$$A_{k+3}(0, t) = \frac{\lambda \tilde{\Omega}_0}{2\lambda_1 + \lambda_2} \frac{n^{(0)}(0, t) n^{(k+2)}(0, t)}{(k+1)!}. \quad (\text{A.45})$$

According to Eq. (A.33), we have

$$B_{k+1}(0, t) = \sum_{q=0}^{k+1} \frac{n^{(q)}(0, t)}{q!} \frac{n^{(k-q+2)}(0, t)}{(k+1-q)!},$$

which is in fact equal to

$$\begin{aligned} B_{k+1}(0, t) &= \frac{2\lambda_1 + \lambda_2}{\lambda \tilde{\Omega}_0} A_{k+3}(0, t) \\ &= \frac{n^{(0)}(0, t) n^{(k+2)}(0, t)}{(k+1)!}, \end{aligned} \quad (\text{A.46})$$

according to Eq. (A.44) and to Eq. (A.45).

We then insert Eqs. (A.42), (A.45) and (A.46) into Eq. (A.36) and obtain

$$\underbrace{-D_0 \frac{k+3}{k+1} \left[1 + n^{(0)}(0, t) \frac{4\lambda_1}{3(2\lambda_1 + \lambda_2)} \tilde{\beta}_0 \tilde{\Omega}_0 \right]}_{\neq 0} n^{(k+2)}(0, t) = 0$$

which implies that

$$n^{(k+2)}(0, t) = 0 \quad (\text{A.47})$$

which corresponds to Eq. (A.41) meaning that Eq. (A.37) is fulfilled.

Eq. (A.37) together with (A.23) as well as Eq. (A.9) (for the case $k = 0$) easily lead to Eq. (A.38).

A.1.2 Lithium flux at the particle center

In the previous section we demonstrated that

$$\left. \frac{\partial n}{\partial r} \right|_{r=0^+} = 0, \quad (\text{A.48})$$

$$\left. u_r \right|_{r=0^+} = 0, \quad (\text{A.49})$$

imply

$$\left. \frac{\partial^{(2p+1)} n}{\partial r^{2p+1}} \right|_{r=0^+} = 0 \quad (p \in \mathbb{N}), \quad (\text{A.50})$$

$$\left. \frac{\partial^{(2p)} u_r}{\partial r^{2p}} \right|_{r=0^+} = 0 \quad (p \in \mathbb{N}), \quad (\text{A.51})$$

in the dilute solution model. Analogously, we argue that

$$\left. \frac{\partial n}{\partial r} \right|_{r=0^+} = 0, \quad (\text{A.52})$$

$$\left. \frac{\partial^3 n}{\partial r^3} \right|_{r=0^+} = 0, \quad (\text{A.53})$$

$$\left. u_r \right|_{r=0^+} = 0, \quad (\text{A.54})$$

also imply Eqs. (A.50) - (A.51) in the phase-field model.

In this part, we will demonstrate that Eqs. (A.50) - (A.51) imply that the lithium flux at the particle center satisfies

$$\mathbf{J} \cdot \mathbf{e}_r \Big|_{r=0^+} = 0 \quad (\text{A.55})$$

which further ensure that the total number of lithium ions N in the particle is conserved. Eq. (A.55) can be rewritten as

$$J_r \Big|_{r=0^+} = J_r^{\text{ch}} \Big|_{r=0^+} + J_r^{\text{cp}} \Big|_{r=0^+} = 0 \quad (\text{A.56})$$

In the dilute solution model we have

$$J_r^{\text{ch}} \Big|_{r=0^+} = -\frac{D_0}{a_0^3} \frac{\partial n}{\partial r} \Big|_{r=0^+}, \quad (\text{A.57})$$

$$J_r^{\text{cp}} \Big|_{r=0^+} = -\frac{D_0 \tilde{\Omega}_0 n}{k_B T} \frac{\partial \sigma_h}{\partial r} \Big|_{r=0^+}, \quad (\text{A.58})$$

according to Eqs. (2.22) - (2.23).

Differently, in the phase-field model, we have

$$\begin{aligned} J_r^{\text{ch}} \Big|_{r=0^+} &= J_r^{\text{mf}} \Big|_{r=0^+} + J_r^{\text{gd}} \Big|_{r=0^+} \\ &= -\frac{D_0}{a_0^3} \left(\alpha_2 \frac{T^{\text{ref}}}{T} n(1-n) + 1 \right) \frac{\partial n}{\partial r} \Big|_{r=0^+} \\ &\quad + \frac{D_0 \kappa n(1-n)}{a_0^3 k_B T} \left(-\frac{2}{r^2} \frac{\partial n}{\partial r} + \frac{2}{r} \frac{\partial^2 n}{\partial r^2} + \frac{\partial^3 n}{\partial r^3} \right) \Big|_{r=0^+} \end{aligned} \quad (\text{A.59})$$

$$J_r^{\text{cp}} \Big|_{r=0^+} = \frac{D_0 \tilde{\Omega}_0 n(1-n)}{k_B T} \frac{\partial \sigma_h}{\partial r} \Big|_{r=0^+}, \quad (\text{A.60})$$

according to Eqs. (3.80) - (3.82).

We first treat, in the dilute solution model, the term $J_r^{\text{ch}} \Big|_{r=0^+}$. According to Eq. (A.50), Eq. (A.57) directly becomes equal to

$$J_r^{\text{ch}} \Big|_{r=0^+} = 0. \quad (\text{A.61})$$

In the phase-field model, according to Eq. (A.50), the term $J_r^{\text{ch}} \Big|_{r=0^+}$ of Eq. (A.59) reduces to

$$J_r^{\text{ch}} \Big|_{r=0^+} = \frac{D_0 \kappa n(1-n)}{a_0^3 k_B T} \left(-\frac{2}{r^2} \frac{\partial n}{\partial r} + \frac{2}{r} \frac{\partial^2 n}{\partial r^2} + \frac{\partial^3 n}{\partial r^3} \right) \Big|_{r=0^+}. \quad (\text{A.62})$$

At this place, we perform a Taylor expansion in a neighborhood of $r = 0^+$ to approximate the function,

$$-\frac{2}{r^2} \frac{\partial n}{\partial r} + \frac{2}{r} \frac{\partial^2 n}{\partial r^2} + \frac{\partial^3 n}{\partial r^3}. \quad (\text{A.63})$$

Since we have

$$\begin{aligned}
-\frac{2}{r^2} \frac{\partial n}{\partial r} &= -\frac{2}{r^2} \frac{\partial n}{\partial r} \Big|_{r=0^+} - \frac{2}{r} \frac{\partial^2 n}{\partial r^2} \Big|_{r=0^+} - \frac{\partial^3 n}{\partial r^3} \Big|_{r=0^+} + \mathcal{O}(r) \\
&= -\frac{2}{r} \frac{\partial^2 n}{\partial r^2} \Big|_{r=0^+} + \mathcal{O}(r),
\end{aligned} \tag{A.64}$$

$$\begin{aligned}
\frac{2}{r} \frac{\partial^2 n}{\partial r^2} &= \frac{2}{r} \frac{\partial^2 n}{\partial r^2} \Big|_{r=0^+} + 2 \frac{\partial^3 n}{\partial r^3} \Big|_{r=0^+} + \mathcal{O}(r) \\
&= \frac{2}{r} \frac{\partial^2 n}{\partial r^2} \Big|_{r=0^+} + \mathcal{O}(r),
\end{aligned} \tag{A.65}$$

$$\begin{aligned}
\frac{\partial^3 n}{\partial r^3} &= \frac{\partial^3 n}{\partial r^3} \Big|_{r=0^+} + \mathcal{O}(r) \\
&= \mathcal{O}(r),
\end{aligned} \tag{A.66}$$

according to Eq. (A.50), the quantity represented by Eq. (A.63), as needed in Eq. (A.62), is approximately equal to

$$-\frac{2}{r^2} \frac{\partial n}{\partial r} + \frac{2}{r} \frac{\partial^2 n}{\partial r^2} + \frac{\partial^3 n}{\partial r^3} = \mathcal{O}(r). \tag{A.67}$$

After insertion of Eq. (A.67) into Eq. (A.62), Eq. (A.62) reduces to

$$J_r^{\text{ch}} \Big|_{r=0^+} = \mathcal{O}(r). \tag{A.68}$$

Eq. (A.61) and Eq. (A.68) demonstrate that

$$J_r^{\text{ch}} \Big|_{r=0^+} = 0.$$

in the first order in r , for the dilute solution model as well as for the phase-field model, respectively.

We then treat the term $J_r^{\text{cp}} \Big|_{r=0^+}$ whose expression is the same in both the dilute and phase-field models. It here holds

$$\frac{\partial \sigma_h}{\partial r} \Big|_{r=0^+} = \lambda \left(\frac{\partial^2 u_r}{\partial r^2} - 2 \frac{u_r}{r^2} + \frac{2}{r} \frac{\partial u_r}{\partial r} \right) \Big|_{r=0^+} - \lambda \tilde{\Omega}_0 \frac{\partial n}{\partial r} \Big|_{r=0^+} \tag{A.69}$$

which reduces to

$$\frac{\partial \sigma_h}{\partial r} \Big|_{r=0^+} = \lambda \left(\frac{\partial^2 u_r}{\partial r^2} - 2 \frac{u_r}{r^2} + \frac{2}{r} \frac{\partial u_r}{\partial r} \right) \Big|_{r=0^+}, \tag{A.70}$$

according to Eq. (A.50) and Eq. (A.51). At this place, we perform a Taylor expansion in a neighborhood of $r = 0^+$ to approximate the function,

$$\frac{\partial^2 u_r}{\partial r^2} - 2 \frac{u_r}{r^2} + \frac{2}{r} \frac{\partial u_r}{\partial r}. \tag{A.71}$$

Since we have

$$\begin{aligned}\frac{\partial^2 u_r}{\partial r^2} &= \left. \frac{\partial^2 u_r}{\partial r^2} \right|_{r=0^+} + \mathcal{O}(r) \\ &= \mathcal{O}(r),\end{aligned}\tag{A.72}$$

$$\begin{aligned}-2\frac{u_r}{r^2} &= -\left. \frac{2}{r^2} u_r \right|_{r=0^+} - \left. \frac{2}{r} \frac{\partial u_r}{\partial r} \right|_{r=0^+} - \left. \frac{\partial^2 u_r}{\partial r^2} \right|_{r=0^+} + \mathcal{O}(r) \\ &= -\left. \frac{2}{r} \frac{\partial u_r}{\partial r} \right|_{r=0^+} + \mathcal{O}(r),\end{aligned}\tag{A.73}$$

$$\begin{aligned}\frac{2}{r} \frac{\partial u_r}{\partial r} &= \left. \frac{2}{r} \frac{\partial u_r}{\partial r} \right|_{r=0^+} + 2 \left. \frac{\partial^2 u_r}{\partial r^2} \right|_{r=0^+} + \mathcal{O}(r) \\ &= \left. \frac{2}{r} \frac{\partial u_r}{\partial r} \right|_{r=0^+} + \mathcal{O}(r),\end{aligned}\tag{A.74}$$

according to Eq. (A.51), the quantity represented by Eq. (A.71), as needed in Eq. (A.70), is approximately equal to

$$\frac{\partial^2 u_r}{\partial r^2} - 2\frac{u_r}{r^2} + \frac{2}{r} \frac{\partial u_r}{\partial r} = \mathcal{O}(r).\tag{A.75}$$

Inserting Eq. (A.75) into Eq. (A.70) leads to

$$\left. \frac{\partial \sigma_h}{\partial r} \right|_{r=0^+} = \mathcal{O}(r).\tag{A.76}$$

Eq. (A.76) demonstrates that the quantity

$$J_r^{\text{cp}} \Big|_{r=0^+} = 0.$$

in the first order in r , for both the dilute solution model phase-field models (see Eq. (A.58) and Eq. (A.60), respectively).

A.2 Two-dimensional particle model

A.2.1 Derivation of the boundary conditions from the system symmetries

We now consider the two-dimensional particle model introduced in Sec. 2.2.3 and in Sec. 3.3.3 in the context of dilute solution and phase-field modeling, respectively. This two-dimensional particle model represents a three-dimensional particle whose geometry is invariant under rotation around the z -axis and under mirror symmetry with respect to the x - y -plane.

In this part we will show that the artificial boundary conditions, Eqs. (2.56) - (2.61) of Sec. 2.2.3, are a direct consequence of the assumptions related to the system symmetries. At this place, we assume that not only the particle geometry but also the unknown functions of the problem being the lithium concentration $n(x, y, z)$ and the mechanical displacement,

$$\mathbf{u}(x, y, z) = u_x(x, y, z)\mathbf{e}_x + u_y(x, y, z)\mathbf{e}_y + u_z(x, y, z)\mathbf{e}_z,$$

are invariant under rotation around the z -axis. At this place, (x, y, z) denotes the usual cartesian coordinates system with orthonormal basis $(\mathbf{e}_x, \mathbf{e}_y, \mathbf{e}_z)$. In the x - z -plane ($y = 0$) it follows from this invariance that

$$n(x, z) = n(-x, z), \quad (\text{A.77})$$

$$u_x(x, z) = -u_x(-x, z), \quad (\text{A.78})$$

$$u_y(x, z) = 0, \quad (\text{A.79})$$

$$u_z(x, z) = u_z(-x, z), \quad (\text{A.80})$$

where the coordinate $y = 0$ has been omitted. From Eqs. (A.78) - (A.80), the displacement vector $\mathbf{u}(x, z)$ reads

$$\mathbf{u}(x, z) = u_x(x, z)\mathbf{e}_x + u_z(x, z)\mathbf{e}_z. \quad (\text{A.81})$$

Under the assumption that n and \mathbf{u} are analytic functions of the cartesian coordinates and due to parity reasons, Eq. (A.77), Eq. (A.78) and Eq. (A.80) are respectively equivalent to

$$\left. \frac{\partial^{(2p+1)} n}{\partial x^{2p+1}} \right|_{x=0, z} = 0 \quad (p \in \mathbb{N}), \quad (\text{A.82})$$

$$\left. \frac{\partial^{(2p)} u_x}{\partial x^{2p}} \right|_{x=0, z} = 0 \quad (p \in \mathbb{N}), \quad (\text{A.83})$$

$$\left. \frac{\partial^{(2p+1)} u_z}{\partial x^{2p+1}} \right|_{x=0, z} = 0 \quad (p \in \mathbb{N}). \quad (\text{A.84})$$

Related to the two-dimensional particle model, these conditions may furnish a set of boundary conditions at the z -axis ($x = 0$).

To take advantage of the rotation invariance in order to reduce the system dimensionality, we use the cylindrical coordinates (ϱ, ϑ, z) with local orthonormal basis $(\mathbf{e}_\varrho, \mathbf{e}_\vartheta, \mathbf{e}_z)$. In this basis, the displacement vector,

$$\mathbf{u}(x, y, z) = u_\varrho(x, y, z)\mathbf{e}_\varrho + u_\vartheta(x, y, z)\mathbf{e}_\vartheta + u_z(x, y, z)\mathbf{e}_z.$$

In the x - z -plane ($y = 0$), i.e. for $\vartheta \in \{0, \pi\}$, we have

$$\mathbf{e}_\varrho = \begin{cases} \mathbf{e}_x & \text{if } x > 0 \\ -\mathbf{e}_x & \text{if } x < 0, \end{cases}$$

$$\mathbf{e}_\vartheta = \begin{cases} \mathbf{e}_y & \text{if } x > 0 \\ -\mathbf{e}_y & \text{if } x < 0. \end{cases}$$

Thus, the displacement vector is expressed as

$$\mathbf{u}(x, z) = \begin{cases} u_\varrho(x, z)\mathbf{e}_x + u_\vartheta(x, z)\mathbf{e}_y + u_z(x, z)\mathbf{e}_z & \text{if } x > 0 \\ -u_\varrho(x, z)\mathbf{e}_x - u_\vartheta(x, z)\mathbf{e}_y + u_z(x, z)\mathbf{e}_z & \text{if } x < 0, \end{cases} \quad (\text{A.85})$$

where the coordinate $y = 0$ has been omitted. We identify Eq. (A.81) to Eq. (A.85) and obtain

$$u_x(x, z) = \begin{cases} u_\varrho(x, z) & \text{if } x > 0 \\ -u_\varrho(x, z) & \text{if } x < 0, \end{cases} \quad (\text{A.86})$$

$$u_y(x, z) = 0 = \pm u_{y\vartheta}(x, z) \quad (\text{A.87})$$

which leads to

$$\mathbf{u}(x, z) = \begin{cases} u_\varrho(x, z)\mathbf{e}_x + u_z(x, z)\mathbf{e}_z & \text{if } x > 0 \\ -u_\varrho(x, z)\mathbf{e}_x + u_z(x, z)\mathbf{e}_z & \text{if } x < 0. \end{cases}$$

Under the assumption that $u_\varrho(x, z)\mathbf{e}_\varrho = u_x(x, z)\mathbf{e}_x$ be analytic, the direction flip of \mathbf{e}_ϱ at $x = 0$, in general implies a nonanalyticity of $u_\varrho(x, z)$ at $x = 0$. Further, for $x = \varrho > 0$ it holds

$$n(x, z) = n(\varrho, z), \quad (\text{A.88})$$

$$u_x(x, z) = u_\varrho(x, z) = u_\varrho(\varrho, z), \quad (\text{A.89})$$

$$u_z(x, z) = u_z(\varrho, z), \quad (\text{A.90})$$

where Eq. (A.89) directly follows from Eq. (A.86). From the above identities, Eqs. (A.88) - (A.90), using Eqs. (A.77)- (A.80), we can obtain boundary conditions for the functions n , u_ϱ and u_z at $\varrho = 0^+$ that also corresponds to the boundary $x = 0^+$. We have

$$0 = \frac{\partial^{(2p+1)}n}{\partial x^{2p+1}} \Big|_{x=0^+, z} = \frac{\partial^{(2p+1)}n}{\partial \varrho^{2p+1}} \Big|_{\varrho=0^+, z} \quad (p \in \mathbb{N}), \quad (\text{A.91})$$

$$0 = \frac{\partial^{(2p)}u_x}{\partial x^{2p}} \Big|_{x=0^+, z} = \frac{\partial^{(2p)}u_\varrho}{\partial \varrho^{2p}} \Big|_{\varrho=0^+, z} \quad (p \in \mathbb{N}), \quad (\text{A.92})$$

$$0 = \frac{\partial^{(2p+1)}u_z}{\partial x^{2p+1}} \Big|_{x=0^+, z} = \frac{\partial^{(2p+1)}u_z}{\partial \varrho^{2p+1}} \Big|_{\varrho=0^+, z} \quad (p \in \mathbb{N}). \quad (\text{A.93})$$

Eqs. (A.91) - (A.93) represent a set of boundary conditions for the function n , u_ϱ and u_z at the z -axis of the two-dimensional particle model.

In a similar manner, in the x - z -plane, we assume that the lithium concentration n as well as the components of the mechanical displacement \mathbf{u} satisfy the following conditions of symmetry

$$n(x, z) = n(x, -z), \quad (\text{A.94})$$

$$u_x(x, z) = u_x(x, -z), \quad (\text{A.95})$$

$$u_y(x, z) = 0, \quad (\text{A.96})$$

$$u_z(x, z) = -u_z(x, -z), \quad (\text{A.97})$$

where the coordinate $y = 0$ has been omitted. From Eq. (A.94), Eq. (A.95) and Eq. (A.97), it follows

that

$$\left. \frac{\partial^{(2p+1)} n}{\partial z^{2p+1}} \right|_{x,z=0} = 0 \quad (p \in \mathbb{N}), \quad (\text{A.98})$$

$$\left. \frac{\partial^{(2p+1)} u_x}{\partial z^{2p+1}} \right|_{x,z=0} = 0 \quad (p \in \mathbb{N}), \quad (\text{A.99})$$

$$\left. \frac{\partial^{(2p)} u_z}{\partial z^{2p}} \right|_{x,z=0} = 0 \quad (p \in \mathbb{N}). \quad (\text{A.100})$$

Consequently, the boundary conditions at $z = 0^+$ read

$$\left. \frac{\partial^{(2p+1)} n}{\partial z^{2p+1}} \right|_{x,z=0^+} = 0 \quad (p \in \mathbb{N}), \quad (\text{A.101})$$

$$\left. \frac{\partial^{(2p+1)} u_x}{\partial z^{2p+1}} \right|_{x,z=0^+} = 0 \quad (p \in \mathbb{N}), \quad (\text{A.102})$$

$$\left. \frac{\partial^{(2p)} u_z}{\partial z^{2p}} \right|_{x,z=0^+} = 0 \quad (p \in \mathbb{N}). \quad (\text{A.103})$$

A.2.2 Reduction of the total number of boundary conditions

Dilute solution model

In the dilute solution approach, we can demonstrate that, in combination with the two local conservation laws, see Eqs. (2.50) - (2.52), the set of Eqs. (A.91) - (A.93) is equivalent to

$$\left. \frac{\partial n}{\partial \varrho} \right|_{\varrho=0^+,z} = 0 \quad \Leftrightarrow \quad \left. \frac{\partial^{(2p+1)} n}{\partial \varrho^{2p+1}} \right|_{\varrho=0^+,z} = 0 \quad (p \in \mathbb{N}), \quad (\text{A.104})$$

$$u_\varrho \Big|_{\varrho=0^+,z} = 0 \quad \Leftrightarrow \quad \left. \frac{\partial^{(2p)} u_\varrho}{\partial \varrho^{2p}} \right|_{\varrho=0^+,z} = 0 \quad (p \in \mathbb{N}), \quad (\text{A.105})$$

$$\left. \frac{\partial u_z}{\partial \varrho} \right|_{\varrho=0^+,z} = 0 \quad \Leftrightarrow \quad \left. \frac{\partial^{(2p+1)} u_z}{\partial \varrho^{2p+1}} \right|_{\varrho=0^+,z} = 0 \quad (p \in \mathbb{N}). \quad (\text{A.106})$$

Similarly, we also can demonstrate that the set of Eqs. (A.101) - (A.103) is equivalent to

$$\left. \frac{\partial n}{\partial z} \right|_{\varrho,z=0^+} = 0 \quad \Leftrightarrow \quad \left. \frac{\partial^{(2p+1)} n}{\partial z^{2p+1}} \right|_{\varrho,z=0^+} = 0 \quad (p \in \mathbb{N}), \quad (\text{A.107})$$

$$\left. \frac{\partial u_\varrho}{\partial z} \right|_{\varrho,z=0^+} = 0 \quad \Leftrightarrow \quad \left. \frac{\partial^{(2p+1)} u_\varrho}{\partial z^{2p+1}} \right|_{\varrho,z=0^+} = 0 \quad (p \in \mathbb{N}), \quad (\text{A.108})$$

$$u_z \Big|_{\varrho,z=0^+} = 0 \quad \Leftrightarrow \quad \left. \frac{\partial^{(2p)} u_z}{\partial z^{2p}} \right|_{\varrho,z=0^+} = 0 \quad (p \in \mathbb{N}). \quad (\text{A.109})$$

The proofs of Eqs. (A.104) - (A.106), on the one hand, and of Eqs. (A.107) - (A.109), on the other hand, is not shown here and can be done analogously to the proof done in Sec. A.1.1 related to the particle model of spherical symmetry.

Phase-field model

In phase-field modeling, we can demonstrate that the set of Eqs. (A.91) - (A.93) is equivalent to

$$\left. \frac{\partial^{(2p+1)} n}{\partial \varrho^{2p+1}} \right|_{\varrho=0^+, z} = 0 \quad (p \in \mathbb{N}) \quad \Leftrightarrow \quad \left. \frac{\partial n}{\partial \varrho} \right|_{\varrho=0^+, z} = 0 \quad \text{and} \quad \left. \frac{\partial^3 n}{\partial \varrho^3} \right|_{\varrho=0^+, z} = 0, \quad (\text{A.110})$$

$$\left. \frac{\partial^{(2p)} u_\varrho}{\partial \varrho^{2p}} \right|_{\varrho=0^+, z} = 0 \quad (p \in \mathbb{N}) \quad \Leftrightarrow \quad u_\varrho \Big|_{\varrho=0^+, z} = 0, \quad (\text{A.111})$$

$$\left. \frac{\partial^{(2p+1)} u_z}{\partial \varrho^{2p+1}} \right|_{\varrho=0^+, z} = 0 \quad (p \in \mathbb{N}) \quad \Leftrightarrow \quad \left. \frac{\partial u_z}{\partial \varrho} \right|_{\varrho=0^+, z} = 0. \quad (\text{A.112})$$

Similarly, we also can demonstrate that the set of Eqs. (A.101) - (A.103) is equivalent to

$$\left. \frac{\partial^{(2p+1)} n}{\partial z^{2p+1}} \right|_{\varrho, z=0^+} = 0 \quad (p \in \mathbb{N}) \quad \Leftrightarrow \quad \left. \frac{\partial n}{\partial z} \right|_{\varrho, z=0^+} = 0 \quad \text{and} \quad \left. \frac{\partial^3 n}{\partial z^3} \right|_{\varrho, z=0^+} = 0, \quad (\text{A.113})$$

$$\left. \frac{\partial^{(2p+1)} u_\varrho}{\partial z^{2p+1}} \right|_{\varrho, z=0^+} = 0 \quad (p \in \mathbb{N}) \quad \Leftrightarrow \quad \left. \frac{\partial u_\varrho}{\partial z} \right|_{\varrho, z=0^+} = 0, \quad (\text{A.114})$$

$$\left. \frac{\partial^{(2p)} u_z}{\partial z^{2p}} \right|_{\varrho, z=0^+} = 0 \quad (p \in \mathbb{N}) \quad \Leftrightarrow \quad u_z \Big|_{\varrho, z=0^+} = 0. \quad (\text{A.115})$$

A.2.3 Lithium flux at the particle inner boundaries

In this part, we will demonstrate the sets of boundary conditions Eqs. (A.91) - (A.93) and Eqs. (A.101) - (A.103) ensure that both the total number of lithium ions N in the particle is conserved. That means that we have to prove that the following set of equations,

$$\left. \frac{\partial^{(2p+1)} n}{\partial \varrho^{2p+1}} \right|_{\varrho=0^+, z} = 0 \quad (p \in \mathbb{N}), \quad (\text{A.116})$$

$$\left. \frac{\partial^{(2p)} u_\varrho}{\partial \varrho^{2p}} \right|_{\varrho=0^+, z} = 0 \quad (p \in \mathbb{N}), \quad (\text{A.117})$$

$$\left. \frac{\partial^{(2p+1)} u_z}{\partial \varrho^{2p+1}} \right|_{\varrho=0^+, z} = 0 \quad (p \in \mathbb{N}) \quad (\text{A.118})$$

implies that

$$\mathbf{J} \cdot \mathbf{e}_\varrho \Big|_{\varrho=0^+, z} = 0 \quad (\text{A.119})$$

is fulfilled. Similarly we have to show that the following set of equations,

$$\left. \frac{\partial^{(2p+1)} n}{\partial z^{2p+1}} \right|_{\varrho, z=0^+} = 0 \quad (p \in \mathbb{N}), \quad (\text{A.120})$$

$$\left. \frac{\partial^{(2p+1)} u_x}{\partial z^{2p+1}} \right|_{\varrho, z=0^+} = 0 \quad (p \in \mathbb{N}), \quad (\text{A.121})$$

$$\left. \frac{\partial^{(2p)} u_z}{\partial z^{2p}} \right|_{\varrho, z=0^+} = 0 \quad (p \in \mathbb{N}) \quad (\text{A.122})$$

implies

$$\mathbf{J} \cdot \mathbf{e}_z \Big|_{\varrho, z=0^+} = 0 \quad (\text{A.123})$$

is satisfied.

In this appendix, we will demonstrate that Eqs. (A.116) - (A.118) imply Eq. (A.119), only. The proof that Eqs. (A.120) - (A.121) imply Eq. (A.123) can be done analogously.

Eq. (A.119) can be rewritten as

$$J_\varrho \Big|_{\varrho=0^+, z} = \left(J_\varrho^{\text{ch}} + J_\varrho^{\text{cp}} \right) \Big|_{\varrho=0^+, z} = J_\varrho^{\text{ch}} \Big|_{\varrho=0^+, z} + J_\varrho^{\text{cp}} \Big|_{\varrho=0^+, z} = 0. \quad (\text{A.124})$$

In the dilute solution model, we have

$$J_\varrho^{\text{ch}} \Big|_{\varrho=0^+, z} = -\frac{D_0}{a_0^3} \frac{\partial n}{\partial \varrho} \Big|_{\varrho=0^+, z}, \quad (\text{A.125})$$

$$J_\varrho^{\text{cp}} \Big|_{\varrho=0^+, z} = \frac{D_0 \tilde{\Omega}_0 n}{k_B T} \frac{\partial \sigma_h}{\partial \varrho} \Big|_{\varrho=0^+, z}, \quad (\text{A.126})$$

according to Eq. (2.40) and Eq. (2.41).

Differently, in the phase-field model, we have

$$\begin{aligned} J_\varrho^{\text{ch}} \Big|_{\varrho=0^+, z} &= J_\varrho^{\text{mf}} \Big|_{\varrho=0^+, z} + J_\varrho^{\text{gd}} \Big|_{\varrho=0^+, z} \\ &= -\frac{D_0}{a_0^3} \left(\alpha_2 \frac{T^{\text{ref}}}{T} n(1-n) + 1 \right) \frac{\partial n}{\partial \varrho} \Big|_{\varrho=0^+, z} \\ &\quad + \frac{D_0 \kappa n(1-n)}{a_0^3 k_B T} \left(-\frac{1}{\varrho^2} \frac{\partial n}{\partial \varrho} + \frac{1}{\varrho} \frac{\partial^2 n}{\partial \varrho^2} + \frac{\partial^3 n}{\partial \varrho^3} + \frac{\partial^3 n}{\partial z^2 \partial \varrho} \right) \Big|_{\varrho=0^+, z} \end{aligned} \quad (\text{A.127})$$

$$J_\varrho^{\text{cp}} \Big|_{\varrho=0^+, z} = \frac{D_0 \tilde{\Omega}_0 n(1-n)}{k_B T} \frac{\partial \sigma_h}{\partial \varrho} \Big|_{\varrho=0^+, z}, \quad (\text{A.128})$$

according to Eqs. (3.90) - (3.92).

We first treat, in the dilute solution model, the term $J_\varrho^{\text{ch}}|_{\varrho=0^+,z}$. According to Eq. (A.116), Eq. (A.125) directly becomes equal to

$$J_\varrho^{\text{ch}}|_{\varrho=0^+,z} = 0. \quad (\text{A.129})$$

In the phase-field model, according to Eq. (A.116), Eq. (A.127) reduces to

$$J_\varrho^{\text{ch}}|_{\varrho=0^+,z} = \frac{D_0 \kappa n (1-n)}{a_0^3 k_B T} \left(-\frac{1}{\varrho^2} \frac{\partial n}{\partial \varrho} + \frac{1}{\varrho} \frac{\partial^2 n}{\partial \varrho^2} + \frac{\partial^3 n}{\partial \varrho^3} \right) \Big|_{\varrho=0^+,z}. \quad (\text{A.130})$$

At this place, we perform a Taylor expansion in a neighborhood of $\varrho = 0^+$ to approximate the function,

$$-\frac{1}{\varrho^2} \frac{\partial n}{\partial \varrho} + \frac{1}{\varrho} \frac{\partial^2 n}{\partial \varrho^2} + \frac{\partial^3 n}{\partial \varrho^3}. \quad (\text{A.131})$$

Since we have

$$\begin{aligned} -\frac{1}{\varrho^2} \frac{\partial^2 n}{\partial \varrho^2} &= -\frac{1}{\varrho^2} \frac{\partial n}{\partial \varrho} \Big|_{\varrho=0^+,z} - \frac{1}{\varrho} \frac{\partial^2 n}{\partial \varrho^2} \Big|_{\varrho=0^+,z} - \frac{1}{2} \frac{\partial^3 n}{\partial \varrho^3} \Big|_{\varrho=0^+,z} + \mathcal{O}(\varrho) \\ &= -\frac{1}{\varrho} \frac{\partial^2 n}{\partial \varrho^2} \Big|_{\varrho=0^+,z} + \mathcal{O}(\varrho), \end{aligned} \quad (\text{A.132})$$

$$\begin{aligned} \frac{1}{\varrho} \frac{\partial^2 n}{\partial \varrho^2} &= \frac{1}{\varrho} \frac{\partial^2 n}{\partial \varrho^2} \Big|_{\varrho=0^+,z} + \frac{\partial^3 n}{\partial \varrho^3} \Big|_{\varrho=0^+,z} + \mathcal{O}(\varrho) \\ &= \frac{1}{\varrho} \frac{\partial^2 n}{\partial \varrho^2} \Big|_{\varrho=0^+,z} + \mathcal{O}(\varrho), \end{aligned} \quad (\text{A.133})$$

$$\begin{aligned} \frac{\partial^3 n}{\partial \varrho^3} &= \frac{\partial^3 n}{\partial \varrho^3} \Big|_{\varrho=0^+,z} + \mathcal{O}(\varrho) \\ &= \mathcal{O}(\varrho), \end{aligned} \quad (\text{A.134})$$

according to Eq. (A.116), the quantity represented by Eq. (A.131), as needed in Eq. (A.130), is approximatively equal to

$$-\frac{1}{\varrho^2} \frac{\partial n}{\partial \varrho} + \frac{1}{\varrho} \frac{\partial^2 n}{\partial \varrho^2} + \frac{\partial^3 n}{\partial \varrho^3} = \mathcal{O}(\varrho). \quad (\text{A.135})$$

After insertion of Eq. (A.135) into Eq. (A.130), Eq. (A.130) reduces to

$$J_\varrho^{\text{ch}}|_{\varrho=0^+,z} = \mathcal{O}(\varrho). \quad (\text{A.136})$$

Eq. (A.129) and Eq. (A.136) demonstrate that

$$J_\varrho^{\text{ch}}|_{\varrho=0^+,z} = 0.$$

in the first order in ϱ , for the dilute solution model as well as for the phase-field model, respectively.

We then treat the term $J_\varrho^{\text{cp}} \Big|_{\varrho=0^+,z}$ whose expression is the same in both the dilute and phase-field models. It here holds

$$\frac{\partial \sigma_h}{\partial \varrho} \Big|_{\varrho=0^+,z} = \lambda \left(\frac{\partial^2 u_\varrho}{\partial \varrho^2} - \frac{u_\varrho}{\varrho^2} + \frac{1}{\varrho} \frac{\partial u_\varrho}{\partial \varrho} + \frac{\partial^2 u_\varrho}{\partial \varrho \partial z} \right) \Big|_{\varrho=0^+,z} - \lambda \tilde{\Omega}_0 \frac{\partial n}{\partial \varrho} \Big|_{\varrho=0^+,z} \quad (\text{A.137})$$

which reduces to

$$\frac{\partial \sigma_h}{\partial \varrho} \Big|_{\varrho=0^+,z} = \lambda \left(\frac{\partial^2 u_\varrho}{\partial \varrho^2} - \frac{u_\varrho}{\varrho^2} + \frac{1}{\varrho} \frac{\partial u_\varrho}{\partial \varrho} \right) \Big|_{\varrho=0^+,z}, \quad (\text{A.138})$$

according to Eq. (A.116) and Eq. (A.118). At this place, we perform a Taylor expansion in a neighborhood of $\varrho = 0^+$ to approximate the function,

$$\frac{\partial^2 u_\varrho}{\partial \varrho^2} - \frac{u_\varrho}{\varrho^2} + \frac{1}{\varrho} \frac{\partial u_\varrho}{\partial \varrho}. \quad (\text{A.139})$$

Since we have

$$\begin{aligned} \frac{\partial^2 u_\varrho}{\partial \varrho^2} &= \frac{\partial^2 u_\varrho}{\partial \varrho^2} \Big|_{\varrho=0^+,z} + \mathcal{O}(\varrho) \\ &= \mathcal{O}(\varrho), \end{aligned} \quad (\text{A.140})$$

$$\begin{aligned} -\frac{u_\varrho}{\varrho^2} &= -\frac{1}{\varrho^2} u_\varrho \Big|_{\varrho=0^+,z} - \frac{1}{\varrho} \frac{\partial u_\varrho}{\partial \varrho} \Big|_{\varrho=0^+,z} - \frac{1}{2} \frac{\partial^2 u_\varrho}{\partial \varrho^2} \Big|_{\varrho=0^+,z} + \mathcal{O}(\varrho) \\ &= -\frac{1}{\varrho} \frac{\partial u_\varrho}{\partial \varrho} \Big|_{\varrho=0^+,z} + \mathcal{O}(\varrho), \end{aligned} \quad (\text{A.141})$$

$$\begin{aligned} \frac{1}{\varrho} \frac{\partial u_\varrho}{\partial \varrho} &= \frac{1}{\varrho} \frac{\partial u_\varrho}{\partial \varrho} \Big|_{\varrho=0^+,z} + \frac{\partial^2 u_\varrho}{\partial \varrho^2} \Big|_{\varrho=0^+,z} + \mathcal{O}(\varrho) \\ &= \frac{1}{\varrho} \frac{\partial u_\varrho}{\partial \varrho} \Big|_{\varrho=0^+,z} + \mathcal{O}(\varrho), \end{aligned} \quad (\text{A.142})$$

according to Eq. (A.117), the quantity represented by Eq. (A.139), as needed in Eq. (A.138), is approximatively equal to

$$\frac{\partial^2 u_\varrho}{\partial \varrho^2} - \frac{u_\varrho}{\varrho^2} + \frac{1}{\varrho} \frac{\partial u_\varrho}{\partial \varrho} = \mathcal{O}(\varrho). \quad (\text{A.143})$$

Inserting Eq. (A.143) into Eq. (A.138) leads to

$$\frac{\partial \sigma_h}{\partial \varrho} \Big|_{\varrho=0^+,z} = \mathcal{O}(\varrho). \quad (\text{A.144})$$

Eq. (A.144) demonstrates that the quantity

$$J_{\varrho}^{\text{cp}} \Big|_{\varrho=0^+, z} = 0.$$

in the first order in ϱ , for both the dilute solution model phase-field models (see Eq. (A.126) and Eq. (A.128), respectively).

B Appendix B

Mean-field approximation

In this appendix, we demonstrate how to calculate the system free energy in the mean-field approximation starting from the Hamiltonian Eq. (3.9) that represents the internal energy of intercalating lithium ions into a rigid host material which is not allowed for deforming. According to Eq. (3.9), this Hamiltonian reads

$$\mathcal{H}\{n_\alpha\} = \overbrace{U_0 \sum_{\alpha} n_{\alpha}}^{\text{one-body term}} + U \underbrace{\sum_{\langle \alpha, \alpha' \rangle} n_{\alpha} n_{\alpha'}}_{\text{two-body term}}. \quad (\text{B.1})$$

To avoid the calculation of the canonical partition function $\mathcal{Z}_c(T, N)$ which represents some mathematical difficulties, the system free energy $F(T, N)$ is computed using the grand canonical partition function $\mathcal{Z}_{\text{gc}}(T, \mu)$ which is however related to the system grand canonical potential $J(T, \mu)$ instead of being related to the system free energy. As introduced in Sec. 3.2.1, it holds, upon the grand canonical potential, the following relationship between the free energy and the grand canonical partition function:

$$\mathcal{Z}_{\text{gc}}(T, \mu) = \sum_{\{n_{\alpha}\}} \exp\left(-\frac{\mathcal{H}\{n_{\alpha}\} - \mu \sum_{\alpha} n_{\alpha}}{k_B T}\right), \quad (\text{B.2})$$

$$J(T, \mu) = -k_B T \ln \mathcal{Z}_{\text{gc}}(T, \mu), \quad (\text{B.3})$$

$$N = -\left. \frac{\partial J(T, \mu)}{\partial \mu} \right|_T, \quad (\text{B.4})$$

$$F(T, N) = J(T, \mu) + \mu(T, N)N, \quad (\text{B.5})$$

where $\mu(T, N)$, as usual, denotes the chemical potential of the system. It can be expressed as a function of the total number of lithium ions N in the particle by means of a self-consistent relation as we shall see it in the following.

Due to the interaction (two-body) term between the lithium ions in the system Hamiltonian, Eq. (B.1), the calculation of the grand canonical partition function is rather difficult. The mean-field approximation allows for the replacement of this two-body term by a one-body term under the assumption that the value of n_{α} does not deviate much from the average number of lithium occupation \bar{n} performed

over the entire particle. Note that such a deviation, referred to as δn_α , arises as consequence of thermal fluctuations. We further have

$$n_\alpha = \bar{n} + \delta n_\alpha \quad (\text{B.6})$$

with $\frac{\delta n_\alpha}{\bar{n}} \ll 1$.

Inserting Eq. (B.6) into the two body term of Eq. (B.1), we obtain

$$\begin{aligned} \sum_{\langle \alpha, \alpha' \rangle} n_\alpha n_{\alpha'} &= \sum_{\langle \alpha, \alpha' \rangle} (\bar{n} + \delta n_\alpha) (\bar{n} + \delta n_{\alpha'}) \\ &= \bar{n}^2 \sum_{\langle \alpha, \alpha' \rangle} 1 + 2\bar{n} \sum_{\langle \alpha, \alpha' \rangle} \delta n_\alpha + \sum_{\langle \alpha, \alpha' \rangle} \delta n_\alpha \delta n_{\alpha'}. \end{aligned} \quad (\text{B.7})$$

The term $\sum_{\langle \alpha, \alpha' \rangle} 1$ represents the sum over the interacting pair of lithium ions and is hence equal to

$$\sum_{\langle \alpha, \alpha' \rangle} 1 = \frac{\mathcal{N}\Gamma}{2},$$

\mathcal{N} being the total number of interstitial lattice sites available for the lithium ions in the host material and Γ the number of nearest-neighboring interstitial lattice sites.

After insertion of Eq. (B.6), the term $2 \sum_{\langle \alpha, \alpha' \rangle} \delta n_\alpha$ reduces to

$$\begin{aligned} 2 \sum_{\langle \alpha, \alpha' \rangle} \delta n_\alpha &= 2 \frac{\Gamma}{2} \sum_{\alpha} (n_\alpha - \bar{n}) \\ &= \Gamma \sum_{\alpha} n_\alpha - \mathcal{N}\Gamma\bar{n}. \end{aligned}$$

The term $\sum_{\langle \alpha, \alpha' \rangle} \delta n_\alpha \delta n_{\alpha'}$ stands for the contribution of the correlations between fluctuations and is neglected in the mean-field approximation. Under these considerations the two-body term, Eq. (B.7), simplifies to a one-body term given by

$$\sum_{\langle \alpha, \alpha' \rangle} n_\alpha n_{\alpha'} = -\frac{\mathcal{N}\Gamma\bar{n}^2}{2} + \Gamma\bar{n} \sum_{\alpha} n_\alpha. \quad (\text{B.8})$$

Finally, Eq. (B.8) is inserted into Eq. (B.1) and the effective mean-field Hamiltonian reads

$$\mathcal{H}^{\text{eff}}\{n_\alpha\} = (U_0 + U\Gamma\bar{n}) \sum_{\alpha} n_\alpha - \frac{\mathcal{N}U\Gamma\bar{n}^2}{2}. \quad (\text{B.9})$$

Up to now we have seen how to replace the two-body Hamiltonian of Eq. (B.1) by an effective one-body Hamiltonian, Eq. (B.9), in the context of the mean-field approximation. Note that, due to this replacement, an unknown quantity related to the average lithium concentration \bar{n} has been introduced. We will now use this effective Hamiltonian to calculate the grand canonical partition function, Eq. (B.2).

Inserting Eq. (B.9) into Eq. (B.2) gives

$$\begin{aligned}
\mathcal{Z}_{\text{gc}}(T, \mu) &= \sum_{\{n_\alpha\}} \exp \left(-\frac{(U_0 + U\Gamma\bar{n} - \mu) \sum_\alpha n_\alpha - \frac{\mathcal{N}U\Gamma\bar{n}^2}{2}}{k_B T} \right) \\
&= \exp \left(\frac{\mathcal{N}U\Gamma\bar{n}^2}{2k_B T} \right) \prod_\alpha \sum_{n_\alpha \in \{0,1\}} \exp \left(-\frac{(U_0 + U\Gamma\bar{n} - \mu)}{k_B T} n_\alpha \right) \\
&= \exp \left(\frac{\mathcal{N}U\Gamma\bar{n}^2}{2k_B T} \right) \prod_\alpha \left(1 + \exp \left(-\frac{U_0 + U\Gamma\bar{n} - \mu}{k_B T} \right) \right) \\
&= \exp \left(\frac{\mathcal{N}U\Gamma\bar{n}^2}{2k_B T} \right) \left(1 + \exp \left(-\frac{U_0 + U\Gamma\bar{n} - \mu}{k_B T} \right) \right)^{\mathcal{N}}. \tag{B.10}
\end{aligned}$$

Eq. (B.10) is further inserted into Eq. (B.3) to obtain the grand canonical potential which reads

$$\begin{aligned}
J(T, \mu) &= -k_B T \ln \mathcal{Z}_{\text{gc}}(T, \mu) \\
&= -k_B T \ln \left(\exp \left(\frac{\mathcal{N}U\Gamma\bar{n}^2}{2k_B T} \right) \left(1 + \exp \left(-\frac{U_0 + U\Gamma\bar{n} - \mu}{k_B T} \right) \right)^{\mathcal{N}} \right) \\
&= -\frac{\mathcal{N}U\Gamma\bar{n}^2}{2} - \mathcal{N}k_B T \ln \left(1 + \exp \left(-\frac{U_0 + U\Gamma\bar{n} - \mu}{k_B T} \right) \right). \tag{B.11}
\end{aligned}$$

Using this last expression the relationship between the total number of lithium ions N and the chemical potential μ , represented by Eq. (B.4), can be calculated. We obtain

$$N = -\left. \frac{\partial J(T, \mu)}{\partial \mu} \right|_T = \mathcal{N} \frac{\exp \left(-\frac{U_0 + U\Gamma\bar{n} - \mu}{k_B T} \right)}{1 + \exp \left(-\frac{U_0 + U\Gamma\bar{n} - \mu}{k_B T} \right)}$$

which is equivalent to

$$\bar{n} = \frac{1}{1 + \exp \left(\frac{U_0 + U\Gamma\bar{n} - \mu}{k_B T} \right)} \tag{B.12}$$

$$\text{with } \bar{n} = \frac{N}{\mathcal{N}}.$$

Eq. (B.12) cannot be easily solved with respect to \bar{n} but it is rather solvable straightforward with respect to μ . Eq. (B.12) is equivalent to

$$\begin{aligned}
\exp \left(-\frac{\mu}{k_B T} \right) &= \exp \left(-\frac{U_0 + U\Gamma\bar{n}}{k_B T} \right) \left(\frac{1 - \bar{n}}{\bar{n}} \right) \\
\Leftrightarrow -\frac{\mu}{k_B T} &= -\left(\frac{U_0 + U\Gamma\bar{n}}{k_B T} \right) + \ln \left(\frac{1 - \bar{n}}{\bar{n}} \right) \\
\Leftrightarrow \mu &= U_0 + U\Gamma\bar{n} + k_B T \ln \left(\frac{\bar{n}}{1 - \bar{n}} \right). \tag{B.13}
\end{aligned}$$

Finally, Eq. (B.11) and Eq. (B.13) are both inserted into Eq. (B.5) to obtain the free energy of the system in the mean-field approximation. It holds

$$\begin{aligned} F(T, N = \bar{n}\mathcal{N}) &= J(T, \mu) + \mu \bar{n}\mathcal{N} \\ &= -\frac{\mathcal{N}U\Gamma\bar{n}^2}{2} - \mathcal{N}k_B T \ln \left(1 + \exp \left(-\frac{U_0 + U\Gamma\bar{n} - \mu(T, \bar{n})}{k_B T} \right) \right) + \mu(T, \bar{n}) \bar{n}\mathcal{N} \end{aligned}$$

where $\mu(T, \bar{n})$ is given by the self-consistent relationship, Eq. (B.13). After simplification, we obtain

$$F(T, \bar{n}) = \mathcal{N} \left(U_0 \bar{n} + \frac{U\Gamma}{2} \bar{n}^2 + k_B T (\bar{n} \ln(\bar{n}) + (1 - \bar{n}) \ln(1 - \bar{n})) \right). \quad (\text{B.14})$$

C

Appendix C

Estimate of the interfacial energy term

In this appendix, we will see how to estimate the interfacial energy term κ introduced in Sec. 3.2.3. This parameter depends on the crystalline structure of the sublattice where the lithium ions have the possibility to sit when being inserted into the host material. In Sec. 3.1.1 it was shown that this sublattice made of two shifted face-centered cubic sublattices could be approximated by an “effective” cubic sublattice of lattice parameter $a = a_0$. Such an approximation obviously leads to the neglecting of several microscopic details. But, in a coarse-graining approach the knowledge of such details is not required, hence we may use this approximation in order to evaluate the parameter κ .

An estimate of the parameter κ can be obtained from the microscopic Hamiltonian Eq. (3.9) whose expression reads

$$\mathcal{H}\{n_\alpha\} = U_0 \sum_{\alpha} n_\alpha + U \sum_{\langle \alpha, \alpha' \rangle} n_\alpha n_{\alpha'} \quad (\text{C.1})$$

In the mean-field approximation introduced in Sec. 3.2.1, the correlations between the thermal fluctuations of two different interstitial site states, referred to as n_α and $n_{\alpha'}$ ($\alpha \neq \alpha'$), were neglected. By introduction of an effective constant field \bar{n} , identified to the average number of lithium occupation, it was possible to decouple the two-body interaction term,

$$U \sum_{\alpha, \alpha'} n_\alpha n_{\alpha'},$$

appearing in Hamiltonian Eq. (C.1), which further simplifies the evaluation of the thermodynamical potentials. However, by analysis of the mean-field free energy (see Sec. 3.2.2), non-physical system states were revealed pointing out the insufficiency of the mean-field approximation. To overcome this difficulty, using a coarse-graining approach, the mean-field free energy was extended in Sec. 3.2.3 by a free energy functional, Eq. (3.32), where the number of lithium occupation appears as a spatial dependent field denoted by $\mathbf{n}(\mathbf{r})$. Its expression reads

$$\begin{aligned} \Psi[\mathbf{n}(\mathbf{r}), T] = \int_{V_0} \frac{dV}{a_0^3} \left(U_0 \mathbf{n}(\mathbf{r}) + \frac{U\Gamma}{2} n^2(\mathbf{r}) + \frac{\kappa}{2} |\nabla \mathbf{n}(\mathbf{r})|^2 \right. \\ \left. + k_B T \left(\mathbf{n}(\mathbf{r}) \ln \mathbf{n}(\mathbf{r}) + (1 - \mathbf{n}(\mathbf{r})) \ln (1 - \mathbf{n}(\mathbf{r})) \right) \right). \quad (\text{C.2}) \end{aligned}$$

In the following the replacement of the microscopic Hamiltonian Eq. (C.1) by the free energy functional Eq.(C.2) will be motivated. Considering that

$$n_\alpha n_{\alpha'} = \frac{1}{2} \left(n_\alpha^2 + n_{\alpha'}^2 - (n_\alpha - n_{\alpha'})^2 \right),$$

the microscopic Hamiltonian, Eq. (C.1) first simplifies to

$$\begin{aligned} \mathcal{H}\{n_\alpha\} &= U_0 \sum_{\alpha} n_\alpha + \frac{U}{2} \sum_{\langle \alpha, \alpha' \rangle} \left(n_\alpha^2 + n_{\alpha'}^2 - (n_\alpha - n_{\alpha'})^2 \right) \\ &= U_0 \sum_{\alpha} n_\alpha + \frac{U}{2} \sum_{\langle \alpha, \alpha' \rangle} 2n_\alpha^2 - \frac{U}{2} \sum_{\langle \alpha, \alpha' \rangle} (n_\alpha - n_{\alpha'})^2 \\ &= U_0 \sum_{\alpha} n_\alpha + \frac{U}{2} \frac{\Gamma}{2} \sum_{\alpha} 2n_\alpha^2 - \frac{U}{2} \sum_{\langle \alpha, \alpha' \rangle} (n_\alpha - n_{\alpha'})^2 \\ &= U_0 \sum_{\alpha} n_\alpha + \frac{U\Gamma}{2} \sum_{\alpha} n_\alpha^2 - \frac{U}{2} \sum_{\langle \alpha, \alpha' \rangle} (n_\alpha - n_{\alpha'})^2, \end{aligned} \quad (\text{C.3})$$

where Γ refers to the number of nearest neighboring interstitial sites of a given interstitial lattice site. Since the effective sublattice available for the lithium ions is cubic, $\Gamma = 6$. Note that Eq. (C.3) being an *exact* expression of the Hamiltonian Eq. (C.1) still contains a two-body term,

$$-\frac{U}{2} \sum_{\langle \alpha, \alpha' \rangle} (n_\alpha - n_{\alpha'})^2,$$

which will be evaluated by means of a coarse-graining approach.

In this context, the microscopic variable n_α is replaced by

$$n_\alpha = n(\mathbf{r}_\alpha). \quad (\text{C.4})$$

Here, n is a function representing the number of lithium occupation and $n(\mathbf{r}_\alpha)$ denotes its evaluation at the position \mathbf{r}_α . As for the site α , the state of any arbitrary interstitial site α' , nearest neighbor of the site α is given by

$$n'_{\alpha} = n(\mathbf{r}_\alpha \pm a_0 \mathbf{e}_i) \quad (\text{C.5})$$

where $\mathbf{e}_i \in \{\mathbf{e}_x, \mathbf{e}_y, \mathbf{e}_z\}$ is a unit vector oriented along one the principal directions, the x -, y - or z -axis, of the sublattice available for the lithium ions. Assuming that the dimension of the sublattice is much larger than the lattice parameter, e.g. $\|a_0 \mathbf{e}_i\| \ll \|\mathbf{r}_\alpha\|$, the second term of Eq. (C.5) is approximated by

$$\begin{aligned} n(\mathbf{r}_\alpha \pm a_0 \mathbf{e}_i) &\approx n(\mathbf{r}_\alpha) + a_0 \left. \frac{\partial n}{\partial (\pm \mathbf{e}_i)} \right|_{\mathbf{r}_\alpha} (\pm \mathbf{e}_i) \\ &\approx n(\mathbf{r}_\alpha) + a_0 \left. \frac{\partial n}{\partial \mathbf{e}_i} \right|_{\mathbf{r}_\alpha} \mathbf{e}_i \\ &\approx n(\mathbf{r}_\alpha) + a_0 \left. \nabla n \cdot \mathbf{e}_i \right|_{\mathbf{r}_\alpha}. \end{aligned} \quad (\text{C.6})$$

Inserting Eq. (C.6) into Eq. (C.5), we have

$$n'_\alpha \approx n(\mathbf{r}_\alpha) + a_0 \nabla n \cdot \mathbf{e}_i \Big|_{\mathbf{r}_\alpha}. \quad (\text{C.7})$$

From Eq. (C.4) and Eq. (C.7), the interacting term of Hamiltonian Eq. (C.3) is first simplified to

$$\begin{aligned} -\frac{U}{2} \sum_{\langle \alpha, \alpha' \rangle} (n_\alpha - n_{\alpha'})^2 &= -\frac{U}{2} \frac{1}{2} \sum_{\alpha} \sum_{i \in \{x, y, z\}} \left(2 a_0 \nabla n \cdot \mathbf{e}_i \Big|_{\mathbf{r}_\alpha} \right)^2 \\ &= -U a_0^2 \sum_{\alpha} \nabla n(\mathbf{r}_\alpha) \cdot \nabla n(\mathbf{r}_\alpha) \\ &= -U a_0^2 \sum_{\alpha} |\nabla n(\mathbf{r}_\alpha)|^2, \end{aligned}$$

before being inserted into Eq. (C.3) which then reads

$$\mathcal{H}\{n_\alpha\} = U_0 \sum_{\alpha} n(\mathbf{r}_\alpha) + \frac{U\Gamma}{2} \sum_{\alpha} n^2(\mathbf{r}_\alpha) - U a_0^2 \sum_{\alpha} |\nabla n(\mathbf{r}_\alpha)|^2. \quad (\text{C.8})$$

Note that the Hamiltonian of the system, Eq. (C.8), now does not contain any interaction term. This term has been incorporated in a *gradient term* by means of the coarse-graining procedure. At this place, we should remark that the notations appearing in Eq. (C.8) are not mathematically properly defined. Indeed, in the same expression, both discrete and continuous operators¹ coexist.

To overcome this problem, the discrete summation in Eq. (C.8) is substituted by an integral performed over the volume of the sublattice according to

$$\sum_{\alpha} (\dots) = \int_{V_0} \frac{dV}{a_0^3} (\dots).$$

The volume element a_0^3 stands for a mesoscopic volume needed when undergoing from a discrete microscopic formulation to a continuous mesoscopic formulation. It appears a constant factor ensuring that the dimensionality of the discrete microscopic quantities and the related continuous mesoscopic quantities is the same. Thus, in our model, this factor is simply an arbitrary constant. Without losses of generalities, the volume element a_0^3 is identified to the volume occupied by a lithium ion when the average lithium concentration is equal to \bar{n} .

After this substitution has been done, the continuous formulation of Eq. (C.8), referred to as $\mathcal{E}[n(\mathbf{r})]$, holds

$$\mathcal{E}[n(\mathbf{r})] = \int_{V_0} \frac{dV}{a_0^3} \left(U_0 n(\mathbf{r}) + \frac{U\Gamma}{2} n^2(\mathbf{r}) - U a_0^2 |\nabla n(\mathbf{r})|^2 \right).$$

We further introduce

$$\kappa = -2U a_0^2,$$

and then obtain

$$\mathcal{E}[n(\mathbf{r})] = \int_{V_0} \frac{dV}{a_0^3} \left(U_0 n(\mathbf{r}) + \frac{U\Gamma}{2} n^2(\mathbf{r}) + \frac{\kappa}{2} |\nabla n(\mathbf{r})|^2 \right) \quad (\text{C.9})$$

¹The discrete summation operator \sum_{α} coexists with the continuous gradient operator ∇ .

which is identified to the system internal energy. Furthermore, the system free energy $\Psi[n(\mathbf{r})]$, equal to

$$\Psi[T, n(\mathbf{r})] = \mathcal{E}[n(\mathbf{r})] - T\mathcal{S}_0[n(\mathbf{r})] \quad (\text{C.10})$$

where $\mathcal{S}_0[n(\mathbf{r})]$ is the entropy of a *noninteracting* system of lithium ions as indicated in Sec. 3.2.3 whose expression is given by

$$\mathcal{S}_0[n(\mathbf{r})] = -k_B \int_{V_0} \frac{dV}{a_0^3} \left(n(\mathbf{r}) \ln n(\mathbf{r}) + (1 - n(\mathbf{r})) \ln (1 - n(\mathbf{r})) \right), \quad (\text{C.11})$$

according to Eq. (3.26). Finally, inserting Eqs. (C.9) - (C.11) into Eq. (C.10), we obtain

$$\begin{aligned} \Psi[n(\mathbf{r}), T] = \int_{V_0} \frac{dV}{a_0^3} \left(U_0 n(\mathbf{r}) + \frac{U\Gamma}{2} n^2(\mathbf{r}) + \frac{\kappa}{2} |\nabla n(\mathbf{r})|^2 \right. \\ \left. + k_B T \left(n(\mathbf{r}) \ln n(\mathbf{r}) + (1 - n(\mathbf{r})) \ln (1 - n(\mathbf{r})) \right) \right). \end{aligned}$$

which is identical to Eq. (C.2).

Bibliography

- [1] Bruno Scrosati. Recent advances in lithium ion battery materials. *Electrochimica Acta*, 45(15–16): 2461 – 2466, 2000.
- [2] Antti Väyrynen and Justin Salminen. Lithium ion battery production. *The Journal of Chemical Thermodynamics*, 46(0):80 – 85, 2012.
- [3] Doron Aurbach, Ella Zinigrad, Yaron Cohen, and Hanan Teller. A short review of failure mechanisms of lithium metal and lithiated graphite anodes in liquid electrolyte solutions. *Solid State Ionics*, 148(3–4):405 – 416, 2002. Proceedings of the Symposium on Materials for Advanced Batteries and Fuel Cells. Organised in conjunction with the International Conference on Materials for Advanced Technologies (ICMAT 2001).
- [4] Katerina E. Aifantis, editor. *High energy density lithium batteries : materials, engineering, applications*. Wiley-VCH, Weinheim, 2010.
- [5] Masataka Wakihara, editor. *Lithium ion batteries: fundamentals and performance*. Wiley-VCH, Weinheim, 1998. Chp. 10.
- [6] J. Vetter, P. Novák, M.R. Wagner, C. Veit, K.C. Möller, J.O. Besenhard, M. Winter, M. Wohlfahrt-Mehrens, C. Vogler, and A. Hammouche. Ageing mechanisms in lithium-ion batteries. *Journal of Power Sources*, 147(1–2):269 – 281, 2005.
- [7] D. Zhang, B.S. Haran, A. Durairajan, R.E. White, Y. Podrazhansky, and B.N. Popov. Studies on capacity fade of lithium-ion batteries. *Journal of Power Sources*, 91(2):122 – 129, 2000.
- [8] R. Spotnitz. Simulation of capacity fade in lithium-ion batteries. *Journal of Power Sources*, 113(1):72 – 80, 2003.
- [9] Jonghyun Park, Wei Lu, and Ann Marie Sastry. Numerical Simulation of Stress Evolution in Lithium Manganese Dioxide Particles due to Coupled Phase Transition and Intercalation. *Journal of The Electrochemical Society*, 158(2):A201–A206, 2011.
- [10] Qi Zhang and Ralph E. White. Calendar life study of Li-ion pouch cells. *Journal of Power Sources*, 173(2):990 – 997, 2007. X Polish Conference on Systems with Fast Ionic Transport.
- [11] S. Bach, M. Henry, N. Baffier, and J. Livage. Sol-gel synthesis of manganese oxides. *Journal of Solid State Chemistry*, 88(2):325 – 333, 1990.
- [12] P. Barboux, J.M. Tarascon, and F.K. Shokoohi. The use of acetates as precursors for the low-temperature synthesis of LiMn_2O_4 and LiCoO_2 intercalation compounds. *Journal of Solid State Chemistry*, 94(1):185 – 196, 1991.

- [13] Haifeng Wang, Young-Il Jang, Biying Huang, Donald R. Sadoway, and Yet-Ming Chiang. TEM Study of Electrochemical Cycling-Induced Damage and Disorder in LiCoO_2 Cathodes for Rechargeable Lithium Batteries. *Journal of The Electrochemical Society*, 146(2):473–480, 1999.
- [14] Di Chen, Zungsun Choi, Dominik Kramer, and Reiner Mönig. Mechanical Degradation of $\text{LiMn}_{1.95}\text{Al}_{0.05}\text{O}_4$ electrodes. *Meeting Abstracts*, MA2013-02(14):1011, 2013.
- [15] Guohua Li, Yukiko Iijima, Yoshihiro Kudo, and Hideto Azuma. Structural changes of manganese spinel at elevated temperatures. *Solid State Ionics*, 146(1–2):55 – 63, 2002.
- [16] Guohua Li, Atsuo Yamada, Yuzuru Fukushima, Kiyoshi Yamaura, Takamitsu Saito, Takuya Endo, Hideto Azuma, Koji Sekai, and Yoshio Nishi. Phase segregation of $\text{Li}_x\text{Mn}_2\text{O}_4$ ($0.6 < x < 1$) in non-equilibrium reduction processes. *Solid State Ionics*, 130(3–4):221 – 228, 2000.
- [17] Qi Zhang and Ralph E. White. Capacity fade analysis of a lithium ion cell. *Journal of Power Sources*, 179(2):793–798, 2008.
- [18] Magalie Huttin and Marc Kamlah. Phase-field modeling of stress generation in electrode particles of lithium ion batteries. *Applied Physics Letters*, 101:133902, 2012.
- [19] J.M. Tarascon and M. Armand. Issues and challenges facing rechargeable lithium batteries. *Nature*, 414(6861):359–367, 2001.
- [20] Martin Winter, Jürgen O. Besenhard, Michael E. Spahr, and Petr Novák. Insertion Electrode Materials for Rechargeable Lithium Batteries. *Advanced Materials*, 10(10):725–763, 1998.
- [21] M. Endo, C. Kim, K. Nishimura, T. Fujino, and K. Miyashita. Recent development of carbon materials for Li ion batteries. *Carbon*, 38(2):183 – 197, 2000.
- [22] Diego Lisbona and Timothy Snee. A review of hazards associated with primary lithium and lithium-ion batteries. *Process Safety and Environmental Protection*, 89(6):434 – 442, 2011.
- [23] Han Eol Park, Chang Hyun Hong, and Woo Young Yoon. The effect of internal resistance on dendritic growth on lithium metal electrodes in the lithium secondary batteries. *Journal of Power Sources*, 178(2):765 – 768, 2008.
- [24] Jeffrey W. Fergus. Recent developments in cathode materials for lithium ion batteries. *Journal of Power Sources*, 195(4):939–954, 2010.
- [25] A. K. Padhi, K. S. Nanjundaswamy, and J. B. Goodenough. Phospho-olivines as Positive-Electrode Materials for Rechargeable Lithium Batteries. *Journal of The Electrochemical Society*, 144(4):1188–1194, 1997.
- [26] M. M. Thackeray. Structural Considerations of Layered and Spinel Lithiated Oxides for Lithium Ion Batteries. *Journal of The Electrochemical Society*, 142(8):2558–2563, 1995.
- [27] J. M. Tarascon, E. Wang, F. K. Shokoohi, W. R. McKinnon, and S. Colson. The Spinel Phase of LiMn_2O_4 as a Cathode in Secondary Lithium Cells. *Journal of The Electrochemical Society*, 138(10):2859–2864, 1991.

- [28] Dong H. Jang and Seung M. Oh. Electrolyte Effects on Spinel Dissolution and Cathodic Capacity Losses in 4 V Li / $\text{Li}_x\text{Mn}_2\text{O}_4$ Rechargeable Cells. *Journal of The Electrochemical Society*, 144(10):3342–3348, 1997.
- [29] Takayuki Aoshima, Kenji Okahara, Chikara Kiyohara, and Kenji Shizuka. Mechanisms of manganese spinels dissolution and capacity fade at high temperature. *Journal of Power Sources*, 97–98(0):377 – 380, 2001.
- [30] John Christensen and John Newman. Stress generation and fracture in lithium insertion materials. *Journal of Solid State Electrochemistry*, 10:293–319, 2006.
- [31] John Christensen and John Newman. A Mathematical Model of Stress Generation and Fracture in Lithium Manganese Oxide. *Journal of The Electrochemical Society*, 153(6):A1019–A1030, 2006.
- [32] B.C. Han, A. Van der Ven, D. Morgan, and G. Ceder. Electrochemical modeling of intercalation processes with phase field models. *Electrochimica Acta*, 49(26):4691 – 4699, 2004.
- [33] Pankaj Arora, Ralph E. White, and Marc Doyle. Capacity Fade Mechanisms and Side Reactions in Lithium-Ion Batteries. *Journal of The Electrochemical Society*, 145(10):3647–3667, 1998.
- [34] Tsutomu Ohzuku, Masaki Kitagawa, and Taketsugu Hirai. Electrochemistry of Manganese Dioxide in Lithium Nonaqueous Cell: III. X-Ray Diffractational Study on the Reduction of Spinel-Related Manganese Dioxide. *Journal of The Electrochemical Society*, 137(3):769–775, 1990.
- [35] W. Liu, K. Kowal, and G. C. Farrington. Mechanism of the Electrochemical Insertion of Lithium into LiMn_2O_4 Spinels. *Journal of The Electrochemical Society*, 145(2):459–465, 1998.
- [36] X. Q. Yang, X. Sun, S. J. Lee, J. McBreen, S. Mukerjee, M. L. Daroux, and X. K. Xing. In Situ Synchrotron X-Ray Diffraction Studies of the Phase Transitions in $\text{Li}_x\text{Mn}_2\text{O}_4$ Cathode Materials. *Electrochemical and Solid-State Letters*, 2(4):157–160, 1999.
- [37] K. Raveendranath, J. Ravi, R.M. Tomy, S. Jayalekshmi, R.V. Mangalaraja, and S.T. Lee. Evidence of Jahn-Teller distortion in $\text{Li}_x\text{Mn}_2\text{O}_4$ by thermal diffusivity measurements. *Applied Physics A*, 90:437–440, 2008.
- [38] A. Van der Ven, C. Marianetti, D. Morgan, and G. Ceder. Phase transformations and volume changes in spinel $\text{Li}_x\text{Mn}_2\text{O}_4$. *Solid State Ionics*, 135(1–4):21 – 32, 2000. Proceedings of the 12th International Conference on Solid State.
- [39] Gerbrand Ceder and Anton Van der Ven. Phase diagrams of lithium transition metal oxides: investigations from first principles. *Electrochimica Acta*, 45(1-2):131 – 150, 1999.
- [40] Abiko Hironobu, Hibino Mitsuhiro, and Kudo Tetsuichi. Phase transition observed in potential-composition profiles of $\text{Li}_x\text{Mn}_2\text{O}_4$. *Journal of Power Sources*, 124(2):526 – 532, 2003.
- [41] Xiangchun Zhang, Wei Shyy, and Ann Marie Sastry. Numerical Simulation of Intercalation-Induced Stress in Li-Ion Battery Electrode Particles. *Journal of The Electrochemical Society*, 154(10):A910–A916, 2007.
- [42] C. M. Doyle. *Design and Simulation of Lithium Rechargeable batteries*. PhD thesis, University of California, Berkeley, CA, 1995.

- [43] S. Prussin. Generation and Distribution of Dislocations by Solute Diffusion. *Journal of Applied Physics*, 32(10):1876–1881, 1961.
- [44] Jeong Hun, Myoungdo Chung, Myounggu Park, Sang Woo, Xiangchun Zhang, and Ann Marie Sastry. Generation of Realistic Particle Structures and Simulations of Internal Stress: A Numerical/AFM Study of LiMn_2O_4 Particles. *Journal of The Electrochemical Society*, 158(4):A434–A442, 2011.
- [45] M. D. Chung, J. H. Seo, X. C. Zhang, and A. M. Sastry. Implementing Realistic Geometry and Measured Diffusion Coefficients into Single Particle Electrode Modeling Based on Experiments with Single LiMn_2O_4 Spinel Particles. *Journal of The Electrochemical Society*, 158(4):A371–A378, 2011.
- [46] Y.-H. Chen, C.-W. Wang, G. Liu, X.-Y. Song, V. S. Battaglia, and A. M. Sastry. Selection of conductive additives in li-ion battery cathodes. *Journal of The Electrochemical Society*, 154(10):A978–A986, 2007.
- [47] T. Mori and K. Tanaka. Average stress in matrix and average elastic energy of materials with misfitting inclusions. *Acta Metallurgica*, 21(5):571 – 574, 1973.
- [48] Stephanie Golmon, Kurt Maute, and Martin L. Dunn. Numerical modeling of electrochemical-mechanical interactions in lithium polymer batteries. *Computers & Structures*, 87(23–24):1567 – 1579, 2009.
- [49] R. Edwin Garcja, Yet-Ming Chiang, W. Craig Carter, Pimpa Limthongkul, and Catherine M. Bishop. Microstructural Modeling and Design of Rechargeable Lithium-Ion Batteries. *Journal of The Electrochemical Society*, 152(1):A255–A263, 2005.
- [50] Helmut Mehrer. *Diffusion in solids : fundamentals, methods, materials, diffusion-controlled processes; with 27 tables*. Springer series in solid-state sciences ; 155. Springer, Berlin, 2007.
- [51] Deyuan Fan and Ralph E. White. Mathematical Modeling of a Nickel-Cadmium Battery: Effects of Intercalation and Oxygen Reactions. *Journal of The Electrochemical Society*, 138(10):2952–2960, 1991.
- [52] G.G. Amatucci, C.N. Schmutz, A. Blyr, C. Sigala, A.S. Gozdz, D. Larcher, and J.M. Tarascon. Materials’ effects on the elevated and room temperature performance of C/ LiMn_2O_4 Li-ion batteries. *Journal of Power Sources*, 69(1–2):11 – 25, 1997.
- [53] Eberhard Klingbeil. *Tensorrechnung für Ingenieure*. BI-Hochschultaschenbücher ; 197. BI-Wiss.-Verl., Mannheim, 2., überarb. Aufl. edition, 1989.
- [54] Venkat R. Subramanian and Ralph E. White. New separation of variables method for composite electrodes with galvanostatic boundary conditions. *Journal of Power Sources*, 96(2):385 – 395, 2001.
- [55] Ester Bohn. *Partikel-Modell für Lithium-Diffusion und mechanische Spannungen einer Interkalationselektrode*. PhD thesis, Karlsruher Institut für Technologie, Karlsruhe, 2011.

-
- [56] Marc Doyle, John Newman, Antoni S. Gozdz, Caroline N. Schmutz, and Jean-Marie Tarascon. Comparison of Modeling Predictions with Experimental Data from Plastic Lithium Ion Cells. *Journal of The Electrochemical Society*, 143(6):1890–1903, 1996.
- [57] J.M. Tarascon and D. Guyomard. New electrolyte compositions stable over the 0 to 5 V voltage range and compatible with the $\text{Li}_{1+x}\text{Mn}_2\text{O}_4$ /carbon Li-ion cells. *Solid State Ionics*, 69(3–4):293 – 305, 1994.
- [58] John Newman and William Tiedemann. Porous-electrode theory with battery applications. *AIChE Journal*, 21(1):25–41, 1975.
- [59] John S. Newman and Karen E. Thomas-Alyea. *Electrochemical systems*. Wiley, Hoboken, NJ, 3. ed. edition, 2004. Chp. 22.
- [60] D. A. G. Bruggeman. Berechnung verschiedener physikalischer Konstanten von heterogenen Substanzen. I. Dielektrizitätskonstanten und Leitfähigkeiten der Mischkörper aus isotropen Substanzen. *Annalen der Physik*, 416(7):636–664, 1935.
- [61] John S. Newman and Karen E. Thomas-Alyea. *Electrochemical systems*. Wiley, Hoboken, NJ, 3. ed. edition, 2004. Chp. 11.
- [62] Marc Doyle, Thomas F. Fuller, and John Newman. The importance of the lithium ion transference number in lithium/polymer cells. *Electrochimica Acta*, 39(13):2073 – 2081, 1994.
- [63] Heike Emmerich. *The Diffuse Interface Approach in Materials Science : Thermodynamic Concepts and Applications of Phase-Field Models*. Lecture Notes in Physics, Monographs; 73. Springer-Verlag Berlin Heidelberg, Berlin, Heidelberg, 2003.
- [64] Michael Tinkham. *Introduction to superconductivity*. Dover books on physics. Dover Publ., Mineola, NY, 2. ed. edition, 2004.
- [65] Nele Moelans, Bart Blanpain, and Patrick Wollants. An introduction to phase-field modeling of microstructure evolution. *Calphad*, 32(2):268 – 294, 2008.
- [66] C. N. Yang and T. D. Lee. Statistical Theory of Equations of State and Phase Transitions. I. Theory of Condensation. *Phys. Rev.*, 87:404–409, Aug 1952.
- [67] T. D. Lee and C. N. Yang. Statistical Theory of Equations of State and Phase Transitions. II. Lattice Gas and Ising Model. *Phys. Rev.*, 87:410–419, Aug 1952.
- [68] Benjamin Völker. *Phase-field modeling for ferroelectrics in a multi-scale approach*. PhD thesis, Karlsruher Institut für Technologie (KIT), Karlsruhe, 2011.
- [69] Wenwu Cao and L. E. Cross. Theory of tetragonal twin structures in ferroelectric perovskites with a first-order phase transition. *Phys. Rev. B*, 44:5–12, Jul 1991.
- [70] Cahn John W. and Hilliard John E. Free Energy of a Nonuniform System I. Interfacial Free Energy. *The journal of Chemical Physics*, 28:258–267, 1958.
- [71] Morton E. Gurtin. Generalized Ginzburg-Landau and Cahn-Hilliard equations based on a micro-force balance. *Physica D: Nonlinear Phenomena*, 92(3–4):178 – 192, 1996.
-

- [72] W.R. McKinnon and R.R. Haering. Physical Mechanisms of Intercalation. In Ralph E. White, J.O'M. Bockris, and B.E. Conway, editors, *Modern Aspects of Electrochemistry*, pages 235–304. Springer US, 1983.
- [73] Paul M. Chaikin and T. C. Lubensky. *Principles of condensed matter physics*. Cambridge Univ. Press, Cambridge, 1. paperback ed., repr. edition, 2003.
- [74] Daniel Sherwood and Bosco Emmanuel. A Madelung-Buckingham Model for the Variation of the Cubic Lattice Constant of $\text{Li}_x\text{Mn}_2\text{O}_4$ during the charge and discharge of the Lithium-ion Battery. 2004. arXiv:cond-mat/0403163v2.
- [75] A. S. Wills, N. P. Raju, C. Morin, and J. E. Greedan. Two-Dimensional Short-Range Magnetic Order in the Tetragonal Spinel $\text{Li}_2\text{Mn}_2\text{O}_4$. *Chemistry of Materials*, 11(7):1936–1941, 1999.
- [76] A. S. Wills, N. P. Raju, and J. E. Greedan. Low-Temperature Structure and Magnetic Properties of the Spinel $\text{Li}_x\text{Mn}_2\text{O}_4$: A Frustrated Antiferromagnet and Cathode Material. *Chemistry of Materials*, 11(6):1510–1518, 1999.
- [77] David M. Pickup, Daniel Simon, Michael Fookan, Horst Krampitz, Ernst R. H. van Eck, and Erik M. Kelder. ^6Li MAS NMR study of stoichiometric and chemically delithiated $\text{Li}_x\text{Mn}_2\text{O}_4$ spinels. *J. Mater. Chem.*, 13:963–968, 2003.
- [78] Y. Liu, T. Fujiwara, H Yukawa, and M Morinaga. Chemical bonding in lithium intercalation compound $\text{Li}_x\text{Mn}_2\text{O}_4$ ($x=0,1,2$). *Electrochimica Acta*, 46(8):1151 – 1159, 2001.
- [79] Kenji Tateishi, Douglas du Boulay, and Nobuo Ishizawa. The effect of mixed Mn valences on Li migration in LiMn_2O_4 spinel: A molecular dynamics study. *Applied Physics Letters*, 84:529, 2004.
- [80] M. M. Thackeray, Y. Shao-Horn, A. J. Kahaian, K. D. Kepler, E. Skinner, J. T. Vaughery, and S. A. Hackney. Structural Fatigue in Spinel Electrodes in High Voltage (4 V) Li / $\text{Li}_x\text{Mn}_2\text{O}_4$ Cells. *Electrochemical and Solid-State Letters*, 1(1):7–9, 1998.
- [81] M. D. Levi, K. Gamolsky, D. Aurbach, U. Heider, and R. Oesten. Evidence for Slow Droplet Formation during Cubic-to-Tetragonal Phase Transition in $\text{Li}_x\text{Mn}_2\text{O}_4$ Spinel. *Journal of The Electrochemical Society*, 147(1):25–33, 2000.
- [82] Hironobu Abiko, Mitsuhiro Hibino, and Tetsuichi Kudo. Temperature Dependence of the Potential-Composition Profiles of $\text{Li}_x\text{Mn}_2\text{O}_4$ Spinel. *Electrochemical and Solid-State Letters*, 1(3):114–116, 1998.
- [83] Yuan Gao, J. N. Reimers, and J. R. Dahn. Changes in the voltage profile of $\text{Li}/\text{Li}_{1+x}\text{Mn}_{2-x}\text{O}_4$ cells as a function of x . *Phys. Rev. B*, 54:3878–3883, 1996.
- [84] T. Kudo and M. Hibino. Theoretical dependences of the free energy and chemical potential upon composition in intercalation systems with repulsive interaction between guest ions. *Electrochimica Acta*, 43(7):781 – 789, 1997.
- [85] S. Thomas Lee, K. Raveendranath, Rajive M. Tomy, Nibu A. George, S. Jayalekshmi, and Jyotsna Ravi. Evidence of band structure modification due to Jahn-Teller distortion in $\text{Li}_x\text{Mn}_2\text{O}_4$ by photoacoustic spectroscopy. *Journal of Physics D: Applied Physics*, 40(12):3807, 2007.

-
- [86] Kaoru Miura, Atsuo Yamada, and Masahiro Tanaka. Electric states of spinel $\text{Li}_x\text{Mn}_2\text{O}_4$ as a cathode of the rechargeable battery. *Electrochimica Acta*, 41(2):249 – 256, 1996.
- [87] Kiyoshi Kanamura, Hidetoshi Naito, Takeshi Yao, and Zen-ichiro Takehara. Structural change of the LiMn_2O_4 spinel structure induced by extraction of lithium. *J. Mater. Chem.*, 6:33–36, 1996.
- [88] Do Kyung Kim, P. Muralidharan, Hyun-Wook Lee, Riccardo Ruffo, Yuan Yang, Candace K. Chan, Hailin Peng, Robert A. Huggins, and Yi Cui. Spinel LiMn_2O_4 Nanorods as Lithium Ion Battery Cathode. *Nano Letters*, 8(11):3948–3952, 2008.
- [89] Helena Berg, Erik M. Kelder, and John O. Thomas. Neutron diffraction study of stoichiometric spinel $\text{Li}_{1+x}\text{Mn}_2\text{O}_4$ showing octahedral 16c-site Li-occupation. *J. Mater. Chem.*, 9:427–429, 1999.
- [90] H. Berg and J.O. Thomas. Neutron diffraction study of electrochemically delithiated LiMn_2O_4 spinel. *Solid State Ionics*, 126(3–4):227 – 234, 1999.
- [91] K. Binder. Theory of first-order phase transitions. *Reports on Progress in Physics*, 50(7):783, 1987.
- [92] Ken Suzuki, Yasunori Oumi, Seiichi Takami, Momoji Kubo, Akira Miyamoto, Masahiro Kikuchi, Nobuyuki Yamazaki, and Muneo Mita. Structural Properties of $\text{Li}_x\text{Mn}_2\text{O}_4$ as Investigated by Molecular Dynamics and Density Functional Theory. *Japanese Journal of Applied Physics*, 39 (Part 1, No. 7B):4318–4322, 2000.
- [93] C. Y. Ouyang, S. Q. Shi, Z. X. Wang, H. Li, X. J. Huang, and L. Q. Chen. Ab initio molecular-dynamics studies on $\text{Li}_x\text{Mn}_2\text{O}_4$ as cathode material for lithium secondary batteries. *EPL (Europhysics Letters)*, 67(1):28, 2004.
- [94] Masataka Wakihara, editor. *Lithium ion batteries: fundamentals and performance*. Wiley-VCH, Weinheim, 1998. Chp. 2.
- [95] E. V. Vakarin, A. E. Filippov, and J. P. Badiali. Distortion of a Substrate Induced by Adsorption at Solid-Liquid Interfaces. *Phys. Rev. Lett.*, 81:3904–3907, Nov 1998.
- [96] Qi-Hui Wu. *Photoelectron Spectroscopy of Intercalation Phases: Na and Li in V_2O_5 Thin Films and LiMn_2O_4* . PhD thesis, Darmstadt University of Technology, Darmstadt, 2003.
- [97] R. A. Johnson. Relationship between Two-Body Interatomic Potentials in a Lattice Model and Elastic Constants. *Phys. Rev. B*, 6:2094–2100, Sep 1972.
- [98] R. A. Johnson. Relationship between two-body interatomic potentials in a lattice model and elastic constants. II. *Phys. Rev. B*, 9:1304–1308, Feb 1974.
- [99] E.V. Vakarin and J.P. Badiali. Cation intercalation under a host restructuring. Application to crystalline Li_xWO_3 and Na_xWO_3 compounds. *Electrochimica Acta*, 46(26–27):4151 – 4157, 2001.
- [100] Torsten Fließbach. *Lehrbuch zur theoretischen Physik*, volume 4: Statistische Physik. Elsevier, Spektrum Akademischer Verl., Heidelberg, 4. aufl. edition, 2007.
- [101] Evgenij M. Lifšic and Lev P. Pitaevskij. *Course of theoretical physics*, volume Vol. 5: Statistical physics, Pt. 1. 3. ed., revised and enlarged, reprint. edition, 2001.
-

- [102] Kerson Huang. *Statistical mechanics*. Wiley, New York, 2. ed. edition, 1987.
- [103] Daniel H. Rothman and Stéphane Zaleski. Lattice-gas models of phase separation: interfaces, phase transitions, and multiphase flow. *Rev. Mod. Phys.*, 66:1417–1479, Oct 1994.
- [104] John W. Cahn. On spinodal decomposition. *Acta Metallurgica*, 9(9):795 – 801, 1961.
- [105] J. Hubbard. Calculation of partition functions. *Phys. Rev. Lett.*, 3:77–78, Jul 1959.
- [106] Santi Prestipino and Paolo V. Giaquinta. Statistical Entropy of a Lattice-Gas Model: Multiparticle Correlation Expansion. *Journal of Statistical Physics*, 96:135–167, 1999.
- [107] M.G. Donato, S. Prestipino, and P.V. Giaquinta. Entropy and multi-particle correlations in two-dimensional lattice gases. *The European Physical Journal B - Condensed Matter and Complex Systems*, 11:621–627, 1999.
- [108] Alexander Altland and Ben D. Simons. *Condensed matter field theory*. Cambridge Univ. Press, Cambridge, 2. ed. edition, 2012. Chp. 5.
- [109] Lev D. Landau and Evgenij M. Lifšic. *Lehrbuch der theoretischen Physik*, volume 7: Elastizitätstheorie. Akad.-Verl., Berlin, 7., unveränd. aufl. edition, 1991. Aus dem Russ. übers.
- [110] John F. Nye. *Physical properties of crystals: Their representation by tensors and matrices*. Clarendon Pr., Oxford, 1. ed. edition, 1957.
- [111] Margrit Hanbücken, editor. *Mechanical stress on the nanoscale: simulation, material systems and characterization techniques*. Wiley-VCH, Weinheim, 2011.
- [112] Akira Onuki. Ginzburg-Landau Approach to Elastic Effects in the Phase Separation of Solids. *Journal of the Physical Society of Japan*, 58(9):3065–3068, 1989.
- [113] Akira Onuki. *Phase transition dynamics*. Cambridge University Press, Cambridge, 1. publ. edition, 2002. Chp. 10.
- [114] Charles M. Elliott and Zheng Songmu. On the Cahn-Hilliard equation. *Archive for Rational Mechanics and Analysis*, 96(4):339–357, 1986.
- [115] Stanislaus Maier-Paape, Ullrich Miller, Konstantin Mischaikow, and Thomas Wanner. Rigorous numerics for the Cahn-Hilliard equation on the unit square. *Revista matemática complutense*, 21(2):351–426, 2008.
- [116] David Bettinson and George Rowlands. Stability of the two- and three-dimensional kink solutions to the Cahn-Hilliard equation. *Phys. Rev. E*, 55:5427–5432, May 1997.
- [117] Eberhard Klingbeil. *Variationsrechnung*. BI-Wiss.-Verl., Mannheim, 2. überarb. aufl. edition, 1988.
- [118] M.D Levi and D Aurbach. Frumkin intercalation isotherm — a tool for the description of lithium insertion into host materials: a review. *Electrochimica Acta*, 45(1-2):167 – 185, 1999.
- [119] L. Ramírez-Piscina, A. Hernández-Machado, and J. M. Sancho. Fluctuations in domain growth: Ginzburg-Landau equations with multiplicative noise. *Phys. Rev. B*, 48:119–124, Jul 1993.

- [120] Wolfgang Dreyer, Clemens Gohlke, and Robert Huth. The behavior of a many-particle electrode in a lithium-ion battery. *Physica D: Nonlinear Phenomena*, 240(12):1008 – 1019, 2011.
- [121] G. E. Grechnev, R. Ahuja, B. Johansson, and O. Eriksson. Electronic structure, magnetic, and cohesive properties of $\text{Li}_x\text{Mn}_2\text{O}_4$: Theory. *Phys. Rev. B*, 65:174408, Apr 2002.
- [122] A Paolone, R Cantelli, G Rousse, and C Masquelier. The charge order transition and elastic/anelastic properties of LiMn_2O_4 . *Journal of Physics: Condensed Matter*, 15(3):457, 2003.
- [123] Yue Qi, Haibo Guo, Louis G. Hector, and Adam Timmons. Threefold Increase in the Young's Modulus of Graphite Negative Electrode during Lithium Intercalation. *Journal of The Electrochemical Society*, 157(5):A558–A566, 2010.
- [124] V.B. Shenoy, P. Johari, and Y. Qi. Elastic softening of amorphous and crystalline Li-Si Phases with increasing Li concentration: A first-principles study. *Journal of Power Sources*, 195(19): 6825 – 6830, 2010.
- [125] Thomas Maxisch and Gerband Ceder. Elastic properties of olivine Li_xFePO_4 from first principles. *Phys. Rev. B*, 73:174112, May 2006.
- [126] Rutooj Deshpande, Yue Qi, and Yang-Tse Cheng. Effects of Concentration-Dependent Elastic Modulus on Diffusion-Induced Stresses for Battery Applications. *Journal of The Electrochemical Society*, 157(8):A967–A971, 2010.
- [127] Rutooj D. Deshpande. *Understanding and improving lithium-ion batteries through mathematical modeling and experiments*. PhD thesis, University of Kentucky, Lexington, KY, 2011.

Acknowledgment

The present thesis has been realized at the Institute for Applied Materials (IAM-WBM) of the Karlsruhe Institute of Technology (KIT).

During my PhD, I met so many people who have directly and indirectly contributed to this work and at this place I want to express them all my gratitude.

First I owe my deepest gratitude to my supervisor Prof. Dr. Marc Kamlah for giving me the opportunity to work on such an interesting project. Especially I am thankful for the inspiring and fruitful discussions, for his encouragement but also for the freedom he gave me during my work. I could not imagine having a better mentor for my thesis.

I would like to thank all the members of my thesis committee, Prof. Dr. H. J. Seifert and Prof. Dr. C. Proppe. I am especially grateful to Prof. Dr. H. J. Seifert for accepting to be the second referee.

Furthermore, I would like to thank all my colleagues not only for the friendly atmosphere at the institute but also for supporting me whenever I needed help. In particular I thank my office mates: Shuo Zhao, Ratna Kumar Annabattula, Di Chen who all contribute to the open and excellent atmosphere needed for doing research. At this place, I would like to give a special mention to Ratna Kumar Annabattula for his readiness to help me when I had problems by running Linux.

I here acknowledge all the members of Marc Kamlah's group I worked with over the years: Benjamin Völker, Holger Schwaab, Ratna Kumar Annabattula, Manuel Feuchter, Julia Ott. Here, I especially thank Benjamin Völker with whom I worked before I begin my thesis and who helped me when I learnt using Comsol.

It is also a pleasure to thank all my friends and my family for their support, and especially my best friend and flat mate Pablo Robert for listening to me and for his efforts to entertain me. Finally, I express my loving thanks to Stéphane Ngo Dinh. He always was here for me during this time and supported me in any possible ways: with his valuable advice, with fruitful discussions, with proofreading the manuscript, with his continuous encouragement and still so much. Thank you from the bottom of my heart.